Development of *In-Vitro* Models of the Bone Marrow Stem Cell Niche

Christian Albert James Mifsud

May 2025

A thesis submitted in partial fulfilment of the

requirements of Nottingham Trent University

for the degree of Doctor of Philosophy

Acknowledgments

Firstly, I would like to thank Dr Glen Kirkham, my Director of Studies for all the aid I have received throughout my PhD. His empathetic care and support through the highs and lows of my time at NTU have been beyond appreciation. I thank him for giving me the opportunity to complete a PhD, a dream I have had for as long as I can recall.

I would also like to thank my closest friends and lab mates, Nick Weir, Lydia Hardowar, Max Pickup, Laura Leston, Nacho Rodriguez and Bisher Shibani whose camaraderie through the rigors of PhD life made the journey enjoyable. In particular, I would like to thank Max for teaching me everything I know about RTq-PCR and for always being willing to lend and ear when I needed it most.

I thank both Dr Graham Hickman and Dominic Craske for their expert support with microscopy, and Dr Biola Egbowon for all her aid supporting us in IBRC. I would also like to thank Prof Miles Padgett and Dr Graham Gibson for all their support with the holographic optical tweezers, thank Prof Matthew Dalby for support with the Nanokick and Dr Richard Hulse for supplying the animal cadavers.

Finally, I would like to thank my parents, Dr Albert Mifsud and Mrs Susan Mifsud, and my sisters, Dr Cecilia Mifsud and Miss Gabriella Mifsud for all their help, love and encouragement. Without all their love and support I would not be where I am today. I am forever grateful, and I hope I have made them all proud.

Abstract

The bone marrow stem cell niche is a complex microenvironment with osteogenic and haematopoietic lineage cells, generated from differentiation of haematopoietic and mesenchymal stem cells (MSCs). A niche is defined by its cells, microenvironment, physical and chemical interactions. The niche is not fully understood with respect to the cellular components, location, and internal interactions. In this study, to develop the understanding of the biological structure and systems underpinning the niche, models were developed focusing on the osteogenic lineage. There is the potential for this work to inform the development of therapeutics, supporting the development of therapeutics in the future.

A fully realised, novel model was developed at the macroscopic level, integrating MSCs and human osteosarcoma (HOS) cells in co-culture, seeded onto a scaffold of decellularised rat bone with mechanical stimulation and cultured in osteogenic media. A model at the microscopic level was then developed utilising cellular control in a manner and extent not previously developed. This was accomplished utilising micro-manipulation techniques using holographic optical tweezers (HOTs) based micromanipulation technique, bespoke equipment that can manipulate cells and other objects in 3D space, allowing the precise positioning of MSCs and HOS on a fragment of decellularised rat bone.

In the macroscopic model, cells, extracellular matrix, and physical and chemical stimuli were incorporated, and a highly significant increase in osteogenic content was detected in comparison with controls. This novel model could be used to understand the complex interactions within the niche better and can be used in drug testing. For the microscopic model, a dynamic patterning system to reproduce two cell types independently and reproducibly in the same dish was developed, allowing MSC and HOS to be patterned together. The use of HOTs in this model allows novel insights into the biological microenvironment of the niche and has great potential to help determine cellular microenvironment function in a wide variety of tissue types.

Abbreviations

Basal media	BM
Basic multicellular unit	BMU
Bone gamma-carboxyglutamic acid-containing protein	*BGLAP*
Bone morphogenetic protein	BMP
Bovine serum albumin	BSA
Cluster Differentiation	CD
Complimentary DNA	cDNA
Computer aided design	CAD
Diamidino-2-phenylindole	DAPI
Dimethyl sulfoxide	DMSO
Distilled deionised water	ddH_2O
Dulbecco's Modified Eagle Medium	DMEM
Embryonic basal media	eBM
Extracellular matrix	ECM
Feeder free mouse embryonic stem cell	ff-mESC
Fetal bovine serum	FBS
Fibroblast growth factor 2	FGF-2
Glyceraldehyde-3-phosphate dehydrogenase	*GAPDH*
Green fluorescent protein	GFP
Haematopoietic stem cells	HSC
Holographic optical tweezers	HOTs
Human mesenchymal stem cell(s)	hMSC(s)
Human osteosarcoma	HOS
Immortalised human mesenchymal stem cell(s)	ihMSC(s)

Immunohistochemical	IHC
Industrial methylated spirit	IMS
Insulin-like growth factor	IGF
L-ascorbic acid	VIT C
Leukaemia inhibitory factor	LIF
L-glutamine	L-g
Mesenchymal cell growth supplement	MCGS
Mesenchymal stem cell basal medium	MSCBM
Mesenchymal stem cell growth media	MSCGM
Mesenchymal stem cell(s)	MSC(s)
Oligomeric proanthocyanidins	OPC
Osteocalcin	OCN
Osteoconductive media	OCM
Osteopontin	OPN
Parathyroid hormone	PTH
Penicillin/Streptomycin	P/S
Phosphate-buffered saline	PBS
Poly lactic-co-glycolic acid	PLGA
Real-time quantitative polymerase chain reaction	RT-qPCR
Ribonucleic acid	RNA
Runt-related transcription factor 2	*RUNX2*
Sarcoma osteogenic	SaOS-2
Scanning electron microscope	SEM
Secreted phosphoprotein 1	*SPP1*
Spatial light modulator	SLM
Texus red	TXR
Threshold cycle	Ct

Transforming growth factor–β	TGF-β
Ultraviolet	UV
Vascular endothelial growth factors	VEGF
Volume/volume	v/v
Weight/volume	w/v
β-glycerophosphate	β-gp

Contents

List of Figures

1. Introduction

Scientific modelling is the process of constructing and analysing a simplified representation of a system. Models can be physical, mathematical, or computational in nature and can be used to explore hypotheses, predict outcomes, test theories or understand a system better. Biological models are used to explore a wide range of scientific questions, from molecular and cellular mechanisms underlying biological processes, to the dynamics of biological niches in the human body. They can be used to predict how biological systems will behave under different conditions and to test hypotheses that are difficult or impossible to study *in vivo*. During experimentation into the design and evaluation of a model of the bone marrow stem cell niche, an appreciation and understanding of the field is important. This chapter covers the biology of human bone and bone marrow, cellular scaffolds, and the history and science of the optical trap, precursor to the holographic optical tweezers (HOTs).

1.1 Bone Function and Morphology

The adult human skeleton is made up of 206 bones, which provide structural support, protect vital organs and enable movement (Cowan et al., 2024). Bones are connected to each other at joints, which allow for varying degrees of movement depending on the joint type. Hinge joints, for example, as seen in the elbow, allow for movement in a single direction, while ball-and-socket joints, such as the shoulder, allow a wider range of multidirectional motion. Bones are connected to muscles by tendons, tough bands of connective tissue primarily consisting of collagen I fibres. When muscles contract, they pull on the tendons, which in turn move the attached bone. Ligaments are another form of connective tissue, connecting bones to other bones at the joints, stabilising and supporting the skeleton.

1.1.1 Overall Function

The skeleton is divided into two main parts, the axial skeleton, which includes the skull, spine, and rib cage, and the appendicular skeleton, which consists of the limbs and girdles (such as the hip and shoulder bones) that attach them to the axial skeleton (Clarke, 2008a).Bone is not a uniform tissue but consists of both organic and mineral phases. It can be categorised as a connective tissue and (rigid) organ which, along with cartilage, makes up the endoskeleton of animals. Bones have a multitude of functions including structural support, enabling mobility through muscle anchor points, organ protection such as the rib cage protecting the heart and lungs, production of blood cells and mineral storage. Bones change over the human lifespan, going through a process of remodelling which involves the resorption of old or damaged bone and the deposition of new bone (Rowe et al., 2023).

1.1.2 Bone Structure

In order to understand the composition of bone, it is worth considering its structure from the smallest elements and follow its structural formation as more complex architecture forms. An understanding of the bone at all levels, from skeletal to microarchitecture is important for understanding the system, and key for model development.

Collagen encompasses approximately 90% of protein found in bone with type I being the most plentiful of said proteins (Mohamed, 2008). At its most basic level, bone is made up of collagen fibrils which have been mineralised. Type I collagen fibrils are made of three polypeptide alpha chains formed into a triple helical structure (Kadler et al., 1996). These fibrils are mineralised with a carbonated apatite called dahllite which is the only mineral type found in mature bone (Weiner & Wagner, 1998). The remaining major component of bone is water. Found in the intra and extrafibrillar space (Katz & Li, 1973), water provides a source of various ions for metabolism, as well as providing structural support, varying in quantity between different bone types (Timmins & Wall, 1977). At the next hierarchical level, the mineralized collagen fibrils align in different directions with different degrees of alignment

along their length (Reznikov et al., 2014). The structures vary, forming the optimal configuration for functional needs such as withstanding tensional or compressive force. When taking a parallel array formation, the fibrils form what is known as lamellar bone, which is mechanically strong.

Unlike other mineralised collagens such as dentine, bone goes through a remodelling process having two main stages of formation: primary and secondary osteogenesis. It is through this two stage process that lamellar bone is formed, as this bone type is not initially present during fetal development. Formed primarily during embryonic development, woven bone has a disorganised fibril arrangement which is replaced by lamellar bone during the first three to four years of life (Fuchs et al., 2019). Lamellar bone has greater stiffness than woven and, as such is the primary building block of human bone at the microscopic level.

When moving up to the macroscopic level, bone takes two forms: cortical bone (also called compact bone) and cancellous bone (also called trabecular or spongy bone). The two bone types are often formed next to each other, such as in long and flat bones (as described below). Cortical bone is primarily made up of osteons, also known as Haversian systems, lamellar bone having formed cylindrical vascular channels named sinusoids. Thousands of these stacked and parallel osteons with interstitial lamellae filling in the gaps form the cortical bone (Dahl & Thompson, 2011). The outer surface of cortical bone is covered in a layer of connective tissue, the periosteum. This layer contains nerves, blood vessels and various bone cells which facilitate the maintenance of the bone. Cancellous bone by contrast is porous, made from a network of plates and rods of lamellae with the spaces between filled with red bone marrow (as described below). Similar to the periosteum, a layer of connective tissue covers the surface of cancellous bone but is comprised of only a thin cellular layer of bone cells. The porosity difference between bone at this level is so great that the bone types can be determined by the naked eye, cortical bone having a porosity of 3-5% and cancellous having a porosity of 70-85% (Burr & Akkus, 2013). Cortical and cancellous bone are found next to each other in the

human skeleton. This can be seen in Figure 1.1 along with the aforementioned lamellar structural arrangement into osteons.

At the highest hierarchical level, bones of the human body can be sorted into five categories generally differentiated by shape and composition: long bones, short bones, flat bones, irregular bones and sesamoid bones. Of these five, the long and flat bones are of particular interest as they were the types used for the design of both the macroscopic and microscopic models of the bone marrow stem cell niche in this study.

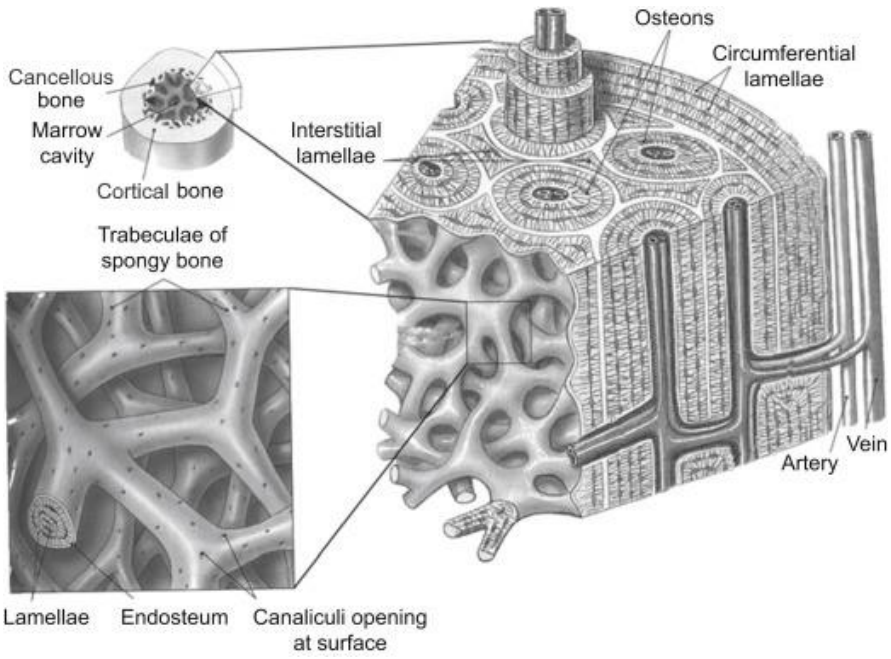

Figure 1.1: Human bone morphology

The internal structure of a human longbone showing the two types of bone; cortical and cancellous. The structural subunits of osteons housing arteries and veins in the cortical bone and lamellae in the cancellous bone can also be seen. Adapted from Lacroix, (2019).

Long bones are longer than they are wide and include bones such as the femur and humerus. They all have a hollow shaft called the diaphysis and a flared region at either end, the metaphysis, which continues to the growth plate and the bone is rounded off with the epiphysis (Clarke, 2008b). The diaphysis is primarily made from cortical bone while the metaphysis and epiphysis contain mostly cancellous bone. Flat bones by comparison are as

the name suggest thin, relatively broad and flat, and include bones such as the ribs and parts of the skull. Flat bones have a section of cancellous bone sandwiched between two thin layers of cortical bone. This broad variety and complexity needs to be considered in the development of any scaffold for *in vitro* modelling relating to bone.

1.1.3 Bone Marrow

Found in the cavities of cancellous bone within flat bones and the diaphysis canals of long bones in a region called the medullary cavity, marrow is a soft and fatty tissue.

Marrow can be found in two different forms, red and yellow. This colour difference is due to the relative need and therefore prevalence of blood cells or fat cells changing the colour from red to yellow respectively. Red bone marrow is the primary site of haematopoiesis and in adults is found primarily in the sternum, pelvis, and epiphyses of long bones (Travlos, 2006b). In these regions there are low levels of adipocytes and it is here that the body creates all new blood cells (erythropoiesis), platelets (thrombopoiesis) and leukocytes (leukopoiesis). Yellow bone marrow found in the diaphysis of long bones is not actively involved in the creation of new blood cells, instead acting in a supportive role as a storage of fat cells (Romaniuk et al., 2016).

Bone marrow contains numerous cell types including stem cells. Stem cells are characterised by their ability to self-renew and differentiate into multiple cell types. What makes bone marrow truly unique among human tissue is the presence of two distinct and separate stem cells co-existing and functioning co-operatively (Bonnet, 2003). These two stem cell types are haematopoietic stem cells (HSC) which differentiate into all types of blood cells, and mesenchymal stem cells (MSCs) which differentiate into both mesodermal and endodermal lineages. There are numerous other cell types inhabiting bone marrow which make up the haematopoietic components, those which are indirectly involved in haematopoiesis and those connected with bone regulation (Travlos, 2006a).

1.1.4 Stem Cells

Stem cells are undifferentiated cells that possess the unique ability to both self-renew through mitotic cell division and differentiate into specialized cell types. These cells are essential for the body's regenerative processes, playing a critical role in maintaining tissue homeostasis and enabling repair after injury (Weissman, 2000). Stem cells are categorized based on their potency, or their capacity to differentiate into various cell types. There are five main categories of stem cells, distinguished by their differentiation potential: totipotent, pluripotent, multipotent, oligopotent and unipotent stem cells

Totipotent stem cells have the greatest differentiation potential, capable of giving rise to all cell types, including both embryonic and extraembryonic tissues. Totipotent stem cells are only present during the early stages of embryonic development, specifically in the first two divisions of a fertilized zygote (Rossant, 2008). As development progresses, these cells give rise to pluripotent stem cells, which can differentiate into almost any cell type derived from the three germ layers, the ectoderm, endoderm, and mesoderm (with the exception of extraembryonic tissues). Embryonic stem cells, used in various research contexts, are an example of pluripotent stem cells (Evans & Kaufman, 1981).

More specialized than pluripotent cells are multipotent stem cells, which can only differentiate into a limited range of cell types within specific lineages. The primary stem cells used in this project, MSCs, are multipotent and can differentiate along osteogenic, adipogenic, and chondrogenic cell lines (Pittenger et al., 1999). This restricted differentiation potential makes them invaluable in tissue engineering and regenerative medicine.

In addition to these categories, there are oligopotent stem cells, which have the ability to differentiate into a few cell types, such as myeloid stem cells, which give rise to various blood cell types. Finally, unipotent stem cells are the most restricted, capable of differentiating into only one cell type, such as epidermal stem cells responsible for skin regeneration (Blanpain &

Fuchs, 2006). Stem cell potency is crucial to understanding their role in regenerative biology and their application in various therapeutic and research contexts.

1.1.5 Bone Cells

When discussing the hierarchical levels of bone, beyond the structural makeup of the tissue, the various cells that inhabit said tissue need to be considered. As previously mentioned, there are numerous different types of cells present in bone, however only the two stem cell types and the cells involved in bone remodelling will be covered in this section as they are most relevant to this research.

1.1.5.1 Haematopoietic Stem Cells

As the primary site of haematopoiesis, red bone marrow is heavily populated with HSCs. HSCs are multipotent, able to maintain both their population and differentiate into all blood cell lineages (Wilson & Trumpp, 2006). It is this capacity to maintain the haematopoietic environment that defines them, originally studied in murine models where transplanted HSCs could rebuild the haematopoietic system of lethally irradiated mice fully (Siminovitch et al., 1963). This ability is also seen in human transplants, although their therapeutic use is relatively new. HSC transplants are part of the standard care of thousands of patients with congenital or acquired disorders of the hematopoietic system or with chemosensitive, radiosensitive, or immunosensitive malignancies (Gratwohl et al., 2010).

HSCs can differentiate into common lymphoid progenitor cells or common myeloid progenitor cells (Gunsilius et al., 2001). The common lymphoid progenitor cells differentiate further into different lymphoblasts which will mature into different lymphocytes such as natural killer cells, naïve B-cells and pre-T-cells. On the common myeloid progenitor lineage of HSC differentiation, myeloblasts can form cells which eventually become granulocytes such as neutrophils and basophils. They can also differentiate into megakaryocytes which rupture releasing platelets, and erythroblasts which mature losing their nucleus becoming erythrocytes otherwise known as red blood cells. Finally, the common myeloid progenitors

can differentiate into mast cell precursors and promonocytes (Bishop et al., 2002). It is the monocyte branch of this lineage which is important in bone regulation as it gives rise to the osteoclast, a tissue specific macrophage. Mononucleated osteoclasts fuse to become multinucleated osteoclasts which reabsorb bone, a key role in bone remodelling (J. M. Kim et al., 2020). The differentiation pathways of HSCs can be seen in Figure 1.2.

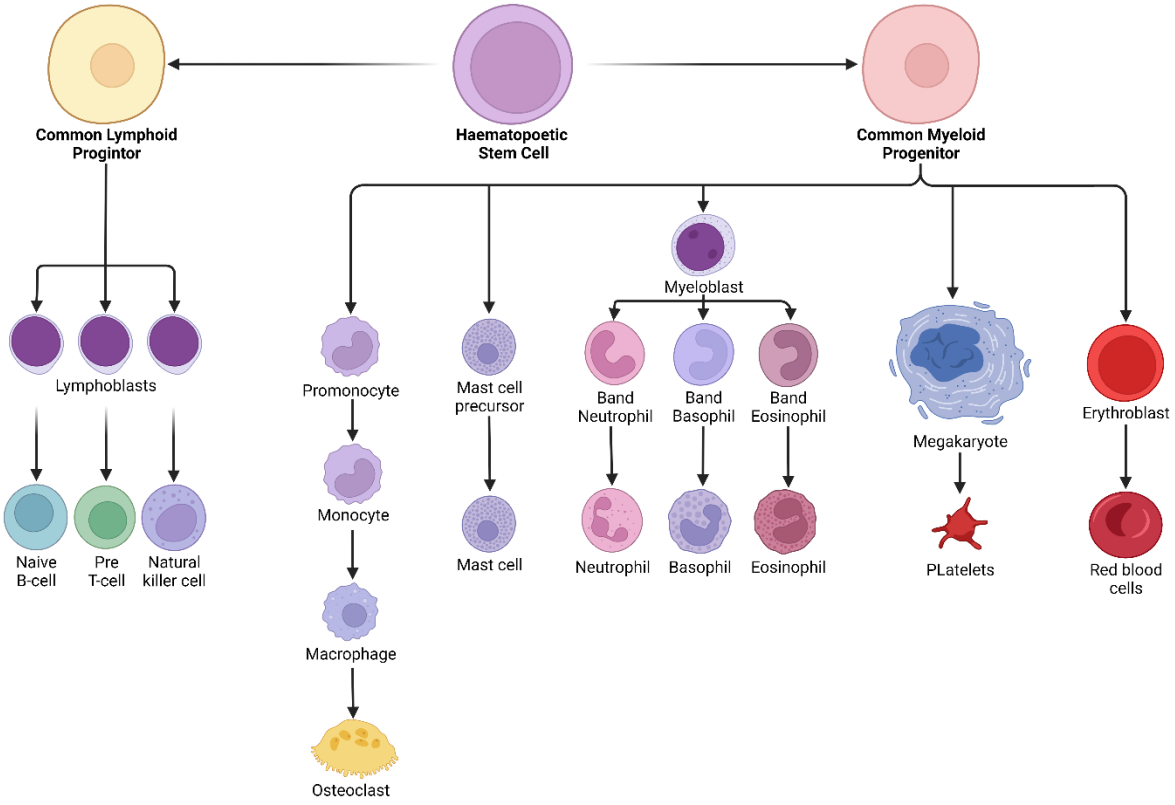

Figure 1.2: Haematopoiesis differentiation pathways

Representative diagram of the differentiation of Haematopoietic stem cells and their descendants including osteoclasts. Arrows indicate direction of differentiation. Created by the author with BioRender.com

1.1.5.2 Mesenchymal Stem Cells

Also known as multipotential stromal cells, mesenchymal progenitor cells and mesenchymal stromal cells, MSCs are multipotent cells which differentiate into the mesodermal lineage including bone, cartilage, fat, tendon, muscle, and marrow stroma (Pittenger et al., 1999b). Akin to HSCs, MSCs have a high capacity for self-renewal being able to maintain their

population under the right conditions. Of the different mesodermal lineages that MSCs can follow, the formation of bone cells, osteogenic differentiation, is of particular interest.

MSCs are able to differentiate into osteoblasts which later form into osteocytes, cells crucial to bone formation and remodelling. Osteogenic differentiation of MSCs is regulated by a number of extracellular signals, shown in Figure 1.3. Systemic hormones including parathyroid hormone (PTH), glucocorticoids, oestrogens and local growth factors including bone morphogenetic protein (BMP), Wnt/β-catenin, transforming growth factor–β (TGF-β), fibroblast growth factor 2 (FGF-2), insulin-like growth factor (IGF), vascular endothelial growth factors (VEGF) and cytokine modulators (prostaglandins) all regulate differentiation (Carbonare et al., 2012). These all activate various signalling pathways controlling specific transcription factors, the most important of which being the master gene runt-related transcription factor 2 (*RUNX2*). *RUNX2*, regulated by the Wnt/β-catenin pathway induces the commitment of MSCs to osteogenic differentiation (Valenti et al., 2016). Ultimately these signalling molecules and transcription factors cause the commitment of MSCs to the osteogenic precursor and its ultimate differentiation to a mature osteoblast.

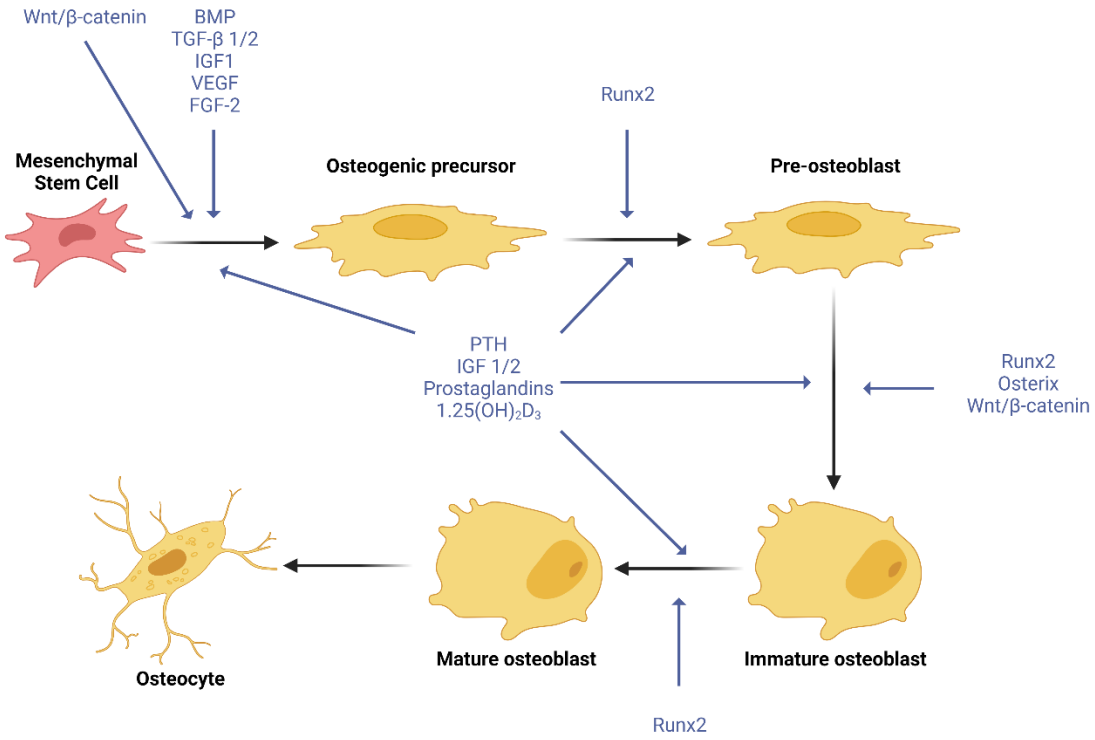

Figure 1.3: Mesenchymal stem cell osteogenic differentiation pathway

Representative diagram of the differentiation of mesenchymal stem cells down the osteogenic pathway in the production of osteoblasts and osteocytes. Black arrows indicate direction of differentiation, blue arrows indicate stages in the process the linked extracellular signals. Created by the author with BioRender.com

1.1.5.3 Human Mesenchymal Stem Cells *In-Vitro*

Human Mesenchymal Stem Cells (hMSCs) as previously mentioned, are multipotent progenitor cells possessing remarkable regenerative capabilities. Due to their nature, they are extensively studied for their therapeutic potential in tissue engineering and regenerative medicine (Bara et al., 2014).

hMSCs typically exhibit a spindle-shaped morphology when cultured *in vitro*, presenting as elongated, fibroblast-like cells adhering to the culture substrate (Dominici et al., 2006). This characteristic morphology facilitates their migration, proliferation, and interaction with the extracellular environment. hMSCs possess a high capacity for adhesion to tissue culture

surfaces, which is crucial for their maintenance and expansion *in vitro* (Simmons & Torok-Storb, 1991). They adhere to the culture substrate through interactions with specific cell adhesion molecules such as integrins, facilitating their proliferation and growth. Their growth rate *in vitro* can vary depending on various factors such as culture conditions, passage number, and donor variability but when optimal conditions are met, hMSCs exhibit robust proliferation enabling their expansion to large numbers for research and therapeutic applications (Colter et al., 2001). Like all cultured cells, hMSCs are susceptible to cellular senescence and aging over time *in vitro*. Passage number, culture conditions, and donor age and health all influence the onset of senescence and can impact the proliferative capacity and functional properties of hMSCs (Stolzing et al., 2008).

hMSCs express characteristic cell surface markers in their immunophenotypic profile along with the absence of other makers. Cluster differentiation (CD) markers were first extracted as adherent stromal cells, which were a heterogeneous population of unknown phenotypes. Their adherent nature was the only means of sorting them from the other, non-adherent, cells. Later, these markers were accepted as known indicators of the phenotype, although the phenotype is still not fully understood (Xiao et al., 2022). Commonly used markers to identify hMSCs include CD73, CD90, and CD105, CD166 and CD44 while they generally lack expression of hematopoietic markers CD14, CD19, CD34, CD45 and HLA-DR (Dominici et al., 2006; Ramos et al., 2016). This immunophenotypic profile is often assessed using techniques such as flow cytometry, a routine piece of equipment and protocol used in most clinical laboratories.

In vitro, hMSCs exhibit remarkable plasticity characterized by their ability to differentiate into multiple cell lineages under appropriate culture conditions as they would naturally in the human body (Pittenger et al., 1999a). These include osteogenic, adipogenic, and chondrogenic lineages. The osteogenic differentiation potential of hMSCs *in vitro* refers to their ability to undergo lineage commitment towards said lineage, resulting in the formation of mature osteoblasts capable of producing mineralized extracellular matrix (ECM) (Ducy et al., 1997). This process is orchestrated by a cascade of molecular events involving the

activation of specific transcription factors and signalling pathways, including RUNX2, Osterix (SP7), and BMP signalling as shown in Figure 1.3, page 10. This differentiation potential is a key aspect of their therapeutic utility in regenerative medicine (Caplan, 2007).

Osteogenic stimulation of hMSCs in vitro typically involves the supplementation of culture media with osteogenic-inducing factors, including dexamethasone, β-glycerophosphate, and ascorbic acid (Jaiswal et al., 1997). These factors act to promote osteogenic differentiation by facilitating the expression of osteogenic genes, promoting ECM mineralization, and fostering the maturation of osteoblasts.

Dexamethasone is a synthetic glucocorticoid and in the context of osteogenic differentiation, it acts modulating gene expression and signalling pathways associated with osteogenesis (Eerden et al., 2003). Specifically, dexamethasone promotes the upregulation of osteogenic transcription factors, including RUNX2 which is considered the master regulator of osteoblast differentiation (Komori, 2010). Dexamethasone also enhances the expression of other osteogenic markers such as alkaline phosphatase (ALP), osteopontin (OPN) and osteocalcin (OCN), facilitating the progression of hMSCs towards the osteoblastic lineage (Jaiswal et al., 1997).

β-Glycerophosphate is a source of inorganic phosphate, an essential component for mineralization of the ECM during osteogenesis (Malaval et al., 1994). β-Glycerophosphate serves as a substrate for osteoblasts to produce inorganic phosphate ions, which are then incorporated into hydroxyapatite crystals, the mineral component of bone (Chung et al., 1992). This process promotes the formation of mineralized nodules, a sign of osteogenic differentiation. β-glycerophosphate may also function as a signalling molecule, activating downstream pathways involved in osteoblast differentiation and function (Golub, 2009).

Ascorbic acid, also known as vitamin C, plays a crucial role in collagen synthesis, which is essential for the formation and maturation of the ECM during osteogenesis. Ascorbic acid serves as a cofactor for the enzyme prolyl hydroxylase, which catalyses the hydroxylation of

proline residues in procollagen, the precursor to collagen (Franceschi, 1992). The hydroxylation reaction is necessary for the stability and cross-linking of collagen fibres, contributing to the structural integrity of bone tissue (Franceschi & Iyer, 1992). Ascorbic acid also exhibits antioxidant properties, which may protect osteoblasts from oxidative stress and promote their survival and function during osteogenic differentiation (Gęgotek & Skrzydlewska, 2023).Ascorbic acid in its salt form was used as it is more stable compared to pure ascorbic acid which degrades quickly.

Markers indicative of osteogenic differentiation in hMSCs encompass several critical biomolecules and processes that are integral to the formation and maturation of bone. These markers include ALP, OCN, OPN, bone sialoprotein (BSP) and mineral deposition (Malaval et al., 1994).

ALP is an enzyme involved in the primary stages of osteogenic differentiation. The enzyme facilitates the formation of hydroxyapatite (HA) crystals by providing the necessary phosphate ions which combine with calcium to form the mineralized matrix incorporating into the ECM (Golub, 2009). ALP activity is often used as an early indicator of osteogenic differentiation, reflecting the initiation of the mineral deposition process.

OCN, also known as bone gamma-carboxyglutamic acid-containing protein (BGLAP), is a non-collagenous protein synthesized by mature osteoblasts. It is highly specific to bone tissue and is involved in the regulation of mineralization and calcium ion homeostasis, binding strongly to hydroxyapatite crystals, stabilizing the bone matrix (Ducy et al., 1997). It is also involved in regulation of bone remodelling in its interaction with osteoclasts influencing their activity (N. K. Lee et al., 2007). OCN serves as a late marker of osteogenic differentiation, indicative of mature osteoblast function.

OPN is another vital non-collagenous protein involved in the bone remodelling and mineralization process. It functions as a mediator of cell-matrix interactions and is involved in the regulation of osteoclast activity (Denhardt & Guo, 1993). OPN binds to hydroxyapatite

and influences the adhesion, migration, and survival of osteoblasts and osteoclasts (Franceschi & Iyer, 1992). It also plays a role in the inhibition of ectopic calcification (pathological bone growth in soft tissue), ensuring that mineralization occurs only within the bone matrix (Denhardt & Guo, 1993). OPN expression is upregulated during osteogenic differentiation and serves as a marker of both early and late stages of osteoblast development (Franz-Odendaal et al., 2006a). Both OPN and OCN are highly specific to bone tissue with OCN in particular being a definitive marker of mature osteoblasts exclusively synthesized by these cells in the bone matrix (Zoch et al., 2016a). OPN is expressed early in the differentiation process and continues to be involved in bone remodelling and mineralization through maturation (Franz-Odendaal et al., 2006a). OCN, on the other hand, is a late marker of osteoblast maturation, indicating advanced stages of bone matrix formation (Zoch et al., 2016a). Using both markers together allows for the monitoring of the entire differentiation timeline from early osteoblast activity to mature bone formation. Both are well-characterized and have robust commercially available antibodies for immunohistochemistry (IHC) (Boskey & Posner, 1984).

BSP is a glycoprotein that plays a critical role in the nucleation and growth of hydroxyapatite crystals, regulating the mineralization process (Oldberg et al., 1988). BSP is highly expressed during the early stages of osteoblast differentiation and contributes to the formation of the mineralized bone matrix by promoting the deposition of calcium and phosphate ions (Ganss et al., 1999).

The definitive hallmark of osteogenic differentiation is the deposition of a mineralized matrix which is primarily composed of hydroxyapatite crystals. The mineralized matrix provides the structural framework for bone tissue, providing mechanical strength and rigidity. The degree of mineralization is often conducted using techniques such as Alizarin Red S staining, which when added to a sample, binds to calcium deposits allowing detection of bone matrix (Gregory et al., 2004).

In summation, hMSCs represent a promising cell source for osteogenic tissue engineering and regenerative medicine applications. This is due to their natural multipotency and ability to undergo osteogenic differentiation *in vitro*, regulated *via* specific markers and characterized by the deposition of mineralized ECM. Understanding the intricate mechanisms underlying hMSC osteogenesis *in vitro* holds significant implications for the development of regenerative therapies aimed at addressing skeletal disorders, bone defects and fracture healing and is the driving reasoning behind this project.

1.1.5.4 Osteoblasts, Osteocytes and Osteoclasts

Osteoblasts, having differentiated from MSCs, are immature bone cells which line the periosteum of cortical bone in a monolayer. Osteoblasts synthesise and secrete bone matrix and are involved in the mineralization of bone, regulating phosphate and calcium levels. Osteoblasts also synthesise important proteins which incorporate into the bone matrix including OCN (Manolagas, 2000). OCN is among the most abundant proteins produced solely by osteoblasts which acts to regulate bone matrix mineralization (as well as having a hormonal role) and as such is routinely used as a marker of osteoblastic bone formation (Zoch et al., 2016).

Once bone formation for a given osteoblast has concluded, it can apoptose, revert to a bone lining phenotype or the bone matrix around it hardens and the osteoblast can become trapped (Franz-Odendaal et al., 2006). If entrapped in the bone matrix it produced, the osteoblast is now termed an osteocyte (as the definition of an osteocyte is based on its location) and will undergo morphogenic changes (Terpos & Christoulas, 2015). Terminally differentiating, the osteocytes develop long neuron like processes called canaliculi allowing communication between other osteocytes and surface osteoblasts (McGee-Lawrence et al., 2013). The regions where osteocytes are embedded are called the lacunae, located between the lamellae.

As previously mentioned, osteoclasts originate from the HSC lineage having differentiated from monocytes and macrophages. They are multinucleated cells which reabsorb bone through remodelling of bone matrix. Osteoclasts bind to the bone surface integrin vitronectin, sealing off the area below the cell creating an environment for bone resorption by the secretion of acids and proteases (Feher, 2017). The components of bone which were broken down are absorbed by the osteoclast for release into the body.

Along with OCN, another important protein marker produced by both osteoblasts and osteoclasts is OPN. OPN is associated with osteoclasts as it is the protein which binds the cell to the bone surface, holding a major role in the formation of the sealing zone and therefore motility of osteoclasts (A. Singh et al., 2018). OPN is also produced by osteoblasts enabling adherence to the mineralised matrix. It has also been shown to be expressed by pre-osteoblastic cells during early bone development as well as by mature osteoblasts at bone remodelling sites (Sodek et al., 1995).

1.1.6 HOS as an Osteoblast Analogue

Human osteosarcoma (HOS) cells are frequently utilized in research as a surrogate model for studying osteoblast biology and bone-related processes. Derived from human osteosarcoma, a type of bone cancer, HOS cells exhibit osteoblastic characteristics, making them a widely accepted model system (Tattersall et al., 2020). These cells synthesize extracellular matrix proteins such as OCN and OPN and can undergo mineralization *in vitro* under osteogenic conditions (Ikeda et al., 1992).

A significant advantage of using HOS cells is their immortalized nature, allowing continuous proliferation in culture without undergoing senescence. This property arises from genetic and epigenetic alterations typical of cancer cells, including dysregulated cell cycle control and enhanced telomerase activity (de Bardet et al., 2023). Unlike primary osteoblasts, which have limited proliferation potential and are highly donor-dependent, HOS cells provide a consistent, reproducible model system (Mohseny et al., 2011). This reproducibility is essential

for experiments requiring large cell numbers or extended culture periods, such as studies on osteogenesis, drug screening, and biomaterials testing.

It is, however, important to acknowledge the limitations of using HOS cells as an analogue for osteoblasts. As cancer-derived cells, HOS cells exhibit altered signalling pathways and genomic instability, which may not reflect the behaviour of normal, non-transformed osteoblasts accurately. For instance, their response to certain osteogenic stimuli or mechanical forces may differ from that of primary osteoblasts, highlighting the need to interpret findings within the context of their immortalized origin (Ikeda et al., 1992).

Nevertheless, their osteoblast-like phenotype and ability to mineralize make them a suitable and practical model for investigating fundamental aspects of osteoblast function and bone formation. Using a cell line also enables the ability to produce large quantities of cells. This is not a viable option when working with primary cells as gaining large numbers of cells is difficult, expensive and the inherent variations between donor cells could lead to a variety of cellular responses. Using a cell line in comparison, enables large quantities of cells to be produced and they are more likely to have uniform responses. For proof of principle and highly experimental optimization work, using a cell line like HOS is an ideal cost effective option.

1.1.7 Bone Fracture Epidemiology

Bone fractures are a significant health care concern across the globe. Many millions of people sustain one or more fractures each year with 178 million new fractures in 2019 and 455 million prevalent cases of acute/long-term fracture symptoms in the same year (Wu et al., 2021). In the UK, hip fractures were the most common type of fracture requiring hospitalisation followed by distal radius, ankle and hand (Jennison & Brinsden, 2019).

Fractures are more prevalent in older adults, primarily due to decreased bone density and increased fall risk. Women, particularly postmenopausal women, are at a higher risk for osteoporotic fractures due to oestrogen deficiency (Khosla & Monroe, 2018). In younger

populations, fractures are often a result of high-energy trauma such as accidents and sports injuries. Specifically in the England, over the ten year period from 2004 to 2014, there were 2,489,052 fracture admissions to hospital making the risk of admission for fracture 47.84 per 10,000 population (Jennison & Brinsden, 2019). The direct cost burden on the NHS for hip fractures alone reached £869 million in 2017/18 with that cost continually rising with a growing and aging population (Glynn et al., 2020). Current treatments for fractures primarily involve surgical and non-surgical approaches such as immobilization and internal fixation alongside pain management.

There are numerous complications and challenges associated with healing from a fracture. These can include delayed healing where the bone takes longer than expected to achieve union, generally considered to be four months (Gómez-Barrena et al., 2015). This delay in healing can be due to numerous factors including patient health and comorbidities, poor blood supply, mechanical instability or even infection. When the delay in healing progresses beyond a six month time frame, the injury is considered a non-union and is associated primarily with the severity of the injury and surgical treatment technique used (Zura et al., 2016). The approximate average rate of occurrence for delayed healing and non-union is in the range of 5 – 10% for all bone fractures but with varying rates depending on fracture type and its management (Gómez-Barrena et al., 2015). Non-unions are managed generally with surgical interventions including revised surgery and bone grafts. Bone grafting is the surgical process of transplanting bone tissue to the non-union site to stimulate bone healing and restore structural integrity. The types of bone graft available include autografts, allografts and synthetic grafts, all of which are detailed further in section 1.2.3, page 32. The surgery involves exposing the fracture site and cleaning all fibrous and any infected tissue, the shaped graft placed into the non-union site in contact with the bone and the site stabilised into proper alignment. The perfect bone graft is osteoconductive, osteoinductive and osteogenetic, without risking transferral of pathogenic microbes, readily available, manageable, biocompatible, and bioresorbable (Calori et al., 2011). Unfortunately, no one graft available

today can meet all these parameters, especially when cost effectiveness is also considered, hence the need for medical science to focus research on enhancing bone healing.

In such cases as non-union fracture, were for whatever the reason normal osteogenic capacity is reduced or impaired a consideration of the underlying mechanisms underlying bone repair and function are the lynch pin of future regenerative procedures. In the clinical context, stem cell therapies aim to replace or repair damaged tissues. For example, Hematopoietic stem cell transplantation (HSCT) is a well-established treatment for certain blood disorders and cancers such as lymphoma, leukaemia and immune-deficiency illnesses (Hatzimichael & Tuthill, 2010). Mesenchymal stem cells, as detailed in section 1.1.5.28, have the ability to differentiate into osteogenic, chondrogenic, and adipogenic cells. If encouraged to differentiate down the osteogenic pathway they could contribute directly to new bone formation. If applied in a suitable fashion, MSCs could aid in the healing process of fractures and as such are of great interest to the medical research community. This research started in the 1990s using MSCs with site-specific delivery vehicles to repair tissues such as cartilage, bone, tendon and other connective tissues and has advanced to the seeding of MSCs in tissue engineered bone graft scaffolds (Caplan, 2005) (X. Wang et al., 2013). Stem cell therapies are one example of research being conducted with an aim of correcting the insufficient osteogenesis. An important consideration, however, is that to date the development of safe and effective stem cell therapies require a significant amount of research and clinical trials before becoming a possibility for mainstream health care (Aly, 2020; Malige et al., 2024).

1.1.8 MSCs used in Therapy

MSCs have become a key element in regenerative medicine due to their ability to differentiate into multiple lineages, modulate the immune response, and secrete bioactive factors and their application spans diverse therapeutic areas (Bara et al., 2014). In musculoskeletal repair, MSCs have been utilized in cartilage regeneration for osteoarthritis and other degenerative conditions, enhancing extracellular matrix production and promoting chondrocyte

differentiation (Barry & Murphy, 2013). Similarly, in bone healing, MSC-based therapies support osteogenesis, with promising outcomes in critical-sized bone defects and fracture non-union (Gao et al., 2016). Beyond skeletal applications, MSCs exhibit potent immunomodulatory effects, making them a viable treatment for conditions such as graft-versus-host disease by dampening T-cell proliferation and cytokine release (Le Blanc et al., 2004). Cardiovascular applications have also shown potential, with MSCs improving myocardial function and stimulating angiogenesis in ischemic heart disease via paracrine signalling (Hare et al., 2009). In neurology, MSC-derived factors are being explored for their neuroprotective and regenerative properties, offering therapeutic potential in conditions such as spinal cord injury and stroke (Joyce et al., 2010). This breadth of applicability underscores the promise of MSCs in advancing regenerative medicine and restoring tissue function across multiple domains.

MSCs have demonstrated remarkable versatility across a range of therapeutic applications, from musculoskeletal repair to immune modulation and neuroprotection. Their unique combination of differentiation potential, immunomodulatory capacity, and paracrine effects positions them as a potential future cornerstone of regenerative medicine, with ongoing research poised to reveal even broader clinical applications in the future.

1.1.9 Bone Remodelling

Bone is a dynamic tissue which undergoes constant remodelling, the removal or resorption of old bone being replaced by new tissue. While the job of osteoblasts and osteoclasts to create and reabsorb bone respectively has been discussed in isolation, the different cell types are highly interconnected and reliant on each other for proper function. The bone remodelling process has five phases: activation, resorption, reversal, formation and termination.

1.1.9.1 Activation

The activation of bone remodelling is initiated *via* different potential signals, either mechanical or hormonal. The cluster of cells (osteoclasts, osteoblasts and osteocytes) which collaborate in the process of bone remodelling are classed a “basic multicellular unit” (BMU). BMU organisation in cortical and cancellous bone differ morphologically, but not biologically (Hadjidakis & Androulakis, 2006). Osteocytes are believed to have an important role in the translation of mechanical strain into signals to start active bone remodelling, directing osteoclast and osteoblast activity (Bonewald, 2007). Osteocytes release TGF-β under normal conditions which inhibits osteoclast genesis (Heino et al., 2002). With osteocyte apoptosis due to, for example, damage to the bone matrix, osteoclast formation increases. In conjunction with TGF-β, an important hormone involved in the activation phase of bone remodelling is PTH. PTH binds to receptors on osteoblasts causing a cascade of molecular signalling that ultimately recruits osteoclast precursors and induce their differentiation and activation, establishing bone resorption (Raggatt & Partridge, 2010).

1.1.9.2 Resorption

Having recruited osteocyte precursors to the site of bone remodelling, they form into multinucleated osteoclasts. In response to suitable mechanical and hormonal signals, osteoblasts release matrix metalloproteinases which initiate the resorption phase by degrading the unmineralized outer layer of osteoid, exposing the mineralised bone surface beneath (Birkedal-Hansen et al., 1993). This allows the binding of osteoclasts to the bone surface and the release of hydrogen ions, dissolving the mineralised matrix into calcium and phosphate ions for release into the blood stream. This cavity region of bone carved out by the osteoclasts is called the Howship’s lacuna (Hadjidakis & Androulakis, 2006). As the activation of osteoclasts slows and they complete their resorption, they apoptose.

1.1.9.3 Reversal

The reversal phase involves the preparation of the bone surface for osteoblastic bone formation. Bone lining cells from the osteoblastic lineage phagocytose remaining demineralized collagen in the Howship's lacuna, preparing the area for new bone formation (Everts et al., 2002).

1.1.9.4 Formation

As discussed in section 1.1.5.2, page 8, there are numerous signals which are involved in the differentiation process of MSCs into osteoblasts with TGF-β being a key signal for their recruitment to the site of bone remodelling (Raggatt & Partridge, 2010). The osteoblasts synthesise the new bone matrix made from collage type I and alkaline phosphatase which forms hydroxyapatite. As the osteoblasts synthesise the new bone, they can become trapped as previously mentioned, becoming osteocytes.

1.1.9.5 Termination

The remodelling process is complete when the resorbed bone volume has been filled with new bone matrix. The exact signalling pathways which terminate the formation stage are not fully understood with its exact mechanisms still debated (Bolamperti et al., 2022).

1.1.10 Wolff's Law and Mechanotransduction

As previously mentioned, bone is a mechano-sensitive tissue that responds to external stimuli. First described by Julius Wolff in the late 19th century, it was observed that bone adapts to the mechanical forces it is subjected to, changing in shape and structure. If bone is subjected to increased mechanical stress, it remodels and becomes stronger by increasing bone mass and altering its structure. Conversely, in the absence of mechanical stress, bone density decreases (Papachroni et al., 2009). This phenomenon is termed Wolff's Law and explains why, for example, athletes develop stronger bones due to increased mechanical loading, while individuals suffering from conditions like anorexia or prolonged immobilization may develop osteoporosis due to reduced mechanical stimulation. These processes are

primarily governed by mechanotransduction, the biological mechanism by which cells sense and respond to mechanical stimuli, converting these physical forces into biochemical signals.

1.1.10.1 Mechanotransduction

Mechanotransduction is the process by which cells sense and respond to mechanical stimulation from their environment, converting the physical signals into biochemical responses (Paluch et al., 2015). The process involves multiple components including the ECM, cell membrane receptors, the cytoskeleton, and various signalling pathways. This process is particularly important in bone as a dynamic tissue that constantly remodels in response to mechanical loads. In bone, osteocytes, which are the most abundant cells embedded within the mineralized matrix, serve as the primary “sensors” of mechanical force. Osteocytes are interconnected through a network of canaliculi, which allows them to communicate with other bone cells, such as osteoblasts and osteoclasts which is essential for the regulation of bone formation and resorption in response to mechanical stress (Santos et al., 2009).

The multistep process of mechanotransduction begins with the transduction of mechanical forces such as fluid shear stress, compressive forces or tensile strain, acting upon bone which are detected by sensor cells (Ramaswamy et al., 2015). Fluid shear stress refers to the tangential force exerted by fluid flow over a surface. In biological systems, it occurs when cells are exposed to moving fluids, such as blood flow within vessels or interstitial fluid in tissues (Chistiakov et al., 2017). Compressive forces refer to mechanical loads that act to compact a structure, reducing its volume or thickness. These forces are prevalent in biological tissues subjected to weight-bearing or external pressure (Mow et al., 1984). Tensile strain occurs when a force stretches or elongates a material, leading to an increase in its length relative to its original size and is experienced by tissues such as tendons, ligaments, and bones during movement and mechanical loading (J. H. C. Wang, 2006).

The mechanical stimulus is typically detected by mechanoreceptors on the surface of osteocytes (the most abundant cells in bone), which are embedded in the bone mineralised

matrix and interconnected through networks of canaliculi (Bonewald, 2011). The mechanoreceptors include integrins, stretch-activated ion channels, and primary cilia (Bonewald, 2011; Papachroni et al., 2009). Integrins are transmembrane receptors that form physical connections between the ECM and the cell's cytoskeleton (Danen, 2013). When external forces deform the ECM, integrins transmit these forces across the cell membrane, initiating the mechanotransduction process (Humphrey et al., 2014). Additionally, primary cilia, which are sensory organelles, play a role in detecting fluid shear stress and stretch, while ion channels allow for the influx of calcium ions in response to mechanical deformation (Thompson et al., 2012).

One of the primary mechanotransduction pathways activated by mechanical loading (compressive forces) is the Wnt/β-catenin signalling pathway (Baron & Kneissel, 2013). Mechanical strain on osteocytes leads to the stabilization of β-catenin, which transfers to the nucleus and promotes the expression of genes that are essential for osteoblast differentiation and bone formation (Robinson et al., 2006). In addition, mechanical forces have been shown to activate signalling cascades such as the mitogen-activated protein kinase (MAPK) pathway, which plays a role in cell proliferation, and the production of signalling molecules such as prostaglandins and nitric oxide, both of which are involved in bone remodelling and repair (K. Lee et al., 2018; Santos et al., 2009).

1.1.10.2 Mechanical Stimulation in Research

Given the natural and fundamental importance of mechanical stimulation in the human body, *in vitro* models for the study of bone should ideally incorporate mechanical stimuli to accurately replicate the *in vivo* environment as static models fail to account for the critical role of mechanotransduction in bone homeostasis and remodelling. The introduction of mechanical stimulation into such models through compression, tensile forces, or fluid shear stress can significantly enhance the differentiation of MSCs into osteoblasts, promoting osteogenesis and the production of mineralized bone tissue (McCoy & O'Brien, 2010).

Bioreactors are commonly utilized to deliver mechanical stimulation *in vitro* by providing a controlled system with a desired environment, maintaining specific conditions. These devices can apply dynamic compressive or tensile forces to cell-seeded scaffolds, mimicking the physiological stresses experienced by bone (McCoy & O'Brien, 2010; Naing & Williams, 2011). Another method, fluid flow systems which apply controlled fluid movement over or through biological tissues or scaffolds, generates fluid shear stress, which has been shown to upregulate the expression of osteogenic markers such as ALP and OPN, further promoting matrix mineralization (Riehl et al., 2017; Steward & Kelly, 2015).

One innovative approach to mechanical stimulation is the application of high-frequency mechanical vibrations, such as those used in the Nanokick technology. The Nanokick platform, developed by Professor Matthew Dalby and his team, utilizes nanoscale sinusoidal vibrations producing a compressive force to stimulate hMSCs to differentiate into bone cells (Dalby et al., 2007). The device employs precise sinusoidal vibrations, typically around 1 kHz frequency and 22 nm amplitude, to mimic mechanical cues found in the natural bone environment (Childs et al., 2016; Kennedy et al., 2021; Robertson et al., 2018a). These high-frequency vibrations are capable of promoting osteogenic differentiation in MSCs by stimulating mechanotransductive pathways without the need for traditional chemical inducers of osteogenesis (Nikukar et al., 2013). This method enables the creation of clinically relevant 3D bone tissues with the potential for bone grafting and repair. The Nanokick's ability to apply mechanical stimulation in a controlled manner makes it a valuable tool for developing more physiologically relevant *in vitro* bone models.

1.1.11 Bone Marrow Stem Cell Niche

A "stem cell niche" can be used to describe the microenvironment within a given tissue not only concerning the location where stem cells are found but also considering their function. Having discussed the individual elements of bone, it is clear that its content is a highly complex interconnected system. As previously stated, the stem cells of the bone marrow niche include

both HSCs and MSCs making this niche unique possessing two stem cell types. Beyond the presence of both stem cells, the two are intertwined in their processes having a close relationship for osteogenesis and haematopoiesis. It is also understood that the osteogenic descendant of MSCs, the osteoblast, has a role in the formation and function of the bone marrow stem cell niche, demonstrated by mice lacking *RUNX2*, the most important transcription factor for the formation of osteoblasts, having defective bone marrow (Wilson & Trumpp, 2006). Conversely, increasing the osteoblast population in the trabecular region has been shown to cause a parallel increase in the population of HSCs (Calvi et al., 2003; J. Zhang et al., 2003). While these three cells may be the primary cells of the niche, they are by no means the only cellular constituents. This is one of the many challenges faced in defining any niche, particularly the bone marrow stem cell niche, as determining which cells neighbour and regulate both HSCs and MSCs is difficult. Achieving an accurate look into a healthy niche is difficult when the primary method of investigating the niche is through bone sections. Retaining the histological integrity within a bone when sectioned along with the complexity of immunostaining leaves determining the cellular constituents difficult (Morrison & Scadden, 2014). Not only are sections of bone variable, the bone sections available for study are often in a diseased state and not necessarily indicative of a healthy functional niche environment.

The bone marrow niche is defined not just by its stem cell population, but also by its structural and biochemical intricacies. HSCs and MSCs are at the core of this niche, but recent advances have illuminated a much broader spectrum of cellular and molecular participants. MSCs themselves exhibit remarkable heterogeneity, giving rise to osteoblasts, adipocytes, and chondrocytes, each influencing the niche's regulatory framework (Pittenger et al., 1999a). Osteoblasts, particularly those derived from CXCL12-abundant reticular (CAR) cells, secrete essential factors like stem cell factor (SCF) and CXCL12, which maintain HSC quiescence and retention (Fröbel et al., 2021). Adipocytes, on the other hand, can exhibit opposing roles—supporting or inhibiting haematopoiesis depending on their spatial and functional state within the marrow (Zhou et al., 2017).

The morphological features of the bone marrow niche contribute significantly to its function. The niche is broadly divided into the endosteal and perivascular regions, each with distinct roles. The endosteal region, localized near trabecular bone, is characterized by lower oxygen tension and supports HSC quiescence., conversely, the perivascular region, situated closer to the vasculature, facilitates active haematopoiesis and stem cell mobilization (L. Ding et al., 2012). Both regions are interconnected by arterioles and sinusoids, which regulate oxygen gradients and mechanical signals essential for cellular function (Pereira et al., 2024).

Recent work on regulatory pathways has further underscored the complexity of this ecosystem. Notch signalling, mediated by Jagged1 expressed by the *JAG 1* gene, is pivotal in HSC self-renewal and lymphoid lineage commitment (Calvi et al., 2003). Additionally, TGF-β signalling is emerging as a critical regulator, promoting HSC quiescence through direct and indirect mechanisms (Blank & Karlsson, 2015). CXCL12-CXCR4 interactions remain foundational, ensuring HSC retention and niche anchorage, while factors such as angiopoietin-1 and SCF modulate vascular integrity and cellular differentiation (Xiao et al., 2022).

Structurally, the bone marrow niche is supported by an ECM composed of collagen, laminin, and fibronectin, which not only provide mechanical support but also serve as reservoirs for growth factors (X. D. Chen et al., 2007). ECM stiffness and composition are increasingly recognized as modulators of lineage differentiation, with stiffer environments promoting osteogenic pathways while softer matrices favour adipogenesis (T. Zhang et al., 2018). Such biophysical properties underscore the niche's adaptability to both physiological and pathological states, including aging and malignancies (Fröbel et al., 2021).

Methodologically, challenges in studying the niche stem from its dynamic nature and spatial heterogeneity. Emerging technologies like single-cell RNA sequencing and high-resolution 3D imaging are now providing unprecedented insights into cellular hierarchies and interactions (Baccin et al., 2019; Sánchez-Lanzas et al., 2022). These techniques have revealed many

distinct subpopulations within the marrow, including NG2+ pericytes, LepR+ cells, and Schwann cells, each contributing uniquely to HSC regulation (Baryawno et al., 2019; Omatsu, 2023).

While most models of the niche are centred on its primary cellular constituents, contemporary studies highlight the niche's complexity as an integrated and migratory ecosystem which dynamically responds to extrinsic signals adapting to a changing physiological environment (Kwon et al., 2024). Understanding this intricate network of cells, signals, and structures is critical not only for elucidating hematopoietic and osteogenic mechanisms, but also for developing therapeutic interventions aimed at restoring or modifying niche function in disease contexts. Up until recently, there hasn’t been the technology available to control microenvironmental factors *in vitro* at a level of precision that would enable these cellular structures to be reproduced. The HOTs system has the potential to enable this level of control, and this project is part of the early stages of that process.

A common representation of the niche has yet to be fully developed and as such there are variations in how the niche is depicted as shown in Figure 1.4. While there are common core components, HSCs, MSCs and osteoblasts, the exact location and constituents of this niche are yet to be fully determined with more interconnections being discovered. An example of this can be seen in the figure below in the location of the MSC.

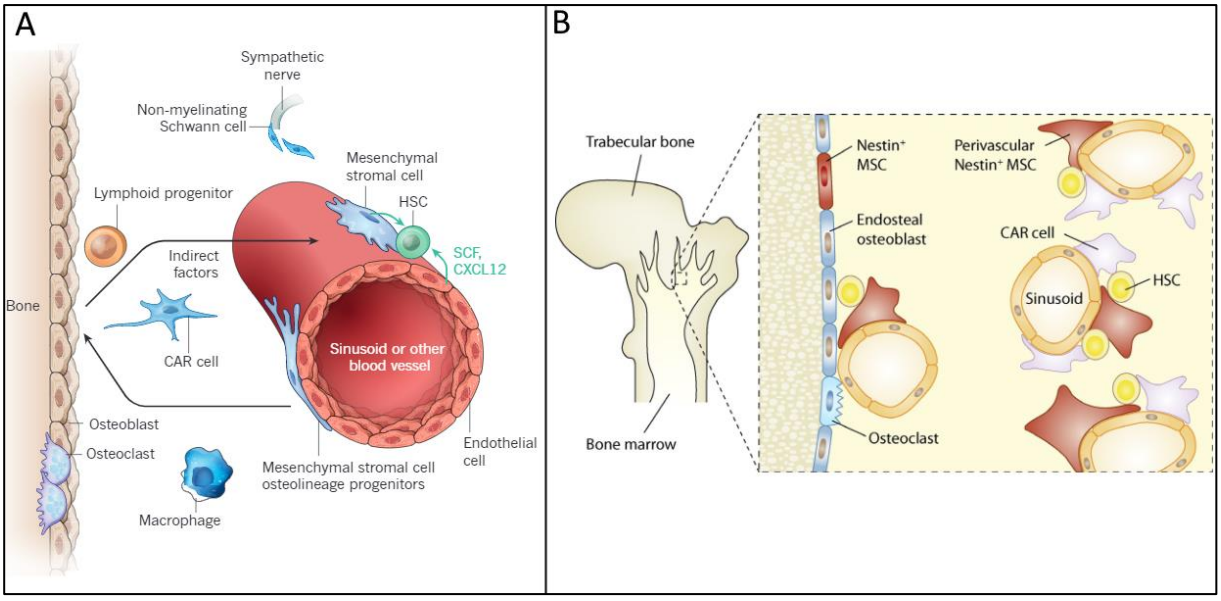

Figure 1.4: Comparison of representations of the bone marrow stem cell niche

A comparison of the bone marrow stem cell niche as represented in two different publications: (A) - Morrison & Scadden, 2014 & (B) - Ehninger & Trumpp, 2011. In A, the MSCs are show inhabiting the wall of sinusoids, while in B, they are also found in the endosteal bone wall.

1.1.12 Bone Disease in the UK

Musculoskeletal conditions, including bone diseases, affect a significant portion of the UK population and impose substantial costs on the NHS. Below is an overview of the prevalence of a few of these conditions and their associated healthcare expenditures.

Osteoarthritis: Approximately 10 million people in the UK are affected by osteoarthritis, with an estimated 5.4 million cases of knee osteoarthritis and 3.2 million cases of hip osteoarthritis (NICE, 2023).

Osteoporosis**:** Among individuals aged 50 and above, 21.9% of women and 6.7% of men are estimated to have osteoporosis (Willers et al., 2022).

Total Musculoskeletal Conditions**:** Over 20 million people in the UK live with a musculoskeletal condition, accounting for approximately one third of the population (Versus Arthritis, 2024).

While specific annual costs for bone diseases are not always readily available, musculoskeletal conditions are a leading cause of disability and contribute significantly to healthcare expenditures. In 2016, musculoskeletal conditions reported annual spending of approximately £5 billion, accounting for the third largest area of spending within the NHS (Leal et al., 2016).

It is evident that bone diseases and musculoskeletal conditions affect a significant portion of the UK population, leading to considerable healthcare expenditures. While exact current annual costs specific to bone diseases are not readily available, the overall impact on the NHS is substantial. Despite the high costs associated with drug development, the importance of continued research, effective prevention and management strategies for these conditions is essential. By conducting research such as ours, the ultimate goal would be the generation of therapies which aid in bone healing as a result of a greater understanding of the bone marrow stem cell niche. There may also be the potential for the creation of therapies using the HOTs system to pattern individual cells and structural elements in 3D on an implantable scaffold.

1.2 Cellular Scaffolds

There are multiple different types of scaffolds for biological research, including natural, synthetic, and composite materials, each offering unique properties for tissue engineering applications (B. S. Kim et al., 2000). These scaffolds can be bioactive, antimicrobial and even have specific nano topographies to illicit a given cellular response (Keane & Badylak, 2014; Place et al., 2009). Some of the most commonly used scaffolds in research are hydrogels, decellularised tissues, microfabricated scaffolds, and electrospun nanofiber scaffolds (Jana et al., 2014; K. Y. Lee & Mooney, 2001; Zhao et al., 2018). Important considerations when selecting a scaffold are biocompatibility, especially if the scaffold is intended for therapeutic use, and capturing the complexity of biological structures, particularly at the microscopic level.

Biomaterials, which form the basis of these scaffolds, are materials engineered to interact with biological systems, often for therapeutic or diagnostic applications. They are essential in tissue engineering, where they help form the scaffolding on which cells grow, differentiate, and ultimately regenerate tissue. Biomaterials can be categorized into three main types: natural, synthetic, and composite materials, each with its own characteristics, advantages, and limitations.

1.2.1 Types of Biomaterials

Natural biomaterials are derived from biological sources, such as collagen, gelatin, and chitosan and are inherently biocompatible and promote cell attachment. These materials, such as collagen and gelatin used in hydrogels, are particularly useful in cellular scaffolds due to their ability to closely mimic the natural extracellular matrix (O'Brien, 2011).

Synthetic Biomaterials like poly(lactic acid) (PLA), poly(ethylene glycol) (PEG), and poly(glycolic acid) (PGA) offer more controlled mechanical properties, tuneable degradation rates, and higher reproducibility compared to natural materials (Middleton & Tipton, 2000)., PEG, for example, is a synthetic material used to create hydrogels with good biocompatibility, and has been experimented with for the tethering of ECM derived bioactive molecules (Zhu, 2010).

Composite Biomaterials combine the benefits of both natural and synthetic materials. An example is the incorporation of hydroxyapatite into synthetic scaffolds for bone regeneration, which improves mechanical strength and bioactivity (Rezwan et al., 2006).

1.2.2 Hydrogels as Cellular Scaffolds

Hydrogels are a 3D network of polymer chains that can be formed into a gel-like structure. These materials, made from either natural or synthetic polymers, are water absorbent and highly customizable, making them ideal as scaffolds in tissue engineering. Hydrogels can be categorized into two groups: conventional hydrogels and stimuli-responsive hydrogels.

Conventional hydrogels are lightly crosslinked, hydrophilic polymers that can swell significantly in water, while stimuli-responsive hydrogels react to environmental factors such as pH or temperature (Rosiak & Yoshii, 1999).

Hydrogels can incorporate and suspend cells, growth factors, and other bioactive agents uniformly throughout their structure, facilitating the efficient diffusion of nutrients and metabolites (M. R. Singh et al., 2016). The customizability of hydrogels allows for the tailoring of mechanical properties, making them applicable across a wide range of tissue engineering applications. Collagen, for instance, is the primary structural component of the extracellular matrix, making it an attractive hydrogel choice. It has been shown that 3D culture in a collagen hydrogel can aid the differentiation of MSCs into osteoblasts, presenting similar phenotypes to in vivo cells (Naito et al., 2013).

Gelatin scaffolds, though similar to collagen, offer greater tunability in terms of porosity and mechanical strength. Biocompatible and highly porous, gelatin hydrogels facilitate the exchange of nutrients, oxygen, and waste products, providing an environment conducive to tissue growth (Kang et al., 1999). Similarly, Matrigel™, a commercially available matrix, consists of collagen IV, laminin, and enactin, aiding the attachment and differentiation of cells (Hughes et al., 2010).

1.2.3 Decellularized Scaffolds

Decellularised scaffolds are derived from natural tissues such as bone, cartilage, or heart muscle, where cellular components are removed, leaving behind the extracellular matrix. This matrix acts as a biomimetic scaffold with structural and functional proteins that support tissue growth (Rana et al., 2017). The decellularization process is crucial as it removes potential antigens, reducing the likelihood of immune rejection. The process, however, can affect the mechanical and biochemical properties of the scaffold (Gilbert et al., 2006).

Decellularised bone matrix, for example, is often used in bone grafting. While autografts and allografts are standard treatments for bone defects, decellularized bone offers a more

scalable and less immunogenic alternative (Ho-Shui-Ling et al., 2018). Xenografts, sourced from animal tissues, show promise due to their greater availability, though research is ongoing regarding their long-term viability and immunological safety (Drosos et al., 2007).

Decellularized bone scaffolds retain the native ECM components, including collagen, hydroxyapatite, and other bioactive molecules which are critical for promoting osteogenesis and cell attachment while minimizing immunogenic responses (Sawkins et al., 2013). This process removes cellular content while preserving the intricate architecture and mechanical strength of the bone, making these scaffolds ideal for bone repair and reconstruction in critical-sized defects. Additionally, decellularized bone ECM contains growth factors such as bone morphogenetic proteins (BMPs) that enhance osteoinductive properties, further supporting their use in orthopaedics and tissue engineering (Crapo et al., 2011). Advances in decellularization protocols, such as perfusion-based and enzymatic approaches, have improved the efficacy of cell removal and the preservation of ECM integrity, offering scalable solutions for clinical applications (Amirazad et al., 2022). These scaffolds represent a promising biomaterial for bone regeneration, combining the benefits of natural bioactivity with reduced risk of immune rejection.

1.2.4 Microfabricated and Electrospun Nanofiber Scaffolds

Microfabricated scaffolds are produced using techniques like photolithography or microcontact printing. They are typically made from polymers, ceramics, or metals and have precise features at the microscale, allowing for control over cell-scaffold interactions. Microfabricated scaffolds can be designed to mimic the native tissue microarchitecture and provide a microenvironment that supports cell growth and tissue regeneration. As an example, a homogeneous scaffold can be created with a specific pore size creating a viable 3D microenvironment characteristic of native islets of the pancreas (Daoud et al., 2011). Such methods enable precise control over the scaffold's architecture, allowing for the creation of a microenvironment tailored to the tissue being regenerated.

Similarly, electrospun nanofiber scaffolds offer a high surface-area-to-volume ratio, mimicking the architecture of the ECM, created through the process of electrospinning, which forms fibres from a polymer solution by the application of an electric field. These scaffolds, produced through electrospinning, provide a highly porous network that supports cell adhesion and growth (Kumbar et al., 2008). Electrospun nanofiber scaffolds can be designed to mimic the native tissue microarchitecture and provide a microenvironment that supports cell growth and tissue regeneration.

1.2.5 Summary

Biomaterials play an essential role in the development of scaffolds for tissue engineering, offering a range of mechanical and biological properties that can be tuned to support various cell types and tissue structures. Scaffolds, whether derived from natural, synthetic, or composite biomaterials, provide the necessary support for tissue regeneration and have applications across medicine and biomedical research. The choice of scaffold material and manufacturing technique remains a critical factor in ensuring successful cell/tissue growth and integration. Hydrogels and decellularized scaffolds remain central to tissue engineering research due to their versatile properties. Hydrogels, with their ability to mimic the soft tissue environment, are particularly useful in encapsulating cells and facilitating tissue regeneration. Decellularized materials, on the other hand, can provide a more direct approach by mimicking the complex architecture of native ECM, making them highly effective for organ regeneration and tissue repair (Rana et al., 2017).

1.2.6 Co-culture on 3D Models

The use of 3D co-culture models can offer a more physiologically relevant system to study cell-cell and cell-matrix interactions compared with standard 2D culture methods. In a 2D monolayer culture, cells are forced into an unnatural environment and position, where they adhere to flat, rigid surfaces, often leading to altered morphology, signalling, and function. In

contrast, 3D models allow cells to grow within an environment that mimics the *in vivo* tissue architecture more closely (Edmondson et al., 2014).

One of the advantages of a 3D co-culture system, is the ability to replicate cellular microenvironments better, providing more accurate data on cellular behaviour and interactions. In a 3D model, cells are surrounded by an ECM or scaffold that resembles native tissue architecture more closely. This results in more realistic cell polarization, gene expression, and differentiation patterns to name a few (Anton et al., 2015). The spatial arrangement of cells in 3D models also enables enhanced cell-cell signalling, crucial for understanding complex biological processes such as tissue development and regeneration (Baker & Chen, 2012).

Additionally, 3D co-cultures improve the mechanotransduction of cells, where cells sense and respond to mechanical stimuli. This is particularly relevant in tissues like bone and cartilage, where mechanical forces play a pivotal role in cellular function and differentiation. The dynamic nature of 3D systems makes them ideal for the study of stem cell differentiation, offering insight into how physical and biochemical cues regulate cellular functions in a more realistic manner (Fang & Eglen, 2017).

In the context of bone cells, 3D co-culture models provide a more relevant platform for studying osteogenesis and bone remodelling. Bone is a mechanically active tissue, and bone cells such as osteoblasts, osteoclasts, and osteocytes rely heavily on the three-dimensional arrangement of the ECM and cell-cell interactions for proper function. Traditional 2D models fail to provide the complexity of these relationships, whereas 3D systems allow for the study of bone cells in an environment that closely resembles their native structure (Barabaschi et al., 2015).

One of the key advantages of 3D co-culture models in bone research is their ability to study the coupling of osteogenesis and angiogenesis. Co-culturing osteoblasts with endothelial cells in 3D scaffolds mimics the interaction between bone-forming cells and blood vessels in vivo,

providing insights into how vascularization influences bone regeneration (Fedorovich et al., 2011). Such models have been used to study bone regeneration processes *in vitro*, offering a powerful tool for designing and testing new materials for bone tissue engineering.

3D models also enable the study of mechanical forces on bone cells. By applying mechanical stimuli, such as compression or shear stress, researchers can simulate the mechanical environment experienced by bone cells *in vivo*. This is particularly important for understanding how bone cells respond to mechanotransduction and how mechanical forces contribute to bone formation and remodelling (Yourek et al., 2010). Over the course of this project, we subjected our 3D models to mechanical stimuli using the Nanokick platform as described in Section 2.2.1.8, page 60.

While 3D co-culture models provide a more relevant platform for studying bone cells, they also face challenges. One of the main limitations is the difficulty in maintaining osteogenic differentiation over time. Although 3D scaffolds promote cell-cell interactions and matrix deposition, it can be challenging to ensure that cells within the scaffold maintain their osteogenic potential, especially in long-term cultures (Dutta & Dutta, 2009). Given the stage of optimisation reached during this project, this was not a consideration, however, it would be taken into consideration for future work with this research. Another limitation is the lack of vascularisation in many 3D bone models. While efforts have been made to co-culture bone cells with endothelial cells, achieving a fully functional vascular network within 3D constructs remains a significant challenge. The addition of vascularisation alongside blood cells to a model while desirable, would be too time consuming and introduce further variables which are not desirable at this stage of model optimisation. This is why our models were limited to bone cells alongside chemical and physical variables.

The application of 3D co-culture models in bone tissue engineering is vast. These models are used to design scaffolds for bone regeneration, with the goal of restoring bone tissue in cases of trauma, defects, or disease. Co-culturing osteoblasts and MSCs on scaffolds enhances

osteogenic differentiation and matrix mineralization, making these systems ideal for testing new biomaterials and osteogenic supplements (Tare et al., 2008). Additionally, 3D models are used in drug testing, where they provide a platform for evaluating the efficacy of bone-targeting drugs in an environment closer to their biological counterpart when compared to 2D (Pirosa et al., 2018).

1.3 Optical Manipulation

The 2018 Nobel Prize in Physics in part went to Arthur Ashkin for his application of laser physics, "for the optical tweezers and their application to biological systems". The work was initially conducted in the 1970s where he developed an optical levitation trap, using optical forces to displace and levitate dielectric particles (Ashkin & Dziedzic, 1975). The optical tweezers were refined and developed over many decades to their current state, the HOTs which were utilised during this project.

1.3.1 Optical Traps

The fundamental principle in the creation of an optical trap is that light has momentum and can therefore impart a force if there is a change in direction. This is in keeping with Newton's third law of motion, the law of action and reaction, where bodies interact and apply forces to each other, they are equal and opposite in magnitude and direction respectively. Since light is an electromagnetic oscillation, comprising an electric field and a magnetic field oscillating perpendicularly to each other, there is a resulting electromagnetic force which acts in the direction of the light's propagation.

Despite its lack of mass, light can impart momentum because it has energy which is seen in the non-simplified version of Einstein's equation:

$$Simplifed\ form\colon\ \ E = mc^2$$

$$Full\ equation\colon\ \ E^2 = (mc^2)^2 + (pc)^2$$

$$For\ photons\colon\ \ E = pc$$

Where E is relativistic energy, m is mass, c is the speed of light and p is momentum. The full equation shows that the energy of an object is dependent on its mass and momentum. As photons have zero mass, the equation simplifies showing its energy is proportional to its momentum. Since light has energy, it therefore must also have momentum.

Momentum is a vector and as such, the direction of movement is an important consideration. When the direction of light changes, it is imparting momentum to the object it is interacting with and exerting a force. Although unnoticeable, when light reflects off glass, because the path of light changes direction, a force is applied to the glass as momentum must be conserved. This instead can be applied to a lens, through which light bends when interacting with it. If light is shone through just the left side of the lens as shown in Figure 1.5 (A), the light bends to the right. To conserve momentum, the lens itself must therefore be pushed to the left. In the same figure (B), it is shown that by illuminating the lens equally on either side uniformly, the net force on the lens is zero.

Instead of a standard light source, a laser with the highest intensity at the centre of the beam which gets weaker towards the edges can be used - a Gaussian laser. If a microscopic glass sphere is placed in the path of this laser, it will be held in place. If the sphere is displaced upwards, the laser is refracted in such a way that the most intense region of the laser is bent upwards, and the weaker region downwards as seen in Figure 1.6 (A). There is a net laser momentum movement upwards so to conserve momentum, the sphere must attain a momentum downwards. This pushes the sphere back towards the centre of the laser.

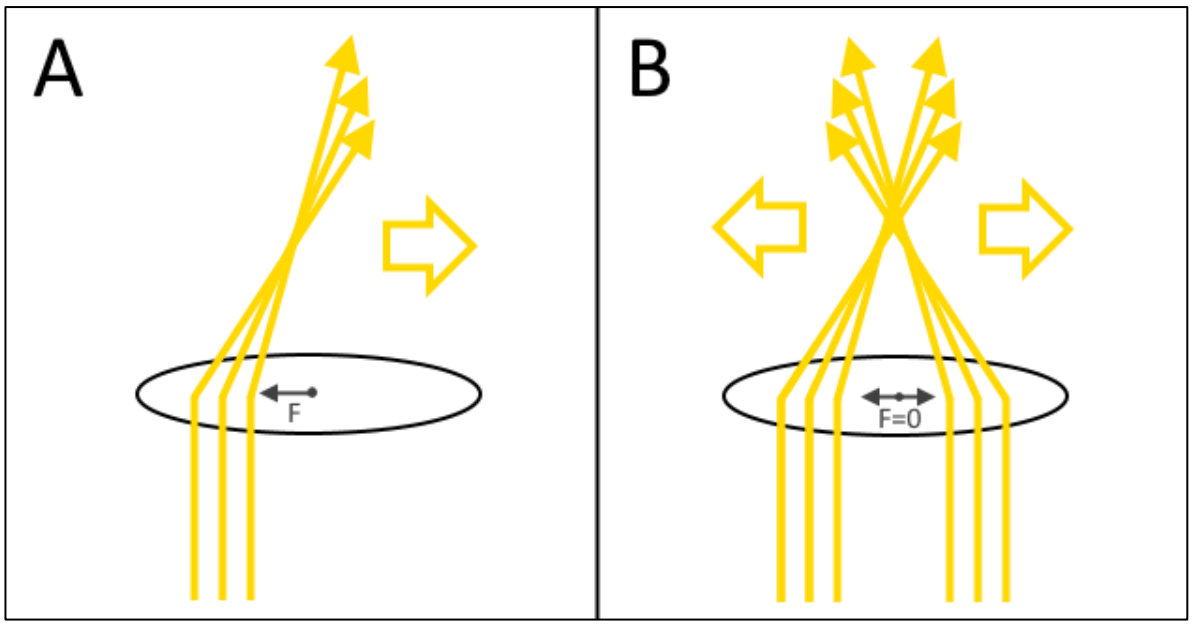

Figure 1.5: Light imparting force though a lens

Simplified diagram displaying the forces acting on a lens as a result of light being shined through the left side (A) and equally distanced on either side of the lens centre (B). Yellow arrows indicate the direction of momentum of light and black arrows indicate the direction of force acting on the lens.

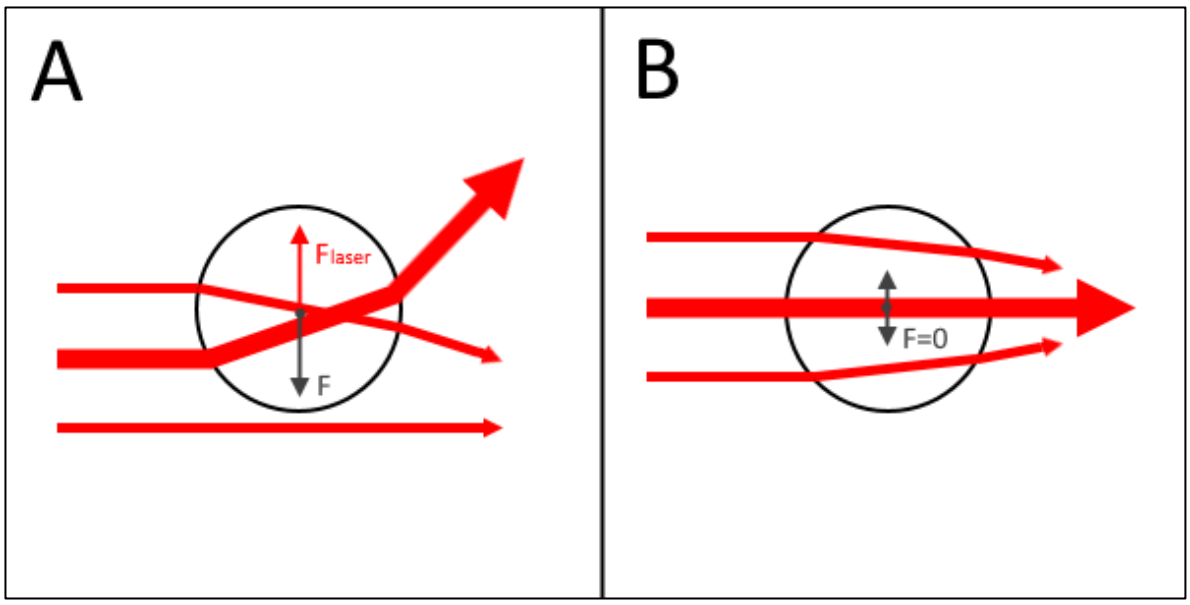

Figure 1.6: Laser refraction through a glass sphere

Simplified diagram of a gaussian laser refracted through a glass sphere off centre (A) and through the centre (B). Red arrows indicate the direction of force of the laser and black arrows the direction of force acting on the sphere.

With the sphere in the centre of the laser, the forces are balanced, and it is kept in place as seen in (B). If the sphere were to move downwards, the opposite would occur and again the sphere would be returned upwards to the centre of the beam. This model, however, does not accommodate the “push” of the laser. As some of the light is absorbed by the sphere, the transfer of momentum would push the sphere along the direction of the laser. The model also does not account for the effects of gravity, however, the earliest experiments created a levitation trap by rotating the model such that gravity is acting against the push of the laser (Ashkin & Dziedzic, 1971). This model, however, wasn’t very stable and needed refinement. Figure 1.7 describes this model through two rays a and b of a converging beam where movement in any direction returns the sphere to the focal point f.

By shining the laser through a lens with a high numerical aperture, such as a microscope objective, the laser reaches the sphere as a highly convergent beam. The laser is still refracted through the sphere and arbitrary displacement of the sphere away from the focus point provides a restorative force directed back to said focus (Ashkin, 1992). The term ‘optical tweezers’ is used in the application of an optical trap. By directing the laser focal point, the sphere can be moved assuming limited external forces such as drag. Not only can this system be used to hold something very delicately, but it can be used to detect any force acting on the held object. An example of this is the testing of DNA elasticity by attaching the DNA to the end of a bead and using optical tweezers to detect the movement (Perkins et al., 1994; Smith et al., 1996).

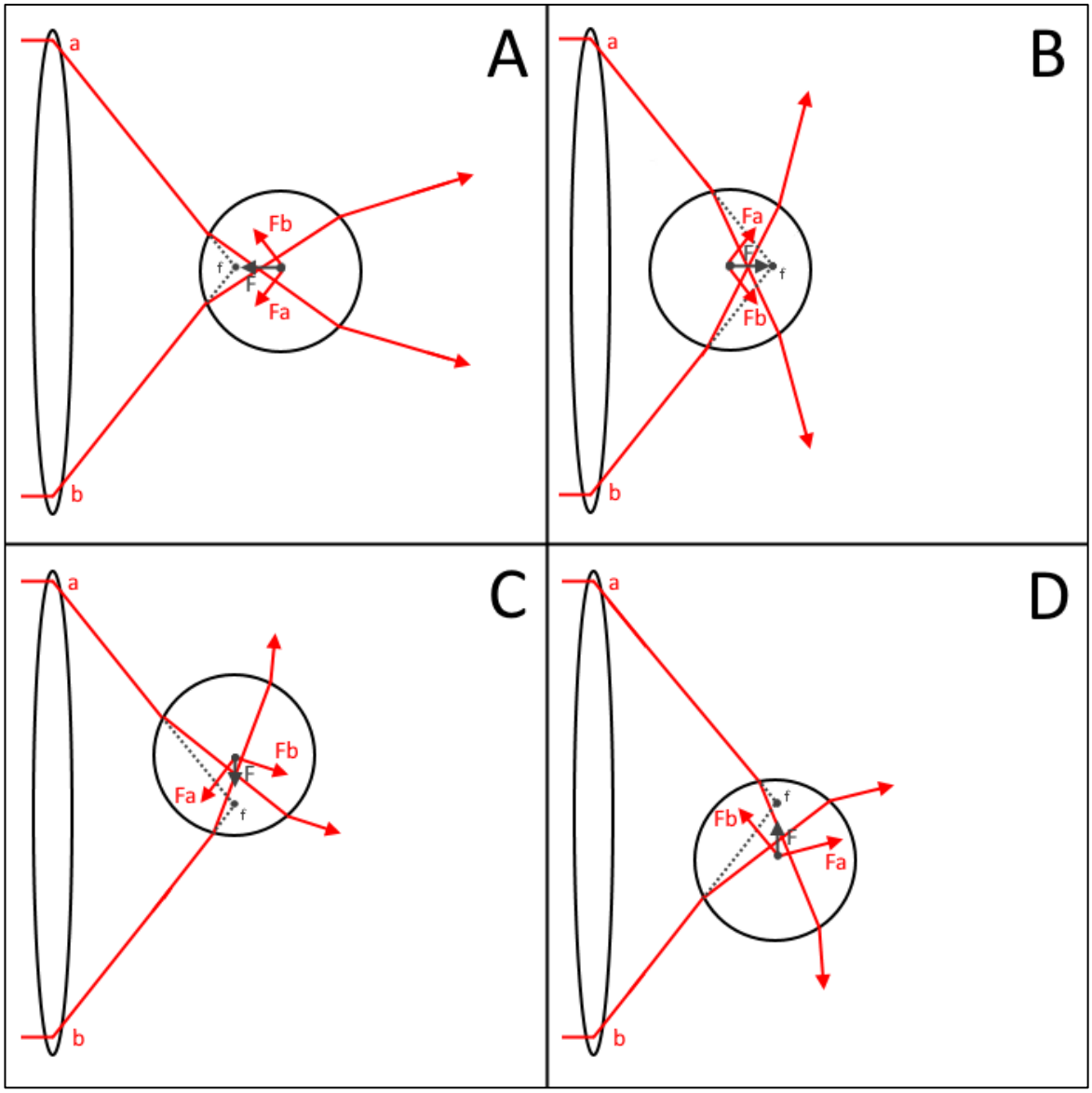

Figure 1.7: Optical trap stability

Simplified diagram of the workings of the optical trap. Each diagram shows how the resultant force F acting on the sphere always moves it in the direction of the focal point f as a result of geometric optics. Red arrows indicate the direction of force of the laser and black arrows the direction of force acting on the sphere. Displacement axially (A & B) or transversely (C & D) result in a net force returning the sphere to the focal point.

1.3.2 Holographic Optical Tweezers

HOTs are the further implementation of optical tweezers, using holographic techniques to manipulate and control multiple traps in 3D, used for both force sensing and force application on live cells over a range of force, from 0.1pN to 200pN and potentially up to 600pN. A

hologram in this case is a computer generated pattern of light intensity created by the combination of laser beams with specific phase difference and intensity. This computational control comes from the use of a spatial light modulator (SLM), a device that allows the dynamic control of diffractive optical elements to manipulate multiple traps (Gibson et al., 2012).The system can render a hologram to produce the correct intensity pattern producing multiple fully controllable traps in all dimensions (Bowman et al., 2014). This technology offers unparalleled spatial resolution and control, allowing the manipulation of not only cells with high precision, but other objects such as small bone fragments. Unlike other methods, HOTs do not require any form of labelling, reducing potential alterations to cell function and can trap and move cells without physical contact, minimizing mechanical stress and damage. This ability to adjust the traps in real-time adds to their versatility and potential effectiveness in complex biological studies, such as the bone morrow stem cell niche. Of note, for this projects HOTs system, the device had been designed into a compact form compared to standard HOTs systems. This allowed the device to be placed inside an incubator for prolonged cell culture experiments (Kirkham et al., 2015).

1.3.3 Cell Manipulation

Optical trapping and manipulation techniques have been found to exhibit remarkable versatility across a diverse spectrum of particle types. These techniques have been successfully applied to particles tens of nanometres to hundreds of micrometres in size, ranging from atoms and molecules to submicron particles and macroscopic dielectric particles (Grier, 2003). Notably, the scope of laser trapping and manipulation extends even to living biological cells.

Early work with optical tweezers was conducted with cells used an argon laser light which would cause smaller cells such as red blood cells to explode. This, however, was not an issue when using an infrared laser (Ashkin et al., 1987). Current optical trapping advancements allow the manipulation and confinement of single living cells, intracellular organelles, and

individual biological molecules as well as the assessment of the mechanical forces and elastic characteristics of both cells and molecules (Ashkin, 2000).

The HOTs system can sort and separate cells by using different holographic patterns. HOTs can trap and move individual cells or groups of cells, enabling sorting and separation of different types of cells based on their size, shape, or other characteristics (Ashok & Dholakia, 2012). HOTs can also be used to manipulate multiple cells in a controlled manner, creating 3D structures with the temporal control of chemical factors which can be used for modelling and the study of *in vitro* microenvironments (Kirkham et al., 2015).

1.3.4 Alternative Cell Trapping and Handling Technologies

While the HOTs were a fundamental constituent of this project and already optimised within the lab group, it is important to consider other available cell trapping and handling technologies. The pros and cons of each technology are summarised in Table 1, page 45 for ease of reference and comparison.

Magnetic tweezers utilise magnetic fields to manipulate cells or particles which have been labelled with magnetic materials. This technology offers a high degree of precision through the manipulation of paramagnetic beads using a gradient of magnetic field with excellent spatial resolution (Sarkar & Rybenkov, 2016). It is a non-invasive process, causing minimal thermal and photodamage to cells. Magnetic tweezers are versatile, suitable for studies in mechanotransduction, cellular biomechanics and even DNA topology (Gunn et al., 2018). A significant limitation, however, is the requirement for magnetic labelling, which can potentially alter cell function. Furthermore, only cells or particles that can be magnetically labelled can be manipulated, and achieving precise 3D control is more challenging compared with optical tweezers. This technology is also limited to the manipulation of single molecules (De Vlaminck & Dekker, 2012).

Acoustic tweezers utilise ultrasonic waves to trap and manipulate cells, bacterial and other particles *via* acoustic radiation forces (Meng et al., 2019). A major advantage of this

technology is the ability to manipulate objects without the need to label, avoiding the need to tag cells for example with beads or other markers like with magnetic tweezers. This method causes minimal physical stress on cells, considered safe and biocompatible (X. Ding et al., 2013). Acoustic tweezers are capable of higher throughput, manipulating multiple cells simultaneously. The technology, however, offers relatively low spatial resolution compared with optical tweezers and requires precise control and calibration of acoustic fields. The range of forces it can generate is also typically lower than those produced by optical or magnetic tweezers (Drinkwater, 2020).

Dielectrophoresis manipulates cells using non-uniform electric fields, utilising the differences in dielectric properties between cells and their suspending medium without the need for biochemical or bioengineered labels because manipulation is based on inherent dielectric properties and enables selective trapping of different cell types (Pethig, 2010). This method is generally integrated into small scale microfluidic devices, facilitating high-throughput applications but limiting its broader applicability. The high electric field strengths required for operation, however, can cause cellular damage and a careful control of the medium's conductivity and permittivity is required (Voldman, 2006).

Optoelectronic tweezers use light-induced dielectrophoresis to manipulate cells. Microscopic objects such as cells can be manipulated directly by inducing a change of electric fields on demand by leveraging the photoconductive effect of semiconductor materials (S. Zhang et al., 2022). Light patterns generate localized electric fields that can trap and move cells. Optoelectronic tweezers allow dynamic control, with light patterns that can be reconfigured to manipulate multiple cells simultaneously. It operates at lower optical powers compared with traditional optical tweezers and is scalable for large-scale parallel manipulation (Chiou et al., 2005). The resolution, however, is limited by the projected light patterns, and integrating optical and electronic systems into *in vitro* experiments can be complex in part due to optical and electrical properties of cell culture media.

Table 1: Trapping Technologies Pros and Cons

A comparison of the available trapping technologies that can be used to manipulate cells *in vitro*

Technology	**Pros**	**Cons**
Magnetic Tweezers	- High precision (pico to nano newton forces) - Minimal thermal and photodamage - Versatile for mechanotransduction studies	- Requires magnetic labelling, which can alter cell function - Limited to magnetic materials - Challenging 3D control
Acoustic Tweezers	- Label-free manipulation - Non-contact and gentle on cells - High throughput	- Lower spatial resolution compared to optical tweezers - Complex setup requiring precise control and calibration - Limited force range
Dielectrophoresis	- Label-free manipulation - Selective trapping of different cell types - Easily integrated with microfluidics for high-throughput	- High electric field strengths can damage cells - Requires careful control of medium's conductivity and permittivity - Effective mainly for small-scale, low-viscosity fluids
Optoelectronic Tweezers	- Dynamic control with reconfigurable light patterns - Lower optical power requirement compared to traditional optical tweezers - Suitable for large-scale parallel manipulation	- Resolution limited by projected light patterns - Complex integration of optical and electronic systems - Performance affected by changes in optical and electrical properties of the medium
Holographic Optical Tweezers	- Unparalleled spatial resolution and control - Label-free manipulation - Non-contact, minimizing mechanical stress on cells - Dynamic adjustment of traps in real-time	- Complex setup and operation - High maintenance requirements

While each cell trapping and manipulation technology has its own strengths and weaknesses, HOTs stand out. The advantages of HOTs are critical in this research due to their precision, label free method and versatility in manipulating individual cells within a 3D environment

ensuring cell health and function is retained. This capability is essential for recreating the intricate cellular arrangements and spatial dynamics of the bone marrow niche model, especially as it increases in complexity. HOTs enable precise positioning and patterning of multiple cell types, such as MSCs and osteoblasts, while maintaining their viability and functionality. This degree of control has the potential and the novelty to allow researchers to study specific cell-cell interactions and microenvironmental influences in unprecedented detail (Kirkham et al., 2015).

The use of HOTs will enable the creation of highly customizable niche models, facilitating a deeper understanding of the molecular and mechanical cues governing stem cell behaviour. Future impacts include the development of optimized scaffolds for stem cell therapy, advanced drug screening platforms that mimic native tissue conditions, and tailored therapeutic strategies for haematological disorders. On a broader scale, these innovations have the potential to revolutionize tissue engineering and regenerative medicine, reducing reliance on donor tissues and improving patient outcomes worldwide.

1.4 Aims

While the HSC side of the bone marrow stem cell niche has been well researched, the importance of MSCs is a relatively new discovery and not yet fully understood. Current investigations on the role and function of the niche have been limited to the analysis of tissue and cell samples, which makes it challenging to understand the dynamic changes in the structure and function of the niche in response to specific stimuli. By developing models of the niche *in vitro* the interactions and processes can be elucidated further. Use of models is particularly important given the difficulties with replicating the complexity of the natural niche environment and even the positions of cells within said environment. Both of these have roles in the mechanisms regulating the niche and should be considered when creating a model.

The aims of this project were two-fold. Firstly, to develop a basic model of the MSC niche which could be used to understand its workings better. This model would be considered "macroscopic" in that large numbers of cells would be utilised and grown on a suitable scaffold. Considerations of the models would be particularly centred around the cells, ECM, the chemical and the physical environment. The macroscopic model enables the analysis of dynamic interactions among different cell types and organizational elements and offers the potential for developing true tissue analogues in the future. Secondly, experimentation with the HOTs system in development of a "microscopic" model. This would involve the manipulation of a small number of individual cells and their patterning. This would focus on the ability to pattern different cells in specific positions to understand cell – cell interaction better. The microscopic model enables the study of fundamental interactions among individual cells and cell types, revealing how individual cellular organization regulate the niche and wound healing. This unique technique enables interrogation at both tissue and cellular levels.

In summary, the aims of this project were the following:

- Develop a "macro" model of the niche incorporating a scaffold and hMSCs
- Further develop the model with the addition of other bone cells
- Further develop the model with chemical adjustments to the media
- Further develop the model with the addition of mechanical stimulation

- Develop a "micro" model enabling the addition of two individual cells of different types using the HOTs system to a central position
- The above requires the testing of different objects as anchor points
- The design, creation and optimisation of a vessel capable of allowing the above model
- Validation of said model by adding two cell types and bringing one of each type to a central point repeatably

1.5 Potential Impact of Research

At the macro level, the data generated by our research has the potential to help improve the understand of the niche. In particular, we hope to learn about the effects of mechanical stimulation and its effect on osteogenesis. Beyond this research, the models have great potential for expansion, building upon the work done with added complexity following avenues of interest. This could include, for example, the addition of other cell types such as HSCs and the introduction of various growth factors. The primary focus of the micro model work is in creating and optimising a method to introduce different cell types to the same dish. Once developed, this method could be used in the profiling of cellular microenvironments, being able to provide information about the chemical signals of individual cells correlated with their relative three dimensional locations.

The potential future clinical implications of designing and modelling the bone marrow stem cell niche are vast, offering new pathways for advancing regenerative medicine and targeted therapies alongside furthering the understanding of the niche itself. By recreating the complex interactions within this niche, researchers could develop systems that enable precise control of stem cell fate, enhancing their therapeutic potential in conditions such as bone marrow failure, haematological conditions, bone fracture and autoimmune disorders. Understanding the microenvironmental cues that govern stem cell behaviour within their niche can provides crucial insights into disease mechanisms, facilitating the creation of more effective drug screening platforms and personalized treatments. This knowledge could lead to breakthroughs in stem cell transplantation protocols and the development of bioengineered niches tailored to patient-specific needs.

An example of a potential impact of this research with regards to medical practices, would be the generation of bespoke patterned replications of the niche, created using the HOTs. By precisely positioning various cells and other relevant particles onto a scaffold, this model

could be implanted into patients with critical fractures at the defect site. The micro model would then output all the necessary cells and signals aiding in the bone healing process.

The societal impact of these advances includes improved outcomes for patients with otherwise incurable conditions, reduced healthcare costs through more efficient therapies, and the potential to alleviate the global burden of donor dependency in stem cell therapies.

2. Materials and Methods

2.1 Materials Used in the Investigation

2.1.1 Reagents and Kits

Reagent	Catalogue Number	Company
0.25% Trypsin-EDTA	25200-072	ThermoFisher
2-Mercaptoethanol	31350010	ThermoFisher
3D printer resin (grey), UV sensitive	-	ANYCUBIC
Alizarin Red S	A5533-25	Merck
Ammonium hydroxide solution	09859-250	Merck
Aquaguard-1	PK-CC01-867-1B	Promocell
Biocleanse concentrate	TK200	Teknon
Bovine serum albumin	BP9702	Fisher Scientific
CellTracker™ Blue CMAC Dye	C2110	ThermoFisher
CellTracker™ Green CMFDA Dye	C2075	ThermoFisher
Collagen I, Rat Tail	A10483-01	ThermoFisher
Dexamethasone	D4902-25	Merck
Dimethyl sulfoxide	D4540-100	Merck
Donkey serum	D9663-10	Merck
Dulbecco's Modified Eagle Medium (DMEM)	11960-044	ThermoFisher
Ecoflex Near Clear trial kit	00-45	Bentley Advanced Materials
ESGRO Leukemia Inhibitory factor	ESG1107	Merck
Ethanol	BP8202	Fisher Scientific
Fetal Bovine Serum, heat inactivated	35-089-CV	Corning
Gelatin Solution	9000-70-8	Merck
Gentamicin solution	G1397-10	Merck
Goat serum	G9023-10	Merck
hMSC Osteogenic Differentiation Basal Medium	PT-3924	Lonza
hMSC Osteogenic Differentiation SingleQuots™ Supplements Kit	PT-4120	Lonza
Hoechst 33258 solution	94403	Merk
Immersion oil		Olympus
L-ascorbic acid	A8960-5	Merck
L-Glutamine (200mM)	25030-081	ThermoFisher
MSCBM™ Basal Media	PT-3238	Lonza
MSCGM™ SingleQuots™ Growth Supplement Kit	PT-4105	Lonza
Paraformaldehyde	P/0840/53	Fisher Scientific
Penicillin/Streptomycin (10,000U/ml)	15140122	ThermoFisher
Phosphate buffered saline tablet	P4417-100	Merck
qPCRBIO cDNA Synthesis Kit	PB30.11-10	PCR Biosystems
qPCRBIO SyGreen Mix Hi-ROX	PB20.12-05	PCR Biosystems
RNeasy® Mini Kit	74106	QIAGEN
TriGene Advance, disinfectant	BUNZ037631_U	VWR
Triton X-100	93443-100	Merck

β-glycerophosphate	G9422-100	Merck

2.1.2 Plasticware

Item	Catalogue Number	Company
µ-Dish, 35mm diameter glass bottom imaging dish	81158	Ibidi
1.5ml microcentrifuge tubes	72.690.001	Sarstedt
15ml sterile tubes	62.554.503	Sarstedt
96 well semi-skirted PCR plates	E1403-6200	StarLab
BD PlastiPak™ Syringe with Luer Lock	15544835	Fisher Scientific
Corning™ Stripette™ (25, 10 & 5mL)	10606151, 10084450 & 10420201 respectively	Fisher Scientific
CryoTube™ Vials	377224	Thermo Scientific
epT.I.P.S.® Standard (50 – 1000µL, 2 – 200µL, 0.5 – 20µL	0030000927, 0030000870 & 0030000650 respectively	Eppendorf
Falcon® 50 mL High Clarity PP Centrifuge Tube	352098	Falcon
Microcaps® micropipettes (20 & 50µL)	1-000-0200 & 1-000-0500 respectively	Drummond
Nunc™ Cell-Culture Treated Multidishes (6 well & 12 well)	140685 & 150628 respectively	Thermo Scientific
Nunc™ Non-Treated Multidishes (12 well)	150200	Thermo Scientific
Nunc™ Non-Treated Multidishes (6 well)	144530	Thermo Scientific
Polyester seal for RT-qPCR (sterile)	E2796-0714	StarLab
Sartorius Minisart™ Plus Syringe Filters, Sterile	10730792	Fisher Scientific
T25 Nunclon Delta treated filter capped flasks	156367	Thermo Scientific
T75 Nunclon Delta treated filter capped flasks	156499	Thermo Scientific

2.1.3 Antibodies

Name	Catalogue number	Company
Alexa Fluor ™ 488 donkey anti-rabbit IgG (H+L) (secondary)	A21206	ThermoFisher
Alexa Fluor ™ 546 donkey anti-goat IgG (H+L) (secondary)	A11056	ThermoFisher
Anti-osteocalcin antibody (primary)	AB10910	Merk
Anti-osteopontin antibody (primary)	AB10911	Merk

2.1.4 Primers

Gene symbol	Gene name	Sense sequence (5'-3')	Anti-sense sequence (5'-3')
ALPL (mouse)	Alkaline phosphatase	TGAGCGACACGGACAAGAA	CCACGTCTTCTCCACCGT
BGLAP (human)	Bone gamma-carboxyglutamate protein/Osteocalcin	GCAGCGAGGTAGTGAAGAGA	CCTCCTGAAAGCCGATGTG
GAPDH (human)	Glyceraldehyde-3-phosphat dehydrogenase	GGGTGTGAACCATGAGAAGT	AGTCCTTCCACGATACCAAAGT
GAPDH (mouse)	Glyceraldehyde-3-phosphat dehydrogenase	CCCAATGTGTCCGTCGTG	GAGTTGCTGTTGAAGTCGCA
IBSP (human)	Integrin binding sialoprotein	AACACTGGGCTATGGAGAGG	GTACTGGTGCCGTTTATGCC
RUNX2 (human)	Runt-related transcription factor 2	ACTGCCACCTCTGACTTCTG	ACTGGCGGGGTGTAAGTAAA
RUNX2 (mouse)	Runt-related transcription factor 2	CTCTGGCCTTCCTCTCTCAG	GTAGGTAAAGGTGGCTGGGT
SP7 (human)	Osterix	TCAACAACTCTGGGCAAAGC	ATGAGTGGGAAAAGGGAGGG
SP7 (mouse)	Osterix	ATGGCGTCCTCTCTGCTTG	GTTGTTGAGTCCCGCAGAG
SPP1 (human)	Secreted phosphoprotein 1/Osteopontin	CGAGGTGATAGTGTGGTTTATGG	GCACCATTCAACTCCTCGCTTTC

2.1.5 Equipment/Machines

Item	Catalogue Number/Model	Company
Bead Mill	15525799	Fisher scientific
BigPrep™ Lysing Matrix M	116959010-CF	MP Biomedicals
BigPrep™ Lysing Matrix Z	1169790-CF	MP Biomedicals
Centrifuge	Harrier 15/80	MSE
Centrifuge	5417 R	Eppendorf
CoolCell™ LX cell freezing container	CLS432002	Merck
EDF 1200 - Centrifuge	C7077/fc4	Envair
Elegoo Mars 3 Pro -3D printer	-	Elegoo
Fisherbrand™ Elite™ Pipette, 0.2 - 2µL	JH69275	Fisher Scientific
Fisherbrand™ Isotemp™ Stirrer	15333518	Fisher Scientific
Fume cupboard	-	Envair
Gilson Pipetman Pipette, 2 - 20µL	NG23939	Scientific Laboratory Supplies
Gilson Pipetman Pipette, 50 - 200µL	NE26821	Scientific Laboratory Supplies
Gilson Pipetman Pipette, 200 - 1000µL	NG21251	Scientific Laboratory Supplies
Holographic optical tweezers	-	University of Glasgow (Padgette Group)
Improved Neubauer counting chamber	0640010	Marienfeld
Incubator	MCO-18AC-PE	Panasonic

JSM 7100F Thermal field emission electron microscope	-	JEOL
Labnet MPS 1000 Mini plate spinner	Z681695-1EA	Merck
Leica DMi1	-	Leica
Leica DMi8	-	Leica
Leica Thunder 3D cell culture imaging system	-	Leica
Microbiological safety cabinet (MSC) Class II	-	Walker
NanoDrop 8000	ND-8000	Thermo Scientific
Nanokick	-	University of Glasgow (Dalby Group)
Q150R Plus – Rotary Pumped Coater	-	Quorum
QuantStudio 5 Real-Time PCR system	A34322	ThermoFisher
Thermocycler	T-100	BIO-RAD

2.1.6 Cell Types

2.1.6.1 HOS

HOS is a human osteosarcoma cell line, originally obtained from the tumour of a 13yo female in 1971 (McAllister et al., 1971). Cells used experimentally ranged in passage from 35 to 97 over the whole project time frame. Cells were produced by the ECACC and purchased through Sigma-Aldrich. HOS were selected as the primary experimental cell type as they can undergo osteoblastic differentiation and are widely used as control cell lines as analogues of osteoblasts (Teti, 2011). The cells were found to adhere and proliferate very well with a relatively high (compared to SaOS-2) number of consistent cells over time making them ideal for early model work due to their consistency over time. They have also been very well characterised within the group.

2.1.6.2 SaOS-2

Sarcoma osteogenic (SaOS-2) is a human osteosarcoma cell line, originally obtained from the tumour of a 11yo female in 1973 (Fogh et al., 1977). Cells used experimentally ranged in passage from 32 to 65 over the whole project time frame. Cells were produced by the ECACC and purchased through Sigma-Aldrich. SaOS-2 were only used in some of the earlier

experiments as although they, like HOS, can undergo osteogenic differentiation, they tend to senesce faster and drift with increased passage number (Czekanska et al., 2012).

2.1.6.3 CGR8

CGR8 is a mouse embryonic stem cell line derived from the inner cell mass of a 3.5 day male pre-implantation mouse embryo (https://www.culturecollections.org.uk/products/celllines/generalcell/detail.jsp?refId=07032901&collection=ecacc_gc). Cells used experimentally ranged in passage from 6 to 24 over the whole project time frame. Cells were produced by the ECACC and purchased through Sigma-Aldrich. CGR8 were utilised as they have been used previously for both Nanokick and HOTs work (Dalby et al., 2007; Kirkham et al., 2015). They were a useful initial optimisation cell as hMSCs were limited. Work has also already been published regarding osteogenesis and MSCs on the Nanokick, so using this cell type would be novel (Pemberton et al., 2015). Finally, embryonic microenvironments are a key future application of the HOTs system, so rather than repeating work we can demonstrate additional applications and novelty.

2.1.6.4 Human Mesenchymal Stem Cells

hMSCs at passage 2 were obtained from Lonza from a 22yo male Black/African American non-smoker with no underlying health conditions. Cell were sorted via CD antigens: positive for CD105, CD166, CD29, & CD44, and negative for CD14, CD34, & CD45. This specific hMSC patient was chosen as the patient was young, healthy and a non-smoker. The antigens also characterise the cells as true hMSCs. Cells used experimentally were all at passage 5 while cells up to passage 8 were used for HOTs optimization tests.

2.2 Methods

2.2.1 Cell Culture

Cell culture and good aseptic technique were the cornerstone of this project and as such great care was taken to ensure the proper care of all cells in use. Cell culture was conducted in a

class II microbiological safety cabinet (Class II MSC, Walker) containing high efficiency particulate air filters. All cell cultures were kept in a humidified 37°C, 5% CO_2 incubator (MCO-18AC-PE, Panasonic) with the water bath treated with Aquaguard-1 solution (Promocell). Day-to-day decontamination of surfaces, equipment and gloved hands was done using 70% industrial methylated spirit (IMS) in distilled deionised water (ddH_2O).

2.2.1.1 Osteosarcoma Cell Line Maintenance

The cells HOS and SaOS-2 were used for protocol optimisation and only HOS for the final models, following identical procedure for maintenance. Culture media was made from Dulbecco's Modified Eagle Medium (DMEM) supplemented with heat-inactivated 10% fetal bovine serum (FBS), 1% Penicillin/Streptomycin (P/S) and 1% L-glutamine (L-g).

Grown directly on treated cell culture plastic, the cells were maintained in 10mL of culture medium with media changes every four days until 80-90% confluence was reached. The passaging process was as follows. Medium was aspirated from a confluent flask and washed with 5mL phosphate-buffered saline (PBS). 2mL of trypsin was added and incubated at 37°C for five minutes. An inverted light microscope (DMi1, Leica) was used to confirm the cells had fully detached and lightly tapped on the side of the flask to aid further detachment as needed. 3mL of media was added to stop the trypsinisation and the cell mix transferred to a universal tube for centrifugation for five minutes at 300g (Harrier 15/80, MSE). The supernatant was discarded, and the pellet resuspended in 1 – 5mL of culture media. 10mL of culture media was added to the number of T75 flasks needed. The suitable dilution ratio for HOS ranges from 1:5 to 1:20 while for SaOS-2, 1:5 to 1:12. Depending on when confluence is needed as well as the number of flasks required, the ratio was chosen, and the suitable volume of cell suspension pipetted into each flask.

2.2.1.2 Embryonic Stem Cell Maintenance

The mouse embryonic stem cell line CGR8 was used for an investigation into the effect of nano vibrations on bone formation. Embryonic basal media (eBM) was made from DMEM

supplemented with heat-inactivated 10% FBS, 1% P/S, 1% L-g and 100µM 2-Mercaptoethanol. Feeder free mouse embryonic stem cell (ff-mESC) media was made from eBM with 1000 units of leukaemia inhibitory factor (LIF).

The ff-mESCs were grown in gelatin coated T25 flasks. Gelatin (Merck) was procured as a 2% solution in H_2O and diluted down to a 0.1% (1:20 dilution) and sterile filtered through a 0.2µm syringe filter. 2mL of the solution was added to as many T25 flasks as required and left overnight at room temperature or for a minimum of 2hrs in an incubator. Excess gelatin was removed preceding use. Cells were maintained in 5mL of ff-mESC culture media with media changes every day until reaching a confluency of 80-90%. Confluency was determined by the size and distribution of individual colonies of cells. The passaging process was as follows.

Media was aspirated from the confluent flask and washed with 5mL PBS. 2mL of trypsin was added and incubated at room temperature for five minutes. During this time, the side of the flask was lightly tapped to aid detachment and checked under a microscope to confirm the cells had detached at the end of the five minutes incubation. 3mL of eBM media was added to stop the trypsinisation and transferred to a universal tube for centrifugation for five minutes at 180g. The supernatant was aspirated and 2 – 5mL of ff-mESC media added depending on the desired splitting ratio, and the pellet resuspended. The suitable range in splitting ratio for this cell type ranges from 1:2 to 1:5. 10mL of ff-mESC media was added to the number of T25 gelatin treated flasks required and the suitable volume of cell suspension added to achieve the desired splitting ratio.

2.2.1.3 Mesenchymal Stem Cell Maintenance

hMSCs were used in both the macro and micro models. Their maintenance largely followed the same protocol as HOS and SaOS-2 as stated above with the following differences. They were maintained in mesenchymal stem cell basal medium (MSCBM) purchased from Lonza. MSCBM was made up from mesenchymal stem cell growth media (MSCGM) along with MSCGM™ SingleQuots™ growth supplement kit which contains mesenchymal cell growth

supplement (MCGS), L-g and P/S. The media was changed every three to four days and post trypsinisation the cell suspension was centrifuged for five minutes at 600g. Suitable dilution ratios range from 1:2 to 1:8, however, given that the cells were received at P2 and used for experimentation at P5, the original vials were split between two T75s. After reaching confluence, the two flasks were split 1:4 and the eventual 8 flasks cryopreserved (P4) for later experimental use as described in 2.2.1.5, page 58.

2.2.1.4 HOS, SaOS-2 & CGR8 Cryopreservation and Reanimation

Cryopreservation media was made from FBS and 10% Dimethyl sulfoxide (DMSO) sterile filtered through a 0.2µm syringe filter before use. The maintenance protocol was followed to the point of resuspending the cell pellet but in 2mL of media. Multiple flasks can be combined after the trypsinisation stage ensuring the suitable volume of media is added. Using an improved neubauer counting chamber, the number of cells was counted. For the three cell types, the desired number of cells per cryovial is $1x10^6$. 1mL of cryopreservation media was added to the cell suspension per $1x10^6$ cells, and 1mL transferred to each cryovial. The cryovials were transferred to a CoolCell™ cryopreservation container (Corning) and stored within a -80^oC freezer for a minimum of one day before transfer to liquid nitrogen long term storage. Whenever working with DMSO, it was paramount to work as quickly possible as the chemical leaves the cells in a fragile state.

With a seeding density of approximately 1.3 x 10^4 for HOS and SaOS-2 and 4 x10^4 for CGR8, the prepared cryovials of 1 x 10^6 cells are ideal for reanimation into one flask each. HOS and SaOS-2 were reanimated into a T75 while CGR8 into a gelatin coated T25 (the same procedure as detailed in section 2.2.1.3, page 55). Prior to reanimation, one universal tube was filled with 9mL of DMEM and one filled with culture media for HOS and SaOS-2 or 9mL of ff-mESC media for CGR8 and warmed to 37^oC. Vials to be reanimated were generously decontaminated with 70% IMS, wiped dry and thawed as quickly as possible (water bath or held in hand). As soon as the vial has thawed, its contents was slowly pipetted just below the meniscus of the prewarmed DMEM. The suspension was centrifuged for five minutes at 300g

if HOS or SaOS-2 and 180g if CGR8. The supernatant was disposed of, and the pellet gently resuspended in the warmed culture media/ff-mESC media and transferred to a suitable flask. Having been transferred to the incubator, cell growth was monitored every 24 - 48hrs to determine the confluence progression.

2.2.1.5 hMSC Cryopreservation and Reanimation

The cryopreservation procedure for hMSCs is largely the same as with HOS, SaOS-2 and CGR8 but with a few alterations (following the maintenance protocol for hMSCs). The cryopreservation media was made of 85% MSCBM, 10% DMSO and 5% bovine serum albumin (BSA) (w/v). The ideal range of cells per vial was from 5 x 10^5 to 1 x 10^6 and a secondary centrifugation was always conducted to ensure the cells were frozen in 100% cryopreservation media.

As with the other cell types, the number of cells cryopreserved was calculated to be suitable for reanimation into one flask per vial. Two universal tubes, one with 5mL and one with 9mL of MSCBM were placed in the incubator to reach 37^{o}C per vial. Vials to be reanimated were decontaminated with 70% IMS, wiped dry and thawed as quickly as possible (water bath or held in hand). As soon as the vial had thawed, its contents were slowly pipetted drop by drop just above the meniscus of the prewarmed 5mL of MSCBM and immediately centrifuged for five minutes at 500g. The supernatant was discarded, and the pellet gently resuspend in the 9mL of warmed MSCBM using a 5mL serological pipette. Having been transferred to the incubator, cell growth was monitored every 24 - 48hrs to determine the confluence progression.

2.2.1.6 Osteogenic Assay

If the given experiment entailed the encouragement of cells to output osteogenic product, specialised media was required. HOS, SaOS-2 and CGR8 require the supplements dexamethasone, β-glycerophosphate (β-gp) and L-ascorbic acid (VIT C). Stock solutions or aliquots were made as follows to be added directly to 39mL of culture media/ff-mESC media

to give a final 40mL of osteogenic media. Stocks and aliquots were stored at -20^{o}C for up to one month.

HOS and SaOS-2 as human cells required a final dexamethasone concentration of 100nM (Langenbach & Handschel, 2013b)while CGR8 required 10µM (Buttery et al., 2001). First, a 25mM stock was made by adding 9.8118mg to 1mL of ethanol. This was diluted down 1:500 times to 50µM in ethanol. This ethanol stock was stored at -20^{o}C until needed and added to 39mL of media (in a 50mL collection tube) to obtain 100nM or 10µM as needed.

The three cell types require 50mM of β-gp which was achieved by its addition directly to the media. 432mg of β-gp was weighed out under sterile conditions and added directly to the 39mL of media and dexamethasone. The tube was gently inverted to dissolve the β-gp, with the use of a vortex if necessary to dissolve fully.

The three cell types also required 50µg/mL of VIT C. For a final 40mL of media, a total of 2mg of VIT C was needed. By dissolving 20mg of VIT C into 10mL of media, this was split into 1mL aliquots which when added to the 39mL of media with dexamethasone and β-gp results in the complete osteogenic media. The media was sterile filtered through a 0.2µm syringe filter and was suitable for use for up to two weeks.

Preparation of osteogenic media for hMSCs only required the addition of osteogenic differentiation SingleQuots^{TM} supplement kit (thawed over night at 4^{o}C) to the osteogenic differentiation basal medium. These supplements included MCGS, P/S, L-g, ascorbate, dexamethasone and β-gp.

No matter the cell type or osteogenic media, their use was the same. After passaging cells, they were kept in the incubator for 24hrs in their regular maintenance media before being gently aspirated and replaced with osteogenic media for the desired time frame. This was 7, 14 and 21 days for mouse cells and 7, 14 and 28 days for human cells. Media was replaced at the standard intervals detailed in sections 2.2.1.1, 2.2.1.2 and 2.2.1.3.

2.2.1.7 Embryoid Body Formation, Dissociation and Seeding

For the purposes of growing mouse embryonic stem cells on a "Nanokick platform" (see section 2.2.1.8, page 60) the cells need to first be allowed to form embryoid bodies before being dissociated and seeded into plates. This stage is necessary as the naïve cells through embryoid body formation trigger their differentiation *in vitro*, facilitating necessary multicellular interactions (Kurosawa, 2007).

Starting with a confluent flask of CGR8, the standard passaging protocol (2.2.1.2, page 55) was followed to resuspension of the cell pellet except 2mL of eBM media was used. The cell number was counted and seeded into a non-treated 100mm diameter petri dish at approximately 2 x 10^6 cells in 10mL of eBM (3.5 x 10^4 cells/cm^2). The dish was incubated at 37^{o}C for three days providing enough time for aggregates to form, floating in the media.

The media and aggregates were transferred to a 15mL collection tube and allowed to settle under gravity. The supernatant was disposed of, 10mL of sterile PBS added and the contents gently agitated. The wash was repeated, after which the PBS was aspirated and 5mL of trypsin added. The tube was set on a roller set to 30rpm inside a 37^{o}C incubator for ten minutes. At the end of the time, 5mL of eBM media was added to inactivate the trypsin and a pipette used to resuspend the cells. The cells were centrifuged at 180g for five minutes, the supernatant discarded, and the pellet resuspended in 10mL of aggregation medium. The cell count could then be taken, and cells seeded at a suitable density onto 0.1% gelatin coated flask or plate.

2.2.1.8 Mechanical Stimulation

Some experiments required the stimulation by high frequency vibrations of flasks/plates hoping to influence osteogenesis. This was achieved via the 'Nanokick platform' designed by Prof Matthew Dalby (University of Glasgow, UK). This device vibrates at a constant 1000Hz frequency and was fitted inside an incubator. It is turned on via a control switch situated on the power box kept outside the incubator and up to two flasks/plates can be place on the platform at any given time.

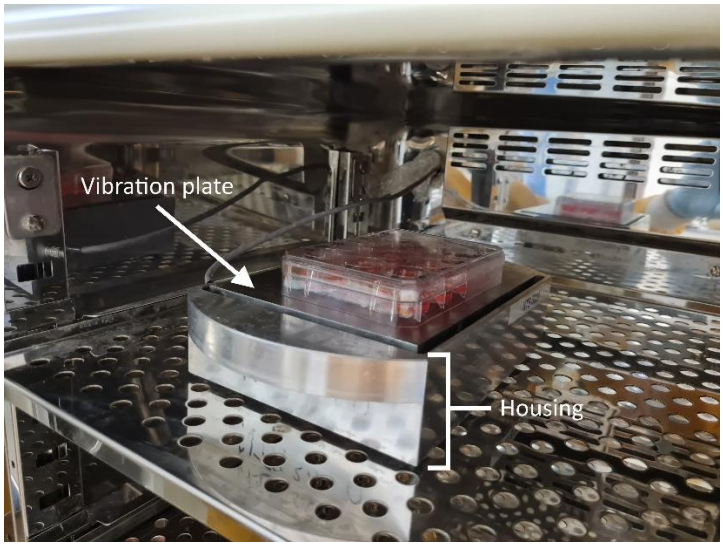

Figure 2.1: Nanokick platform

The Nanokick platform (designed by Prof Matthew Dalby) in position inside an incubator with a single 12 well plate in place as it would be used for all experiments. The control box is located on top of the incubator with all cabling tightly packed to maintain incubator CO_2 and temperature levels.

2.2.2 Collagen Scaffold

Collagen was initially considered as a scaffold material based on its biocompatibility and as such required optimisation (Glowacki & Mizuno, 2008). Collagen I, rat tail from Gibco was procured at a concentration of 3mg/ml in soluble form due to the pH of the buffer. The gelling procedure required the addition of 1N NaOH which reacts with the acid, creating a neutral pH, causing the collagen fibres to reassemble into a gel. The further addition of 10x PBS and ddH_2O in varying quantities, following the manufacturer's protocol calculations, allows the formation of the desired concentration of collagen gel (Publication Number MAN0007327).

$$Collagen\ conc.needed\ [V1] = \frac{Final\ Collagen\ Conc. \times\ Total\ Vol\ [Vt]}{3mg/ml}$$

$$10x\ PBS\ Vol\ [V2] = \frac{Vt}{10}$$

$$1N\ NaOH\ Vol\ [V3] = V1\ \times 0.025$$

$$dH_2O\ Vol\ [V4] = Vt - (V1 + V2 + V3)$$

All reagents were kept on ice during use. The NaOH, 10x PBS and ddH_2O were mixed before the collagen was added slowly and mixed via pipetting up and down. The collagen solution

was pipetted rapidly into the desired well plate and incubated at 37^{o}C for a minimum of 1hr or overnight to ensure a firm gel was formed.

2.2.3 Animal Work

The use of bone as a scaffold in place of collagen was considered after difficulties in its use and procurement occurred. By using bone, not only would there be a biocompatible scaffold, additionally, the native ECM structure and composition would mimic the natural environment of MSCs and hopefully promote cell attachment, proliferation and differentiation (Ghassemi et al., 2018). Rats have a suitably similar physiology to humans to make them a good species for research at this stage of *in-vitro* experimentation (N. B. Robinson et al., 2019).

All animal work was conducted under regulations set out by the UK Home Office and performed under licence of Nottingham Trent University (Nottingham, UK).

Wistar Hans adult rat cadavers were provided by the Hulse lab group (Nottingham Trent University, UK) having had their paws removed for another study. By obtaining the cadavers in this manner, the 3Rs are adhered to, particularly reduction, minimising the number of animals used in research. In short, the rats were considered waste materials that would otherwise have gone for disposal if not used for this work and no procedures were conducted on the rats while alive for the purposes of this work, nor were any animals housed or sacrificed specifically for the purposes of this project. The bodies were stored at -20^{o}C until ready for harvesting.

2.2.3.1 Rat Bone Harvesting

Cancellous bone was needed to act as an *ex-vivo* scaffold and rat bone was selected. Cancellous bone is primarily found in the long bones as well as the ribs, as such the humerus, ulna, femur, tibia and rib cage were harvested.

Having thawed the body overnight at 4^{o}C, the rats were dried and pinned to a board on their back. An inverted Y incision was made over the chest using a new scalpel and the skin

retracted with tweezers presenting the rib cage. Using autopsy scissors, the rib cage was split along the sternum and the heart and lungs carefully removed to show where the ribs meet the spine. The scissors were then used to remove the left and right side of the rib cage from the spine. Tweezers were then used were possible to remove the individual ribs from the intercostal muscles. Where this was not possible, a scalpel was used to cut away the muscle.

To harvest the long bones, the limbs were removed from the body at the shoulder and hip by cutting into the joint, removing the surrounding muscle and using a small amount of force to detach the limb from the socket. The skin on each limb was removed and the large muscle groups detached. The three bones of each limb were separated and the radius from the arms and the fibula from the legs discarded.

Samples were categorised by location (leg, arm and rib) and stored at -20^{o}C.

2.2.3.2 Rat Bone Decellularization

Having thawed the bone, any remaining muscle fibres were removed using a scalpel for larger pieces and tissue paper to sheer off any remaining small pieces of muscle. All cartilage was removed from the joint surfaces. The following method is an adaptation of the protocol developed by Dr Lisa White (University of Nottingham, UK) (Alom et al., 2018) originally based on Lomas et al., 2001.

The ribs were cut into 3-5mm pieces while the long bones were bisected along the length by repeatedly scoring with a scalpel. All cancellous bone was separated from cortical taking particular care to remove the joint heads as they contain the largest volume of cancellous bone. Cancellous and cortical bone were distinguished by their structure under the Nikon SMZ800 inverted microscope. An antibiotic solution was created by diluting gentamicin (provided at 50mg/ml) in PBS at 0.1% w/v. The bone pieces were soaked in the solution for 20 minutes at 37^{o}C having ensured all pieces were fully submerged. All excess fluid was removed following incubation and the bone washed 3 times in deionised water. Fragments

were snap frozen in liquid nitrogen before storing the bone pieces at -20°C prior to fragmentation.

The used gentamicin solution as well as all water used in the washing process was denatured at 37°C over five days then disinfected with trigene for 12hrs before disposal.

2.2.3.3 Rat Bone Fragmentation

The bone fragmentation process evolved over the course of experimental work to introduce a more consistent range of fragment sizes as well as to accommodate the creation of a greater number of fragments. All liquid nitrogen work was conducted in an externally vented fume cupboard.

Initially, fragments were created via pestle and mortar. The desired number of bone pieces were defrosted and gently dabbed with tissue paper to remove as much moisture as possible. Liquid nitrogen was poured into the mortar and the dried bone carefully dropped in. When the majority of liquid nitrogen had evaporated leaving only 1 – 3ml, the pestle was used to fragment the bone by applying direct pressure to each bone piece. A brush was then used to transfer all fragments to a Falcon tube. If there were uncollectable fragments remaining, one would wait until the mortar reached room temperature and PBS was added to suspend the fragments before collection by Pasteur pipette. Fragments were sorted by bone location (leg, arm and rib) and stored at -20°C in PBS. This method created a large number of fragments smaller than 50µm, but a limited number of larger fragments suitable for developing the macroscopic model.

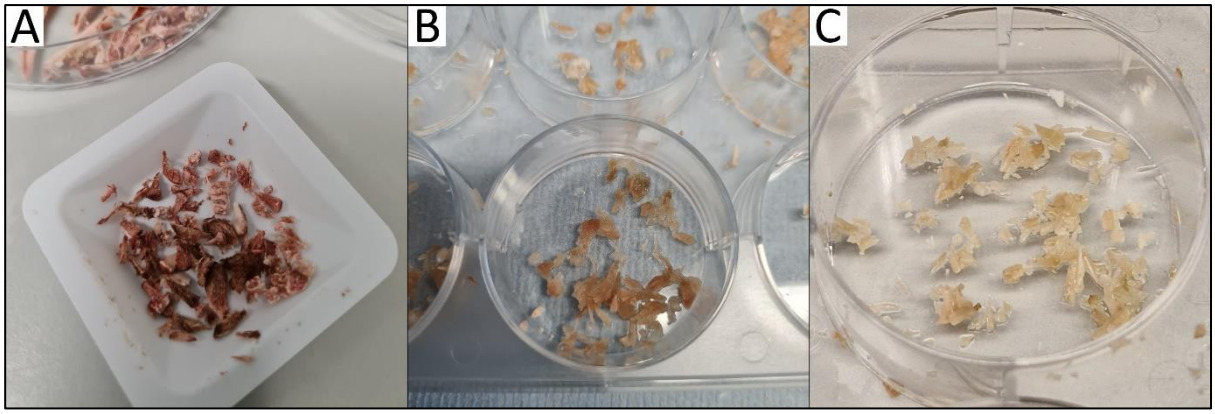

Figure 2.2: Rat bone decellularization and fragmentation stages

Bone pieces and fragments at the different stages of preparation. (A) Shows the bone fragments having just been harvested and separated by leg (shown), arm and rib. (B) Shows the bone pieces (arm) post decellularization. (C) Shows the bone pieces (rib) post fragmentation via Bead Mill.

To produce a more suitable range of bone fragment sizes, a secondary method was developed utilizing the Bead Mill 4 homogeniser (Fisher scientific) provided by Dr Aslihan Ugun-Klusek (Nottingham Trent University, UK). This device reproducibly oscillates (up to four) 2ml tubes for a determinable time at a given "speed setting". To cause the proper fragmentation of bone, beads of variable size and weight need to be added to each tube with the sample. This updated protocol was identical to the previous one, up to adding the bone pieces to the liquid nitrogen. With the bone in the liquid nitrogen, the latter was allowed to evaporate fully. The bone pieces were then extracted with tweezers and placed in a bead mill tube with a given number and size of beads and the cap sealed. With the tube securely positioned in the Bead Mill, the time and speed were set and the run initiated. The process of removing the bone from the mortar to fragmentation in the bead mill must be completed as rapidly as possible to ensure the bone pieces are still cold enough to shatter and fragment. Ultimately a single medium sized (6.35mm) ceramic bead with the mill set at speed five for ten seconds was used as it generated fragments suitable for the macro model. The primary stages of rat bone preparation are shown in Figure 2.2 from harvested bones to decellularised fractured ones.

2.2.3.4 Rat Bone Fragment Measurement

In order to determine the range of bone fragments created by the different fragmentation protocols, a way to determine the range in fragment sizes was needed. This was done by utilising the "Measure" feature in ImageJ (https://imagej.nih.gov/ij). A Pasteur pipette was used to transfer approximately 2ml of bone fragment suspension of each bone type into separate wells of a 6 well plate. Ten bright field images were taken using the Leica DMi8 at 5x magnification. For each image, the LasX software was used to add a micron scale, which was used to register a given number of pixels as a specific length. Each fragment was measured across its longest length and the number recorded. Repeat measurements was prevented by applying a grid system to the image and "crossing-off" measured fragments.

2.2.4 Cell Growth on Bone

Having optimised a protocol for the extraction, decellularization and fragmentation of rat bone, the process of optimising cell growth on said bone was required. Prior to any cell work, bone fragment pieces were defrosted and in a class 2 safety hood selected based on size and type using sterilised tweezers. Generally, selected pieces were greater in length than 1mm ranging to approximately 3mm and transferred to a 6 or 12 well non-treated plate. Media suitable for the cell type to be grown on the fragments were added to each well and transferred to an incubator until needed.

Standard cell culture passage protocol was followed until pellet resuspension and a cell count was conducted. A seeding density of 5000 cells/cm^2 was desirable for successful cell growth on bone. The necessary volume of cell suspension for the number and size of wells was added to a volume of media. For a 6 well plate, 3ml of cell suspension is added and for a 12 well plate, 2ml. To remove the fragments from the incubator, the media was removed before adding the cell suspension, ensuring proper cell distribution through the media was important to ensure equal cell distribution across each well before adding the suspension the wells. The

plates were gently agitated to ensure complete cover across the whole well surface area, including settling on the bone fragments.

2.2.5 Cell Tracking

The aforementioned cell growth on bone protocol was developed through trial and error with cellular position needing to be determined. Successful cell growth on bone was evaluated using CellTracker™ Blue CMAC Dye (Thermo Fisher) after four days. This is a fluorescent dye with blue excitation in the 353/466nm range which is retained for up to 72hrs and is minimally cytotoxic.

The manufacturer's protocol was followed in the preparation and use of the cell tracker (Publication Number MAN0010620). In short, the lyophilized product was first brought to a working concentration of 10mM in high grade DMSO. With a molecular weight of 209.6g/mol, 2.385ml of DMSO was added to the 5mg of cell tracker. This stock solution was later diluted down to the necessary working concentration in serum free media specific to the cell type. The stock solution was stored at -20^{o}C.

Before utilising the tracker to determine cell position on bone, the concentration and incubation time first needed to be optimised for each cell type. The product sheet recommended a range of 5 - 25µM concentration and an incubation time of 15 – 45 minutes. 5, 10, 15, 20 and 25µM concentrations were tested with HOS grown in monolayer under standard conditions at approximately 90% confluence. Incubation time was fixed at 30 minutes. The culture medium was removed, and the pre-warmed (37^{o}C) cell tracker solution added to fully cover the monolayer (2ml in each well of a 6 well plate). Once the incubation time had elapsed, the cell tracker solution was removed and replaced with culture media. Comparing the different working concentrations, it was determined that 10µM was the most suitable as it allowed clear identification of each cell.

Using this as a baseline, the same concentration and incubation time was tested with the hMSCs. They, however, showed no fluorescence at this level. Testing the highest

concentration recommendation of 25µM still resulted in low fluorescence after 30 minutes, so incubation time was increased to 60 minutes which was found to be suitable.

After 4 days, cell attachment and proliferation was assessed using the aforementioned protocol. To avoid confusion between cells growing in monolayer on the well plate base and any cells growing on bone, the fragments were first delicately transferred to a fresh well plate using sterilised tweezers. As the optimisation of this protocol was conducted with HOS, the bone fragments were incubated in 10µM working solution for 30 minutes.

When developing the later iterations of the macro model, the seeding of both hMSC and HOS cells was desirable. In order to track two cell types, a second cell tracker, CellTracker™ Green CMFDA Dye (Thermofisher) was utilised to track hMSC. The tracker had an excitation in the 492/517nm range and like its blue counterpart was brought to a usable working solution using DMSO. With a molecular weight of 464.9g/mol, 215.1µL of DMSO was added to 1mg of the cell tracker producing a 10mM solution. This solution was diluted 1:5000 to a working concentration of 2µM in MSCGM. For the purpose of tracking the two cell types with the separate trackers, an alteration to the aforementioned methodology was required. As the cells could not be stained after seeding into the same well dish, the cells were first individually introduced to their respective chosen trackers at the aforementioned concentrations at confluence in their respective flasks and incubated for 1hr before removal of the tracking solution and splitting the cells. Having seeded the two cells types together, the two could be tracked separately, hMSC in the green fluorescent protein (GFP) range and HOS in the ultraviolet (UV) range.

2.2.6 Hoechst Staining

In order to determine the presence of cells in a sample, Hoechst solution can be used as a nuclear stain to visualise cellular positions in both live, dead and fixed samples. This chemical was utilised in the evaluation of the decellularization protocol used on the rat bone pieces to determine the presence of any residual cells as Hoechst is an established method of

evaluating decellularization (Stone et al., 2021). Decellularised bone fragments were incubated in 1µg/mL of Hoechst solution (diluted in PBS) for 15 minutes, protected from light. After the incubation, the sample was washed three times for 5 minutes with PBS before imaging immediately under fluorescent microscopy, excited with a UV laser. Bright field and UV excited fluorescence images were taken for all samples.

2.2.7 Fixation

Fixation is a necessary stage before conducting further experiments in the analysis of the various model stages. Fixation preserves the structural integrity of cells and tissues stabilising their components and importantly preventing degradation allowing storage of samples before further experimentation. When fixing samples, 3.7% PFA in PBS was used in all situations. The only variables were the incubation time and the volume needed to fully submerge the samples. All work done with PFA was conducted in a class 2 externally vented fume cupboard (Envair). Fixed samples included cells grown in monolayer, cell seeded collagen scaffolds and cell seeded bone fragments. These were incubated at room temperature for 15, 30 and 20 minutes respectively after first washing the sample with PBS. After completing the necessary incubation time, the PFA was removed, being placed in a toxic waste container. The wells were washed two times with PBS and the PFA contaminated wash solution also placed in the toxic waste container for proper disposal. The samples were stored in PBS (3mL per well for 6 well plates, 2mL per well for 12 well plates), sealed with parafilm and stored at 4^{o}C.

2.2.8 Immunohistochemistry

IHC staining is a reliable methodology for detecting and visualizing proteins in samples and was utilised to identify the proteins OPN and OCN, both markers of osteogenesis. All samples had previously been fixed with 3.7% PFA in 6 or 12 well plates. The protocol used was a three-day process and as follows.

On the first day, 1% (w/v) BSA in PBS was made up, the volume dependent on the number of samples to be processed. A 0.1% Triton X-100 (w/v) solution was made up in PBS and placed on a magnetic stirring plate with a flea for approximately 30 minutes to ensure complete dissolution. A 1% BSA solution was used to make a suitable volume of 1:200 OPN primary antibody solution. Acting as a permeabilization agent, 400µL of 0.1% Triton X-100 solution was added to each sample well and incubated at room temperature for 30 minutes. Each well was subsequently washed three times for 5 minutes per wash with PBS. A 3% (v/v) donkey serum blocking solution was made in 1% BSA and 400µL added to each sample well and incubated at room temperature for 30 minutes. Having removed the blocking solution, 400µL of the OPN antibody solution was added to each sample well and incubated overnight at 4^{o}C.

On the second day, the OPN antibody solution was removed and washed three times for five minutes per wash with PBS. The samples were left in 1% BSA for three hours. The sample wells were subsequently blocked with 3% goat serum in 1% BSA for 30 minutes. The 1% BSA was again used to make a suitable volume of a 1:200 OCN primary antibody solution. 400µL was added to each sample well and incubated overnight at 4^{o}C.

On the third day, two secondary antibody solutions were required: a 1:200 secondary donkey anti-goat alexa 546 and a 1:200 secondary goat anti-rabbit alexa 488, both in 1% BSA. The OCN solution was removed, and the sample wells washed three times for five minutes in PBS. 400µL of the donkey anti-goat solution was added and incubated for two hours at room temperature. After removing the donkey anti-goat solution, the samples were washed with PBS three times for five minutes and replaced with 400µL of the secondary goat anti-rabbit solution and incubated again for two hours. During this incubation, a suitable volume of 1 µg/ml Hoechst solution in 1% BSA was made and protected from light (wrapping with foil). With the secondary antibody incubation complete, the solution was removed and washed three times for five minutes, incubated with the 1% Hoechst solution for 15 minutes at room temperature and finally washed again three times for five minutes. The samples were imaged

as quickly as possible but could be stored for a few days in PBS, covered, and at 4^{o}C before losing fluorescence.

2.2.9 Microscopy

The day-to-day microscopy aiding in cell culture, where imaging was not required, was conducted using the Leica DMi1. When capturing both bright field and fluorescent images from five to forty times magnification, the Leica DMi8 inverted microscope was used with fluorescent filter cubes Texas Red, GFP and DAPI (all Leica). This included the analysis of Alizarin red staining, IHC fluorescence, bright field imaging of bone fragments and cell tracking. The final iterations of the macro model were all imaged using the Leica Thunder 3D cell culture imaging system with consistent emission wave lengths and exposure times, for all images taken.

In order to assess the structure and topography of the different bone pieces, scanning electron microscope (SEM) imaging was utilised. Two types of sample were imaged: decellularised bone fragments and decellularised bone fragments which had HOS grown on them as described in section 2.2.4 page 66, over a four day period. The two sample types had different preparation methods. The former simply needed to be completely dry which was accomplished by a series of ethanol washes starting at 50%, followed by 65%, 80% and finally 100% ethanol, all for 6hrs, or until fully evaporated at room temperature. The latter, as the bone pieces were covered in cells, were first fixed in 2.5% glutaraldehyde for 2hrs. After this the samples were gently washed in PBS and subject to the same drying process with ethanol as the other samples.

After preparation, fragments were attached in triplicate to an adhesive conductive carbon. The disks were coated with 5nm of gold using the Q150R Plus rotary pumper coater (Quorum). Electron microscopy was completed using a JSM 7100F SEM with an accelerating voltage at 10kV for samples with fixed cells and 15kV for decellularised bone. Micrographs were taken

at various magnifications at approximately x50, x500, x1500, x6000 and x12000 for most fragments.

Images of the microscopic model were all captured using the internal software capture system of the HOTs (see section 2.2.12.1, page 76). All images were captured with a x40 objective.

2.2.10 Quantification of Osteogenic Markers

In order to determine the arbitrary fluorescent units of the macro model, the software ImageJ (https://imagej.nih.gov/ij) was used. This was utilised specifically in the quantification of OPN and OCN levels generated through IHC and captured on the Leica Thunder. OPN and OCN micrographs were exported separately as '.tif' and imported into ImageJ. For micrographs of cells cultured on bone, due to variance in bone autofluorescence, it was not possible to directly read the fluorescence generated by OPN and OCN and minus off a "background value" accurately. It was found, however, that in all cases a large amount of cellular product was generated by the cells on and directly surrounding the bone fragments as ECM spilled over and out from the bone pieces. Therefore, a 250x250 pixel square was used to measure the mean grey value at ten points equally spaced around each bone fragment. For monolayer controls, ten readings were taken equally distributed across the whole image again with a 250x250 pixel square. For each of the model, three biological and ten technical repeats were compiled for statistical analysis.

2.2.11 Real-Time Quantitative PCR

2.2.11.1 Primer Design

All primers were designed using e!Ensembl (https://www.ensembl.org/index.html), Primer3 (https://primer3.ut.ee/), UCSC genome 83 browser (https://genome.ucsc.edu/) and NCBI primer blast (https://www.ncbi.nlm.nih.gov/tools/primer-blast/). See table 2.1.4, page 52 for the list of all primer sequences designed.

2.2.11.2 RNA Synthesis

Ribonucleic acid (RNA) was extracted using the RNeasy® Mini Kit (QIAGEN) using the manufacturer's protocol (Publication Number HB-0435-006) as follows. Both cells in monolayer and cells grown on bone scaffolds were harvested for real-time quantitative PCR (RT-qPCR). Buffer RLT was added to the samples for harvesting, 600µL for 6 well plates, 350µL for 12 well plates. Samples were incubated at room temperature for five minutes in the buffer with regular agitation to aid in detachment, particularly in the case of bone fragments. Cell lysis could be identified by the naked eye as strands of opaque matter floating in the buffer. Cell lysate and buffer was collected using a Gilson pipette into an Eppendorf tube (which can be stored at -80^{o}C).

Prior to processing the samples, a solution of DNase I needed to be prepared. Using a RNase free needle and syringe, 550µL of RNase free water was introduced to the lyophilized DNase I (1500 Kunitz units). The contents was mixed by gentle inversion of the bottle and divided into single use 80µL aliquots. Aliquots were stored at -20^{o}C.

All centrifugation (Centrifuge 5417 R, Eppendorf) was performed at 12,000g at room temperature. When working from frozen samples, they were thawed on ice and the entire sample transferred into a Qishredder and centrifuge for two minutes disrupting the cells. The column was discarded, and an equal volume of 70% ethanol added to the sample flow through (600 or 350µL). 600µL of the mixture was added to a RNeasy Mini spin column housed in a 2mL collection tube and centrifuged for 15 seconds. The flow through was discarded and the process repeated as necessary until the flow through from the Qishredder was fully processed. 700µL of RW1 buffer was added to the column, centrifuged for 15 seconds and the flow through discarded. A suitable number of DNase I aliquots were thawed and the 80µL added to each column which was left at room temperature for 15 minutes. After this time elapsed, 350µL of RW1 buffer was added to the column, it was centrifuged for 15 seconds and the flow through discarded. 500µL of RPE buffer was added and the samples centrifuged for 15 seconds. The flow through was discarded and the process repeated but centrifuged for

two minutes before discarding the flow through and the tube itself. Only the column was centrifuged with its cap open in a fresh 2mL tube for three minutes. The tube was replaced with a 1.5mL collection tube and the column left to dry at room temperature for 15 minutes. The final step required the addition of 50µL of RNase free water directly to the matrix of the column, waiting for five minutes at room temperature, followed by a one minute centrifugation. As RNA is soluble in water, the flow through containing the sample RNA was retained and the column discarded. Samples were stored at -20^{o}C.

2.2.11.3 First Strand cDNA Synthesis

Complimentary DNA (cDNA) synthesis was completed using the qPCRBIO cDNA Synthesis Kit (PCR BIOSYSTEMS). Prior to cDNA synthesis, RNA was assessed at the NanoDrop 8000 (Thermo Scientific) using the same RNase free water for blanking as used for elution during RNA synthesis. For each sample, RNA concentration in ng/µL and the purity (ratio of absorbance, 260/280) was recorded.

The protocol followed for cDNA synthesis was as detailed by PCR Biosystems and was as follows. A master mix of 4µL of 5x cDNA and 1µL of 5x cDNA per sample was made and kept on ice. RNA was suitably diluted as necessary such that 100ng of total RNA was below 15µL. Into PCR tubes, 5µL of the 5x cDNA and 5x cDNA mix, 100ng of total RNA and enough RNase free water to bring the total volume to 20µL was added. This reaction mixture was placed in a T-100 Thermal Cycler (BIO-RAD) at 42^{o}C for 30 minutes followed by 85^{o}C for ten minutes. The newly formed cDNA was diluted with RNase free water by adding 30µL to each sample to a 50µL total volume and stored at -20^{o}C.

2.2.11.4 cDNA RT-qPCR and Primer Optimisation

RT-qPCR was completed using qPCRBIO SyGreen Mix Hi-ROX (PCR BIOSYSTEMS) where the SyGreen binds to DNA and therefore as more copies of the target gene are formed, fluorescence increases. The protocol followed for RT-qPCR was an altered version of the one detailed by PCR Biosystems and was as follows. A reaction mixture of 5µL of SyGreen Mix

(vortex prior to use), 0.4µL (10µM) of Forward primer, 0.4µL (10µM) of Reverse primer and 3.2µL of RNase free water and suitably extrapolated for the number of wells to be filled was formed and kept on ice. Keeping a PCR plate (StarLab) on ice, 9µL of master mix was added to each well along with 1µL of cDNA, the plate sealed (Polyester seal, StarLab) and centrifuged in a plate spinner (Labnet) briefly. The RT-qPCR machine used was the Quant Studio 5 (applied biosystems) and after loading the plate, the following programme was used. Amplification conditions were one cycle at 95^{o}C for two minutes followed by the PCR stage (denaturation, annealing and elongation) with 40 cycles of 95^{o}C for five seconds then an optimised primer temperature (mouse primers - 60^{o}C, human primers - 62^{o}C) for 30 seconds. Primer annealing temperature optimisation was experimentally determined by running a control cDNA sample through the full RT-qPCR process at different temperatures. The melt curves were compared and the temperature(s) that gives a distinct single peak were selected for use.

2.2.11.5 Analysis

The ΔΔCt (threshold cycle) method was used to analyse the amplification data generated when RT-qPCR was utilised. This method relies on the use of a housekeeper gene, a gene which does not change in expression level across samples. For both RT-qPCR experiments conducted the gene chosen was glyceraldehyde-3-phosphate dehydrogenase (*GAPDH*). For each sample, *GAPDH* expression is subtracted from given gene being assessed, resulting in a normalised expression, ΔCt. The difference between all sample ΔCt and the control sample ΔCt was calculated to give the ΔΔCt. The fold change in a given gene's expression was calculated with the equation $fold\ change = 2^{-\Delta\Delta Ct}$ with control samples allocated a fold change of 1 for comparison. All samples were done in triplicate and the data combined for analysis. Standard deviation was calculated from the Ct values from which mean standard error of the mean (± SEM) was calculated. As a result, the SEM is different for every control as all controls are different and from independent experiments plot on the same graph. This is why for all RT-qPCR graphs, there are bars for control for each gene. For the Nanokick RT-qPCR experiment (Figure 3.5), five biological and two technical repeats were completed. For the Model 3 RT-

qPCR experiment (Figure 3.34 and Figure 3.35), three biological and two technical repeats were completed.

2.2.12 Holographic Optical Tweezers

The HOTs system is a highly advanced custom piece of equipment able to manipulate multiple particles ranging from nanometres to tens of micrometres in all three dimensions. This of course includes the manipulation of individual mammalian cells into precise 3D configurations without causing damage (Kirkham et al., 2015).

2.2.12.1 Technical Specifications

Based on the Nd:YAG laser, the HOTs has a solid state infrared fiber laser with 1070nm 5W output (Laser Quantum). Optical manipulation using multiple optical traps involves expanding the laser beam to the point of exceeding the aperture of the 512 x 512 high-speed, high-efficiency SLM. The SLM is connected to the system, imaging the SLM through a high numerical aperture (1.35) 40x oil immersion microscope objective. A dichroic beam splitter directs >90% of 400-870nm light to camera port (640 x 480, 300 frames per second). The HOTs system used is show in Figure 2.3.

2.2.12.2 Operation and Trapping Procedure

The dishes used with the HOTs are specific in that they need to be glass bottomed to allow the laser to pass through the bottom of a given vessel to create traps. The dishes used throughout the project were Ibidi µ-Dish, 35mm diameter glass bottom (170µm, +/–5µm) imaging dish. With a dish ready for mounting on the stage, a small droplet of immersion oil (Olympus) was placed on the objective lens before lowering the dish into place on the motorised stage (ASI, MS-2000). The stage was controlled in the XY axis using a stage controller joystick (ASI, MS-2000-WK) while the objective Z axis was controlled using an electromechanical clutch on the same controller. Positions in the three directions can be tracked and stored for easy return to a given position as needed.

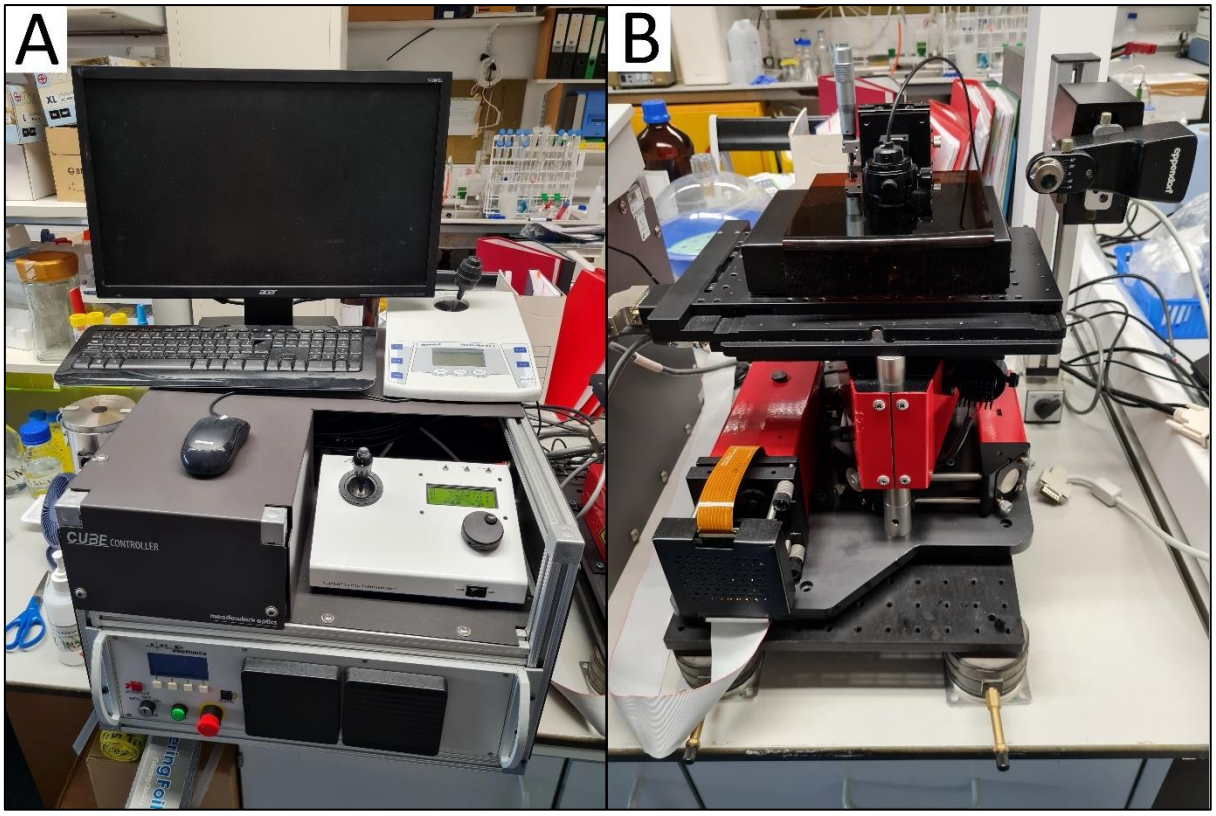

Figure 2.3: Holographic optical tweezers

(A) The HOTs laser (i) control unit with stage joystick and objective control, (ii) laser control box, and monitor for software usage. (B) The HOTs hardware including (iii) spatial light modulator (SLM), (iv) laser cover and (v) anti vibration pads (x4). The optical cable and camera both connect to the system via the back.

The laser master control is operated from the control box which houses the ON/OFF lock, emergency shut off as well as controls to set laser intensity. If the illumination cover is down and the interlock switches closed, the laser was set at 40% intensity for all experiments and "started" via a switch on the panel. Once on, the creation and control of all traps were managed via the PC. The software in question is the 'Red Tweezers' program designed by M.Padgett's group from the University of Glasgow, UK which runs coupled with LabVIEW (National Instruments). The program facilitates the rapid creation of holograms which can be altered on-the-fly without recompiling the program (Bowman et al., 2014), controlling the

SLM. Along with this, the OpenGL 'hologram engine' was run, through which any trap coordinates are transmitted, producing the desired hologram intensity pattern.

In practice, the interface showed a live image of the focal plane where traps could be created by double-clicking the live feed or through the toolbox on the 'current spot' tab. Single or multiple traps could then be selected by clicking on them (and holding shift to select multiple) and moved by mouse movement or precisely adjusted through the toolbox. This procedure allowed the capturing of cells or particles and then their movement to a desired location.

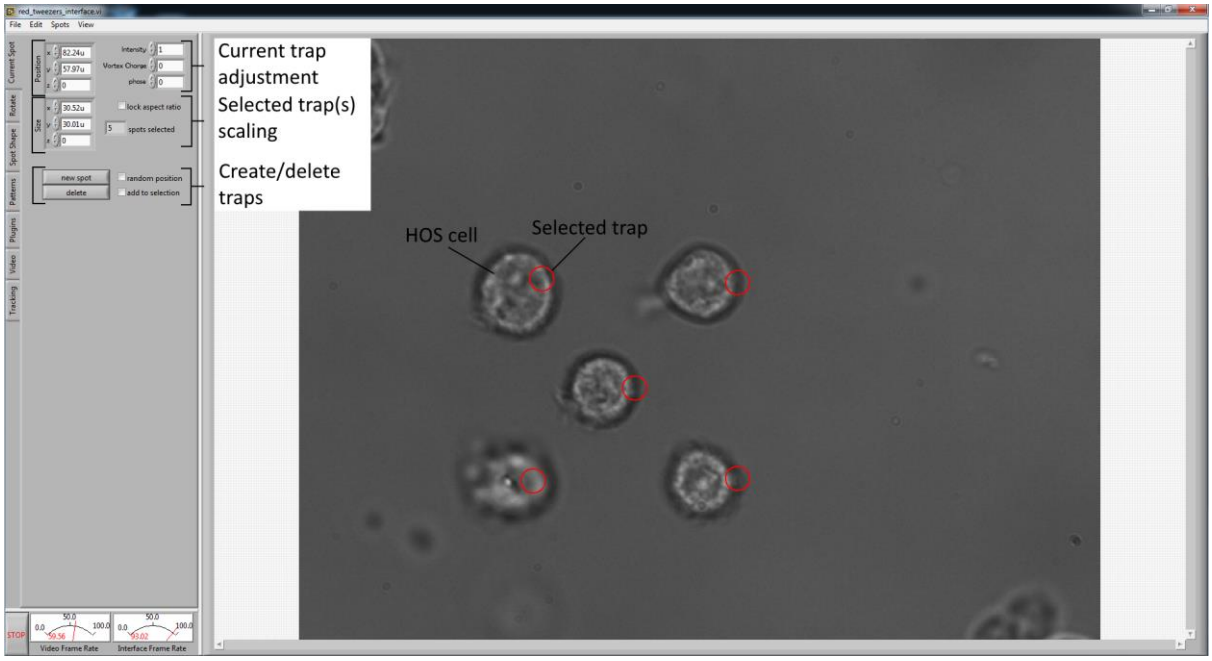

Figure 2.4: Holographic optical tweezer interface

Annotated screen shot of the "Red Tweezers" LabView interface. Optical traps are seen as circles and are red when selected allowing the manipulation of multiple objects. The software was used to create a dice's 5 side using HOS cells.

2.2.13 Mould Design and Creation

As they come, the dishes used with the HOTs did not allow the separation of different cell types or particles as there was only one volume to work in. While there were dishes available with multiple sections, they do not allow movement between the different sections. In order to facilitate the introduction of multiple cell types with the tweezers without "flooding" the

working area, a design needed to be formed which allowed movement between any segmentation. Important considerations were that the glass bottoms of the dishes not be obscured in the areas the laser would be operating and that the design be sterilizable/disinfectable.

The solution to this problem started with the idea to fill the dishes with agarose then create two connected cylindrical wells. A 5% w/v agarose PBS solution was formed by gradually heating the mixture, regularly swirling until fully dissolved. The solution was then poured into as many dishes as required, filling them to just below the rim. The sharpened wide end of a 1ml pipette tip was used to punch two holes in the agarose ensuring the holes were within the inner glass circumference of the dish. After allowing the agarose to set, a channel between the two wells was then cut using a scalpel. The exposed glass was cleaned gently with a brush and 70% ethanol to remove any remaining agarose.

While usable with the HOTs to move cells between the two wells, this design had some issues. Firstly, being made from agarose, each dish was only single use and had limited usable shelf life before the agarose started to contract. Cutting the channel between the wells also presented difficulties. The channel needed to be as thin as possible to simplify moving cells between wells given that the HOTs objective is 40x magnification, even 1mm is equivalent to multiple “screens” worth of movement. Ensuring the walls of the channel were parallel as well as perpendicular to the dish base is vital for the HOTs laser to function properly. Managing these two requirements using a scalpel generally resulted in a wide channel or an unusable mould.

In order to circumvent the difficulties of using a scalpel to cut away agarose, the development of a 3D printed core piece was developed for agarose to be moulded around. It was decided to expand the original design to have three wells with two channels connecting to the central well. This would allow, for example, the introduction of two different cell types with the ability to select one cell from each and be brought to the central well. The designs were created in

Fusion 360 and the computer aided design (CAD) file printed on the ELegoo Mars Pro 3 in Anycubic standard resin.

The design went through a number of iterations changing the width of the channel attempting to make it as thin as possible while maintaining structural stability as well as changing the height to facilitate easier removal from the agarose. The final mould design along with the 3D printed piece is shown in Figure 2.5.

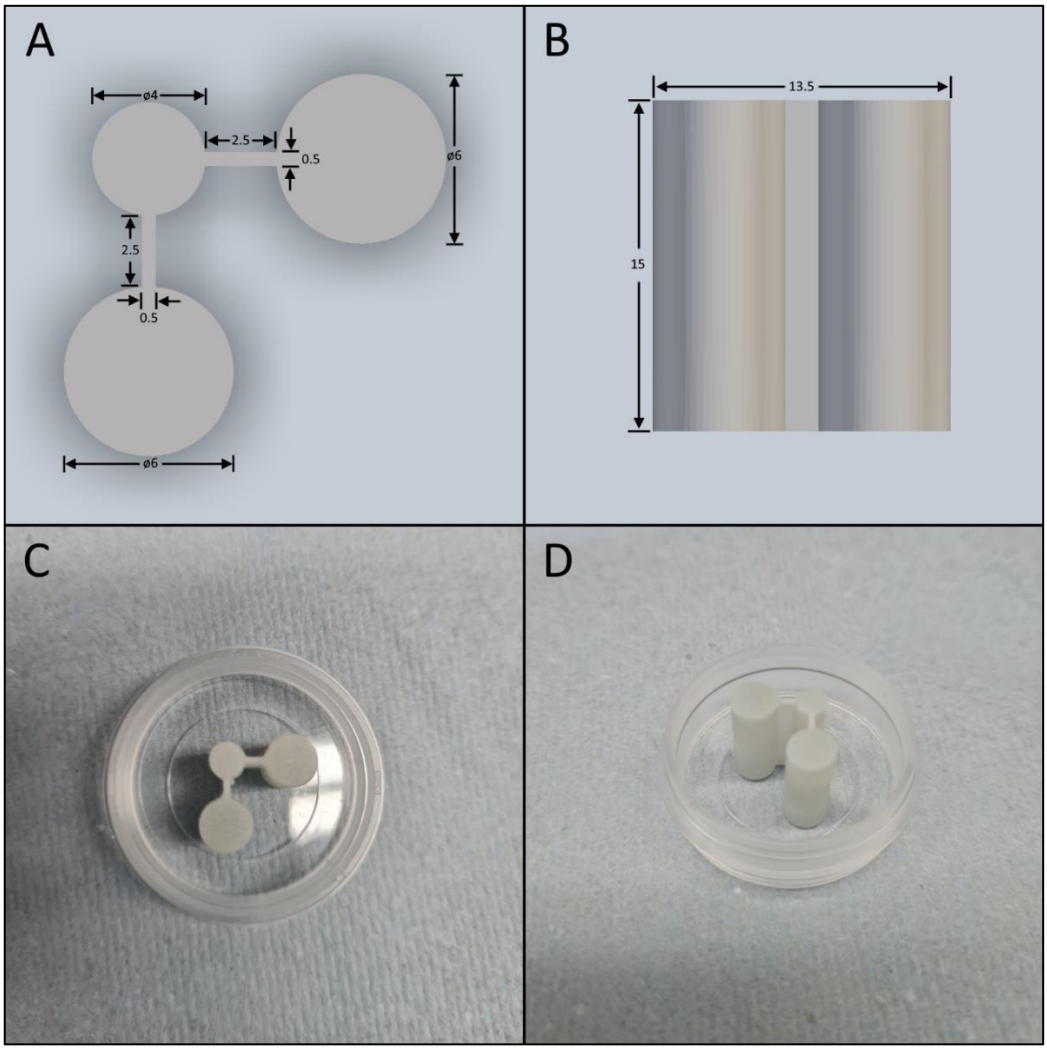

Figure 2.5: Mould final design and printed piece example

(A) Top and (B) side view of the final core piece design. Screen shot taken from Autodesk 123D Make and annotated in paint.net, all dimensions in mm. (C) A top and (D) side view of the printed piece sat in an imaging dish.

With the core piece design finalised, the final change to the design was the mould material. By using silicone (Ecoflex, Bently advanced materials) instead of agarose, the mould becomes multiuse. Silicone was prepared by the thorough mixture of two liquid rubber parts 1:1 and left to set for approximately 2hrs. Silicone could be sterilised under UV and would maintain its form without contracting over time. The final iteration of the mould was created by first using autoclave tape to hold the 3D printed piece securely in place. Silicone was poured around the pieces slowly to approximately 5mm below the top of the dish and left to set. To remove the piece, fine tweezers were used to carefully peel away the silicone at the top and then the piece rocked gently until a small amount of force would release it.

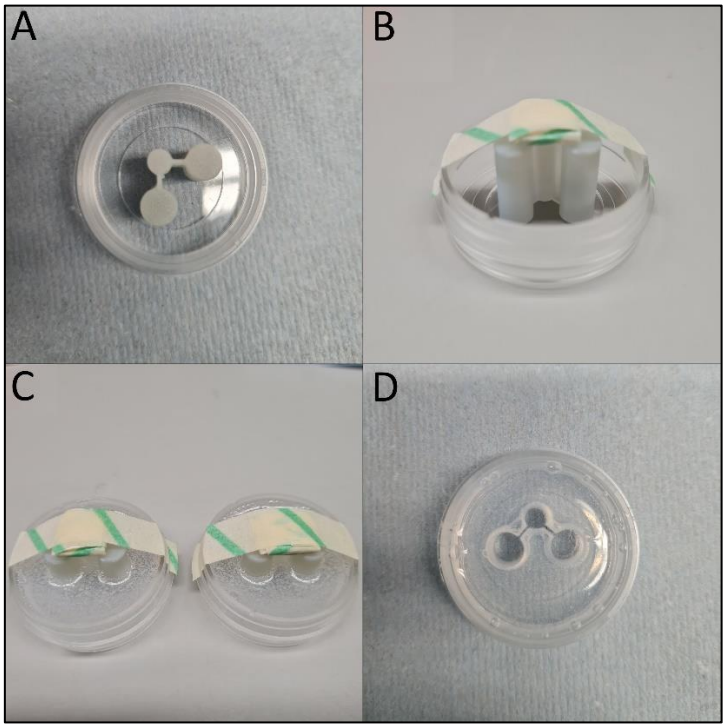

Figure 2.6: Mould creation process
Steps detailing the creation of the microscopic niche model mould for use with the HOTs. (A) Shows the 3D printed piece in place in a glass bottomed dish. (B) Shows the use of autoclave tape to hold the piece in place and reduce silicone seeping underneath. (C) Shows two dishes filled with silicone in the setting stage. (D) shows the final result having removed the mould piece leaving three separate zones for the addition of cells and bone fragments.

2.2.14 Cell Attachment

When patterning cells with the HOTs, one of the difficulties in creating a model for study is working within a strict time frame as patterning is a race against cell attachment to the dish bottom. The ability to pattern cells over time was assessed by counting the number of

manipulable cells per minute over ten minutes. The dish filled with 2mL of DMEM was put in place on the HOTs stage and the objective brought into focus on the base of the well. With the hardware and software set up ready for turning on the laser by pressing the emission button, 20000 cells were added to the dish and the laser turned on. A single trap was created and moved onto a given cell on screen. If it could be manipulated, it was counted as a 'yes', if not a 'no'. The trap was then moved to a new cell and the process repeated. The stage was moved using the joystick as needed when all the cells on screen had been tested. This was continued over ten minutes noting the 'yeses' and 'noes' by what minute they were in (e.g., 7 'yeses' and 4 'noes' within the 3rd minute). These were converted into percentage successful traps and compared over the ten minutes.

Along with the standard untreated dish, various gelatin concentrations along with 3% BSA were compared. It was determined that for most purposes, incubating the dish with 3% BSA overnight provided enough time to pattern cells as needed.

Secondary to cell attachment to the dish bottom, cell-cell attachment needed to be considered. This was particularly difficult to overcome when using hMSCs as these primary cells were particularly "sticky" and would clump to each other rapidly. The only way to minimise this was to ensure vigorous resuspension prior to pipetting into the dish, and to keep the cell number added to a low number.

2.2.15 Cell and Polymer construct co-patterning

Two different forms of polymeric material were co-patterned with cells using the HOTs. Microparticles were created as described by White et al., (2013) via a water-in-oil-in-water emulsion under high loading efficiency. The microparticle batches were subjected to lyophilization, and the resulting powder was vacuum-sealed and stored at 4^{o}C until needed. Electrospun polymer fibres were created as described by Rogers et al., 2014). The fibres were immersed in liquid nitrogen and ground using a mortar and pestle for ten minutes. The

fragments were fractioned and ones <50µm used for patterning. Both materials were separately patterned with CGR8.

2.2.16 ihMSC proliferation

hMSC were immortalised by Lentiviral transfection of hTERT and E6/E7 genes as described (Balducci et al., 2014; Mori et al., 2005) and are genetically modified to express GFP. The cells were modified and provided by Prof Kevin Shakesheff's group (University of Nottingham, UK). A single immortalised hMSC (ihMSC) cell was precisely positioned onto a decellularised bone fragment using the HOTs. The patterned complex was imaged under bright field and again after 48hrs under merged and fluorescent imaging.

2.2.17 Microinjection

When wanting to add small numbers of cells or other particles to a dish for manipulation in the HOTs, pipetting by hand was not necessarily accurate enough in terms of both volume and location. This became particularly apparent when trying to add low numbers of small bone fragments to the central well of the silicone mould. By using a micromanipulator and microinjector, this problem was overcome.

The TransferMan NK2 (Eppendorf) and CellTram vario (Eppendorf) were set up in conjunction with the HOT system to allow the microinjection of cells and bone fragments directly into the silicone mould dishes already in place on the stage. The TransferMan NK2 equipment consists of a control box, motor module and stand. The control box has a panel to set functions and parameters as well as a joystick to control XYZ axis position of the motor module which holds the micro injector. The motor module was fitted onto the stand at a suitable distance from the HOTs to allow the needed range of movement. The CellTram is a manual hydraulic microinjector where injection is controlled directly by two rotary knobs of different transmission ratios. The injector was fitted with a micro pipette tip (Drummond) and by loading a small volume of PBS containing small bone fragments (> 600µm) into the injector,

the smallest volume of liquid could be added to a given well of the mould in a controlled fashion.

While the microinjector was not ultimately use in the creation of the final models due to the decision to move to using larger bone fragments, it was used in the precise positioning of small fragments pieces and will be used in future model creation.

2.2.18 Statistical Analysis

Statistical analyses were conducted using GraphPad Prism 9 software (GraphPad, Inc, USA). The unpaired student's t-test was used in the analysis of relative expression in RT-qPCR data and relative fluorescence in immunohistochemical data having determined normalcy with the D'Agostino-Pearson test. All RT-qPCR data comprised of three biological repeats and five technical repeats. All immunohistochemical fluorescence data comprised of three biological repeats for each type of bone (leg, arm and rib) or no scaffold experiment and ten technical repeats for each. Results where p values <0.05 were considered statistically significant.

3. Macroscopic Model of the Bone Marrow Stem Cell Niche

The following chapter focuses on the design, optimisation and evaluating the performance of the experimental models developed as part of modelling the bone marrow stem cell niche "macroscopically". The objectives of this chapter are to cover the progress from initial scaffold testing to the eventual creation of three models which each build on the previous, ultimately leading to analysing the effects of bone as a scaffold material, the influence of mechanical stimulation and the impact of differentiation media. The work integrates advanced imaging and molecular biology techniques to determine the relative osteogenic potential of each model.

3.1 Results - Model Development

In Chapter 1, the current understanding of the bone marrow stem cell niche was discussed. In this investigation, in an attempt to understand the bone marrow niche better, a macroscopic model suitable for *in vitro* testing was developed by a stepwise 'trial and error' approach, generating models of increasing complexity. The steps are illustrated in the flow diagram below, Figure 3.1.

During the initial stages of research, collagen was selected as the base scaffold for the model due to its abundant presence in cellular matrix as discussed in Chapter 1, section 1.1.12, page 29. Qualitative analyses of cell morphology with both collagen concentration and thickness were undertaken to determine suitable values for both. A high concentration collagen was also tested, however, its high viscosity made its use difficult (accurate pipetting, uneven setting, thin coatings) and it was relatively expensive so the use of this material was abandoned. Initial attempts to alter the mechanical properties of collagen were undertaken using Oligomeric proanthocyanidins (OPC).

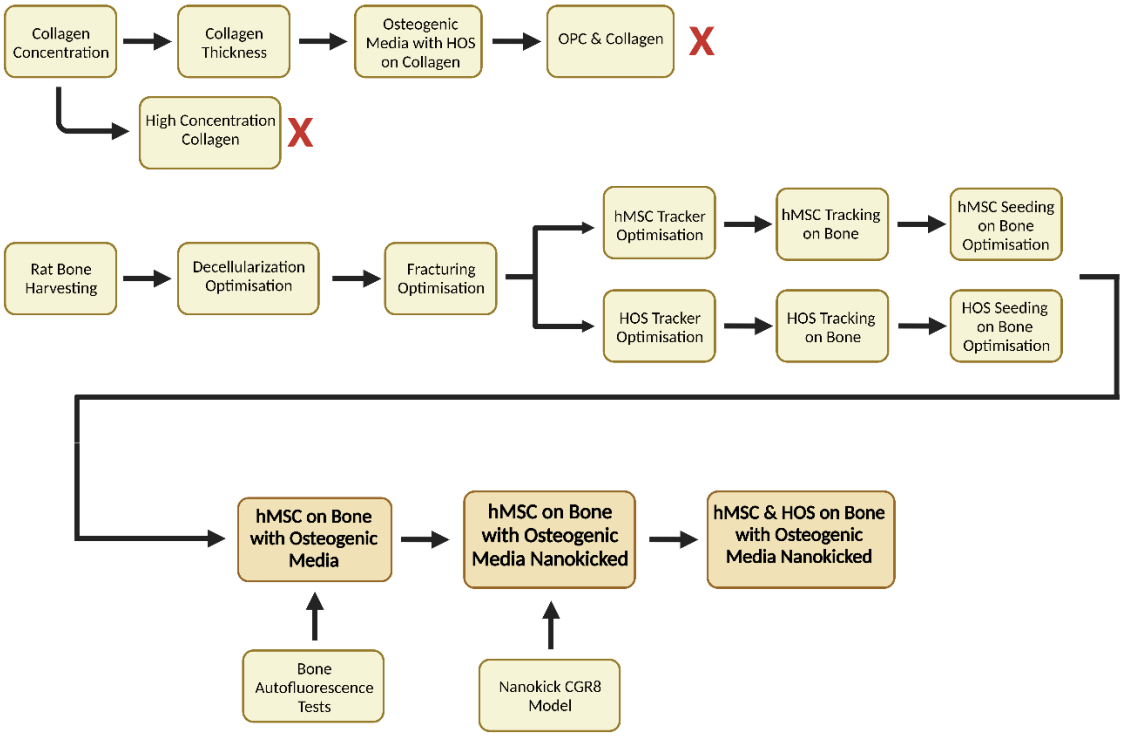

Figure 3.1: Macroscopic model flow chart

Flow chart of steps in development of the bone marrow stem cell niche at a macroscopic level. Arrows indicate how each experiment directly led to the subsequent experiment and the progression of the model. Red crosses indicate the decision to abandon the branch of experimentation.

Theoretically, OPC should have increased the mechanical properties of collagen, cross-linking and stabilizing the collagen network (Choi et al., 2016); unfortunately, only the most minimal of experimentation was able to be conducted. This experimentation started in early 2021, however, there was a shortage of available collagen for scientific research due to the COVID-19 pandemic.

While working with collagen, the use of bone as a potential scaffold started as collagen had specific limitations with its use. It was hypothesised that instead of building up in complexity from collagen, by starting with bone as a scaffold, the native environment of bone cells could be provided by decellularizing rat bone and seeding onto it. As there were no published

papers that investigated the seeding of multiple cell types directly onto small fragments of bone, progress was step-by-step and trial and error.

The first consideration was which regions of bone to use as a scaffold. The cancellous regions of the legs and arms along with the ribs were chosen as they are the primary location of bone marrow. The ribs were harvested whole and cut into approximately 5mm sections while to access the cancellous regions of the legs and arm bones, these were bisected along their length and the inside cut out. To decellularize the bone pieces, a protocol for the decellularization of bovine bone was altered to account for the smaller size of rat bone. Successful decellularization was initially confirmed via inverted light microscopy and subsequently validated during SEM imaging comparing the surface variations of the different bone pieces (Chapter 2, section 2.2.9, page 71).

The final stage of bone preparation for seeding entailed fracturing the bone pieces into smaller fragments. Initially this was done by flash freezing in liquid nitrogen and shattering the pieces with a pestle and mortar. This eventually evolved into using a Bead Mill to produce larger fragments more suitable for seeding.

Before starting the process of trying to seed HOS and hMSC cells onto bone it was first necessary to be able to track cellular position over time. This was achieved using a cellular tracker which, when integrated into the cell's medium and incubated with the cells for a given period, would allow the monitoring of cellular positions in the blue excitation spectra. Having optimised the tracker's ideal concentration and incubation time for both HOS and hMSC, it was then possible to determine whether cells had attached and propagated over the bone surface. The wells containing bone and cells were incubated with the cell tracking media and after the required incubation time, the bone fragments were removed delicately and placed into a new well with the media suitable for that cell. This ensured that only cells which had adhered to the bone surface were present and trackable and not, for example, any cells growing on the tissue culture plastic below.

Success was achieved with both HOS and hMSC when larger bone fragments were used. The fragments were kept as central as possible in each well and cells were dropped at a high density directly onto the bone which had already been submerged in media.

With the fundamental optimisation complete, three models with increasing complexity were developed and incubated over a 28 day period. The first was simply the growth of hMSC on different types of bone: leg, arm and rib pieces in the presence of osteogenic media (Model 1). These samples were seeded into the same well plate as bone fragments and hMSC with basal media (MSCGM) as well as hMSC grown in monolayer with and without osteogenic media. The next model integrated the Nanokick device, repeating the experiment except that the well plates were kept on the vibrating plate for the duration of the 28 days (Model 2). The final model added HOS cells along with hMSC to the model (Model 3). The reasoning behind these choices was always considering matching the native niche environment including their potential locations, mechano-stimulation, chemical environment and cells present.

3.2 Results – Analysis of Outputs

The following sections contain the data generated during the project from optimisation and model development up to analysis of the three final models.

3.2.1 Collagen scaffold

As already discussed, the early stages of the project included the investigation of collagen as a scaffold for the model. Although this experimental pathway was ultimately terminated due to a number of factors, some preliminary experiments were conducted.

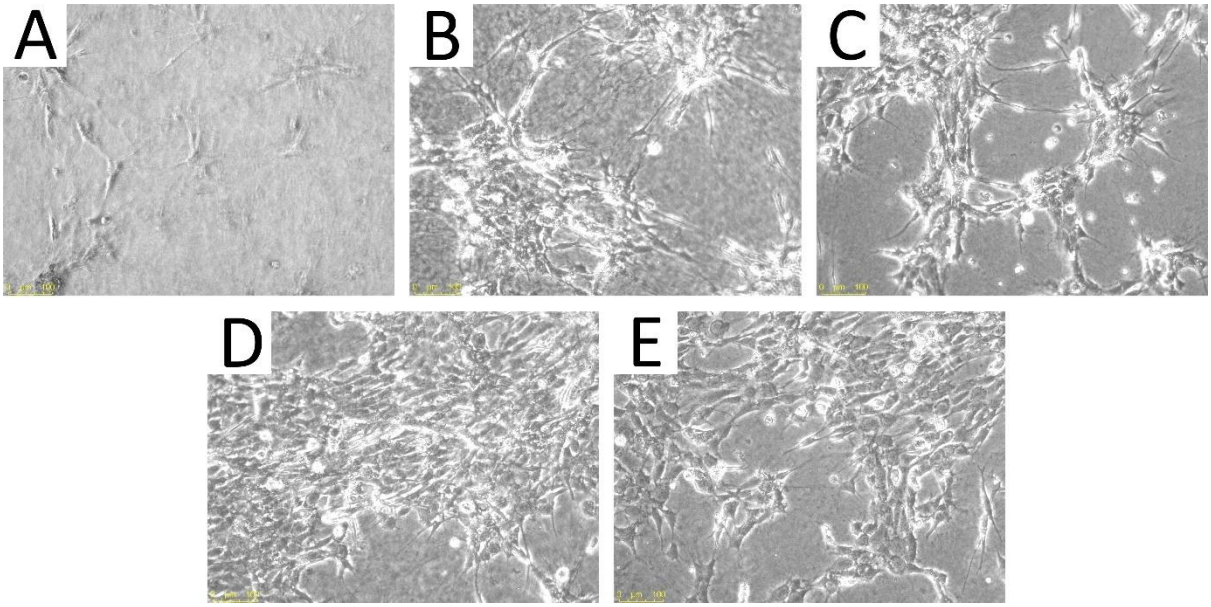

Figure 3.2: HOS cell morphology changes with collagen concentration

HOS cells were grown on collagen of varying concentration; 0.5mg/ml (A), 1.0mg/ml (B), 1.5mg/ml (C), 2.0mg/ml (D) and 2.5mg/ml (E). All samples were seeded at 5000 cells/cm^2.

Early collagen experiments included the testing of optimum collagen thickness and concentrations, an example of which can be seen in Figure 3.2. Such experiments were the basis of developing a suitable scaffold to start model development. Ultimately a concentration of 2.0mg/ml and an average thickness of 1.7mm (600µL of collagen solution in a 12 well dish) was chosen based on cell morphology changes and efficient materials usage.

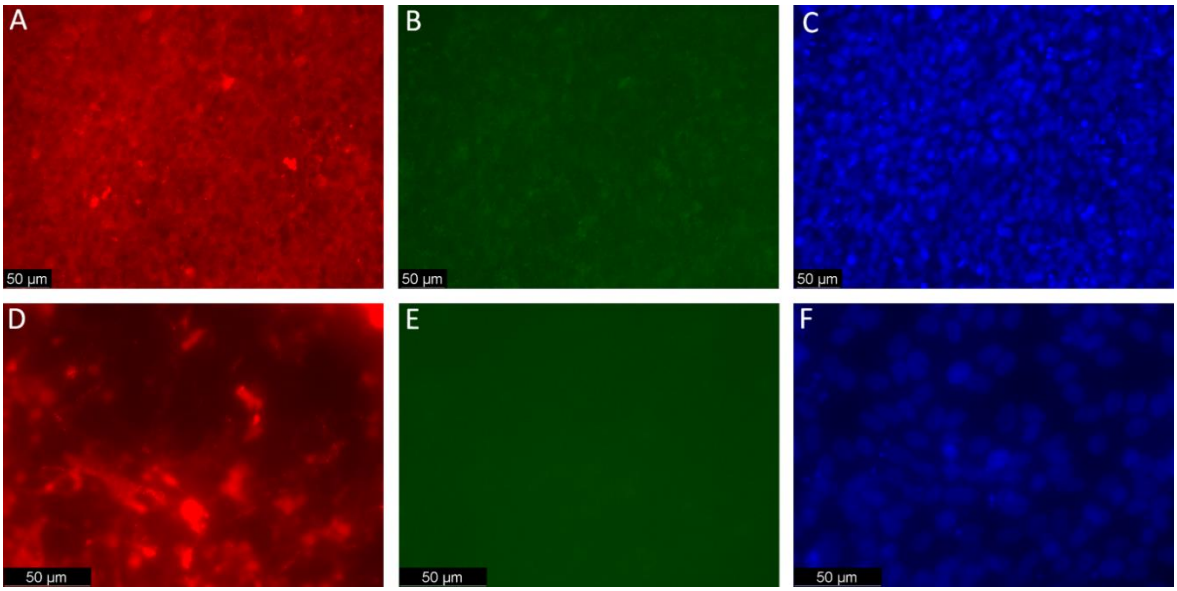

Figure 3.3: HOS grown on collagen and plastic in osteogenic media IHC

HOS cells where seeded onto 2mg/ml collagen (A, B & C) and standard tissue culture plastic (D, E & F) in osteogenic media a incubated over a 28 day period. Each column is either the expression of osteopontin (A & D), osteocalcin (B & E) or a nuclear stain (C & F). All samples were seeded at 5000 cells/cm2.

Early experiments were also conducted into the ability of HOS to produce osteogenic content. As markers of osteogenic formation and mineralization, the proteins OPN and OCN were targeted. Figure 3.3 gives an example of IHC co-staining of these two proteins from HOS which were grown on collagen and standard tissue culture plastic. From a qualitative perspective, it is identifiable that OPN is present in both the collagen and plastic models, possibly higher in the collagen, and that OCN is only identifiable in the collagen. These micrographs were not analysed further due to collagen being abandoned as a scaffold material. Beyond these experiments, plans were put in place to start experimenting with the chemical OPC to alter the mechanical properties of the collagen scaffold, however due to collagen unavailability and further concerns regarding the material, these plans did not progress beyond the planning stage. An example of some of the difficulties experienced with collagen are shown in

Figure 3.4. They demonstrate a common occurrence of the gel not setting (potentially due to collagen degradation) in (A), and detachment and tearing of the gel in (B). The latter was quite common given the long incubation times and need for regular media changes.

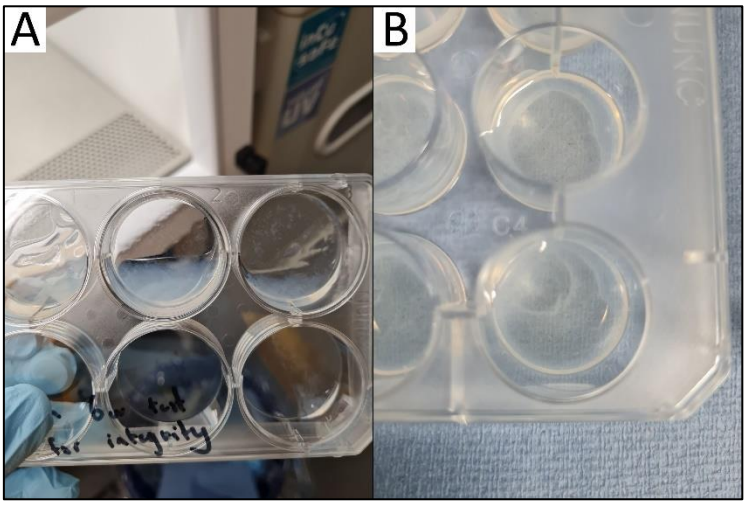

Figure 3.4: Examples of collagen failure

Beyond the lack of availability, collagen samples would often not form as shown in (A) or detach and tear in the centre as shown in (B). This was another factor is the move away from collagen to bone.

3.2.2 Nanokick

The mouse embryonic stem cells CGR8 were used as a primary investigation tool into the potential effects of the Nanokick device on osteogenesis. RT-qPCR was used to investigate the presence of the genes *SP7*, *ALPL* and *RUNX2*, all important genes involved in different aspects of bone formation and skeletal development. As shown in Figure 3.5, each row depicts a different time point and each column a different group, on the Nanokick with osteoconductive media (OCM), on the Nanokick with BM or off the Nanokick with OCM.

Across the graphs, there are numerous examples of the average relative expression of the sample showing high levels of up-regulation but showing no significance. Examples of this include graph A *RUNX2*, graph B *SP7*, graph C *SP7* and *RUNX2* and graph F *RUNX2*. This was generally due to inconsistent raw fold change values with a wide range for some repeats. There are, however, a number of figures of note with significance.

In graph (A) it is shown that there is a significant upregulation of *SP7* and *ALPL* for CGR8 on the Nanokick with OCM at day 7. All other expression values are not significant at day 7. For day 14 samples, as seen in graph (D) for samples grown on the Nanokick with OCM, *RUNX2* is significantly higher than the control and *ALPL* is significantly downregulated. At the same time point seen in graph (F) showing samples only grown in OCM, *SP7* is significantly upregulated. All other expression values are not significant at day 14. For day 21 samples, in graph (G) showing samples grown on the Nanokick in OCM, *SP7* is significantly upregulated. In graph (H) showing samples grown on the Nanokick in BM, both *SP7* and *RUNX2* are significantly upregulated. In graph (I) showing samples only grown in OCM, *RUNX2* is significantly upregulated. All other expression values are not significant at day 21.

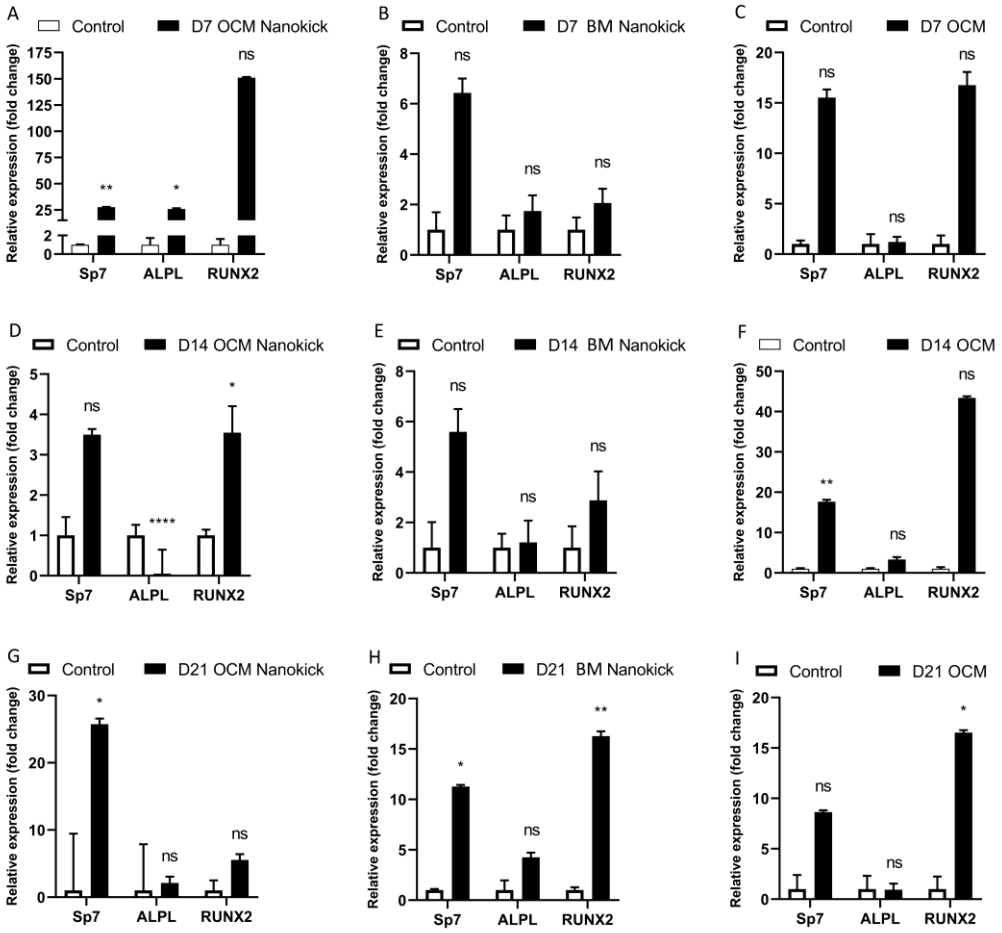

Figure 3.5: RT-qPCR of CGR8 grown on a Nanokick with and without osteogenic media for SP7, ALPL & RUNX2

CGR8 where grown with (OCM) and without (BM) osteogenic media, on and off a Nanokick for 7, 14 and 21 days. Targeted genes were *SP7*, *ALPL* and *RUNX2* with *GAPDH* used as the housekeeper gene. Data is presented as mean ± SEM values (calculated from Ct mean) from three independent experiments. Data shown is from five biological and two technical repeats with **P≤0.01, *P≤0.05 & ^{ns}P>0.05 calculated using the Student's t-test. Graphs are grouped by time point and conditions i.e. Days 7, 14 and 21 and treated with OCM on the Nanokick, BM on the Nanokick and just treated with OCM respectively.

Figure 3.6 below is an examination of the same data as shown in Figure 3.5, but displayed so that the fold change of the three times points are plotted together for a more direct comparison. The individual target genes have also been clustered together.

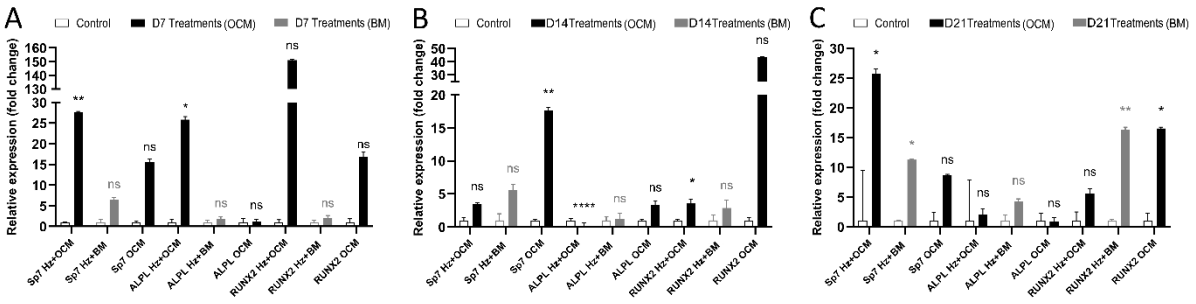

Figure 3.6: RT-qPCR of CGR8 grown on a Nanokick with and without osteogenic media for SP7, ALPL & RUNX2 grouped by time point

CGR8 where grown with (OCM) and without (BM) osteogenic media, on and off a Nanokick (Hz) for 7, 14 and 21 days. Targeted genes were SP7, ALPL and RUNX2 with GAPDH used as the housekeeper gene. Data is presented as mean ± SEM values (calculated from Ct mean) from three independent experiments. Data shown is from five biological and two technical repeats with **P≤0.01, *P≤0.05 & nsP>0.05 calculated using the Student's t-test. Graphs are grouped by time point i.e. Days 7, 14 and 21.

3.2.3 Bone

3.2.3.1 Bone Fragmentation

As described in Chapter 2, section 2.2.3.3, page 64, having fractured the decellularised bone in liquid nitrogen with a mortar and pestle maximal length values were measured. As shown in Figure 3.7 (B), the frequency distribution shows a triangular distribution with the peak fragment length at 10µm. The range in lengths was 2µm to 2mm for the arm fragments, which was representative of all bone types. This work led to using a bead mill to produce the fragments, generating larger fragments >1mm.

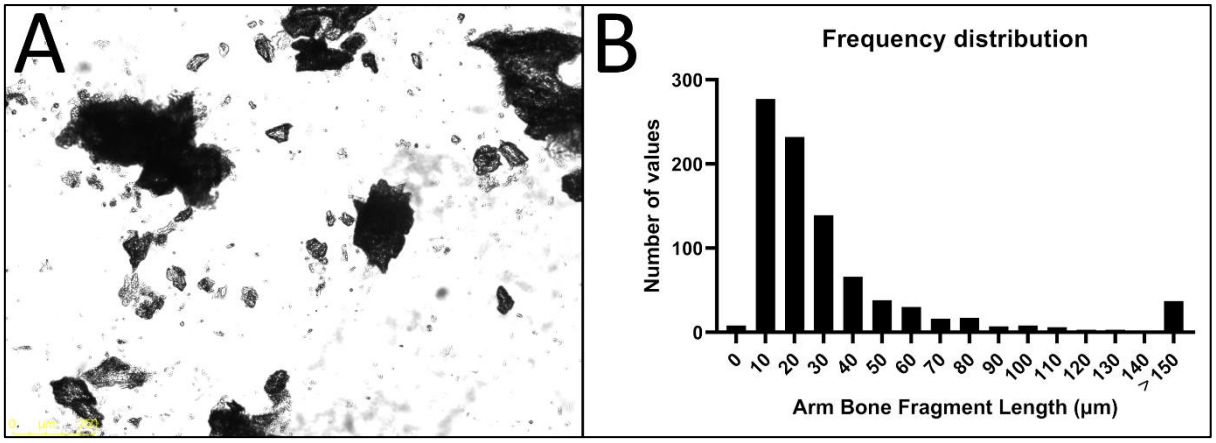

Figure 3.7: Bone fragment measurements

Fragments of a decellularised rat arm bone having been fragmented with liquid nitrogen and a mortar and pestle. (A) Shows a representative x10 magnification of the results of fracturing. A total of ten images were taken of fragments and measured using the measure feature in ImageJ (https://imagej.nih.gov/ij) along each fragments longest section. (B) The length data was compiled for all ten images and converted into a frequency distribution.

3.2.3.2 Bone Autofluorescence

Before being able to analyse any IHC data effectively, it was important to understand the range and degree of autofluorescence present in the decellularised bone fragments to be used in the macro-model. Figure 3.8 shows the range of autofluorescence found in leg, arm and rib fragments along with fluorescence values from each fragment. The absolute fluorescence values were generated from the entire bone piece to determine the range in fluorescence values along with the mean.

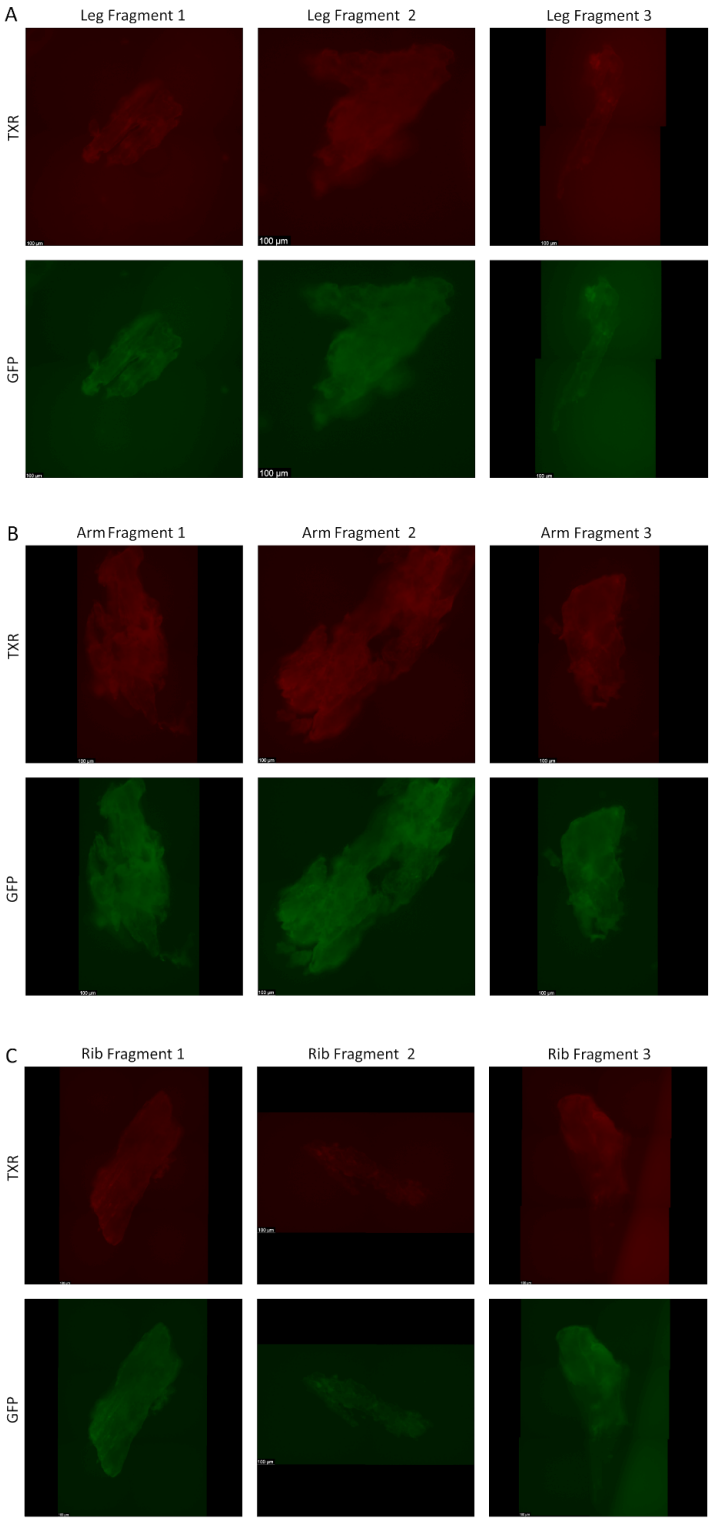

D

Sample	Fluorescence TXR		
	Mean	*Minimum*	*Maximum*
Arm 1	25.871	8	58
Arm 2	28.043	6	72
Arm 3	24.387	8	56
Leg 1	25.145	13	65
Leg 2	26.038	9	50
Leg 3	27.279	12	77
Rib 1	21.683	8	60
Rib 2	15.906	5	42
Rib3	23.398	7	65

E

Sample	Fluorescence GFP		
	Mean	*Minimum*	*Maximum*
Arm 1	23.411	5	53
Arm 2	26.456	7	59
Arm 3	22.406	8	51
Leg 1	21.374	10	47
Leg 2	22.51	10	41
Leg 3	23.219	9	58
Rib 1	18.151	6	47
Rib 2	13.147	5	34
Rib3	20.162	5	56

Figure 3.8: Bone fragment autofluorescence

(A, B & C) Autofluorescence micrographs of leg, arm and rib fragments respectively. For each set, bones were imaged in triplicate and under Texas Red (TXR) and Green Fluorescent Protein (GFP). (D & E) Show tables of mean, minimum and maximum fluorescence values for TXR and GFP respectively. Values were generated from the adjacent micrographs. All images adjusted: +20% brightness and -40% contrast.

Not only did all the fragments display autofluorescence, but across the fragments there was a large range between the minimum and maximum values. This presented a problem for future analysis of IHC data as determining the fluorescence values of OPC or OCN deposited by cell directly on the bone fragments would be complex due to the variable nature of each piece of bone's autofluorescence. The work-around was to allow the samples to incubate for a full 28 days and then to collect data from the cells surrounding the bone fragments, negating the need to remove background fluorescence from each value.

3.2.3.3 Decellularized Fragment Cell Survival

It is important to note that the methodology used to decellularize the rat bone was a modified version of a protocol to both decellularize and demineralise bovine bone. It was therefore important to assess the efficacy of this new protocol. This was done via SEM imaging and nuclear staining. The decellularized fragments were incubated with Hoechst solution which binds to the nuclei of both live and dead cells. If present, the cell's nuclei would be noticeable as they have a highly distinct spherical intense blue form as shown in Figure 3.9.

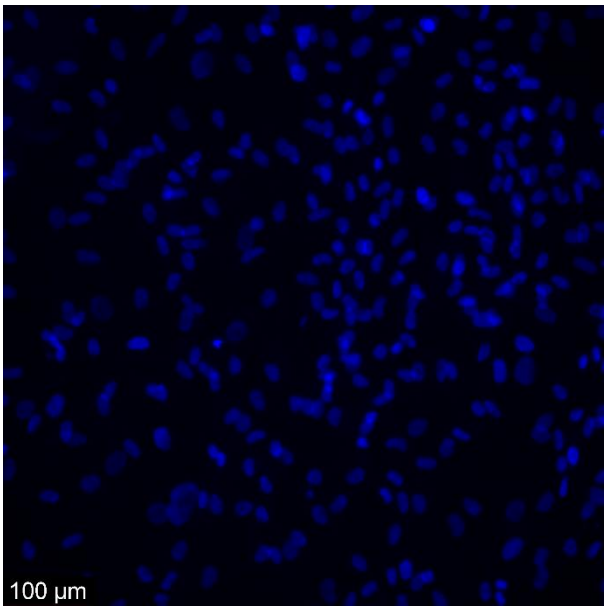

Figure 3.9: Micrograph of hMSCs counterstained with Hoechst solution

Representative micrograph of hMSC cells incubated in Hoechst solution cultured on tissue culture plastic. This image displays the classic spherical regions of intense blue fluorescence due to the binding of Hoechst to the cell nuclei.

Figure 3.10 shows both the merged brightfield and fluorescent (A and B), and the fluorescent micrographs (C and D) of the Hoechst incubated fragments alongside unstained controls. Smaller fragments were used for this experiment as not to waste larger fragments suitable for the models and by using smaller fragments with a larger surface area to volume ratio, more of each fragment is exposed to the Hoechst solution. There was no evidence of occurrences of intense (or otherwise) spherical nuclei stained by the Hoechst solution in all the bone fragments imaged, with Figure 3.10 shown as a representative sample. As seen in (C) and (D), only variable low level autofluorescence is visible, indicating there are no remaining intact cells on the bone fragment surface.

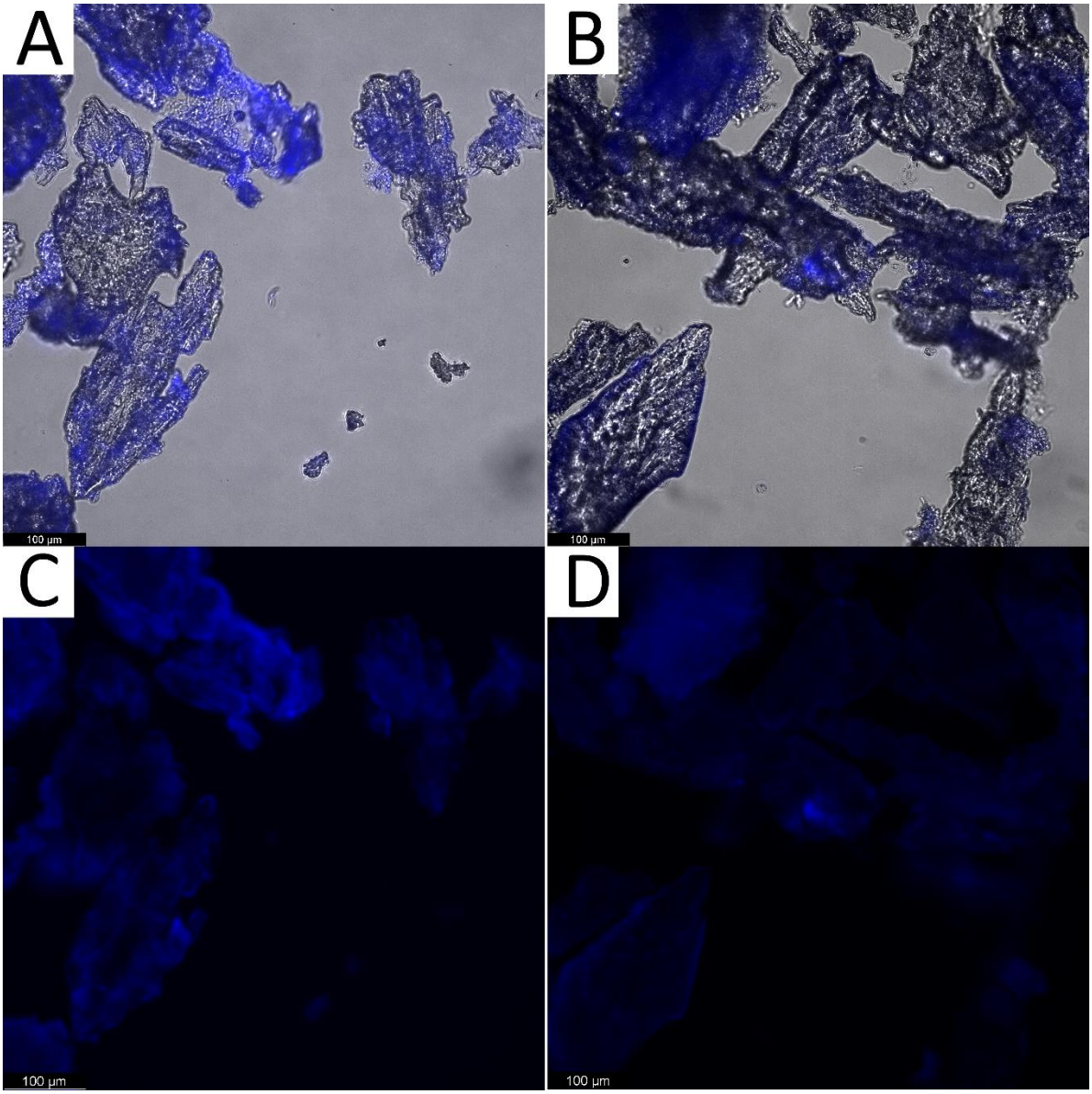

Figure 3.10: Micrographs of decellularized rat bone fragments counterstained with Hoechst solution

Representative fluorescent micrographs of rat bone fragments post decellularization merged with bright field (A & B) and the same micrographs of just the fluorescence (C & D). Image A displays fragments which had been incubated in Hoechst solution, a nuclear counterstain. Image B displays control fragments which had not been subjected to Hoechst solution for comparison. Images C and D are the same as A and B respectively, but with only the fluorescent channel shown.

3.2.3.4 Cell tracking

Initial success or failure to grow cells on bone fragments was validated using the CMAC cell tracker. Having already optimised the tracker, fragments with prospective cells on the surface were incubated in 10µM CMAC for 30 minutes. After this time point, the fragments were

transferred to a new well dish. The primary observation beyond the successful protocol to grow cells on these bone fragments was that cells seemed to show preference for certain areas of the bone, growing in high densities in some regions while not at all on others. This is particularly visible in Figure 3.11 (A) and (B) where the HOS propagated well at the top of the former and on the right side of the latter. Further representative images taken of HOS and hMSC growth on bone, tracked with CMAC can be found in the Appendix, Figure 6.1 and Figure 6.2.

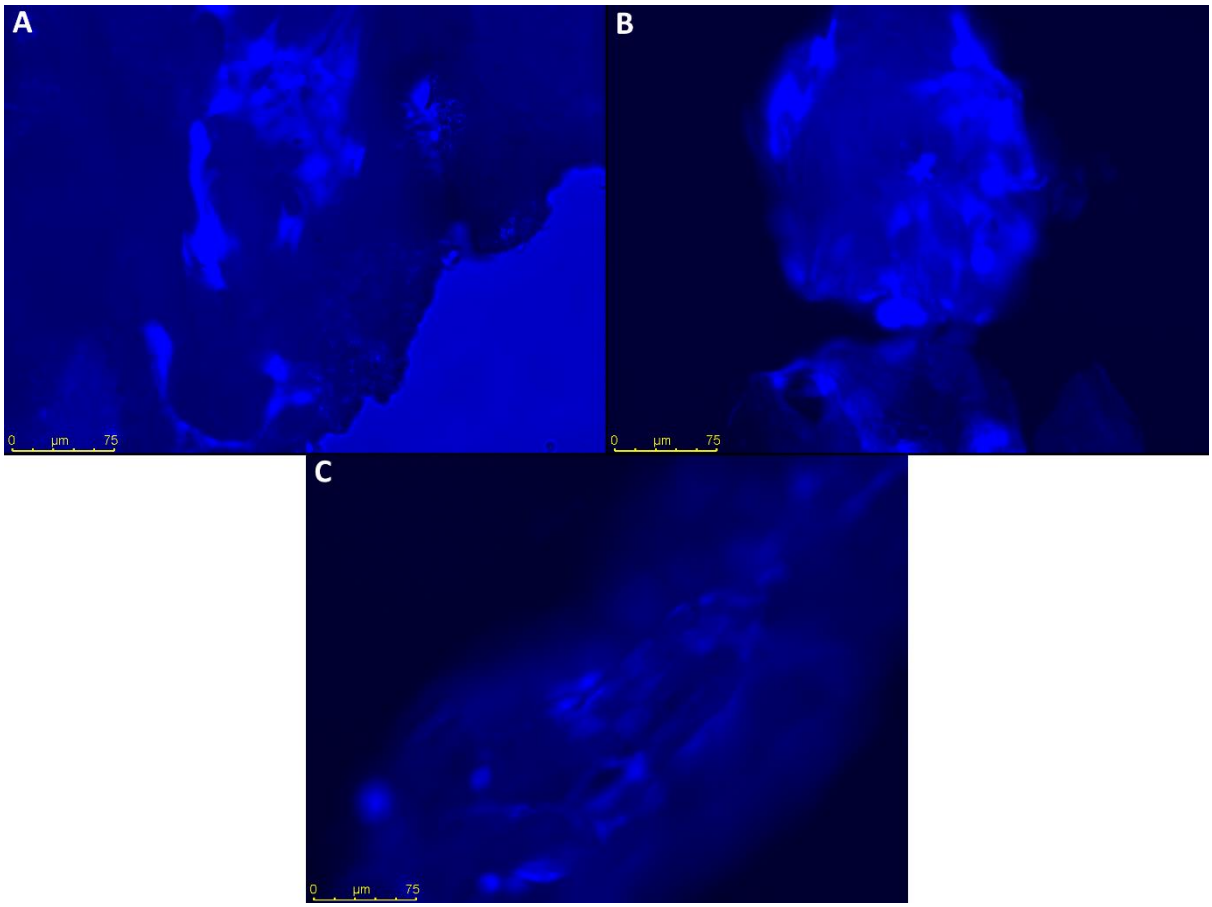

Figure 3.11: Cell tracking of HOS on bone

(A), (B) & (C) show leg arm and rib fragments respectively which had been seeded with HOS cells at 5000 cells/cm^2 and incubated for four days. The fragments were relocated to a fresh well dish and incubated in CMAC cell tracker and imaged afterwards to determine the extent of cellular adhesion.

Before growing both hMSC and HOS on bone fragments for the final model, it was important to determine whether both cell types would grow in co-culture. To ensure this, both cell types

were incubated in different cell trackers prior to splitting and then seeded at the same density of 2500 cells/cm^2 in triplicate. The cells were tracked over a 48hr period as shown in Figure 3.12. In all replicates, hMSC and HOS adhered successfully to the culture plastic and began the early stages of proliferation over the 48hr period. Further replicates can be found in the Appendix, Figure 6.3 to Figure 6.6.

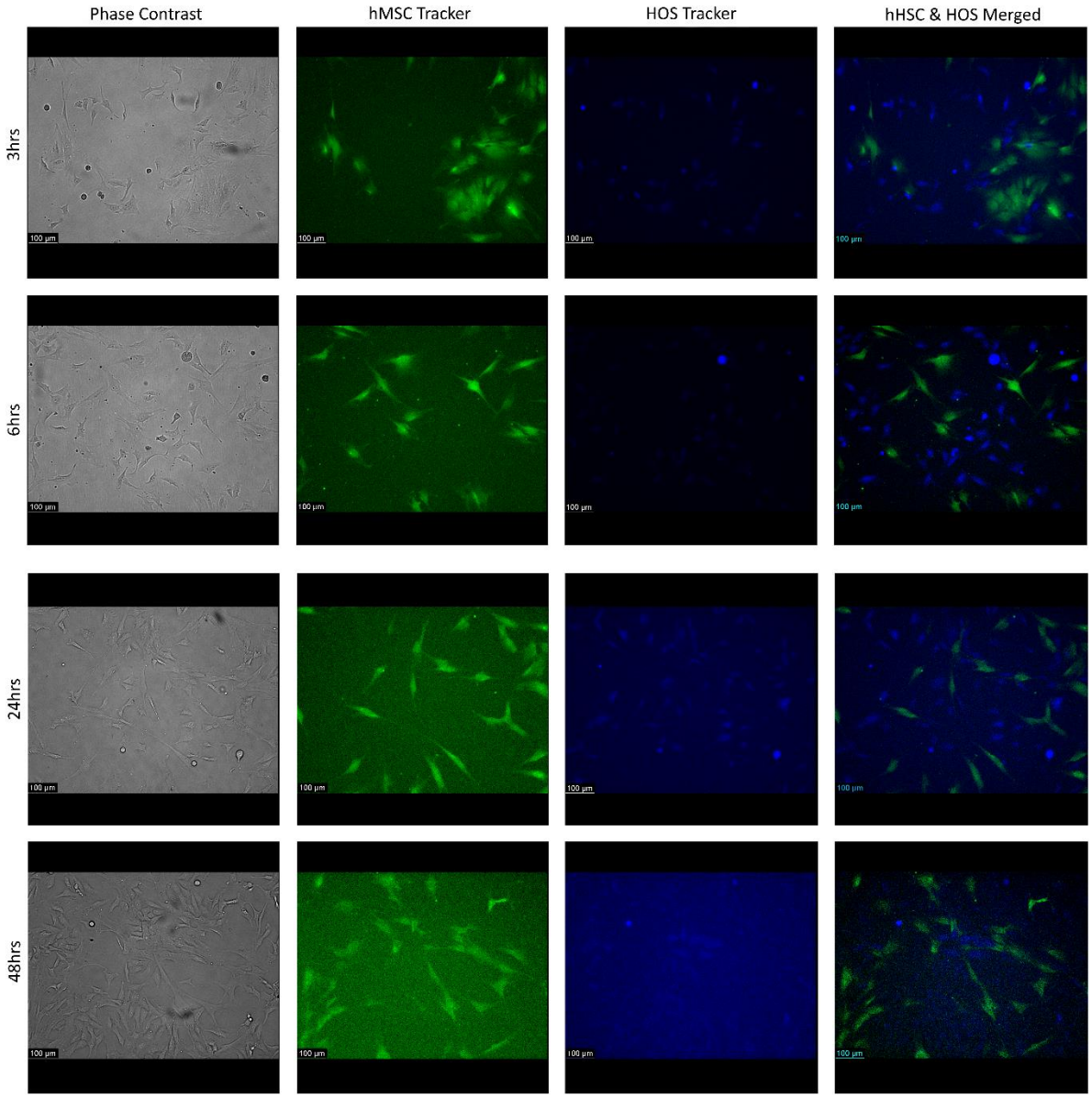

Figure 3.12: Tracking of hMSC & HOS over 48hrs

Representative images of hMSC and HOS cells grown in co-culture on tissue culture plastic over 48hrs. Both hMSC and HOS were introduced to the same well dish seeded at 5000 cells/cm^2 having each been subject to cell trackers. In the green excitation spectra, CMFDA was used to track hMSC and in the blue CMAC to track HOS. Phase contrast images were taken to view all cells. The green hMSC and blue HOS channels were merged using ImageJ by the user.

3.2.3.5 SEM

The bone locations chosen to be the natural scaffolds for the niche models were based on the native environment where the niche is believed to be located. Having harvested bone from

the legs, arms and ribs, and having grown cells successfully on their fragments, it was important to look at the bone at the microscopic level to determine the topography and see whether there was a clear differentiation between the fragments harvested which were theoretically cancellous bone, and pieces of cortical bone which were harvested from the femur shaft and subject to the standard decellularization and fracturing process. It is important to note that cortical bone was not used as a scaffold material in models, but as a comparison against cancellous and rib bone. Figure 3.13 displays representative micrographs taken of cortical, cancellous (leg) and rib fragments at three levels of magnification with a SEM. Further micrographs can be found in the Appendix, Figure 6.7, Figure 6.8 and Figure 6.9.

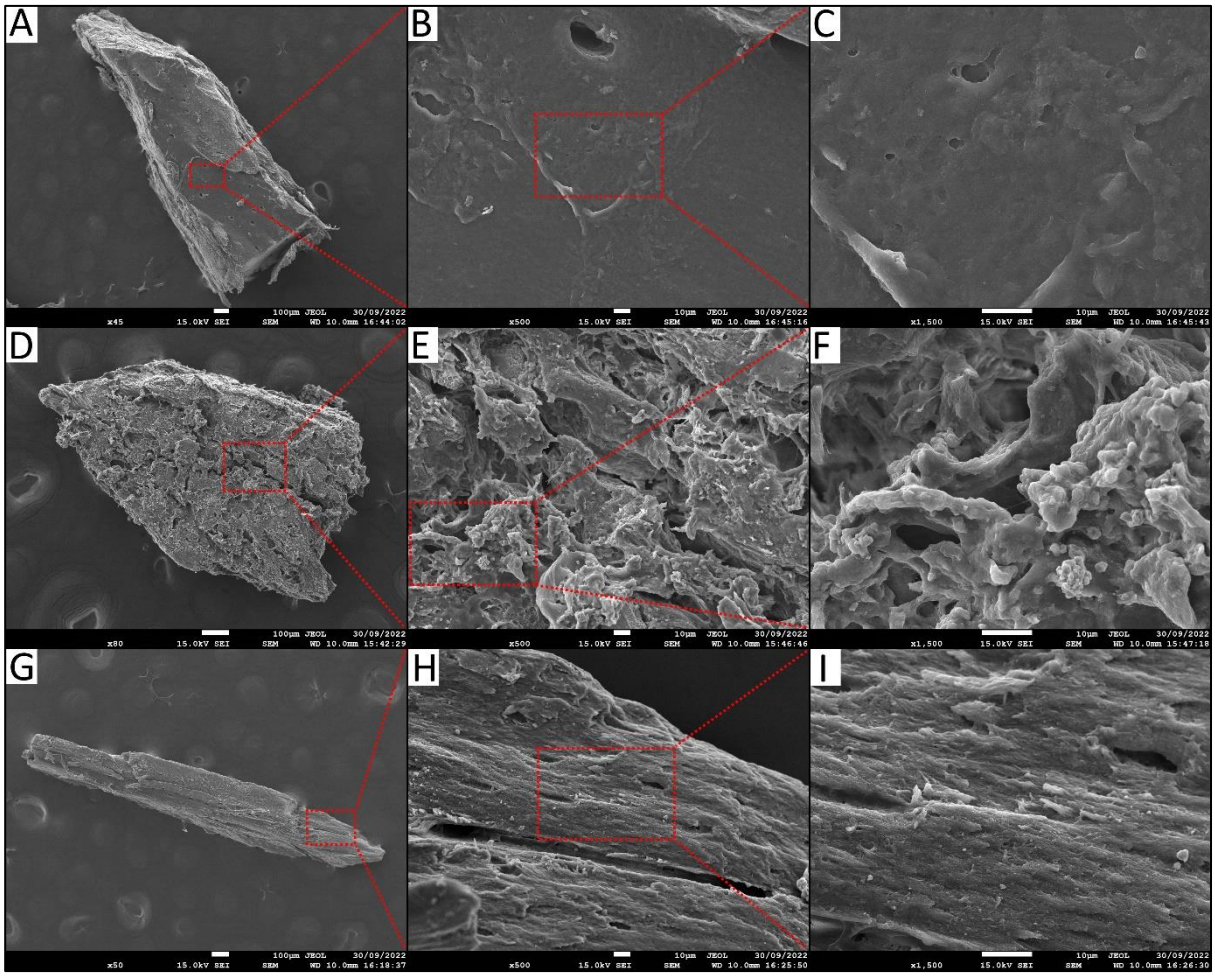

Figure 3.13: SEM micrographs of cortical, cancellous and rib fragments

Representative SEM micrographs of rat bone cortical fragments (A, B & C), cancellous fragments (D, E & F) and rib fragments (G, H & I). Each row of micrographs are sequential higher magnifications of the same fragment (x50/45, x500 & x1500) with red dashed boxes showing the area magnified in the subsequent image.

As expected, the decellularised fragment surface structure varied between cortical, cancellous (leg) and rib fragments. The majority of the cortical surface was observably dense and relatively smooth, with the surface interspersed with Haversian canals, which prior to decellularization, would have housed blood vessels and nerve fibres. The smoothness of the bone surface was particularly noticeable when compared to cancellous bone, especially at higher magnifications, for example comparing B to E. The cancellous bone had a far rougher and porous surface with “ravines” throughout the bone. The irregular surface was not indicative of the standard trabeculae lattice structure; this, however, was likely to have been due to the small size of the piece being just over 1mm in length and sourced from the femoral head of the femur. The rib bone in contrast was somewhere in between the other two in surface roughness and irregularity. The surface also had numerous canals present, more so than the cortical fragments. Ribs are comprised of both cortical and cancellous bone potentially explaining how the fragment shown in (G) fell between those in (A) and (D) in surface structure.

Secondary to determining differences in the bone structure, the SEM micrographs showed the efficacy of the optimised decellularization protocol. Across all imaged fragments, there was no qualitative evidence of any cellular components remaining on the bone surface. This was determined based on the known morphology of bone cells. Osteoblasts are cuboidal in shape when active and flattened when quiescent and measure 20–30 µm in diameter (Florencio-Silva et al., 2015). Osteocytes are stellate shaped cells embedded within the bone matrix, exhibiting dendritic morphology, with long cytoplasmic extensions that traverse the canaliculi, approximately 15–20 µm in diameter, with dendrites extending up to 50 µm in length (Bonewald, 2011). Osteoclasts are large, multinucleated cells with a ruffled border that range from 20–100 µm in diameter depending on the bone surface they occupy (Teitelbaum, 2000). MSCs are spindle-shaped fibroblast-like cells typically measuring 15–30 µm in diameter (Pittenger et al., 1999). No objects were seen in any of the SEM micrographs of the bone fragments falling within the description and size ranges described.

Having imaged the three different bone types and determined the qualitative differences between the fragments, imaging fragments which had HOS grown on them was the next step. This was done to elucidate whether the cells had any preferential bone type or area. HOS were seeded onto bone fragments using the same protocol as for the development of the macro model in basal media but only grown for three days before fixation. Figure 3.14, Figure 3.15 and Figure 3.16 show micrographs of cortical, cancellous and rib fragments respectively, comparing the surface of just bone to bone which had cells grown on them.

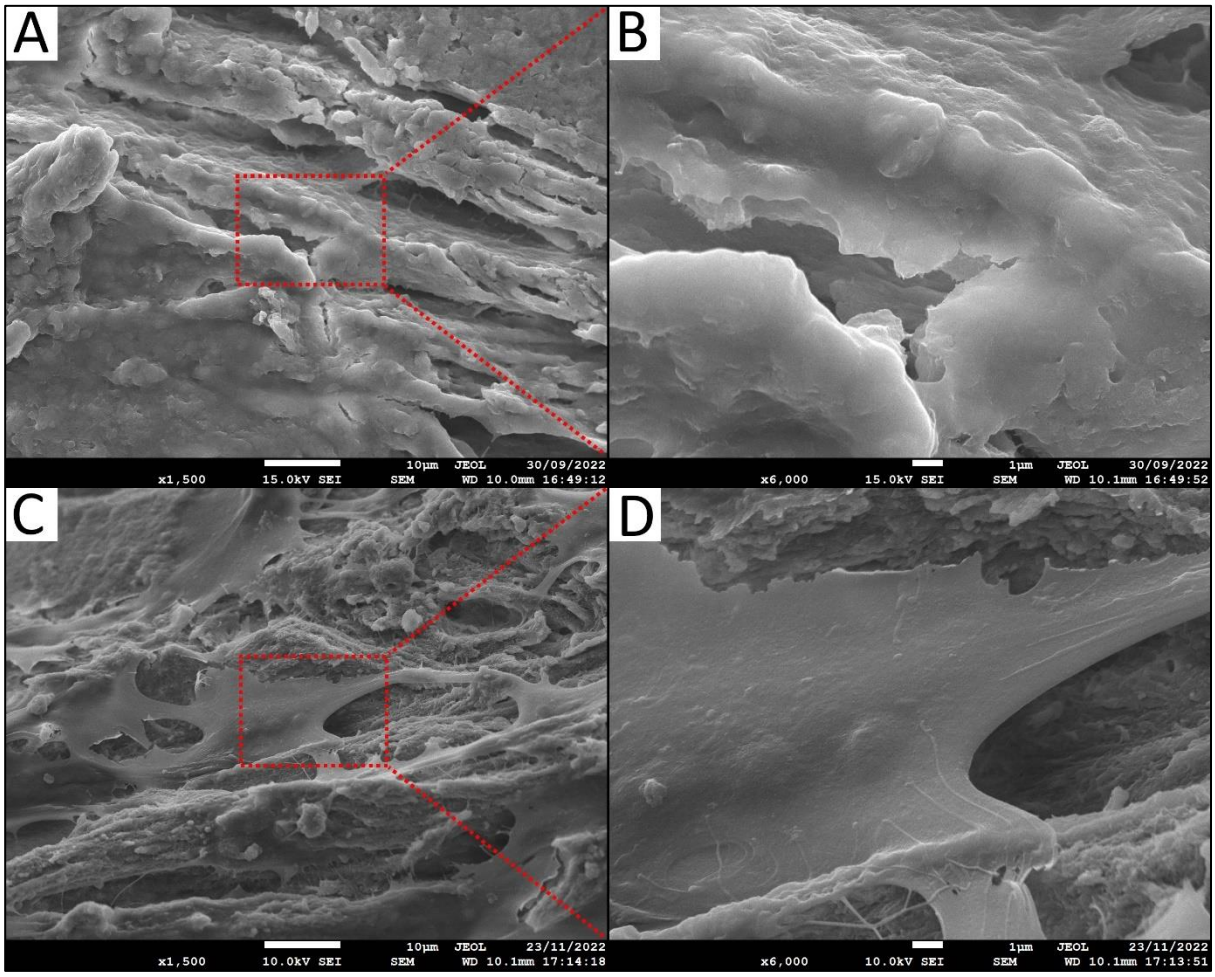

Figure 3.14: SEM micrographs of cortical fragments without and with cells

Representative SEM micrographs of rat bone cortical fragments at x1500 (A & C) and x5000 (B & D). A & B show just decellularised cortical rat bone fragments while C & D show fixed decellularised cortical rat bone with HOS cells grown on the surface. Cells were grown on the bone for three days and seeded at 5000 cells/cm^2. Red dashed boxes show the area magnified in the adjacent image.

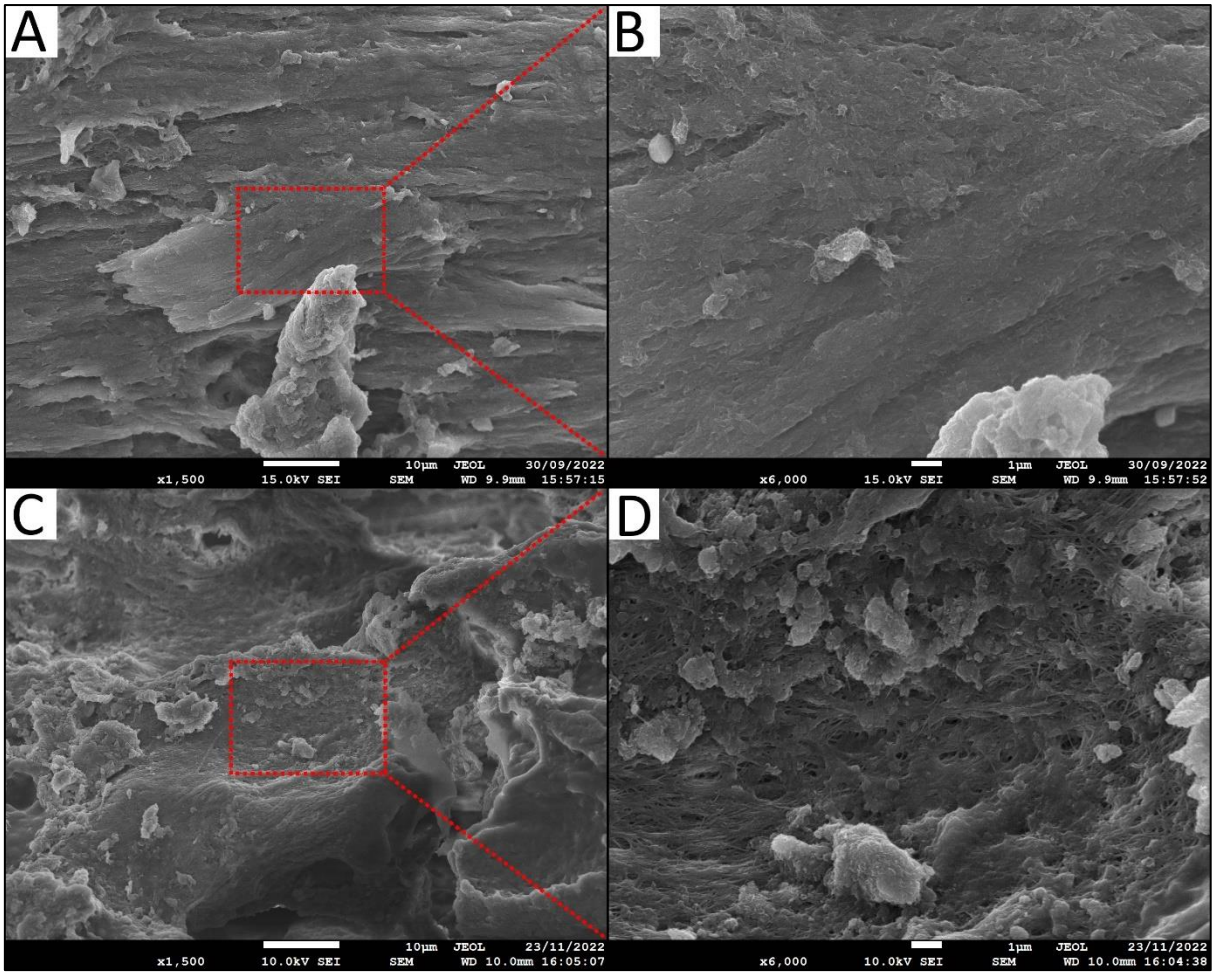

Figure 3.15: SEM micrographs of cancellous fragments without and with cells

Representative SEM micrographs of rat bone cancellous fragments at x1500 (A & C) and x5000 (B & D). A & B show just decellularised cortical rat bone fragments while C & D show fixed decellularised cortical rat bone with HOS cells grown on the surface. Cells were grown on the bone for three days and seeded at 5000 cells/cm^2. Red dashed boxes show the area magnified in the adjacent image.

In all three bone types, HOS were found to have adhered and proliferated over the majority of the bone surface. At lower magnifications, identification of cells was not always obvious but at x500 and above, evidence of cells was easier to determine. Cortical bone had the highest number of regions of low-density cell coverage. As seen in Figure 3.14 micrograph (C), cells can be seen dispersed across the bone with regions 'uncovered' by the cell membrane. The cells were identifiable largely due to the damage taken during fixation causing cracks and cell detachment as is more visible in micrograph (D). By comparison, on both cancellous and rib fragments (Figure 3.15 & Figure 3.16) seeded with cells were almost entirely covered with

cells or cellular product. Over the majority of the bone, the usual rough irregular surface was no longer viable but completely covered with either a smooth coating or a network of fibres. Both are present in Figure 3.16 (D), the left side having a smooth surface and the right covered in fibres.

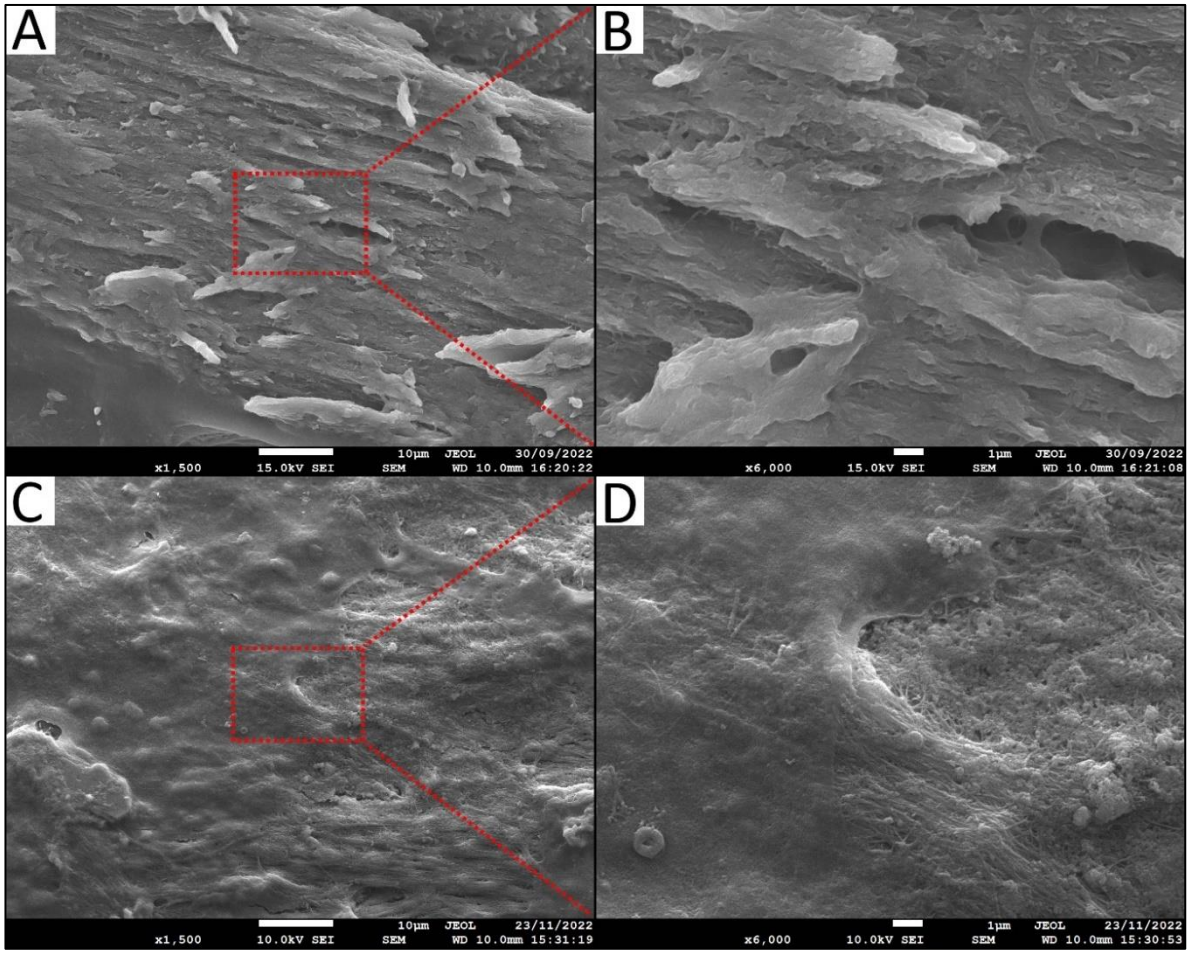

Figure 3.16: SEM micrographs of rib fragments without and with cells

Representative SEM micrographs of rat bone rib fragments at x1500 (A & C) and x5000 (B & D). A & B show just decellularised cortical rat bone fragments while C & D show fixed decellularised cortical rat bone with HOS cells grown on the surface. Cells were grown on the bone for three days and seeded at 5000 cells/cm^2 before fixation. Red dashed boxes show the area magnified in the adjacent image.

Having imaged multiple areas of three different fragments of each bone type, the cell morphology or rather evidence of cellular activity took three different forms. Firstly, there were HOS with clear round morphology in identifiable groupings clearly visible at x500 magnification. An example of this can be seen in Figure 3.17 where cells can be identified

spanning gaps in the bone with filaments from a central body. Cells with this morphology were only found on cortical bone and generally in regions with gaps between the surface bone.

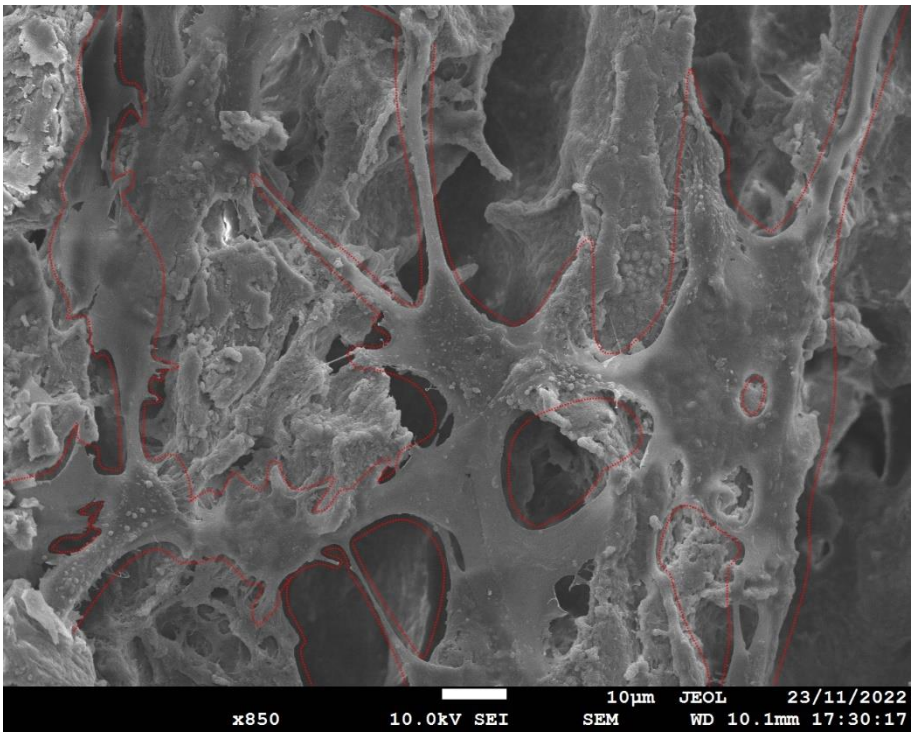

Figure 3.17: SEM micrograph of HOS on bone in identifiable groupings

SEM micrograph of HOS cells on a fragment of cortical bone grown under standard conditions. The cells are in clear groupings with round morphology extended filaments bridging gaps in the bone. A red outline has been generated around a number (but not all) of the cells. Cells were grown on the bone for three days and seeded at 5000 cells/cm^2 before fixation.

In contrast, the remaining two forms did not have individual identifiable cells, but rather there was evidence of cellular presence because the surface was radically different to any bone surface. Found only on cancellous and rib pieces, Figure 3.18 shows a smooth coating sitting above the bone surface.

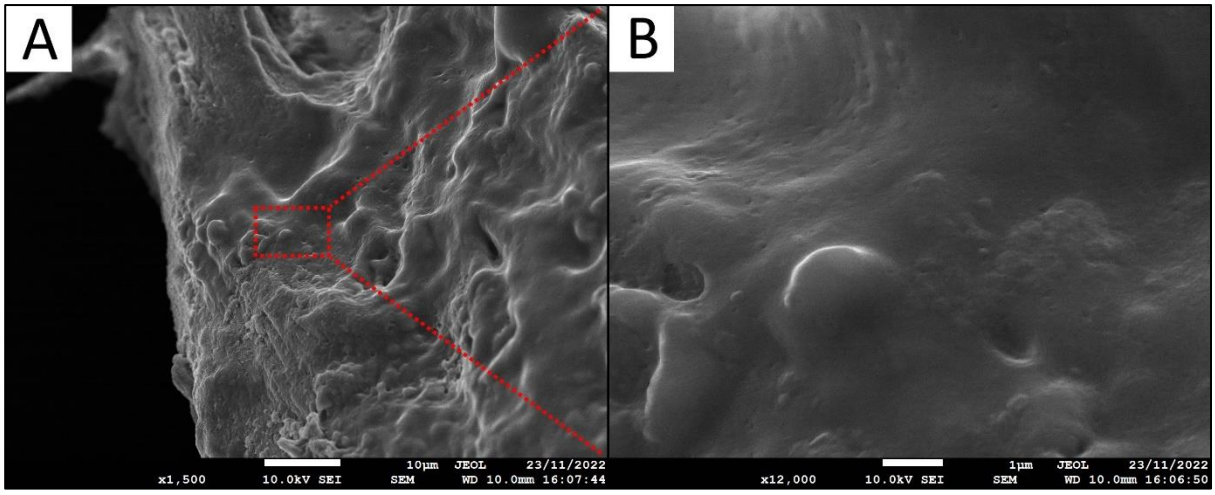

Figure 3.18: SEM micrograph of HOS on bone with smooth coating

SEM micrograph of HOS cells on a fragment of cancellous bone grown under standard conditions. The evidence of cellular presence can be seen in large areas of a smooth coating visually distinct to the underlying bone. Cells were grown on the bone for three days and seeded at 5000 cells/cm^2 before fixation. Micrograph (A) is x1500 magnification and (B) x12000. Red dashed boxes show the area magnified in the adjacent image.

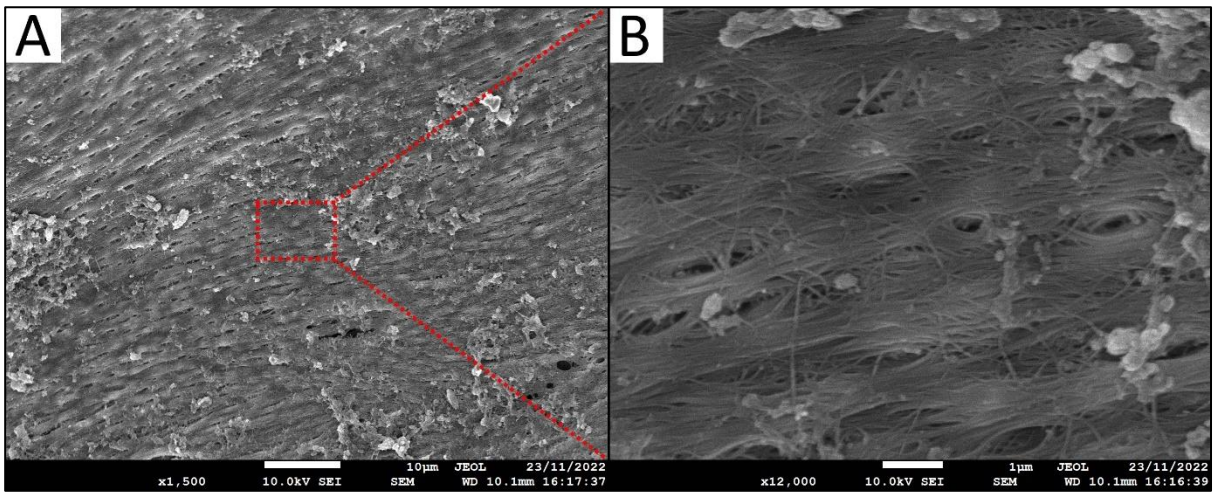

Figure 3.19: SEM micrograph of HOS on bone

SEM micrograph of HOS cells on a fragment of cancellous bone grown under standard conditions. The evidence of cellular presence can be seen in large networks of fibres completely covering the underlying bone surface. Cells were grown on the bone for three days and seeded at 5000 cells/cm^2 before fixation. Micrograph (A) is x1500 magnification and (B) x12000. Red dashed boxes show the area magnified in the adjacent image.

The final form of cellular activity found, looked like fibre networks covering large portions of the bone surface. This was the most common form found and was present on all three bone types, primarily on cancellous bone often forming spiral structures for example, as seen in Figure 3.19. Further micrographs of the three bone types can be found in the Appendix, Figure 6.10, Figure 6.11 and Figure 6.12.

3.2.4 Model Fluorescence

Analysis of the three models generated was conducted by the detection of OPN and OCN. As previously mentioned, both are markers of osteogenesis: OPN, a glycoprotein, is expressed by osteoblasts and is involved in mineralization; OCN, a vitamin K-dependent protein produced by osteoblasts is involved in bone formation and mineralization. Evidence of differentiation and mineralization was quantified via IHC co-staining, a technique that allows for the visualization and localization of the aforementioned proteins. Both markers were found to be present in all models on and around bone fragments.

Each model included leg, arm and rib fragments in triplicate for both osteoconductive media (OCM) and basal media (BM) with the fragments ranging in size from approximately 1 to 3mm. Monolayers were also cultured in triplicate both in OCM and BM as controls. Micrographs of the merged channels for OPN, OCN and nuclear stain can be found in the appendix (Figure 6.13, Figure 6.14 and Figure 6.15).

3.2.4.1 Model 1

The first model generated looked at the output of hMSC grown on bone fragments with and without osteogenic media. Figure 3.20 shows representative micrographs taken from this model. Qualitative analysis of these micrographs showed a few important factors that helped guide analysis moving forward. Firstly, there was positive fluorescence for both OPN and OCN in all samples. There was also low levels of fluorescence from both control samples, those with and without OCM. It was clear from the nuclear staining that large quantities of cells had proliferated on and around the bone fragments.

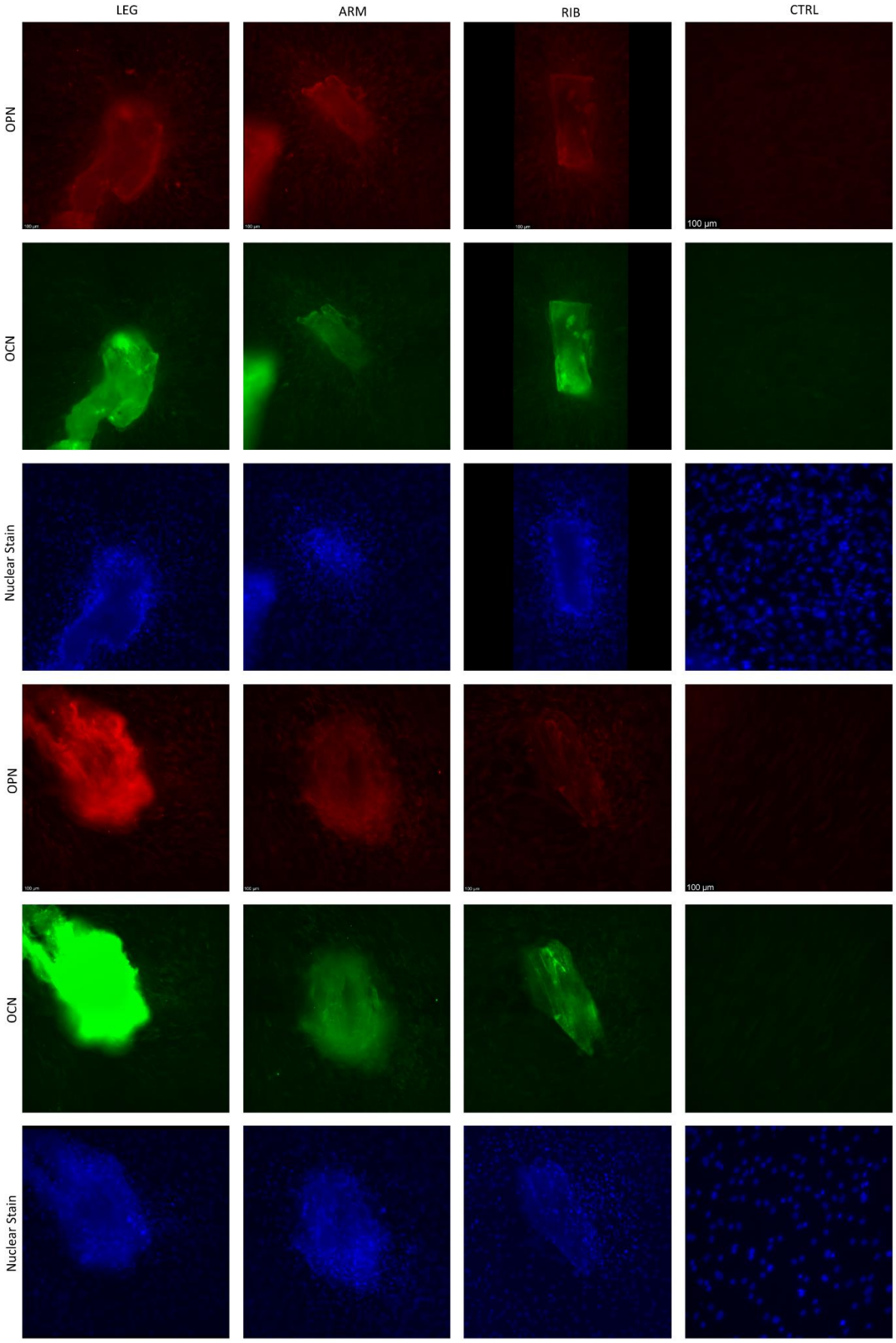
LEG
ARM
RIB
CTRL
OPN
OCN
Nuclear Stain
OPN
OCN
Nuclear Stain
OCM
OCM
OCM
BM
BM
BM
100 µm
100 µm

Figure 3.20: Macroscopic model, Model 1, hMSC on bone with osteogenic media IHC

Representative micrographs from Immunohistochemical staining of Model 1, hMSC seeded onto bone fragments after 28 days incubation. The four columns from left to right are of leg fragments, arm fragments, rib fragments and a monolayer control (Ctrl). Of the six rows, the top three are samples which were incubated in osteogenic media (OCM) and the bottom three incubated in basal media (BM). Each row is also either the expression of osteopontin (OPN), osteocalcin (OCN) or a nuclear stain. Scale bars are present on the OPN micrographs are representative for the lower rows of the same fragment.

As previously mentioned, because of the degree and variation in bone fragment autofluorescence across the bone types, fluorescence values were collated from the cells and ECM surrounding each of the fragments. An extremely significant increase in the amount of OPN was detected in the samples which were grown in OCM compared with samples grown in BM. The same was true for all but the leg samples for OCN levels as is seen in Figure 3.21.

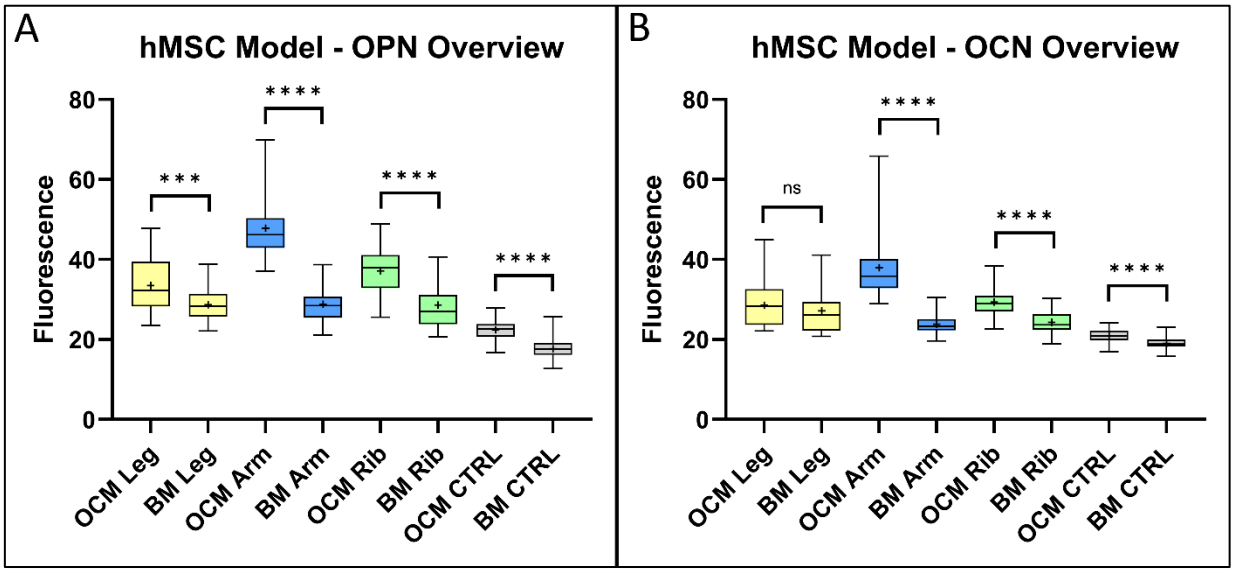

Figure 3.21: Expression of OPN & OCN in Model 1, hMSC on bone with osteogenic media

Box plots overviewing the hMSC grown on bone model for the proteins osteopontin (OPN) (A) and osteocalcin (OCN) (B) after 28 days of incubation. Both plots compare fragments with osteogenic media (OCM) to fragments without in basal media (BM). The box bounds the interquartile ranges divided by the median, a "+" showing the mean and with whiskers from minimum to maximum. Data shown is from three biological and ten technical repeats with ****P≤0.0001, ***P≤0.001 & ^{ns}P>0.05 calculated using the unpaired t-test.

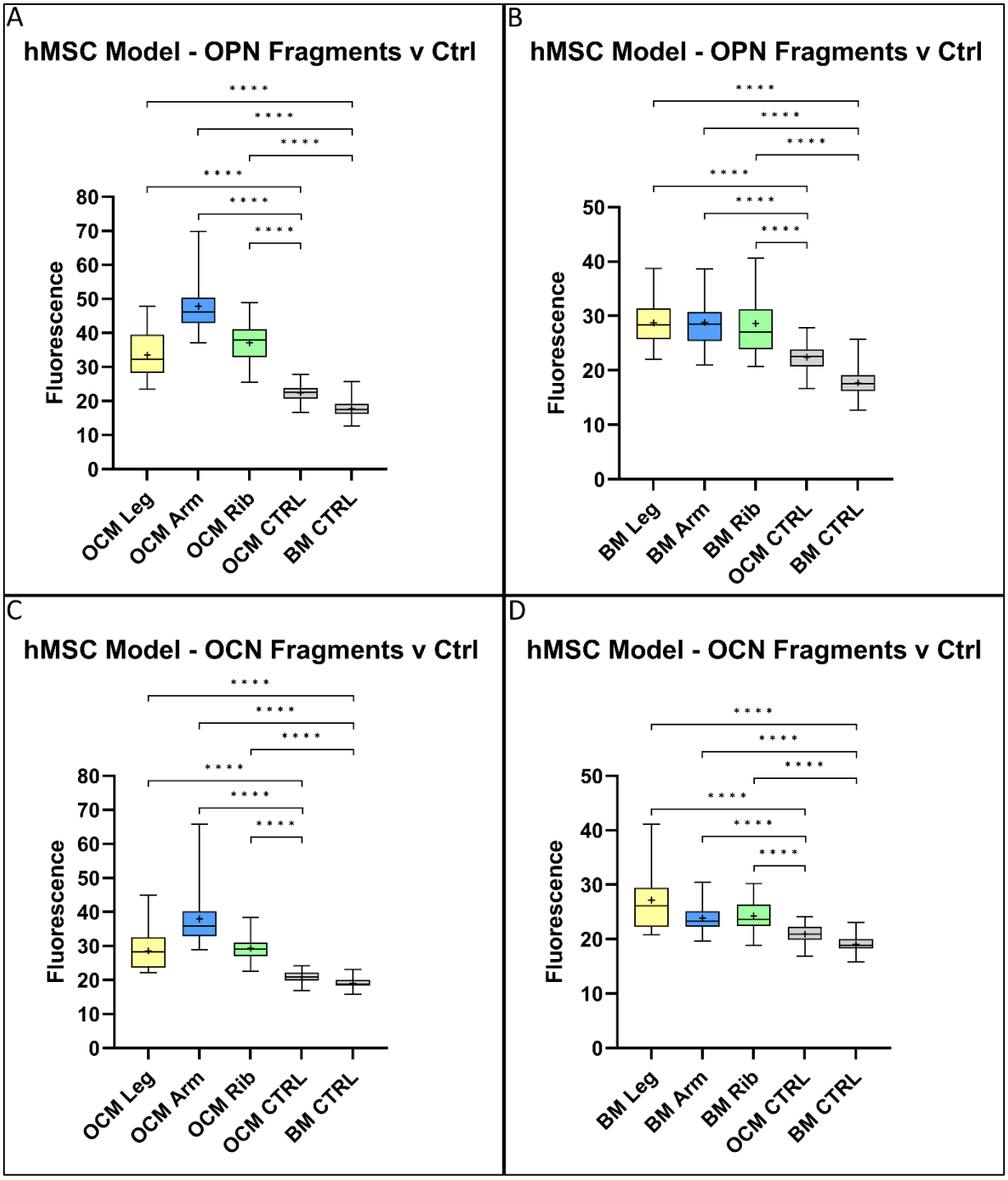

Figure 3.22: Expression of OPN & OCN in Model 1, hMSC on bone with osteogenic media - comparison to control

Box plots comparing bone types to controls for the hMSC grown on bone model for the proteins osteopontin (OPN) (A & B) and osteocalcin (OCN) (C & D) after 28 days of incubation. Plots separately compare fragments and controls with osteogenic media (OCM) (A & C) to fragments and controls without in basal media (BM) (B &D). The box bounds the interquartile ranges divided by the median, a "+" showing the mean and with whiskers from minimum to maximum. Data shown is from three biological and ten technical repeats with ****P≤0.0001, ***P≤0.001 & ^{ns}P>0.05 calculated using the unpaired t-test.

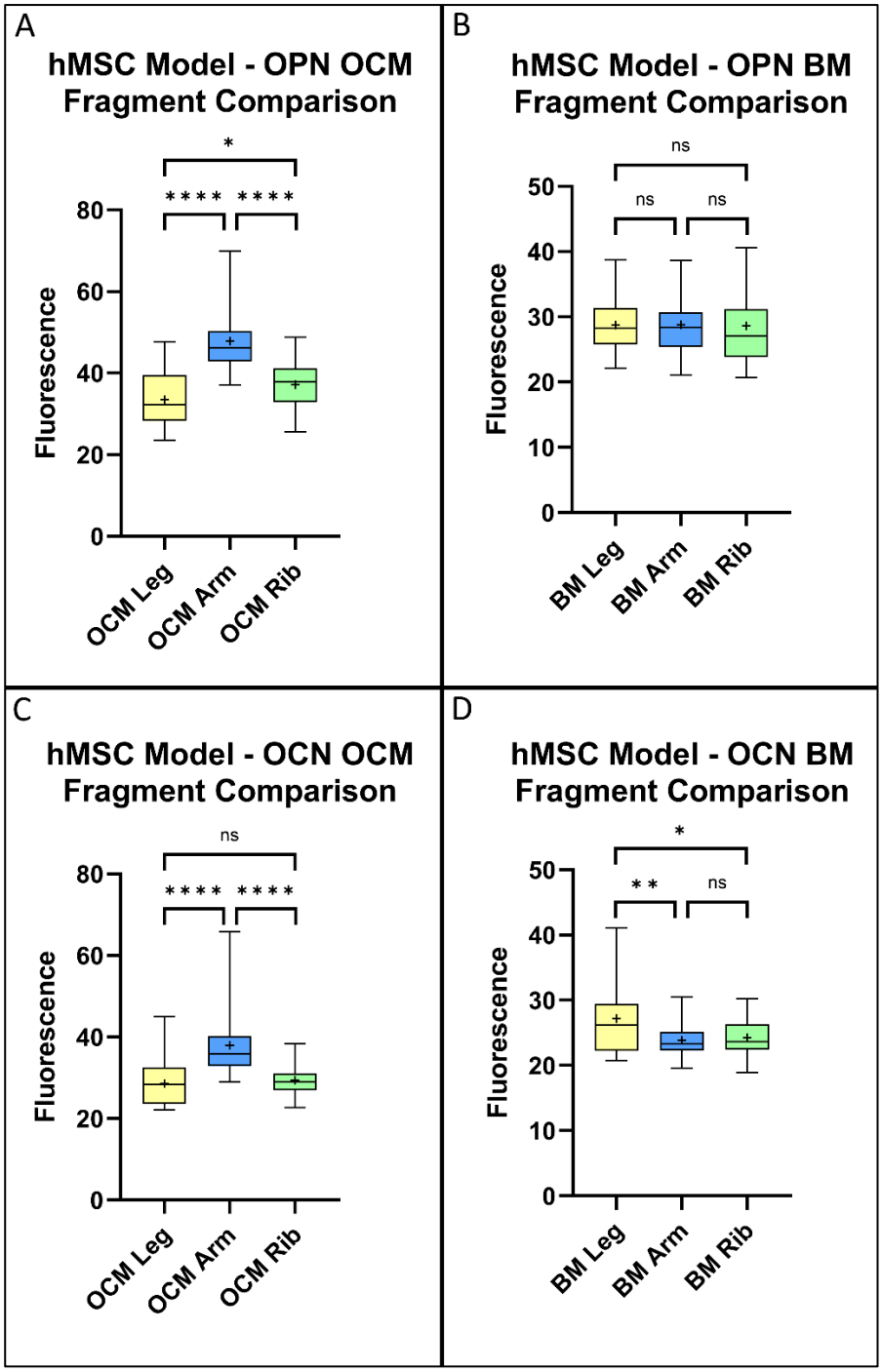

Figure 3.23: Expression of OPN & OCN in Model 1 hMSC on bone with osteogenic media - fragment comparison

Box plots comparing bone types for the hMSC grown on bone model for the proteins osteopontin (OPN) (A & B) and osteocalcin (OCN) (C & D) after 28 days of incubation. Plots separately compare fragments with osteogenic media (OCM) (A & C) to fragments without in basal media (BM) (B & D). The box bounds the interquartile ranges divided by the median, a "+" showing the mean and with whiskers from minimum to maximum. Data shown is from three biological and ten technical repeats with ****P≤0.0001, **P≤0.01, *P≤0.05 & ^{ns}P>0.05 calculated using the unpaired t-test.

Figure 3.22 compares each fluorescence reading with its associated controls. For all samples of both OPN and OCN, cells grown around bone fragments present extremely significant higher levels than both controls with and without OCM. These levels were all $P<0.0001$ calculated using the unpaired t-test.

Differences between the different bone types were also compared (Figure 3.23) to see whether a particular fragment type was most suitable for this model. Observing OPN levels (A & B), for OCM samples arm fragments produced significantly higher values compared with both leg and rib pieces with $P<0.0001$ in both cases. The rib fragments produced slightly higher levels of OPN compared with leg, but with a far lower significance. BM samples however were found to be not significant, suggesting no meaningful difference between the bone type. For OCN levels of the same samples (C & D), a similar trend is seen but with significance levels varying in some comparisons by a small degree. OCM leg and rib fragments have no significant difference between each other, but have an extremely significant difference from arm fragments, the latter being higher. When bone fragments were incubated in BM, the highest OCN levels were highly significantly greater in leg fragments when compared with arm fragments but different to a lesser degree of significance when compared with rib fragments. No significant difference was found between arm and rib fragments.

3.2.4.2 Model 2

This second model saw the introduction of constant vibrations (1000Hz) imparted by the Nanokick platform. When looking at Figure 3.24 compared with Figure 3.20, there is no discernible difference between the models when just looking at the micrographs. The fluorescence data however shows some important differences.

Figure 3.25 comparing fragments and monolayer grown in OCM versus BM shows that in comparison to the previous model, in all cases, levels of OPN and OCN were higher in the BM groups. This difference was significant in all but OCN arm fragments where there was no

significant difference found between the two groups. The monolayer controls however were extremely significant with OCM samples higher than BM for both markers. All samples grown with bone fragments were higher than, and extremely significant compared to both controls as show in Figure 3.26 being higher in all cases.

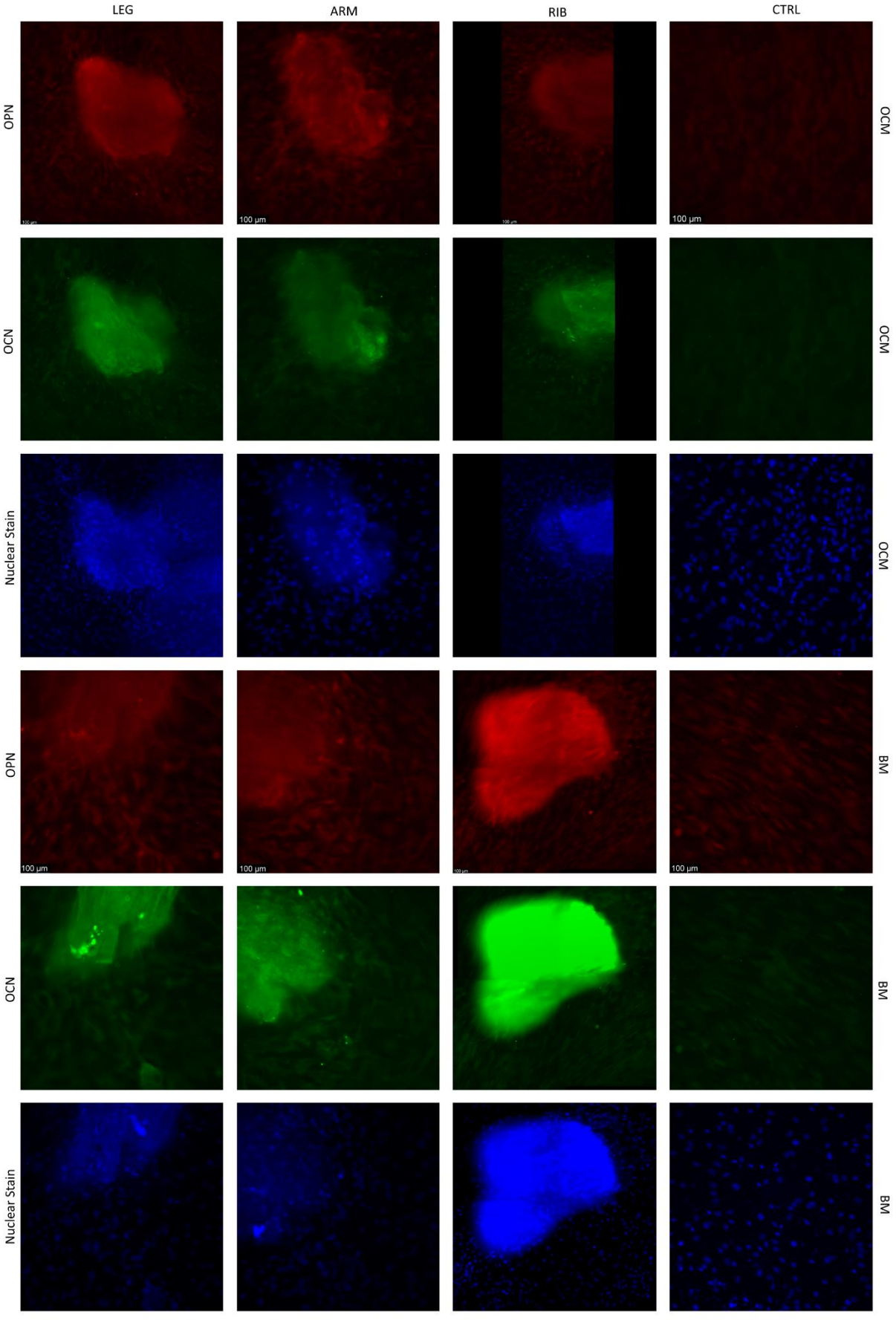
LEG
ARM
RIB
CTRL
OPN
OCN
Nuclear Stain
OPN
OCN
Nuclear Stain
OCM
OCM
OCM
BM
BM
BM
100 µm

Figure 3.24: Macroscopic model, Model 2, hMSC & Hz on bone with osteogenic media

Representative micrographs from Immunohistochemical staining of Model 2, hMSC seeded onto bone fragments after 28 days incubation on the Nanokick device. The four columns from left to right are of leg fragments, arm fragments, rib fragments and a monolayer control (Ctrl). Of the six rows, the top three are samples which were incubated in osteogenic media (OCM) and the bottom three incubated in basal media (BM). Each row is also either the expression of osteopontin (OPN), osteocalcin (OCN) or a nuclear stain. Scale bars are present on the OPN micrographs are representative for the lower rows of the same fragment.

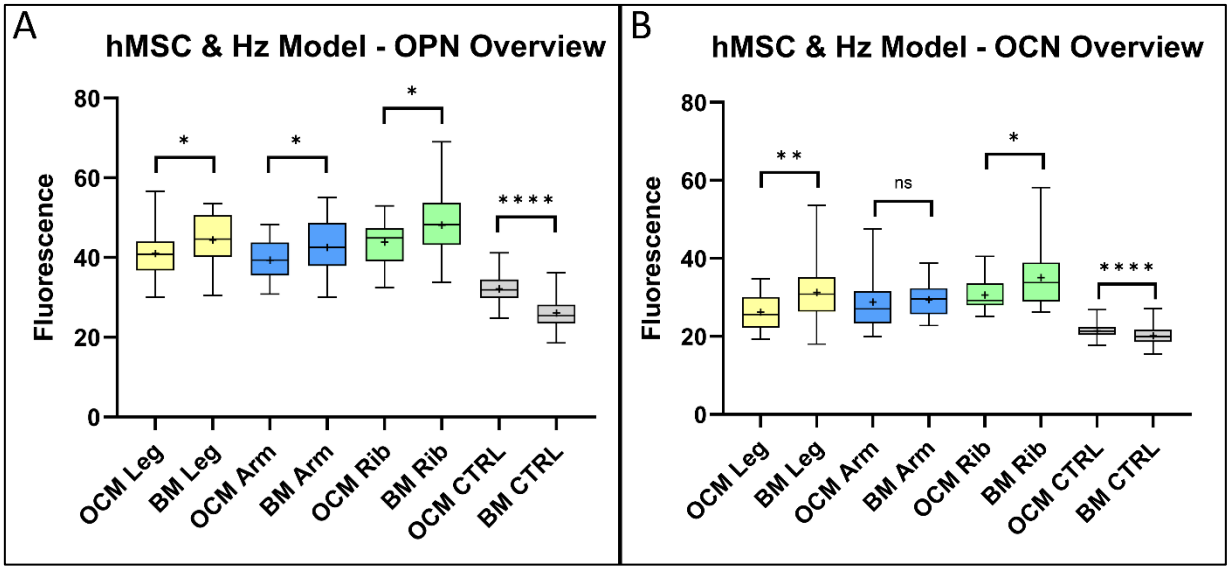

Figure 3.25: Expression of OPN & OCN in Model 2, hMSC & Hz on bone with osteogenic media

Box plots overviewing the hMSC grown on bone on a Nanokick device imparting a constant 100Hz frequency model for the proteins osteopontin (OPN) (A) and osteocalcin (OCN) (B) after 28 days of incubation. Both plots compare fragments with osteogenic media (OCM) to fragments without in basal media (BM). The box bounds the interquartile ranges divided by the median, a "+" showing the mean and with whiskers from minimum to maximum. Data shown is from three biological and ten technical repeats with ****P≤0.0001, **P≤0.01, *P≤0.05 & ^{ns}P>0.05 calculated using the unpaired t-test.

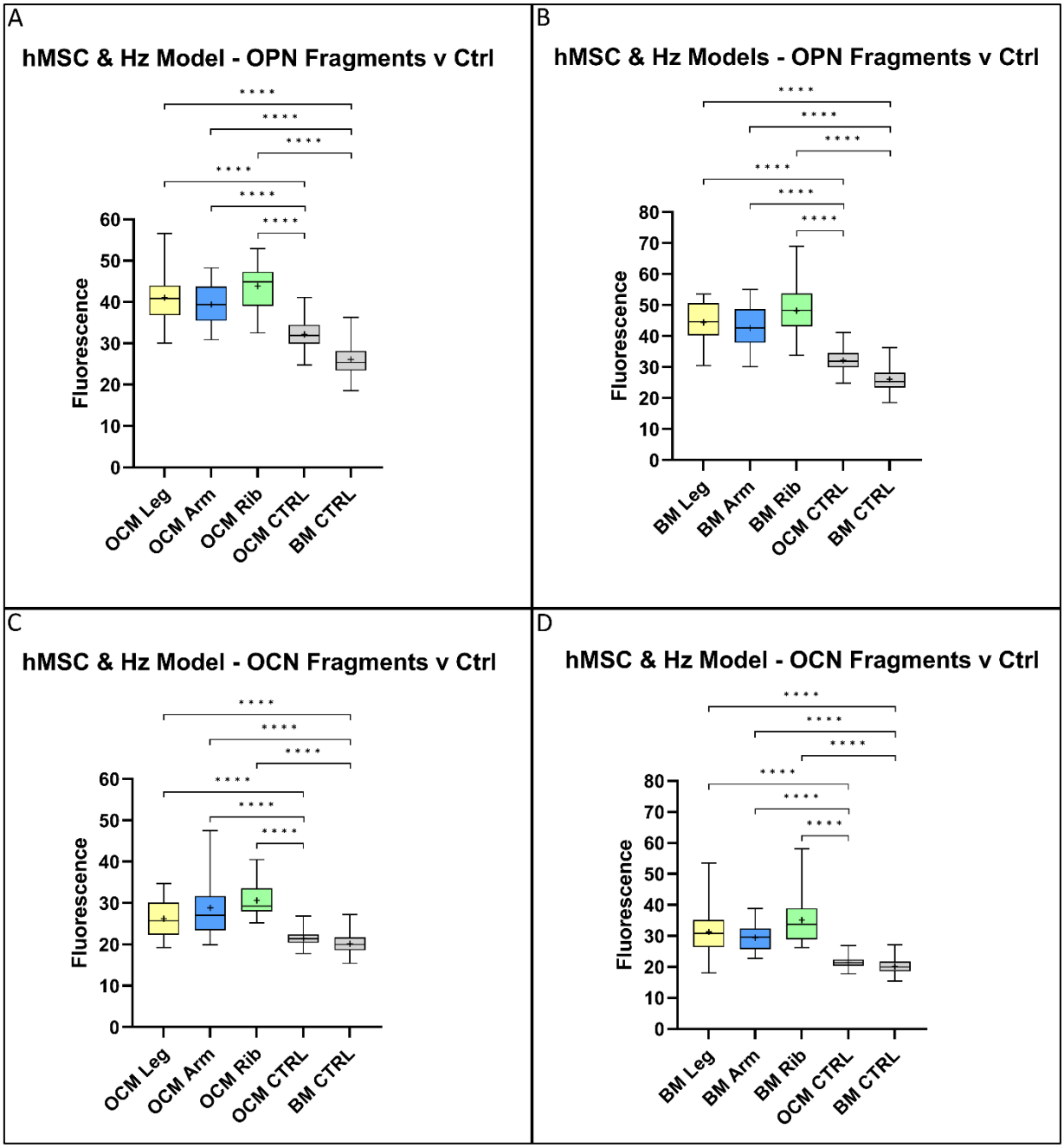

Figure 3.26: Expression of OPN & OCN in Model 2, hMSC & Hz on bone with osteogenic media - comparison to control

Box plots comparing bone types to controls for the hMSC grown on bone on a Nanokick device imparting a constant 100Hz frequency model for the proteins osteopontin (OPN) (A & B) and osteocalcin (OCN) (C & D) after 28 days of incubation. Plots separately compare fragments and controls with osteogenic media (OCM) to fragments and controls without in basal media (BM). The box bounds the interquartile ranges divided by the median, a "+" showing the mean and with whiskers from minimum to maximum. Data shown is from three biological and ten technical repeats with ****P≤0.0001 calculated using the unpaired t-test.

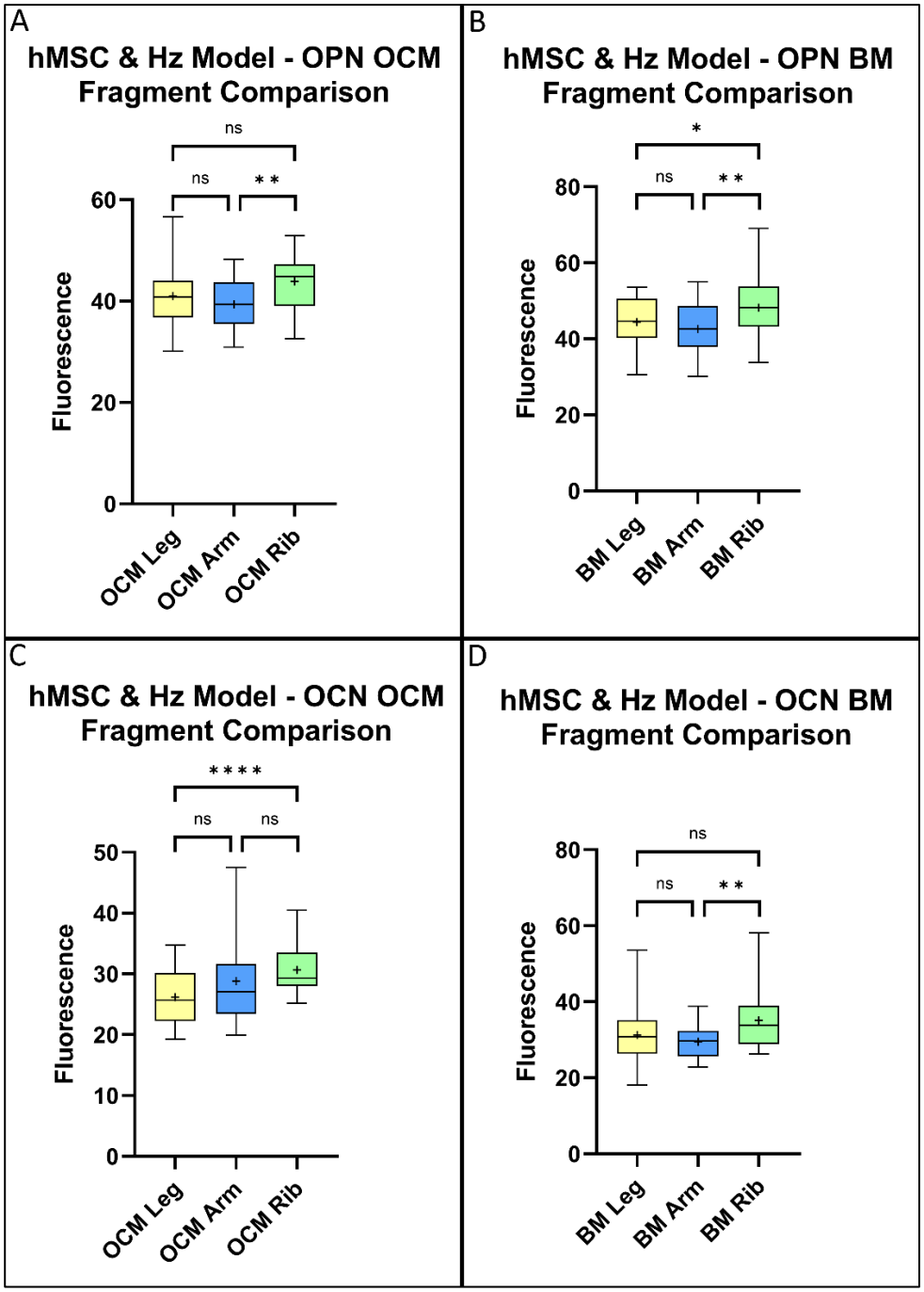

Figure 3.27: Expression of OPN & OCN in Model 2, hMSC & Hz on bone with osteogenic media - fragment comparison

Box plots comparing bone types for the hMSC grown on bone on a Nanokick device imparting a constant 100Hz frequency model for the proteins osteopontin (OPN) (A & B) and osteocalcin (OCN) (C & D) after 28 days of incubation. Plots separately compare fragments with osteogenic media (OCM) (A & C) to fragments without in basal media (BM) (B & D). The box bounds the interquartile ranges divided by the median, a "+" showing the mean and with whiskers from minimum to maximum. Data shown is from three biological and ten technical repeats with ****P≤0.0001, **P≤0.01, *P≤0.05 & ^{ns}P>0.05 calculated using the unpaired t-test.

Figure 3.27 displays the variation in OPN and OCN fluorescence between the different bone types. Graph (A) shows that for OPN and OCM samples: there was no significant difference between leg and arm fragments, and leg and rib fragments. There was a very significant difference between arm and rib fragments with rib samples producing a greater amount of OPN. For the BM samples (B), again there was no significant difference between leg and arm fragments, however, rib fragments were significantly higher than leg. Once more, there was a very significant difference between arm and rib fragments following the same pattern. For the OCN fluorescence, graph (C) shows for OCM samples, there was no significant difference between leg and arm fragments and arm and rib fragments, but an extremely significant difference between leg and rib fragments. Finally, for the BM samples the only significant difference was between arm and rib samples with rib being greater.

3.2.4.3 Model 3

The addition of HOS cells into the model produced a number of noticeable changes. By the end of the 28 day incubation period, the cells had produced a great deal of ECM with a thickness approximated to 1-2mm resulting in some regions to detach from the dish plastic. The extra ECM can be seen in Figure 3.28 as a general lower 'cloudiness' in all micrographs as well as a higher number of cells in all samples most easily visible in nuclear stain images.

A comparison of OCM with BM samples largely reverted back to OCM fragment samples being higher and extremely significant (Figure 3.28). The only exception was OCN arm fragments, which had no significant difference. The monolayer controls however were different in the BM samples having higher fluorescence in both OPN being significant and OCN being extremely significant.

The comparison of fragment samples against controls were largely consistent for Model 3 (Figure 3.30). All samples are significantly higher than both controls except for two samples of BM fragments. As seen in micrograph (D) looking at OCN levels, the rib fragments had no

significant difference from the OCM control and leg samples had no significant difference from the BM control.

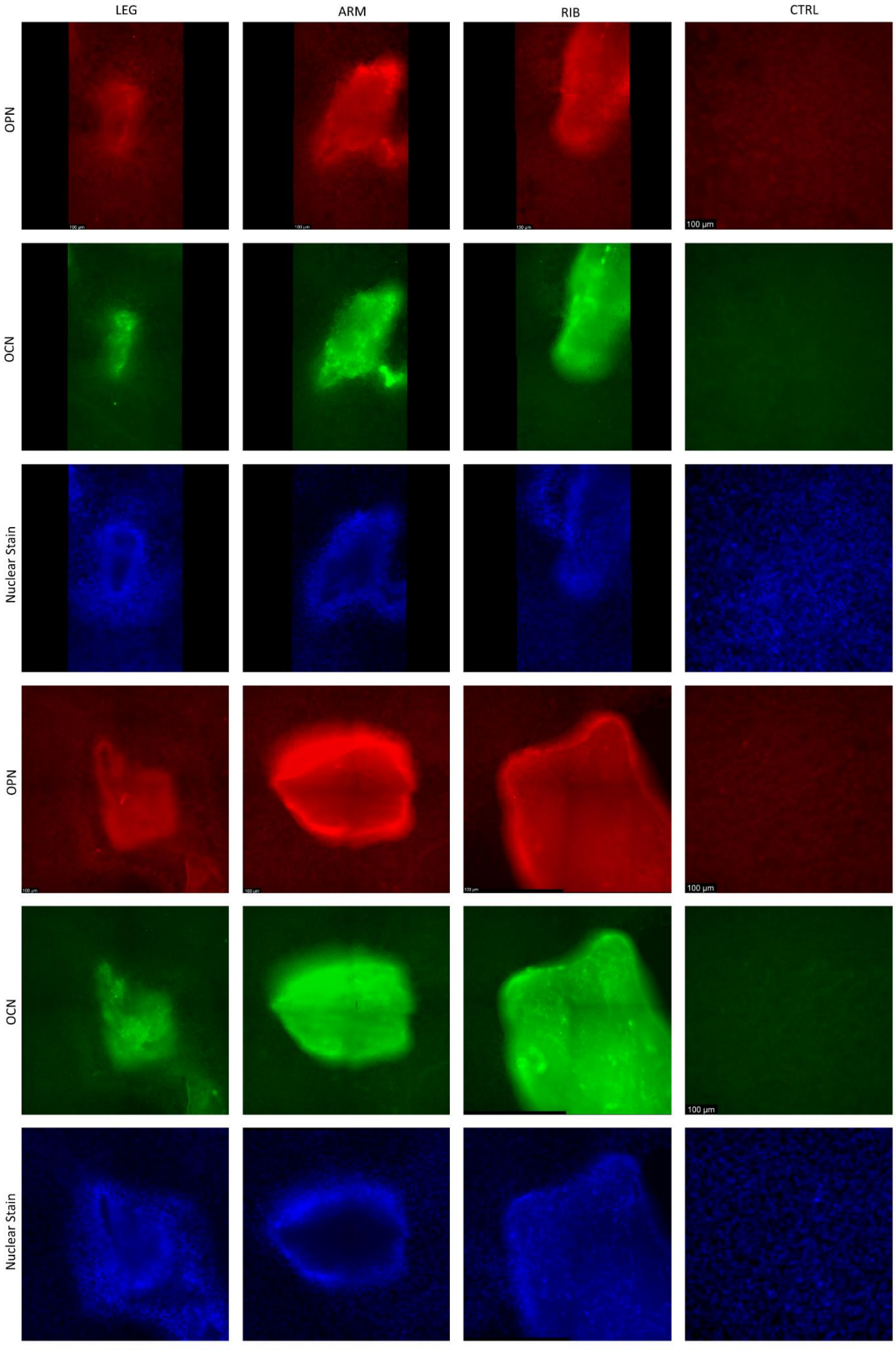
LEG
ARM
RIB
CTRL
OPN
OCN
Nuclear Stain
OPN
OCN
Nuclear Stain
OCM
OCM
OCM
BM
BM
BM
100 µm
100 µm

Figure 3.28: Macroscopic model, Model 3, hMSC, HOS & Hz on bone with osteogenic media

Representative micrographs from Immunohistochemical staining of Model 3, hMSC and HOS seeded onto bone fragments after 28 days incubation on the Nanokick device. The four columns from left to right are of leg fragments, arm fragments, rib fragments and a monolayer control (Ctrl). Of the six rows, the top three are samples which were incubated in osteogenic media (OCM) and the bottom three incubated in basal media (BM). Each row is also either the expression of osteopontin (OPN), osteocalcin (OCN) or a nuclear stain. Scale bars are present on the OPN micrographs are representative for the lower rows of the same fragment.

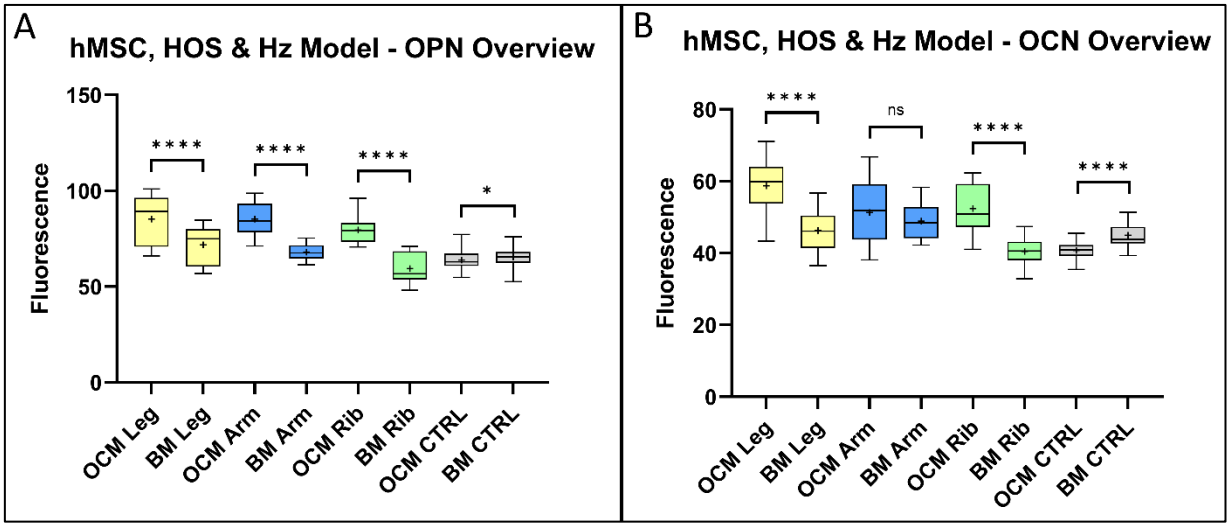

Figure 3.29: Expression of OPN & OCN in Model 3, hMSC, HOS & Hz on bone with osteogenic media

Box plots overviewing the hMSC and HOS grown on bone on a Nanokick device imparting a constant 100Hz frequency model for the proteins osteopontin (OPN) (A) and osteocalcin (OCN) (B) after 28 days of incubation. Both plots compare fragments with osteogenic media (OCM) to fragments without in basal media (BM). The box bounds the interquartile ranges divided by the median, a "+" showing the mean and with whiskers from minimum to maximum. Data shown is from three biological and ten technical repeats with ****P≤0.0001, *P≤0.05 & ^{ns}P>0.05 calculated using the unpaired t-test.

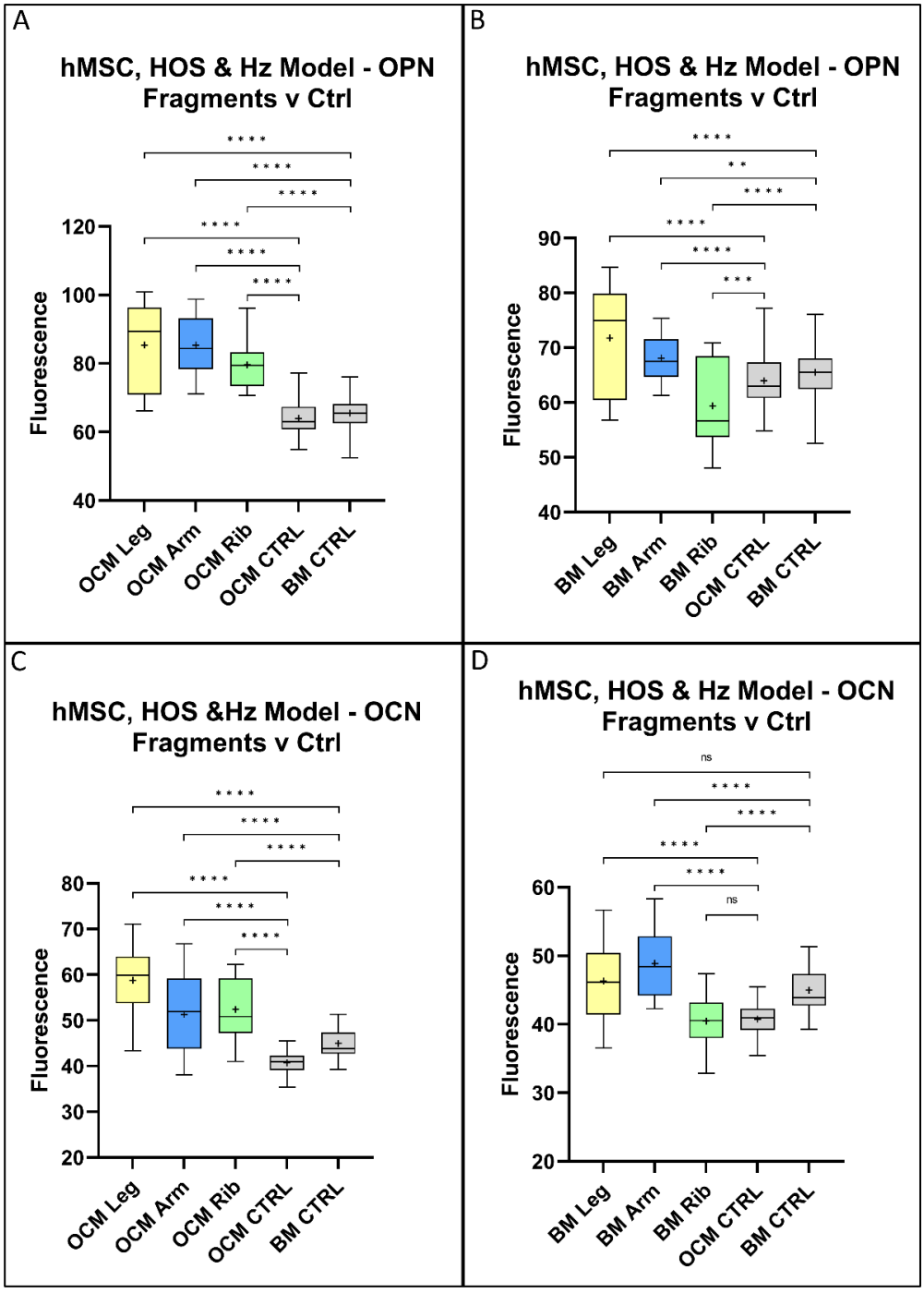

Figure 3.30: Expression of OPN & OCN in Model 3, hMSC, HOS & Hz on bone with osteogenic media - comparison to control

Box plots comparing bone types to controls for the hMSC and HOS grown on bone on a nanokick device imparting a constant 100Hz frequency model for the proteins osteopontin (OPN) (A & B) and osteocalcin (OCN) (C & D) after 28 days of incubation. Plots separately compare fragments and controls with osteogenic media (OCM) to fragments and controls without in basal media (BM). The box bounds the interquartile ranges divided by the median, a "+" showing the mean and with whiskers from minimum to maximum. Data shown is from three biological and ten technical repeats with ****P≤0.0001, ***P≤0.001, **P≤0.01 & ^{ns}P>0.05 calculated using the unpaired t-test.

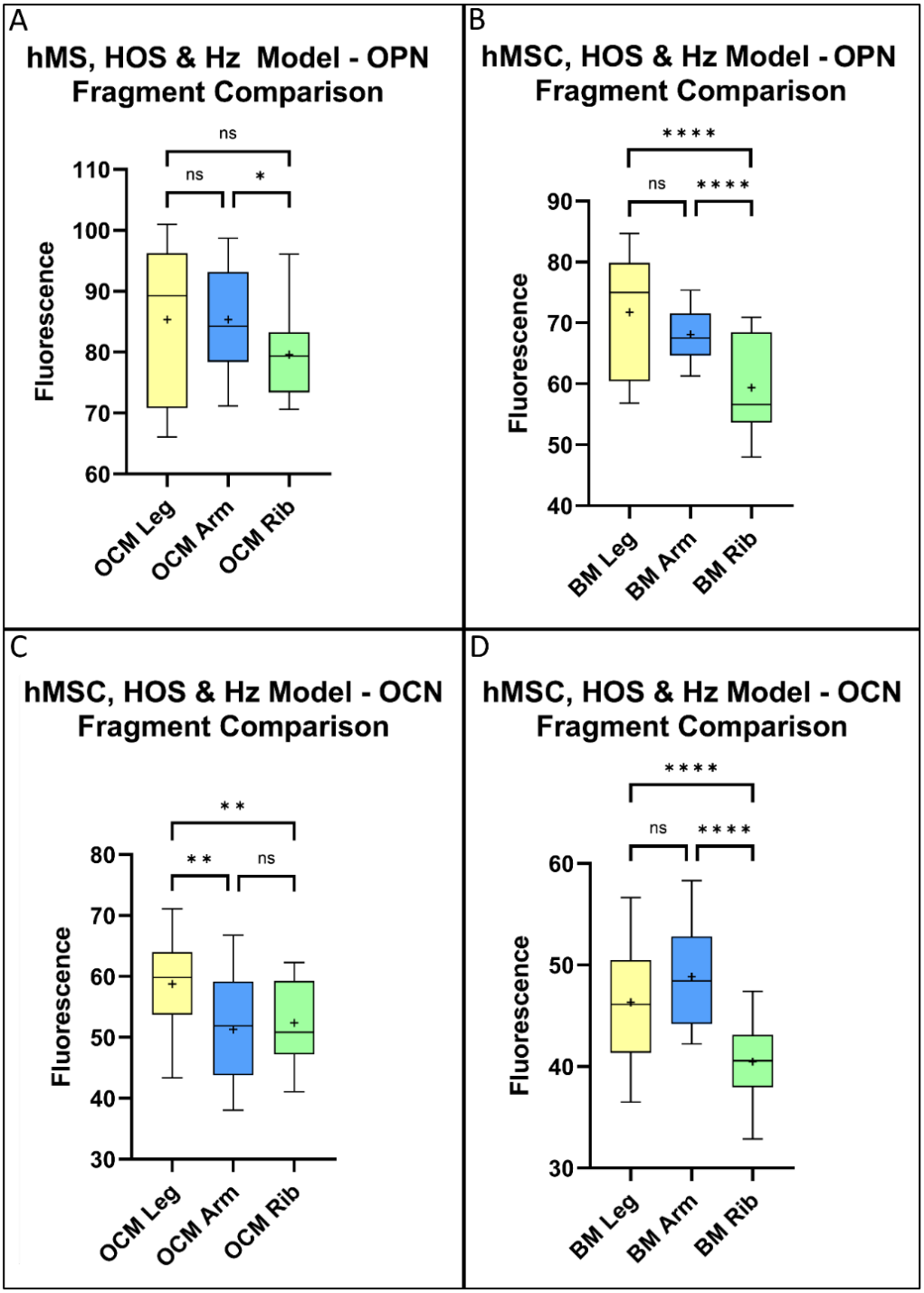

Figure 3.31: Expression of OPN & OCN in Model 3, hMSC, HOS & Hz on bone with osteogenic media - fragment comparison

Box plots comparing bone types for the hMSC and HOS grown on bone on a nanokick device imparting a constant 100Hz frequency model for the proteins osteopontin (OPN) (A & B) and osteocalcin (OCN) (C & D) after 28 days of incubation. Plots separately compare fragments with osteogenic media (OCM) (A & C) to fragments without in basal media (BM) (B & D). The box bounds the interquartile ranges divided by the median, a "+" showing the mean and with whiskers from minimum to maximum. Data shown is from three biological and ten technical repeats with ****P≤0.0001, **P≤0.01, *P≤0.05 & ^{ns}P>0.05 calculated using the unpaired t-test.

The comparison of different bone types (Figure 3.31) showed that for OPN levels, there was no significant difference for OCM samples between leg and the other two bone types, but arm fragments are significantly higher than rib. For the BM samples, there were no significant difference between leg and arm fragments, but rib fragments were lower in expression, this difference being extremely significant. For OCN levels, OCM samples showed no significant difference between rib and arm fragments, but leg fragment samples were significantly higher than the other fragments. BM samples showed no significant difference between leg and arm fragments but were significantly higher than rib fragments while arm fragments were also significantly higher than rib fragments.

3.2.4.4 Model Comparisons

Seeing the differences between the three models is vital for understanding the effects of added complexity. The sequential models were compared directly against each other like for like, for example BM control from Model 1 directly compared with BM control from Model 2 and so on.

The comparison of Model 1 to Model 2 can be seen in Figure 3.32. The leg fragments, rib fragments and controls for both OPN and OCN have matching profiles only varying in the degree of significance in one instance. For OPN fluorescence, Model 2 samples are all higher than Model 1 and extremely significant (graphs A, E & G). For OCN fluorescence, there was no significant difference between the OCM samples of leg, rib and control but a significant difference between BM samples with Model 2 having higher levels of fluorescence (graphs B, F & H). For leg fragments this difference was significant but for rib and controls it was extremely significant. Looking at arm fragments, the profiles are identical for OPN and OCN with Model 1 OCM fragments being extremely significantly higher than Model 2 but for BM samples this is reversed with Model 2 being extremely significantly higher (graphs C & D).

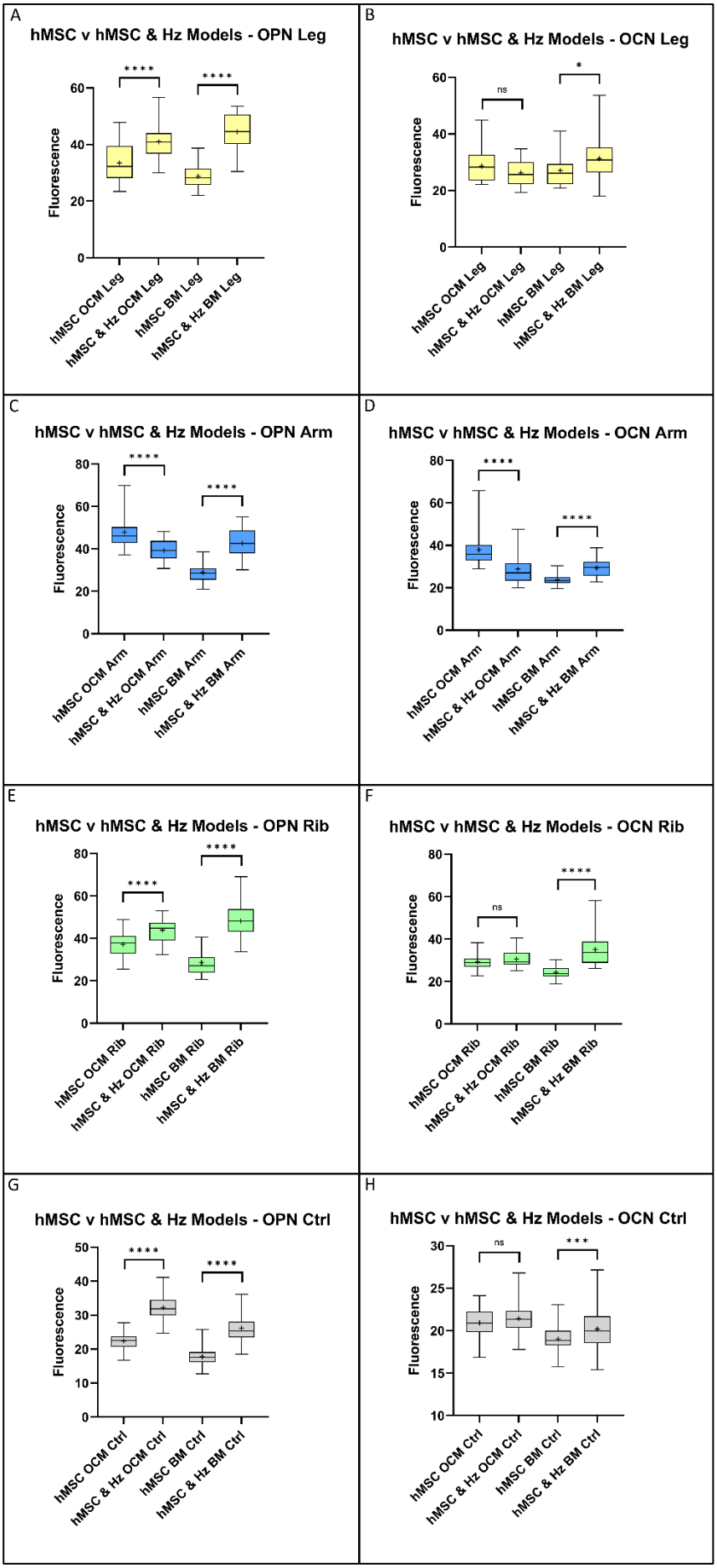
A
hMSC v hMSC & Hz Models - OPN Leg
Fluorescence
****
****
hMSC OCM Leg
hMSC & Hz OCM Leg
hMSC BM Leg
hMSC & Hz BM Leg
B
hMSC v hMSC & Hz Models - OCN Leg
Fluorescence
ns
*
hMSC OCM Leg
hMSC & Hz OCM Leg
hMSC BM Leg
hMSC & Hz BM Leg
C
hMSC v hMSC & Hz Models - OPN Arm
Fluorescence
****
****
hMSC OCM Arm
hMSC & Hz OCM Arm
hMSC BM Arm
hMSC & Hz BM Arm
D
hMSC v hMSC & Hz Models - OCN Arm
Fluorescence
****
****
hMSC OCM Arm
hMSC & Hz OCM Arm
hMSC BM Arm
hMSC & Hz BM Arm
E
hMSC v hMSC & Hz Models - OPN Rib
Fluorescence
****
****
hMSC OCM Rib
hMSC & Hz OCM Rib
hMSC BM Rib
hMSC & Hz BM Rib
F
hMSC v hMSC & Hz Models - OCN Rib
Fluorescence
ns
****
hMSC OCM Rib
hMSC & Hz OCM Rib
hMSC BM Rib
hMSC & Hz BM Rib
G
hMSC v hMSC & Hz Models - OPN Ctrl
Fluorescence
****
****
hMSC OCM Ctrl
hMSC & Hz OCM Ctrl
hMSC BM Ctrl
hMSC & Hz BM Ctrl
H
hMSC v hMSC & Hz Models - OCN Ctrl
Fluorescence
ns
***
hMSC OCM Ctrl
hMSC & Hz OCM Ctrl
hMSC BM Ctrl
hMSC & Hz BM Ctrl

Figure 3.32: Expression of OPN & OCN comparing Model 1 to 2 - hMSC on bone with osteogenic media to hMSC & Hz on bone with osteogenic media for each fragment type and control

Box plots comparing Model 1 to Model 2. Plots separately compare fragments with osteogenic media (OCM) and fragments without in basal media (BM) for leg fragments (A & B), arm fragments (C & D), rib fragments (E & F) and controls (G & H) of osteopontin (OPN) and osteocalcin (OCN) separately. The box bounds the interquartile ranges divided by the median, a "+" showing the mean and with whiskers from minimum to maximum. Data shown is from three biological and ten technical repeats with ****P≤0.0001, ***P≤0.001, **P≤0.01, *P≤0.05 & ^{ns}P>0.05 calculated using the unpaired t-test.

The comparison of Models 2 to 3 (Figure 3.33) is quite simple due to the high levels of OPN and OCN in the latter models in all samples. All but one sample sees Model 3 being extremely significantly higher which equates to a P value <0.0001. The only sample without this particularly high degree of significance is seen in graph (F), OCN rib fragments, with Model 3 being higher than Model 2 and very significant with a P value of 0.0019.

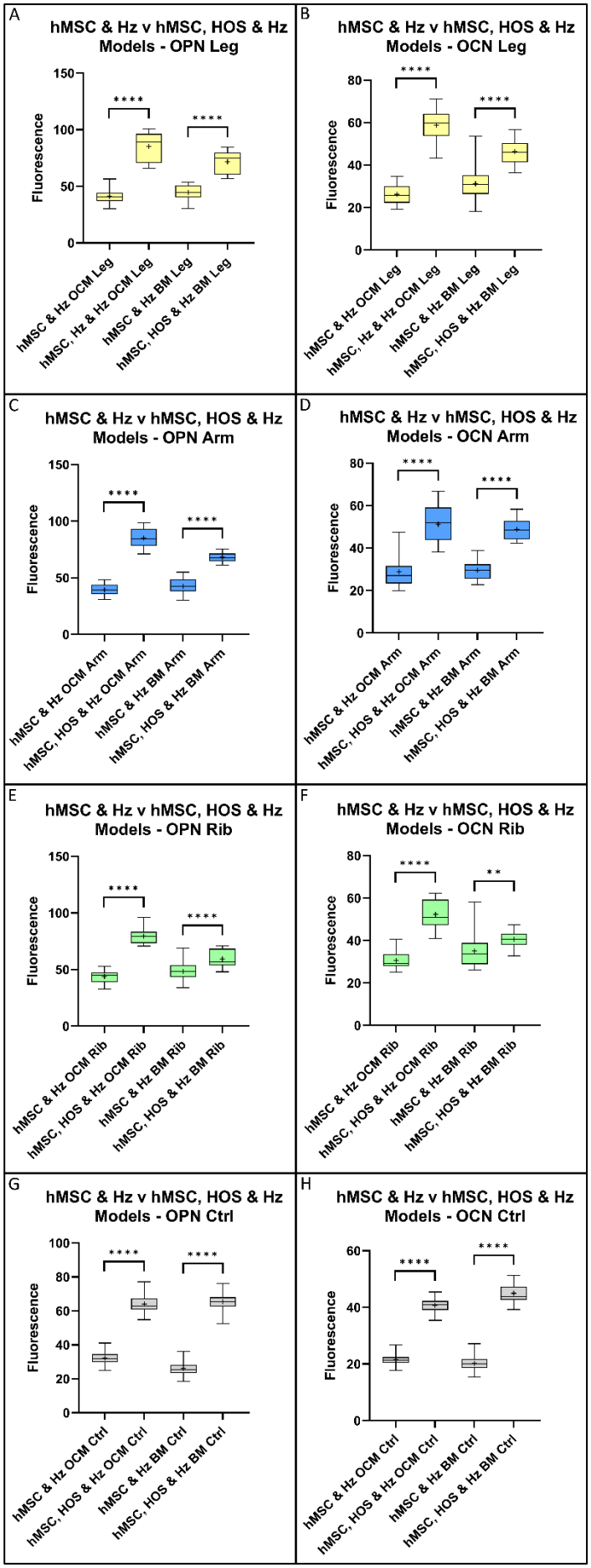
A
hMSC & Hz v hMSC, HOS & Hz Models - OPN Leg
Fluorescence
150
100
50
0
****
****
hMSC & Hz OCM Leg
hMSC, Hz & Hz OCM Leg
hMSC & Hz BM Leg
hMSC, HOS & Hz BM Leg
B
hMSC & Hz v hMSC, HOS & Hz Models - OCN Leg
Fluorescence
80
60
40
20
0
****
****
hMSC & Hz OCM Leg
hMSC, Hz & Hz OCM Leg
hMSC & Hz BM Leg
hMSC, HOS & Hz BM Leg
C
hMSC & Hz v hMSC, HOS & Hz Models - OPN Arm
Fluorescence
150
100
50
0
****
****
hMSC & Hz OCM Arm
hMSC, HOS & Hz OCM Arm
hMSC & Hz BM Arm
hMSC, HOS & Hz BM Arm
D
hMSC & Hz v hMSC, HOS & Hz Models - OCN Arm
Fluorescence
80
60
40
20
0
****
****
hMSC & Hz OCM Arm
hMSC, HOS & Hz OCM Arm
hMSC & Hz BM Arm
hMSC, HOS & Hz BM Arm
E
hMSC & Hz v hMSC, HOS & Hz Models - OPN Rib
Fluorescence
150
100
50
0
****
****
hMSC & Hz OCM Rib
hMSC, HOS & Hz OCM Rib
hMSC & Hz BM Rib
hMSC, HOS & Hz BM Rib
F
hMSC & Hz v hMSC, HOS & Hz Models - OCN Rib
Fluorescence
80
60
40
20
0
****
**
hMSC & Hz OCM Rib
hMSC, HOS & Hz OCM Rib
hMSC & Hz BM Rib
hMSC, HOS & Hz BM Rib
G
hMSC & Hz v hMSC, HOS & Hz Models - OPN Ctrl
Fluorescence
100
80
60
40
20
0
****
****
hMSC & Hz OCM Ctrl
hMSC, HOS & Hz OCM Ctrl
hMSC & Hz BM Ctrl
hMSC, HOS & Hz BM Ctrl
H
hMSC & Hz v hMSC, HOS & Hz Models - OCN Ctrl
Fluorescence
60
40
20
0
****
****
hMSC & Hz OCM Ctrl
hMSC, HOS & Hz OCM Ctrl
hMSC & Hz BM Ctrl
hMSC, HOS & Hz BM Ctrl

Figure 3.33: Expression of OPN & OCN comparing Model 2 to 3 - hMSC & Hz on bone with osteogenic media to hMSC, HOS & Hz on bone with osteogenic media for each fragment type and control

Box plots comparing Model 2 to Model 3. Plots separately compare fragments with osteogenic media (OCM) and fragments without in basal media (BM) for leg fragments (A & B), arm fragments (C & D), rib fragments (E & F) and controls (G & H) of osteopontin (OPN) and osteocalcin (OCN) separately. The box bounds the interquartile ranges divided by the median, a "+" showing the mean and with whiskers from minimum to maximum. Data shown is from three biological and ten technical repeats with ****P≤0.0001, ***P≤0.001, **P≤0.01, *P≤0.05 & ^{ns}P>0.05 calculated using the unpaired t-test.

3.2.5 Final model RT-qPCR

Having quantified the levels of OPN and OCN in the three different models, it was decided to try and quantify the level of gene expression for these proteins for the final model (Figure 3.34). For the purpose of RT-qPCR, OPN is known as secreted phosphoprotein 1 (*SPP1*) and OCN bone gamma-carboxyglutamic acid-containing protein (*BGLAP*). *RUNX2* was also investigated due to its important role as a master regulator of osteoblast differentiation and bone formation.

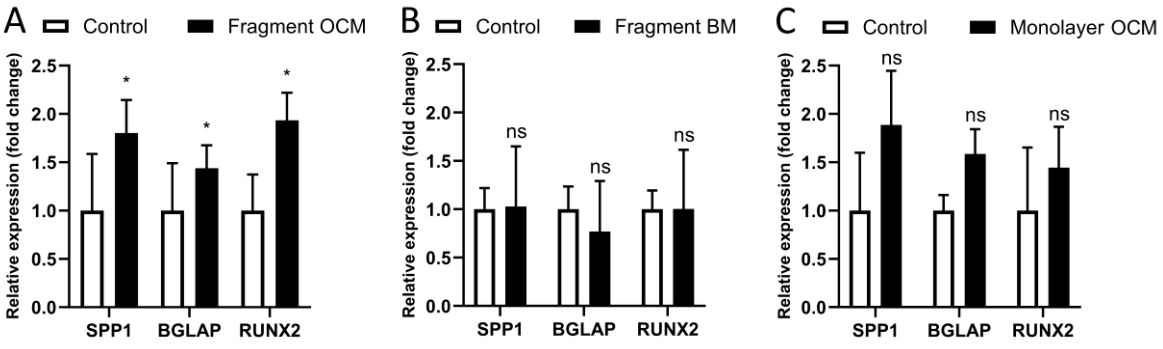

Figure 3.34: RT-qPCR of Model 3 for SPP1, BGLAP & RUNX2

hMSC and HOS were grown on bone fragments with and without osteogenic media (OCM) on a Nanokick device for 28 days prior to RT-qPCR analysis and collated. The data was split by groups; (A) incubated in OCM, (B) in basal media (BM) and (C) the monolayer control in OCM. Targeted genes were *SPP1*, *BGLAP* and *RUNX2* with *GAPDH* used as the housekeeper gene. Data is presented as mean ± SEM values (calculated from Ct mean) from three independent experiments. Data shown is from three biological and two technical repeats with *P≤0.05 & ^{ns}P>0.05 calculated using the Student's t-test.

A significant upregulation of the three genes was seen in samples grown on bone fragments as seen in graph (A). Graph (B) shows that there was no upregulation of the three genes with no significant difference compared with the control group. In graph (C) despite there being a degree of upregulation present across the three genes, the degree of this upregulation was not significant.

Figure 3.34 was generated using all bone fragments, leg, arm and rib data collated for each gene. Figure 3.35 keeps the fragment data separate for a more in-depth assessment. For samples cultured in OCM (graph A), all leg bone samples were significantly upregulated, *SPP1* and *BGLAP* were upregulated for arm samples and only RUX2 upregulated for rib samples. For samples cultured in BM (graph B), most samples saw no significant upregulation, but leg *RUNX2* and rib *BGLAP* were significantly downregulated.

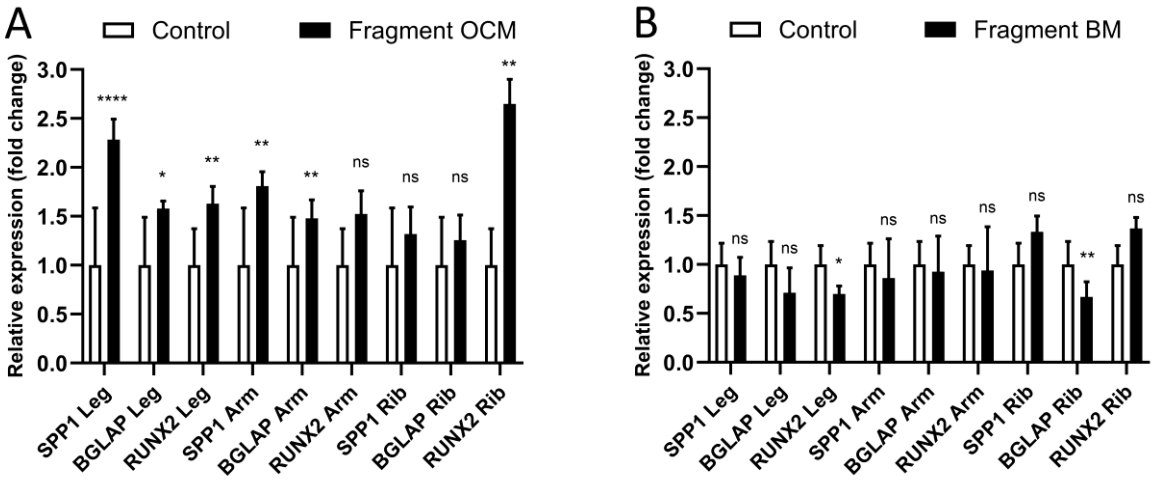

Figure 3.35: RT-qPCR of Model 3, separated fragments for SPP1, BGLAP & RUNX2

hMSC and HOS were grown on bone fragments with and without osteogenic media (OCM) on a Nanokick device for 28 days prior to RT-qPCR analysis and separated by fragment type. The data was split by groups; (A) incubated in OCM and (B) incubated in basal media (BM). Targeted genes were *SPP1*, *BGLAP* and *RUNX2* with *GAPDH* used as the housekeeper gene. Data is presented as mean ± SEM values (calculated from Ct mean) from three independent experiments. Data shown is from three biological and two technical repeats with ****P≤0.0001, **P≤0.01, *P≤0.05 & ^{ns}P>0.05 calculated using the Student's t-test.

3.3 Discussion

When discussing the macroscopic model, it is important to keep the original aim in mind: the generation of a model of the bone marrow stem cell niche at the macroscopic level. A full understanding of the niche has not yet been achieved, it being a complex microenvironment maintaining both blood cells and bone tissue through remodelling and repair. Many of the interactions between cellular elements, the physical environments and chemicals are not fully understood and most research focuses on the HSC population within the niche (Pereira et al., 2024).

This project focused on the interaction of bone cells with ECM and other factors introduced into the model, ultimately assessing the impact on cell differentiation and osteogenesis. By building on the fundamentals of the niche, models were created which ultimately can be used to understand the interactions occurring better, as well as to generate some interesting data into the importance of bone ECM and the impact of mechanotransduction.

The following section is broken up into discussions on the data generated in the development of the models, data collected from the models, and the suitability of said models as an effective analogue for the bone marrow stem cell niche.

3.3.1 Model Development Data

One of the first questions considered when developing the niche model was, “what are important considerations for a good scaffold?”. It should contain suitable biomechanical and chemical properties to support cell attachment, cell proliferation and ultimately, cell differentiation. It needs to be porous to allow nutrient exchange and should also be customisable to match the needs of the specific experiment.

3.3.1.1 Collagen

Use of collagen as a hydrogel in cell culture is broad, with it being used both in a pure form and modulated with additives. Osteoblasts (comparable to HOS cells used in our research)

show enhanced adhesion on collagen gels (Rodrigues et al., 2003) and the scaffold can be augmented with additives, changing its mechanical properties. These include crosslinking agents such as glutaraldehyde and OPC or fillers like hydroxyapatite which increase stiffness (Glowacki & Mizuno, 2008). Collagen also makes up the majority of the organic component of bone. These reasons led to collagen being chosen for early experiments in the development of the niche model.

These experiments only reached the testing of collagen concentration (Figure 3.2), collagen thickness, and the effect of collagen as a scaffold on OPN and OCN levels compared to tissue culture plastic when using osteogenic media (Figure 3.3). Qualitative analysis of the latter figure shows greater degree of OPN and OCN in the collagen samples suggesting it aids HOS osteogenesis. The early experiments were suggestive of collagen being a suitable scaffold for the model, however, a number of issues presented during this time and subsequently. A high concentration collagen was tested but was so viscous it was deemed unsuitable for purpose. The collagen would also often tear, and at worst, not form as shown in Figure 3.4.

These issues, along with unavailability due to covid-19 and minimal progress with the manipulation of collagen mechanical properties, resulted in rethinking the scaffold material. The use of a more complex scaffold was considered during the collagen testing, and with the difficulties encountered, testing was undertaken into the use of bone as a scaffold. Bone was chosen as it retains the natural ECM composition when decellularized, offering a more physiologically relevant environment for the cells and providing the complex microstructure impossible to recreate with other scaffolds. It is mechanical properties also better mimic the natural properties of bone when compared to collagen based scaffolds, including mechanical strength and stiffness.

3.3.1.2 Nanokick

It is well-established that mechanical stimulation plays a significant role in bone homeostasis, with studies having demonstrated its ability to enhance osteogenesis in vitro (Mauney et al.,

2004). If mechanical stimulation can be introduced *in vitro*, it has the potential to increase both the rate of proliferation and osteogenesis induction (Childs et al., 2016).

The Nanokick platform is a relatively new technology, enabling the stimulation of cells via nanoscale sinusoidal vibrations, creating cyclic compressive forces on cells and having demonstrated the ability to induce the differentiation of MSCs towards the osteoblast lineage (Pemberton et al., 2015; Robertson et al., 2018b). Another important consideration is the ability to place standard culture plates on the Nanokick platform. No specific plasticware or equipment is required, other than the devise, which makes it a lot cheaper than other systems such as the Flexcell® system which is widely used in mechanical stimulation research (Matheson et al., 2006). Flexcell® require the use of very expensive, bespoke culture dishes and as a result is limited to purely 2D cell culture. The Nanokick on the other hand is compatible with both 2D and 3D cell culture without the need to purchase culture dishes specifically for the device (Robertson et al., 2018b).

The Nanokick is also a very space efficient system, taking up minimal space in a standard 185L incubator, enhancing reproducibility and scalability all while presenting an aseptic method to mechanically stimulate cells. A number of the important considerations when choosing a mechanical stimulation generator have been summarised in Table 2 below comparing the Nanokick to the Flexcell® system.

Table 2: Mechanical Stimulation, Nanokick vs Flexcell®
A comparison of various in-vitro cell culture considerations between the Nanokick and Flexcell® systems.

Feature	**Nanokick System**	**Flexcell® System**
Mechanism of Force	- Nanoscale sinusoidal vibrations via piezo actuators - Nano-level precision	- Vacuum-induced membrane deformation (macro-scale). - Macro-level mechanical strain
Stimulation Type	- Oscillatory vibration focused on nanoscale displacements	- Cyclic or static tensile/compressive strain
Target Cells	-Primarily mesenchymal stem cells (MSCs) and osteogenic differentiation	- Broad range, including endothelial cells, osteoblasts, fibroblasts
Spatial Application	- Vibrations delivered uniformly across culture wells or scaffolds - Compatible with both 2D and 3D culture systems	- Force applied across the flexible culture surface via positive air pressure for compressive systems - Limited to 2D cell culture on membranes
Applications	- Focused on osteogenesis and biofilm disruption, with potential for wider applications	- Studies in wide range of mechanobiology, tissue engineering, wound healing
Precision	- High precision with nanoscale displacement and frequency tuning	- Coarser mechanical control
Throughput	- Scalable for larger volumes in bioreactors	- Moderate requiring customized plates

The niche model will have a high degree of structural variability and contraction/expansion of the underlying culture surface would destroy this model, whereas the nano-vibrations from the Nanokick are far less likely to do damage the model. While both systems offer valuable tools for mechanotransduction research, they operate on different scales and it is clear why the Nanokick system was ideal for this research, particularly given its prior use researching primary osteogenesis with MSCs and compatibility with 3D cultures.

The Nanokick platform was used to stimulate CGR8 cells at 1000Hz to determine whether the use of this equipment would be suitable for our model development. It is important to note that CGR8, a mouse embryonic stem cell line, was used over hMSCs for these initial

experiments. CGR8 cells are cheap and easy to grow, allowing the generation of high cell numbers ideal for optimisation. hMSCs in comparison are expensive and have a limited usage (only at passage 5) and availability. They are also pluripotent cells suitable for large batch experiments providing consistency and are better able to be used in 3D culture.

CGR8 were grown on and off the Nanokick platform, with and without OCM at days seven, fourteen and twenty-one. The cells were collected and analysed via RT-qPCR, as shown in Figure 3.5, with the expression of *SP7*, *ALPL* and *RUNX2* assessed. *SP7*, also known as osterix, is a transcription factor that is specific to osteoblasts which activates a set of genes that are involved in the differentiation of pre-osteoblasts into mature osteoblasts and osteocytes (Sinha & Zhou, 2013). *ALPL* functions to increase the concentration of inorganic phosphate, which promotes mineralization, and decrease the concentration of extracellular pyrophosphate, which inhibits mineral formation (Golub & Boesze-Battaglia, 2007). *RUNX2* as detailed in Chapter 1 (section 1.1.5.2, page 8) is an important transcription factor in osteoblast differentiation, involved during multiple stages from MSC to osteoblast.

SP7 and *RUNX2* were upregulated in all samples, but only significantly in a handful: For Figure 3.5, page 93, in graphs (A), (F), (G) and (H), and (D), (H) and (I) respectively. ALPL had a low level of expression in all but one sample (relative to *SP7* and *RUNX2*), day seven OCM on the Nanokick (graph A). This is likely due to *ALPL* being produced in the initial stages of osteoblastic differentiation, located on the cell surface and in matrix vesicles, *ALPL* expression reduces where others are upregulated (Vimalraj, 2020). When rearranged, as shown in Figure 3.6, page 94, comparing the upregulation of each gene at day 7, graph (A) shows that for *SP7*, *ALPL* and *RUNX2* the highest upregulation is found for samples cultured with OCM on the Nanokick. For both *SP7* and *RUNX2*, upregulation is the second highest for samples just cultured with OCM with samples cultured with BM on the Nanokick being the lowest. This time point is most indicative of what is seen in the literature, with the combination of OCM and mechanical stimulation causing significant upregulation of osteogenesis (Kennedy et al., 2021; Malaval et al., 1994; Nikukar et al., 2013; Pemberton et al., 2015). It is clear when

directly comparing the three time points in Figure 3.6, that *ALPL* is upregulated at day 7 and is either low or down regulated at days 14 and 21, particularly in OCM samples which is to be expected as an early marker of osteogenic differentiation. *RUNX2* is expected to be upregulated at all time points, but this should be tapering off by day 21 as by week three, osteogenic differentiation is generally thought to have completed. Up regulation is however seen at all time points, but at varying degrees with and without significance, although there is a general trend of up regulation be highest in OCM samples at days 7 and 21. As with *RUNX2*, it is also expected that *SP7* would be upregulated greatest in OCM samples, and this is clearly the case at day 7, but at days 14 and 21 although in both cases wither OCM samples on or off the Nanokick are higher than BM, the other is both cases is lower than BM meaning an explicit conclusion cannot be drawn in this case. Ideally this data set would be repeated and the number of biological repeats increased to account for the sensitive nature of RT-qPCR.

Despite the nature of this data, average relative expression for *SP7* and *RUNX2* were often higher in samples incubated on the Nanokick compared with OCM samples off the device. There was also a clear upregulation in samples on the Nanokick grown with BM compared with the controls, suggesting the mechanical stimulation was having an effect. Due to the nature of this data, containing large upregulation but no significance in many cases due to a large range in fold change, it would be improper to infer any specific links between a given gene's expression and time. If this work were to be repeated, an increase in repeats would be highly beneficial to determine significance. This experiment was, however, sufficient to set the groundwork to include the Nanokick in the final niche model design as there was evidence, albeit inconsistent, that the mechanical stimulation upregulated genes important in MSC differentiation and osteogenesis.

3.3.1.3 HOS & hMSC Co-culture

In the bone marrow stem cell niche, there are multiple different cell types present: MSCs, HSCs, osteoblasts and osteoclasts to name a few (Asada et al., 2017). For the final version of

the models developed (Model 3), it was important to ensure that the bone cells being focused on, HOS and hMSC, would grow in co-culture. The two cells were grown in co-culture with a 1:1 ratio of cells using the basal hMSC media (MSCGM). The cells were tracked over a two day period, as shown in Figure 3.12, using separate cell trackers with difference absorbances. Over this time frame, the two cell types were found to grow well together: both cell types proliferated, being dispersed amongst each other with the occasional cluster of hMSCs forming. The success in co-culturing HOS and hMSC on standard tissue culture plastic allowed for the progression to culturing HOS and hMSC together on decellularised bone as seen in Model 3. All repeats can be found in the Appendix, Figure 6.3 to Figure 6.6.

3.3.1.4 Growing Cells on Decellularised Bone Fragments

As previously mentioned, the consideration of moving from collagen to bone as a scaffold for the niche model was partially due to non-availability of collagen and partially due to it not providing the support medium needed for the aims of this project. Beyond these issues, the prospect of using bone had a number of potential advantages. It has been well documented that cells will change in phenotype and migratory velocity as a response to the physical properties of their ECM, such as stiffness and topology (Charras & Sahai, 2014). It is not currently possible to build a collagen scaffold to match the varying properties of bone. It was therefore considered, instead of building up in complexity from collagen, bone as a scaffold could provide much of the natural physical environment bone cells experience *in vivo*. This includes organic and inorganic components including collagen types I, III and V, glycoproteins and hydroxyapatite (Lin et al., 2020).

The development of a suitable technique to seed HOS cells onto bone was accessed using a cell tracker as shown in Figure 3.11, where successful cell adhesion can be seen. In order to assess cell growth on decellularised bone fragments further, SEM micrographs were taken of bone with and without cells. Figure 3.14, Figure 3.15 and Figure 3.16 show cell growth on cortical, cancellous and rib bone respectively compared to just the bone. In all samples, cells were found to have grown on the fragments, however, they were found to have grown at

different rates (assessed qualitatively) and present different morphologies. Based on the micrographs taken, it was believed that the different figures represent varying degrees of cell proliferation and ECM generation. In Figure 3.14 and Figure 3.17, cells with rounded morphology sparsely distributed across the bone surface show individual or small groups of cells primarily found on cortical bone pieces. Cells with the same morphology suggest a low proliferation and possibly low adherence rate for this type of bone with HOS. This is supported by osteoblasts natively being found near/in the bone marrow and bone surface, not in the cortical bone where osteocytes would be found (Capulli et al., 2014). Figure 3.15 and Figure 3.19 show what is believed to be collagen fibres, generated by the HOS as part of the ECM. The fibres fit the general shape and size of collagen imaged using SEM in the literature (Finlay et al., 1996; Santi et al., 2016). The fibres form heterogeneous patterns, often taking the form of repeating spirals. The generation of collagen would suggest the cells have proliferated well and are on a scaffold which facilitates the production of ECM and under the right conditions, mineralisation of the collagen. In Figure 3.18 a smooth layer on top of the bone surface was found. It is believed that this is the continuation of the generation of ECM, as in Figure 3.16 B, this smooth layer (left of image) seems to be above the fibre layer (right of image) suggesting a progression for fibres to smooth material.

Rounded cells were only found on cortical bone with some regions of fibres. The fibres were found mostly on cancellous pieces with some regions of smooth material. Fibres and smooth material were found in equal amounts on rib fragments. This suggests that HOS attached and proliferated very well on cancellous and rib fragments, potentially best on rib, demonstrating the production of matrix proteins, supporting the assumption that there is ECM synthesis occurring. These findings provided enough evidence for continuing with decellularised bone as a scaffold for the niche model above collagen.

3.3.2 Decellularization Efficacy

Having seen the decellularized bone fragments through SEM, the micrographs showed qualitatively an absence of cells, as there were no discernible cells present in any of the micrographs on any fragment. It was, however, important to verify that cells were not present. This was done by imaging decellularized bone fragments after incubating them in Hoechst solution, a nuclear stain as seen in section 3.2.3.3, page 97. Hoechst solution binds strongly to the minor groove of A-T rich regions of DNA, resulting in significant fluorescence and the clear visualisation of cell nuclei when viewed under a fluorescent microscope (Kubista et al., 1987). Due to this strong interaction, Hoechst solution is widely used in research as a nuclear stain in numerous biological samples (both fixed and live), making it ideal to identify the presence of any remaining cells on the bone fragments having performed the decellularization protocol (Kapuscinski, 1995). As seen in Figure 3.10, page 99, there are no discernible cells on the bone surface. If present, cells would have clear circular nuclei as can be seen in Figure 3.9, page 97 for reference. The lack of cells visible under SEM or via nuclear staining suggests that the protocol is indeed suitable as a method of decellularizing rat bone.

An important consideration of this methodology is that even if some cells did indeed survive the employed decellularization process, the subsequent snap freezing in liquid nitrogen and storage at -20^{o}C, would result in the death of any remaining cells. As the output of the models was the identification of OPN and OCN levels, any hypothetical dead cells would have no impact on the data in this regard.

If we were generating an implantable scaffold, more evaluative work, and probably additional decellularization stages would have been required, however, the project does not focus on the generation of a new decellularized scaffold but for this project, a biocompatible scaffold was needed. The consideration here is what level of decellularization work was required for this project. More time and resources could have spent on this stage, however, it was determined that this level of detail was not required for proof-of-concept research at this

stage. As this research moves forward, more detailed analysis of the cellular residue would be required and based on that, potentially more optimisation of the decellularization process.

3.3.3 Co-culture on Bone

Despite their advantages, 3D co-culture systems come with several limitations. One of the primary challenges is the technical complexity involved in creating and maintaining 3D cultures. Scaffold-based models require precise fabrication techniques to ensure uniform porosity and mechanical integrity, which can be difficult to control (Langhans, 2018). Furthermore, nutrient and oxygen diffusion is often less efficient in 3D models, particularly in larger constructs, which may lead to hypoxia or necrosis in the centre of the scaffold (Duval et al., 2017). However, by utilising decellularised rat bone as a scaffold, the complexities of designing a 3D co-culture system were circumvented allowing the model to as accurate to the native cellular microenvironment as possible.

Another limitation is the difficulty in analysing cellular responses within 3D cultures. Traditional techniques such as microscopy, flow cytometry, and Western blotting are not easily adaptable to 3D systems due to the opacity of scaffolds or the need to disrupt the 3D structure to harvest cells (Pampaloni et al., 2007). This can complicate data collection and analysis, making standardization more challenging.

This proved to be one of the greater challenges of this research project, as establishing osteogenic output when the cells were cultured on bone did not have an obvious solution. A standard method to determine osteogenic output is to record levels of the proteins OPN and OCN via IHC and subsequent fluorescent imaging. The difficulty with this model was that bone is inherently fluorescent, and as shown in Figure 3.2.3.2, page 95, highly variable across different fragments and across the surface of each individual fragment. This meant that it would not be possible to subtract background autofluorescence from micrographs recording OPN and OCN levels. Ideally, the next step would have been to standardise the bone fragments (beyond source location) in both size and composition, narrowing the range of

autofluorescence of each piece. Unfortunately, given the time and resources available, this was not a possibility.

During optimisation of the various macro models, when observing the cellular growth on bone after 28 days, it was evidently clear that the cells were proliferating very well and producing a large amount of ECM. The ECM was thick compared to cells grown on tissue culture plastic and was thickest on and around the bone fragments. Given this growth pattern, the second best option was to measure the protein values directly around each fragment from the surrounding ECM. This was then directly compared to cells grown in 2D on tissue culture plastic (section 3.2.4, page 110), being a suitable comparison as the effect of the bone as a scaffold can be directly inferred from the comparison.

3.3.4 Model Outputs

The model development experiments ultimately led to the creation of three models of increasing complexity, each building on previous one.

- Model 1 – hMSC seeded on decellularised rat bone.
- Model 2 – hMSC seeded on decellularised rat bone and mechanically stimulated.
- Model 3 – hMSC and HOS seeded on decellularised rat bone and mechanically stimulated.

All were incubated with OCM, with sample repeats also cultured in BM to see the effect of the standard osteogenic additives and monolayer controls cultured to see the effect of the bone fragments as scaffolds (as described in Chapter 2 section 2.2.4, page 66). All models also used bone from the leg, arm and rib separately to determine any difference between the site of harvest.

Analysed using IHC after twenty-eight days incubation, the proteins OPN and OCN were assessed. These particular markers were chosen as they are both produced by osteoblasts and are two of the standard markers used to detect osteogenesis. It is important to note that

the growth of hMSC and HOS on decellularised bone as a scaffold is wholly novel and therefore there is no direct comparison available in the literature.

Before covering the findings of the three models, it is worth noting that there was no obvious consistency between models in which bone type was "preferred" by the cells in each. For example, in Model 1, the leg fragments seemed to produce the greatest amount of OPN but not OCN, in Model 2 rib fragments were most successful but in Model 3 they were the worst. Further refinement of the bone sorting process will be necessary in the future as discussed in Chapter 5.

3.3.4.1 Model 1

Model 1 saw the growth of hMSCs on decellularised bone in the presence of OCM. OCM is used regularly for the differentiation and osteogenic maturation of MSCs using ascorbic acid, dexamethasone and β-glycerophosphate. With these additives, hMSCs in a monolayer develop an osteoblastic morphology, exhibiting high alkaline phosphatase activity and depositing a mineralized extracellular matrix rich in calcium (Fiorentini et al., 2011). The osteogenic effect was seen in the model controls for both OPN and OCN, where both proteins were found in the monolayer with OCM with significantly higher levels compared to the BM monolayer (Figure 3.21 A and B). This shows that both the cell line used, and the OCM fed to the cells is in keeping with what would be expected. The same was also found for all but one sample (OCN, leg, Figure 3.21 B) of cells grown on decellularised bone with OCM grown samples being significantly higher than BM grown. This suggests the OCM is having the same or at least similar effect on the samples grown on bone. This is in keeping with the use of other forms of scaffolds, such as poly lactic-co-glycolic acid (PLGA) scaffolds, where osteogenic activity is higher in samples cultured in OCM on scaffolds than those cultured in BM on scaffolds (Yang et al., 2010).

When comparing samples grown on decellularised bone compared with the monolayer controls, all were extremely significantly higher for both OPN and OCN (Figure 3.22). This

suggests the inclusion of the bone as a scaffold has a significant effect on the proliferation, differentiation and osteogenesis of the cells. This is to be expected, as providing an environment similar to the natural *in vivo* conditions would result in the hMSCs presenting with different morphology and behaving closer to how they would naturally, compared to a monolayer on tissue culture plastic (Jauković et al., 2020). This is again as expected as the culturing of cell in 3D scaffolds has been shown to improve hMSC osteogenic differentiation (Yao et al., 2017).

3.3.4.2 Model 2

The second model introduced mechanical stimulation via the Nanokick platform. Mechanical stimulation is known to enhance differentiation, osteogenesis, and mineralisation in MSCs (Ravichandran et al., 2017). By introducing mechanical stimulation, it is hoped that some of the natural mechanical stimulation experienced by MSCs in the bone marrow stem cell niche is mimicked. This model was otherwise the same as the first. As seen in model 1, OPN and OCN were significantly higher in OCM cultured controls than in BM (Figure 3.25 A and B) and all bone seeded samples were significantly higher in OPN and OCN compared to both controls to an extreme degree (Figure 3.26 A and B). When compared to Model 1, as shown in Figure 3.32, Model 2 OPN and OCN expression was significantly higher in all but three samples. Arm OCM for both OPN and OCN was significantly higher in Model 1 (graphs C and D), rib OCM for OCN were there was no significant difference between the models (graph F) and monolater OCM control of OCN were there was no significant difference between the models (graph H). Apart from three outliers, the models suggest that the mechanical stimulation of the system has a beneficial effect on osteogenesis.

As discussed in Chapter 1 (section 1.1.10, page 22), mechanical stimulation can have a profound effect on bone remodelling. The interaction between MSC and the bone matrix is key, as it is through the bone that the mechanical signals reach the cell. In short, integrins sense and respond to mechanical force between cells and ECM (Gauthier & Roca-Cusachs, 2018) while ion channels also respond to mechanical stimulation and may be involved in

mechanical signalling (N. X. Chen et al., 2000). Cells are highly influenced by their environment, in this model, it is likely that hMSCs interact with the local microenvironment, sensing the mechanical stimulation through the bone via integrin interactions, ultimately resulting in the release of osteogenic factors and the promotion of osteogenic differentiation (Sun et al., 2022).

The most interesting variance between the two models, is the difference between samples cultured in OCM versus BM. In all but one sample (OCN, arm, Figure 3.25 B), which had no significant difference between the OCM and BM, all bone samples were significantly higher in OPN and OCN in the BM cultured groups. This finding was unexpected, suggesting that the introduction of OCM somehow reduced the degree of osteogenesis when mechanical stimulation was influencing our model. It would therefore be logical to conclude that additives in OCM, ascorbic acid, dexamethasone and β-glycerophosphate could be the cause. Of the three, dexamethasone, in our estimation is most likely, as it is the only artificial factor in the media. Both β-glycerophosphate and ascorbic acid are involved in the biological process of osteogenic differentiation (Neto et al., 2011), but dexamethasone is not naturally found in the human body. It is included as part of OCM as it mediates MSC differentiation via activation of *RUNX2* expression (Langenbach & Handschel, 2013c) and is a widely established initiator of osteogenesis. It is possible that its presence downregulates the interplay between hMSCs the bone matrix and mechanical stimulation, disrupting the natural, and more effective osteogenesis.

3.3.4.3 Model 3

The third model included everything from the second model, but with the addition of HOS cells. This created a co-culture of HOS and hMSC cultured on decellularised bone on the Nanokick. This model was intended to match the bone marrow stem cell niche more closely. HOS were incubated on bone prior to hMSCs being added to the culture to imitate osteoblasts covering the bone surface and hMSCs adhering on and around them.

Compared to Model 2, Model 3 showed extremely significant upregulation in OPN and OCN in all samples as shown in Figure 3.33. In many cases the upregulation was so extreme that the average fluorescence was over double that of Model 2. This was most likely due to HOS proliferating at an extremely fast rate, producing a large quantity of ECM and promoting osteogenesis. With the addition of HOS to the model, the pattern of OCM compared to BM samples changed again from the previous model. All OCM bone fragment samples, except OCN arm which saw no significant difference, were significantly upregulated compared to BM cultured samples to an extreme degree (Figure 3.29 A and B). Strangely, for the first time, the model controls changed in the degree of upregulation, with BM cultured samples being significantly upregulated compared to OCM samples. When looking at all the fragment data grouped together as shown in Figure 3.34, significant upregulation is seen for all genes, supporting previous findings.

Trying to infer the reasoning behind these changes is very difficult due to the increased complexity and introduction of new interconnections when using a co-culture model. While the change in the monolayer controls cannot be explained, it was believed that the reversion to OCM upregulated over BM is due to the HOS cells. The Model 3 samples had very thick ECM compared to previous models as mentioned in 3.2.4.3, page 121, leading us to believe that HOS was the primary producers of OPN and OCN over hMSCs. As such, HOS can be thought of “drowning out” influence of hMSC osteogenesis, overloading the system due to their rapid proliferation. Even though only one new element had been added to the model, the number of potential interactions had increased greatly. It is difficult to evaluate the interplay between the different elements without further models and experimentation as described in Chapter 5.

For the final model, RT-qPCR was utilised to validate the findings from the fluorescence testing. Only the final model was assessed via this method due to time constraints. The genes assessed were *SPP1* which is OPN, *BGLAP* which is OCN and *RUNX2*. Compared to the original Nanokick RT-qPCR (3.2.2, page 91), *SP7* was dropped as a gene for investigation as *RUNX2*

regulates *SP7* expression early in osteoblast differentiation (Komori, 2011). *SPP1* and *BGLAP* were selected as they were the fluorescent markers used for analysis of the models. All three genes were significantly upregulated in bone grown samples cultured in OCM (Figure 3.34, graph A). This was in keeping with the findings from IHC experiments (Figure 3.30, A and C) for OPN and OCN and as expected for *RUNX2* for an increase in osteogenesis. Bone samples incubated in BM, however, were found to have no significant difference compared to the control monolayer cultured in BM (graph B). Compared to IHC data, this was predominantly not the case, with OPN and OCN being significantly higher than the controls in all but one sample (rib fragments, OCN). Gene expression did not match protein levels in the comparison of monolayers (graph C). The three genes were upregulated, but not significantly in the OCM group, but fluorescence data from the IHC showed significantly higher levels of OPN and OCN in the BM group. These findings may suggest a variance between gene expression and protein production at the 28 day time point in this model, but ultimately the same questions need to be investigated regarding the RT-qPCR data as the fluorescence data. Gene expression and protein levels are measured very differently and have their own associated errors. Importantly, IHC fluorescence values were sourced from the cells nearest (surrounding) the bone fragments, while with RT-qPCR, the whole well fragment and all cells were collected for analysis. This means that the two experiments are not a perfect like-for-like comparison. A delay between gene expression and protein synthesis and deposition should be considered. The model data was likely a consequence of cell proliferation and differentiation over time, which could have resulted in fluctuating or stable expression levels and accumulation of the protein during the 28 day period.

3.3.5 Model Suitability

Healthy bone marrow stem cell niche function is a complex interaction between cells, chemical, physical and ECM which are not understood fully. This was the reasoning behind this project, the development of an *in-vitro* model of the niche to understand it better and

ultimately use this model as a steppingstone for future model development and potential therapeutic advancements.

When assessing the models created, the most important question was “what determines whether a model is appropriate?”. Ultimately it was decided to settle on integration of the aforementioned constituents: cells, chemical, physical and ECM and detection of evidence of cell adherence, proliferation, differentiation and matrix production. The cells incorporated were hMSC and later HOS the former which differentiate into osteoblasts, and both produce osteogenic content under the right conditions. The chemical was the content of OCM which would theoretically aid in differentiation and osteogenesis. The physical was the introduction of the Nanokick to impart mechanical stimulation. The ECM was decellularised rat bone, used as a scaffold for the hMSC and HOS. All three versions of the model were found to increase the production of OPN and OCN, markers for osteogenesis to a significant degree compared to a monolayer of hMSC cultured in basal media.

With the addition of the Nanokick into the models, under the aforementioned assessment criteria, Models 2 and 3 can be considered effective models for the bone marrow stem cell niche as a foundation for further development. Although there are many important factors present in the niche, including HSCs and other bone cells (Calvi et al., 2003), these models have highlighted a number of interesting interplays. Instead of trying to mimic the natural environment with a designed scaffold, the natural environment, rat bone, was taken and incorporated it into an *in vitro* model. This brings an innate complexity to the model, likely with numerous interactions with hMSCs and HOS which need to be evaluated, but certainly result in the generation of more osteogenic product as shown in Figure 3.22. The addition of a source mechanical stimulation increased the production of osteogenic product further (Figure 3.32) but interestingly resulted in OCM having an inhibitory effect on its production (Figure 3.25) which was unexpected. With the addition of HOS to the model this inhibitory effect was seemingly lost, emphasising the complexity of the system and the need to accurately create 3D models that replicate the native biological structure, such as this model.

Rat bone is widely used in the development of *in vitro* research due to its anatomical and cellular similarities to human bone. Structurally, rat long bones share comparable cortical and cancellous regions and their bone marrow supports both haematopoietic and mesenchymal stem cell populations, making them a biologically relevant model for niche studies (Hsu et al., 2016; Matthieu et al., 2015; Oftadeh et al., 2015). There are, however, recognised interspecies differences that may influence translational applicability. For example, differences in osteonal bone occurrence (lacking in rodents), mechanical properties, and cellular composition which can affect how MSCs interact with the matrix (Koh et al., 2024).

A further limitation arises from the use of bone derived from a single rat, which introduces potential concerns related to biological variability. Inter-individual variation in age, genetic background, and metabolic status can significantly influence bone matrix composition, which in turn may affect cell behaviour. Therefore, findings derived from a single animal source, such as ours, should be cautiously interpreted, as it may not reflect broader biological trends within the animal population. The lack of biological replication at the source level may constrain the reproducibility and applicability of results, particularly in the context of accurate niche modelling. As a result, this limitation will be addressed in future work as described in Chapter 5.

The models were ultimately developed to explore biological outcomes of the niche, and with increasing complexity, came different patterns between the sample groups and more questions on the interplay between the different facets of the niche to be elucidated. The future of this model and its further development is covered in full in Chapter 5, where the necessary next steps on the model's evolution are covered along with steps to be taken further down the experimental time frame.

4. Microscopic Model of the Bone Marrow Stem Cell Niche Optimisation

Chapter 4 focuses on the development and optimization of a novel mould system integrated with our HOTs platform, aimed at enabling precise spatial patterning of two distinct cell types. This chapter ultimately addresses the challenge of recreating the highly organized cellular architecture of the bone marrow stem cell niche at a microscopic scale. The design of the mould allows the controlled placement of mesenchymal stem cells and HOS cells into specific configurations, reflecting their interactions within the native niche environment. As a developmental/optimization project, this chapter largely covers the steps in designing the mould along with some experiments displaying the remarkable functionality only available with our HOTs system. The HOTs are a bespoke and unique equipment, and we were generating a methodology from scratch which took a great deal of time and optimisation.

4.1 Results - Model Optimisation

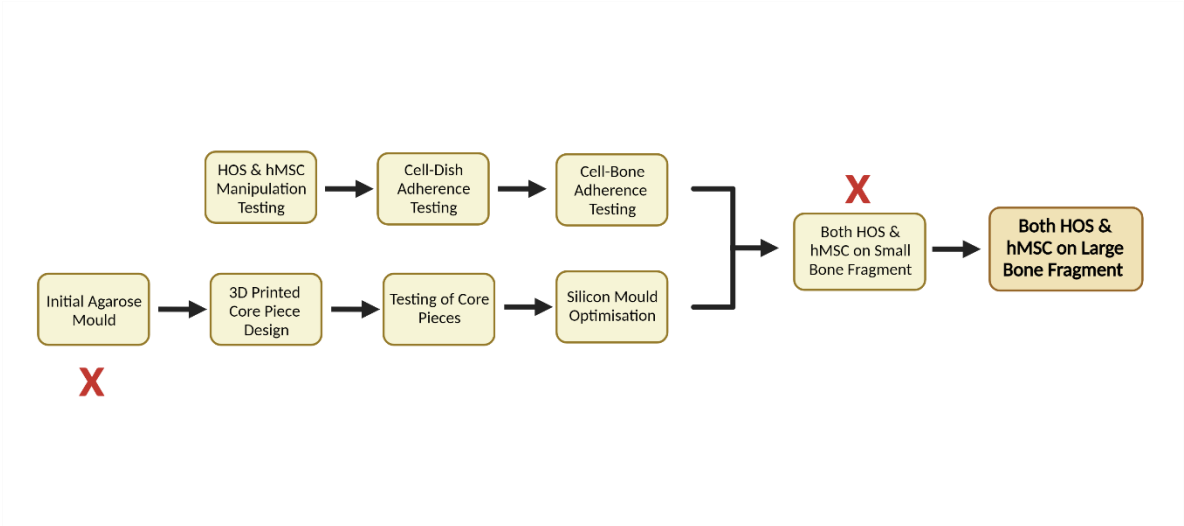

Figure 4.1: Microscopic model flow chart

Flow chart of steps in development of the bone marrow stem cell niche at a microscopic level. Arrows indicate how each experiment directly led to the subsequent experiment and the progression of the model. Red crosses indicate the decision to abandon the branch of experimentation.

In conjunction with the development of a macroscopic model of the bone marrow stem cell niche, a microscopic model was also developed. Over the course of this project, the end goal of the model was the patterning of both hMSC and HOS cells together. In standard macroscopic models, no direct control over cellular position is achievable. The ability to position single cells with a high degree of precision is currently not possible with technology other than HOTs. This technology is ideal for the creation of a microscopic model of the niche as it can position multiple microscopic objects simultaneously and accurately in 3D (Kirkham et al., 2015). The development of the model had two major hurdles that needed to be overcome: introducing two different cell types into a single model and anchoring the cells.

Early experimentation followed two paths as shown in Figure 4.1: testing of the manipulability of the two cell types used in the macroscopic model and the designing a way to introduce the cells to the system independently. Concerning the former, the HOTs system was found to be able to manipulate both HOS and hMSC with relative ease. Both cell types could be captured reliably in a trap and positioned within their dish. Issues became apparent, however, after a short period of time when the cells would start to adhere to the glass bottom of the specialised dishes used with the system. These dishes (35mm glass bottomed μ-Dish, Ibidi) have a specific diameter to fit the HOTs stage and are glass bottomed allowing the laser to interact with the cells. This thin glass bottom is important as thicker glass would reduce the energy of the laser and would not produce an effective optical trap. Both low concentration gelatin and BSA were tested as potential coatings to slow the adherence of cells. BSA was found to be a good choice as it was not only effective at slowing the rate of cells adherence, but it was also easy to prepare and an economical choice when conducting testing (Chapter 2, section 2.2.14, page 81). Following on from these experiments, tests into the manipulation of bone fragments and the adherence of cells onto said fragments was conducted. In parallel to those experiments, the development of a system to introduce two different cell types on bone fragments was investigated.

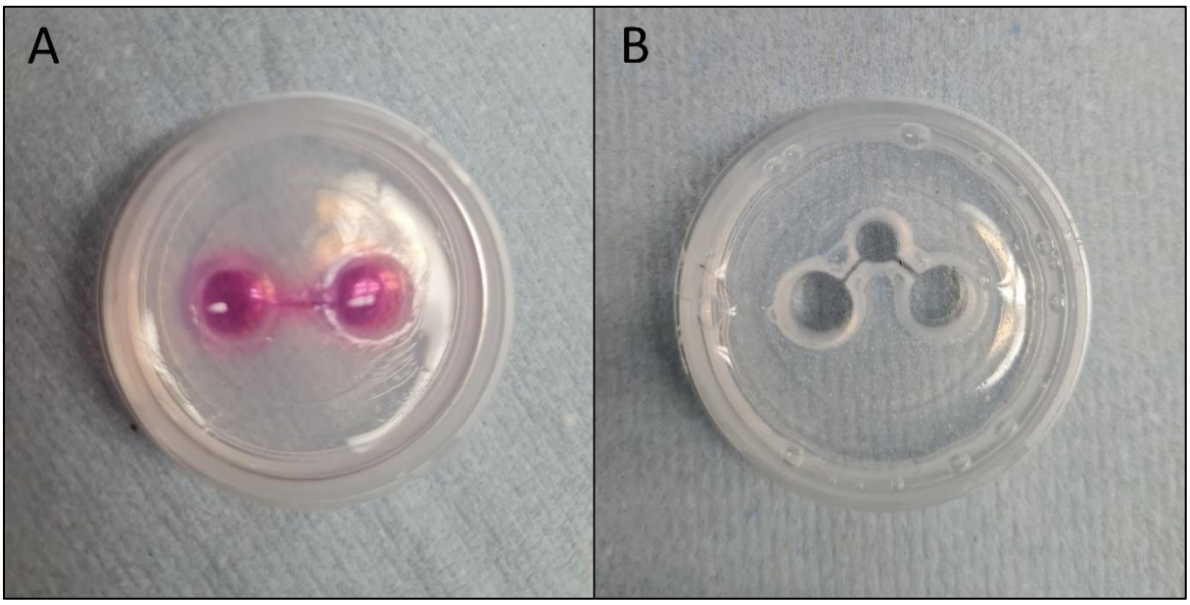

Figure 4.2: First and final mould design

(A) A picture of the initial agarose mould cut with a scalpel (filled with media). (B) A picture of the final mould design formed with silicone having been moulded around a 3D printed core piece.

As previously mentioned, a specific dish was needed to be used with the HOTs so any method to accommodate the needs of the project needed to fit into the dish. The dishes could not be used as designed by the manufacturer, as cells would drift into the patterning area both during patterning, and afterward. A way to contain different cell types within a dish, while preserving a suitable patterning area, was necessary. The earliest iterations of the model involved the casting of agarose gel into a dish and cutting out a region for cells to pass through. This first took the form of two cylindrical wells connected by a channel as shown in Figure 4.2 (A). The cylindrical wells were “punched” out with a 1mL pipette tip base and the channel cut with a scalpel by hand. There were many issues with this early model, primarily that the central channel needed to be cut with parallel lines (to allow the HOTs to work) and doing that by hand resulted in a wide channel of a few millimetres. This meant that any cells added to one well would rapidly diffuse to the other side. This defeated the whole object of a controlled system as the patterning area would be filled with cells which had drifted through the mould. A better way to contain the cells not currently being patterned but were accessible

needed to be found and required a great deal of rethinking. Agarose as a material was also problematic. The agarose moulds only lasted a few days kept in the fridge at 4^{o}C as the agarose would contract and media would seep into the gel if left *in situ*. Despite the issues with agarose, this hurdle was addressed after the mould design was completed as agarose moulds were suitable for quick tests and could be removed easily from the dish for reuse.

While a few different "hand cut" models were experimented with, they all ultimately fell short of requirements, leading to the idea of using a 3D printed core piece to be cast to create the form needed. 3D printing allowed the creation of bespoke CAD models with fine parts. The ultimate shape chosen for the piece was that of three cylinders in a triangular shape with the outermost cylinders connected to the central cylinder via thin channels. This would allow separate cylinders for HOS and hMSC, with a central cylinder for constructing the model. Several different pieces were printed, varying in the size of the cylinders and the length and width of the channel before ultimately selecting the design specifications shown in Chapter 2, Figure 2.5 after testing the moulds created from the pieces. At this stage silicone was chosen as a preferential casting material. It was cast at room temperature by the mixing of two liquid parts, the pieces could easily be stored for long periods of time at room temperature and then decontaminated under UV light prior to use. Furthermore, silicone was highly resistant to media diffusing through it.

The mould casting process took some time to optimise as a big issue encountered was the presence of small silicone pieces trapped in the channels. This occurred due to silicone seeping under the mould piece during casting and fragmenting during its removal. Three steps were taken to minimise the detrimental effects of these pieces of silicone. First, the amount of silicone under the mould piece was minimised by using autoclave tape to ensure that the mould piece was held tightly in place. This was shown in Chapter 2, Figure 2.6. Second, the exposed dish glass was washed carefully, having removed the mould piece. This was done with a fine brush and 70% ethanol, with particular attention being given to cleaning the channels. Third, the channels on the HOTs system were inspected prior to using the given dish

for any experimentation. If any large pieces of silicone were found, the mould was washed again, and the process repeated until the mould was in a usable condition. With these checks in place, the design mould made from silicone was consistent in its utility allowing different cell types to be added to the outermost cylinders and brought independently together to the middle cylinder where bone fragments would already have been placed.

Having designed a workable mould for the HOTs dish and having conducted some experimentation into the manipulation of small bone fragments and HOS together, the process of seeding hMSC (at passage 5) and HOS together started. One of the first obstacles to overcome was the issue of the number of cells to seed. A balance between having enough cells that were easy to find, yet low enough such that they did not spread into the channel and overrun the central cylinder needed to be found. The range of cell numbers ultimately chosen was 2000-6000 cells, based on testing patterning ability against cell spread. The reason for the large range, was that any cell solution added to the dish needed to be as concentrated as possible and at low volumes the cell count had a greater error margin. Low volumes, often only a few microliters, were used because any large addition of media to the mould would cause the fluid level to rise across all sections, causing a flow from the point of addition, along the nearest channel and into the other cylinders. This, of course, could cause the movement of cells out of the intended cylinder and into an unintended location. By adding the cells in a concentrated solution, this issue was largely mitigated.

The next issue encountered was a time constraint with working with two cell types. When working with both hMSCs and HOS, initially both cell types were split and counted ready for addition to the HOTs dish and patterned one at a time. This, however, was problematic because of the time consuming, precise, and sensitive nature of working with cells on the HOTs. By the time a hMSC cell had been captured and taken to a chosen fragment, HOS in the other well would have started to adhere to each other and some to the dish bottom despite the use of 3% BSA. If the HOS were kept in suspension and only added after the hMSC had been positioned while more of them were viable, a large quantity would have adhered to

each other or would have been damaged in the process of breaking up the loosely formed pellet. Splitting the different cell types at staggered time points to counter this issue presented a further issue with the use of small bone fragments.

As previously mentioned, initially small bone fragments approximating 100µm in length were used as the anchor point for the micro model. The issue however was, given their size and weight, the fragments would drift even with cells attached. In some cases, even the low acceleration of the stage being moved would result in the fragments moving resulting in the loss of the model. Given the time delay between addition of the two cell types, it was clear that at this stage, small fragments were not viable. Instead of a solution of small fragments being added to the central cylinder, a single larger fragment in the 1 - 3mm range was added. The larger size minimised movement of the fragment. Having added the fragment to the central cylinder, the dish was added to the HOTs stage and a single point on the fragment chosen as the site for cell adherence and the system "zero" and "home" setting used on the laser control unit (Chapter 2, Figure 2.3) to return to this site easily and the coordinate system was used to navigate when pulling cells to this location. Using this these methods, after much trial and error, it was possible to position one hMSC and two HOS either side (of the hMSC) reproducibly as shown in Figure 4.9, Figure 4.10 and Figure 4.11.

4.2 Results - Analysis of Outputs

Along with data gathered in the creation of the microscopic model, this chapter covers the range and capabilities of the HOTs system as tested during this project and by its collaborators.

4.2.1 Cell Manipulation

The HOTs software developed by the University of Glasgow allows for the creation of precise patterns of cells and other objects, as well as the generation of multiple optical traps that can be controlled independently using HOTs technology. The ability to manipulate both HOS and

hMSCs was tested to assure their suitability for future work. In addition to showcasing the precision and control capabilities of HOTs, Figure 4.3 highlights the potential of direct cellular patterning as a tool for investigating cellular interactions and their impact on behaviours such as differentiation. Patterning can create complex formations not found naturally as well as to pattern different cell types together.

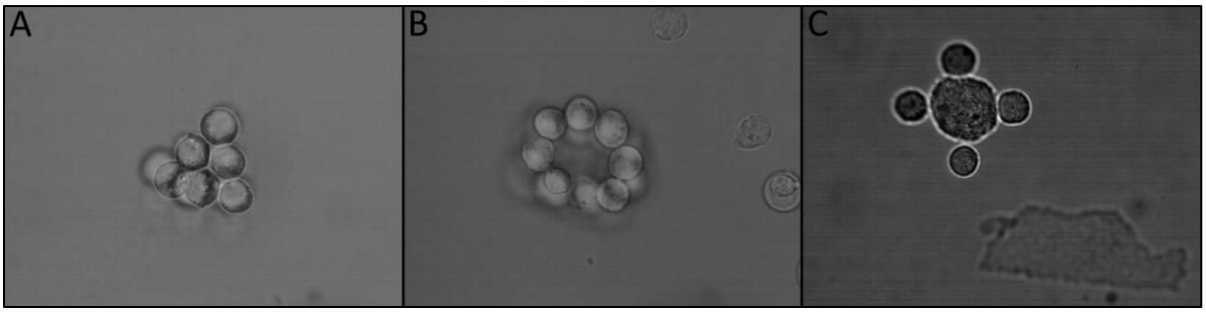

Figure 4.3: Patterning potential of cells using HOTs

Cells positioned by Holographic optical Tweezers into bespoke structures. (A) shows mouse embryonic stem cells CGR8 positioned into a triangle and (B) positioned into a doughnut. (C) shows four CGR8 positioned around a single HOS cell.

Not only can cells be positioned, but so too can polymeric materials. This includes something as simple as PLGA particles but can also include more advanced materials like electrospun polymer fibres and time-release chemical particles. This gives the option for temporal control of the chemical and physical environment within models. Examples of PLGA particles and fibres being positioned with CGR8 cells is shown in Figure 4.4.

The system can also be used in the tracking of a single cell's positioning and subsequent proliferation via fluorescent marking. In Figure 4.5, an ihMSC was positioned onto a fragment of decellularised rat leg bone using the HOTs and incubated over a 48hr period before fluorescent imaging. This allowed the tracking of a single cell's adherence and proliferation post patterning with HOTs.

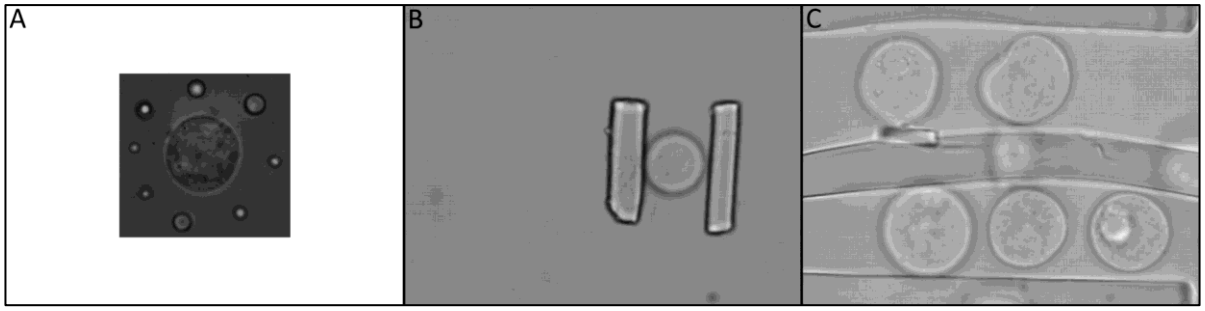

Figure 4.4: Patterning potential of cells with polymer materials using HOTs

Cells and PLGA positioned by Holographic Optical Tweezers into bespoke structures. (A) shows a single mouse embryonic stem cell CGR8 surrounded by eight PLGA particles 2µm in size. (B) shows a single CGR8 cell sandwiched between two PLGA electrospun fibres. (C) shows the same type of fibre and CGR8 cells positioned into a more complex structure of fibre, two cells, fibre, three cells and a fibre from top to bottom. Microparticles and electrospun fibres created as described in Kirkham et al., 2015.

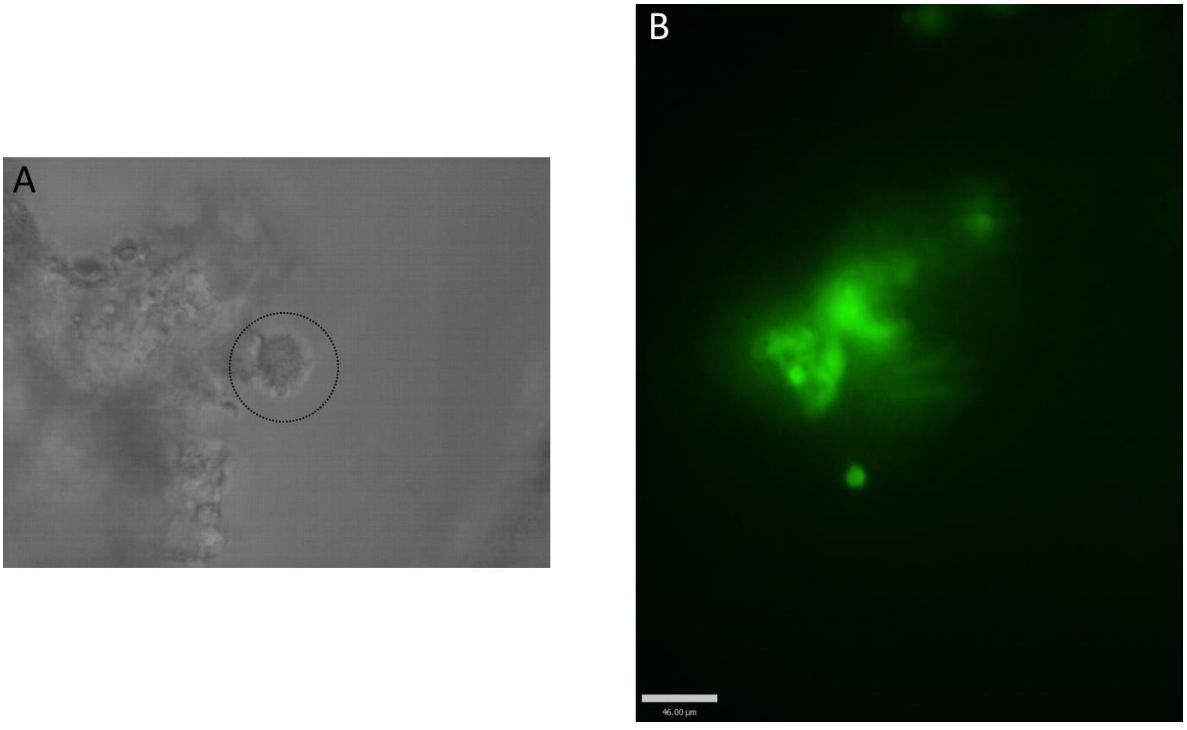

Figure 4.5: ihMSC proliferation after HOTs positioning on bone

An immortalised human mesenchymal stem cell (ihMSC) at P3, fluorescently marked, was positioned using the holographic optical tweezers onto a fragment of decellularised rat leg bone and imaged using the HOTs inbuild bright field camera (A). The cell was left to proliferate and was imaged again after 48hrs (B).

4.2.2 Cell Survivability

The HOTs system has a number of benefits over similar technologies as detailed in Section 1.3.4, page 43. One of the primary advantages of HOTs is the ability to control cellular positioning and organization without direct physical interference supports higher cell survival rates compared to other micromanipulation methods. This optical approach mitigates much of the potential mechanical stress that may otherwise compromise cell integrity and function, particularly critical for delicate or stem cell research. However, some limitations may exist with HOTs, primarily related to potential prolonged exposure to laser light. As the laser utilised by the system is infrared, any potential cellular damage is limited to heat induction (Peterman et al., 2003). For our HOTs system, each optical trap does not exceed 30mW of thermal energy, leading to a localized temperature increase of less than 0.35K, confined to the immediate trapping area of a very small part of the cell membrane.

The HOTs system used throughout this project, has been thoroughly investigated in the past (by members of our lab group) regarding potential cellular death due to optical trapping. In the Kirkham et al., 2015 paper, multiple mouse embryonic stem cells were manipulated into a ring and exposed to a single optical trap for 10, 20 or 30 minutes and compared to cells manipulated but not held in traps as well as to cells not exposed to any optical trapping. It was found that there was no increase in cellular death between any of the groups, suggesting neither manipulation and/or the holding of a mouse embryonic stem cell in an optical trap damages the cell.

While mouse embryonic stem cells were used in some early optimisation tests with the HOTs system, the cells primarily used were HOS and hMSCs. While these cells are known to be relatively resiliant, especially compared to embryonic stem cells, the same level of testing has not been completed. MSCs have, however, been immortalised and positioned with the tweezers as shown in Figure 4.5, page 158, by members of the lab group in the past. These cells were used as a patterning tool and genetically modified to express GFP so that they are easy to visualise over any time frame. The cells were assessed after 48hrs and found to

proliferate, suggesting MSCs can indeed be manipulated with optical traps without damaging the cells in any way that impedes their proliferation. These cells were not used for any work that assessed cellular responses, but were used as a large number of cells were required which were easily visualizable. A further bonus with using an immortalised MSC is that they may adhere to the scaffold in a similar way to primary MSCs.

Long-term experiments with the HOTs were unfortunately not feasible during the project timeframe due to logistical constraints preventing relocation of the equipment into an incubator within the cell culture laboratory. Without this move, it was not possible to keep cells under the right conditions to survive beyond a couple hours. The move into an incubator would be the first step in future optimisation of this model, primarily to determine the survivability and proliferation of the cells positioned within the designed model.

4.2.3 Cell-Dish Attachment

As mentioned earlier, cell to dish attachment was one of the early issues encountered during the microscopic model development. For each coating to be tested, 20,000 HOS cells were added to the dish, and over a ten minute period, the number of manipulable cells recorded. This was converted into a percentage of movable cells for each minute and plotted as shown in Figure 4.6. As seen in both gelatin plots (A and B), the percentage of moveable cells rapidly dropped off with every minute, both being below 40% at the ten minute mark. The reduction in ability to move cells in dishes coated with BSA was much slower in comparison. Both with a 1% BSA solution (C) and a 3% BSA solution (D), the percentage reduction was much lower over the 10 minutes, both being above 60% after 10 minutes. A 3% BSA coating was ultimately used as it produced the highest cell manipulability, with 75% of cells being moveable after ten minutes.

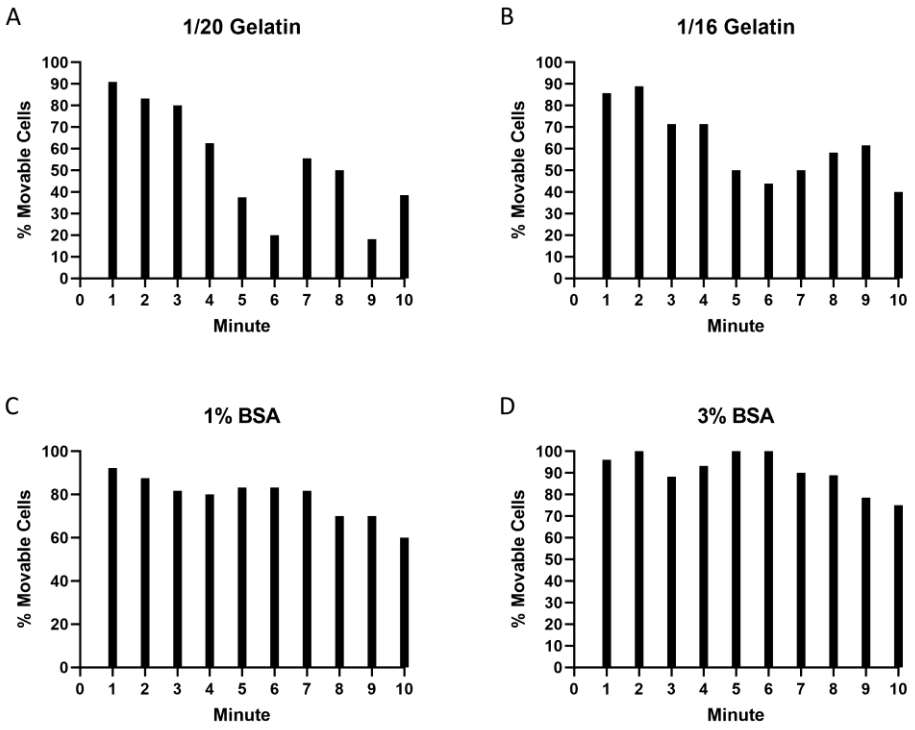

Figure 4.6: HOTs cell manipulability changes with surface coatings

Graphical representations of the change in the percentage of moveable cells over a ten minute period using Holographic Optical Tweezers with changes in dish surface coatings. A 1/20 dilution gelatin (A), 1/16 gelatin, 1% BSA (C) and 3% BSA (D) are shown.

4.2.4 Small Fragment Cell Attachment

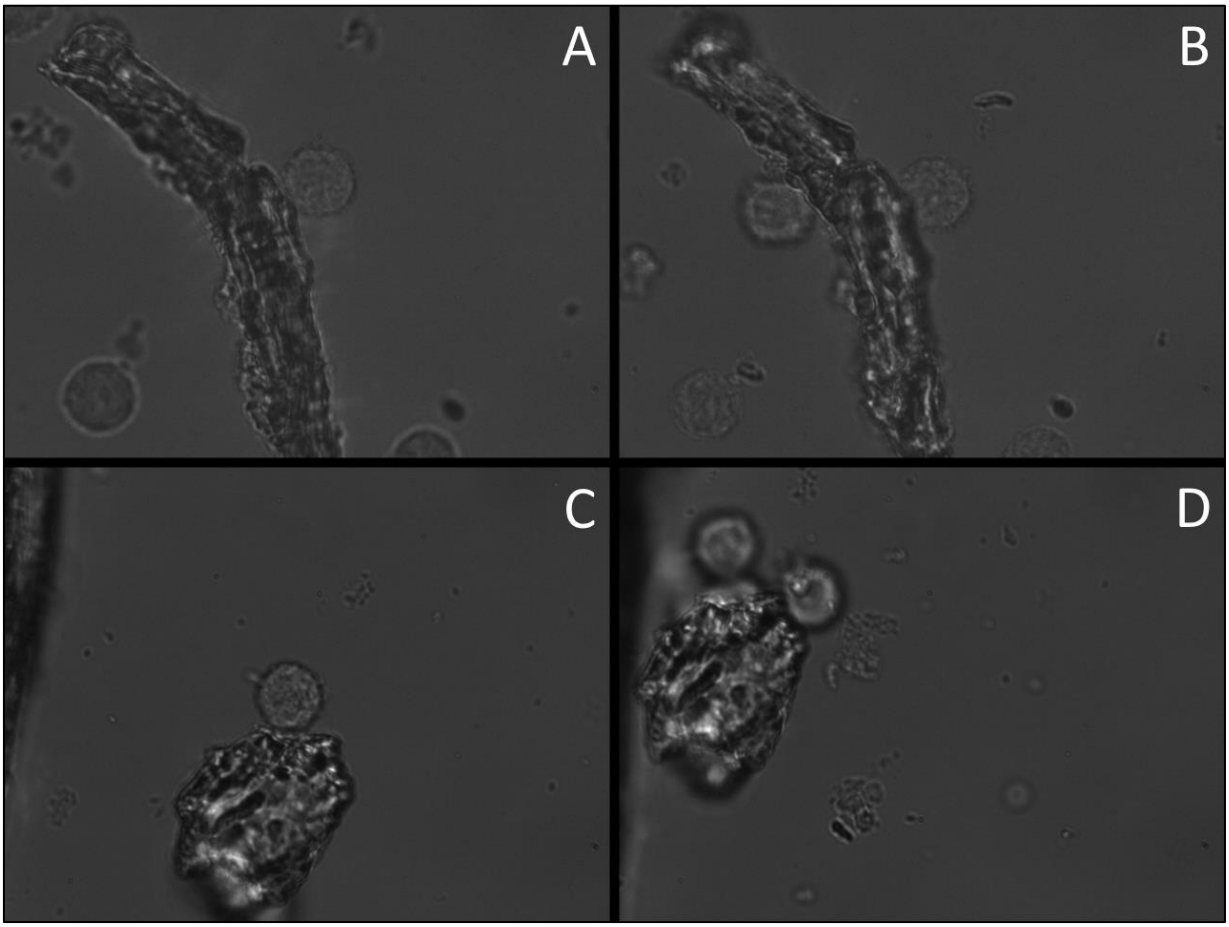

Figure 4.7: Manipulation of HOS cells onto small rat bone fragments using HOTs

Images captured through the Holographic Optical Tweezers of HOS cells being manipulated and placed onto small decellularised rat bone fragments in a glass bottomed imaging dish. Two examples are shown, (A & B) and (C & D) where two HOS cells were brought to a bone fragment in each.

As part of the early optimisation of the microscopic model development, the ability to adhere HOS onto decellularised bone fragments was tested as shown in Figure 4.7. The ability to manipulate the bone fragments varied with their shape but HOS could repeatably be brought to these fragments and attached. The cells stayed in place, rapidly adhering to the bone after a short time kept in place with the HOTs. Screenshots taken of the software interface while positioning the cells and fragments can be found in the Appendix, Figure 6.16.

4.2.5 Large Fragment Cell Attachment

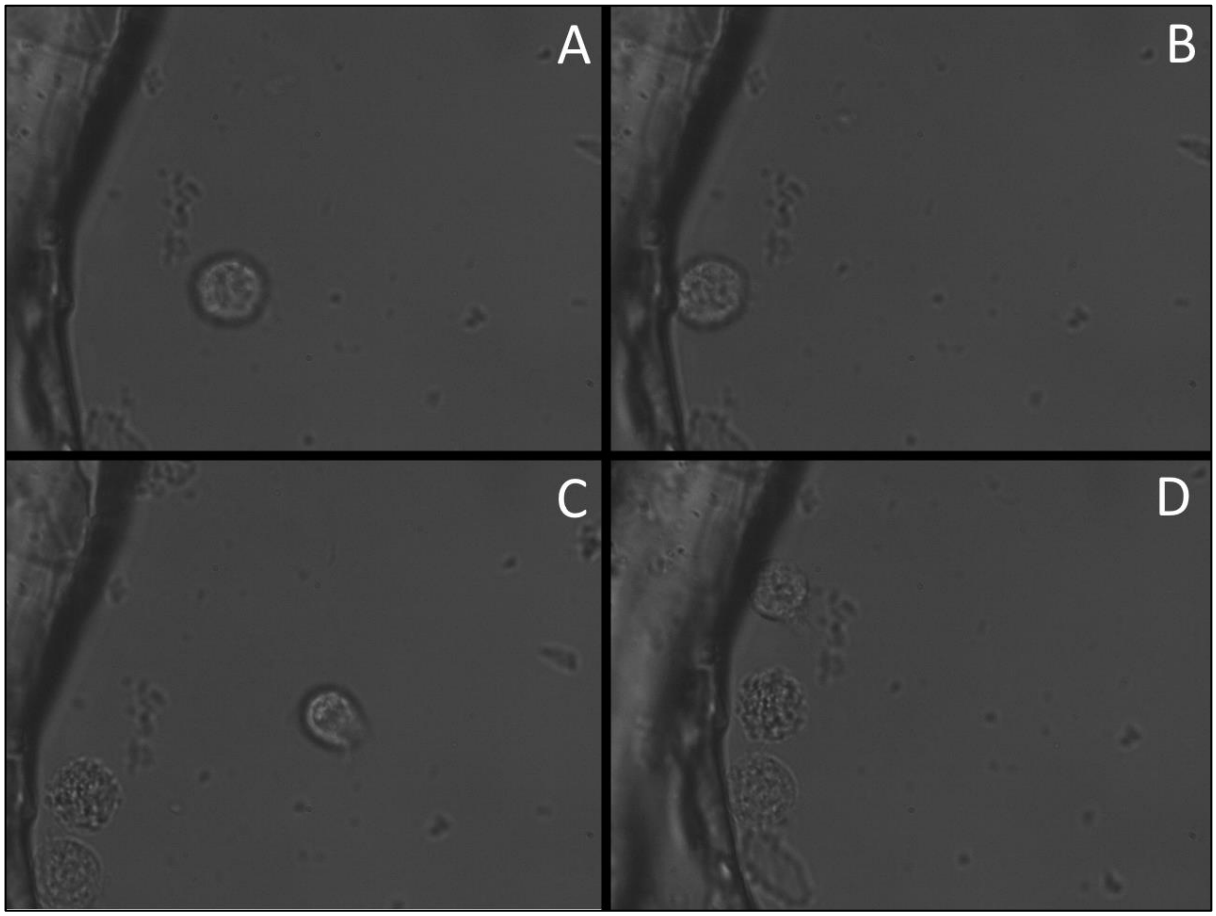

Figure 4.8: Manipulation of HOS cells onto a large rat bone fragment using HOTs

Images captured through the Holographic Optical Tweezers of HOS cells being manipulated and placed onto a large decellularised rat bone fragment in a glass bottomed imaging dish. Across the four images (A to D), the sequential addition of HOS cells is shown. By image (D), three individual HOS cells had been manipulated and patterned into place on the bone surface. Image (D) was taken 10 minutes after patterning the third cell.

Having progressed to using a single large decellularised rat bone fragment, the same experiment as shown in Figure 4.7 was repeated but with a different fragment. Figure 4.8 shows multiple HOS cells being positioned onto the surface of a large fragment. This method was very stable as there was minimal bone movement as shown in image (D) which was taken ten minutes after positioning all the cells.

4.2.6 Two Cell Type Attachment

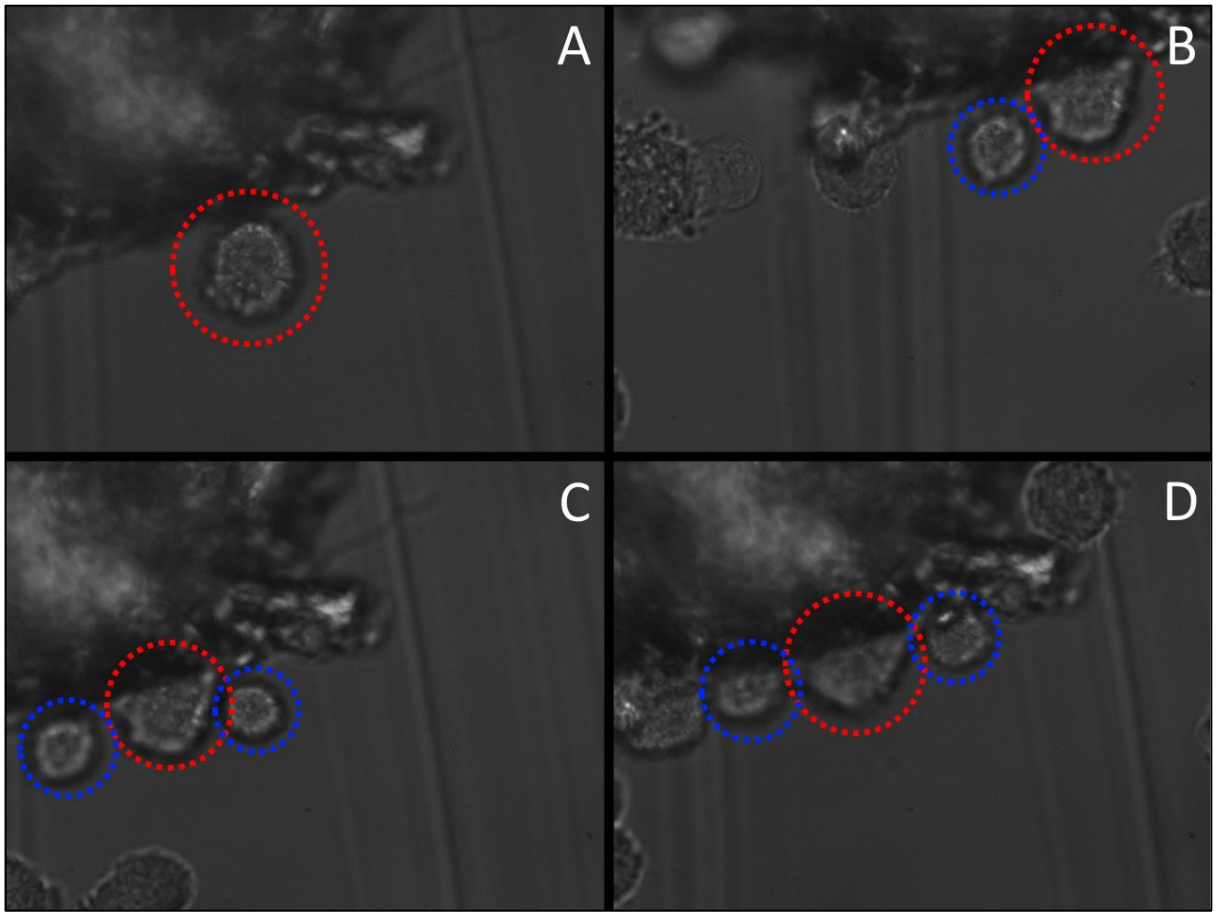

Figure 4.9: Manipulation of hMSC and HOS onto decellularised rat bone – repeat 1

Images captured through the Holographic Optical Tweezers of patterning of both hMSC and HOS cells manipulated and positioned onto a large decellularised rat bone fragment in a glass bottomed imaging dish. Images (A) through (D) were taken sequentially with the hMSC cell encircled in red and the two HOS cells in blue. (A) sees the hMSC positioned onto the bone surface while (B) and (C) see HOS cells being positioned either side of it. (D) shows the model 10 minutes after the positioning of the third cell. These set of images were the first of three repeats.

The patterning of both hMSC and HOS together against a large bone fragment was possible using the HOTs system. This model has been formed in triplicate as shown in Figure 4.9, Figure 4.10 and Figure 4.11. In the first repeat, Figure 4.9, the bone fragment had well defined edges and having brought the cells together, it was evident from their morphology change (image D after 10 minutes) that they had adhered to the bone. This repeat had the issue of having cells flood the central chamber which were drawn to the attachment site due to the zero

order of the HOTs. The zero order is a location of laser intensity which, when no trap/hologram is created, acts on the sample. It is created when the laser hits the SLM and the power is distributed. Normally a system would position the zero order in the centre of the focal plane, however, to be able to pattern without disruption, it was positioned at the top left out of view. Unfortunately, it could have the effect of drawing in cells and particles from the surrounding area towards it.

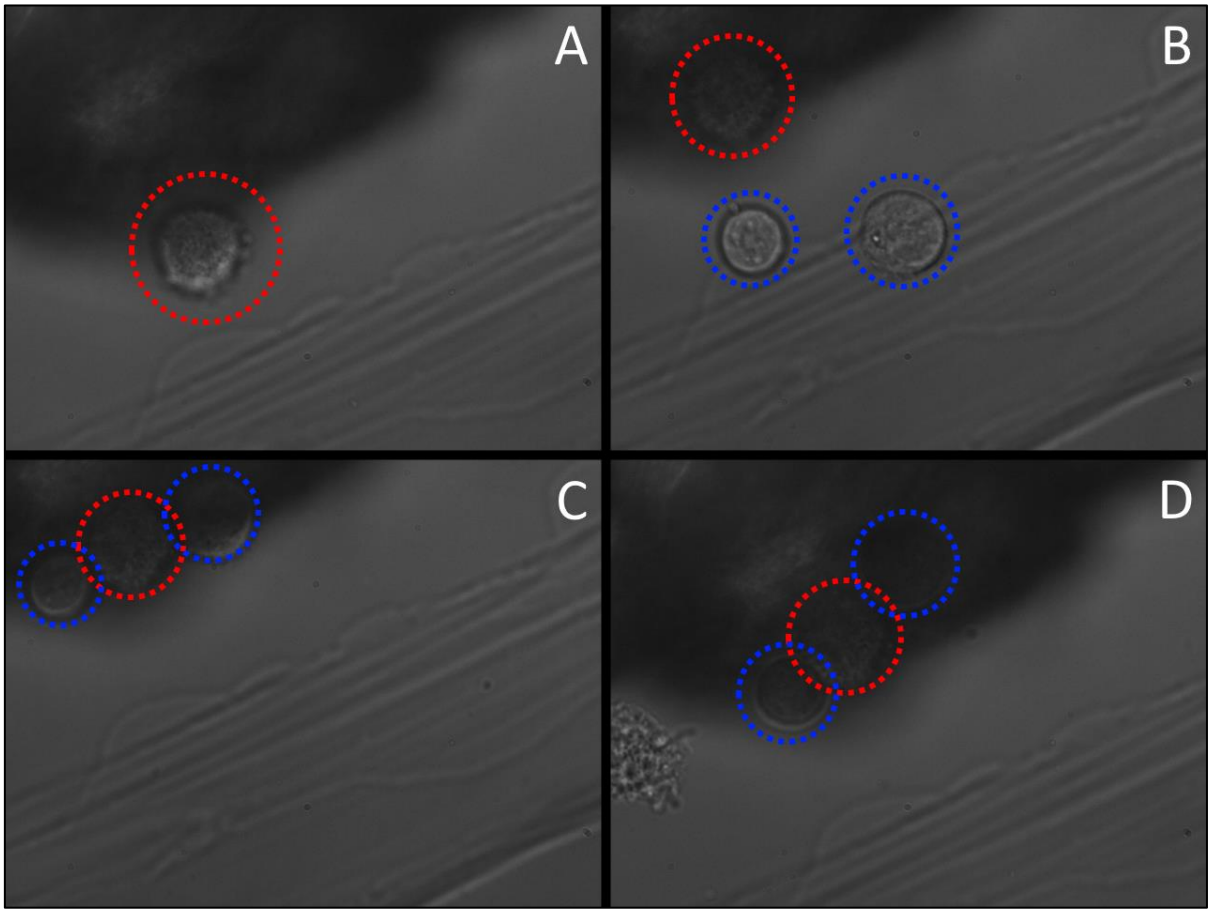

Figure 4.10: Manipulation of hMSC and HOS onto decellularised rat bone – repeat 2

Images captured through the Holographic Optical Tweezers of patterning of both hMSC and HOS cells manipulated and positioned onto a large decellularised rat bone fragment in a glass bottomed imaging dish. Images (A) through (D) were taken sequentially with the hMSC cell encircled in red and the two HOS cells in blue. (A) sees the hMSC positioned onto the bone surface while (B) and (C) see HOS cells being positioned either side of it. (D) shows the model 10 minutes after the positioning of the third cell. These set of images were the second of three repeats.

The second repeat of the model, Figure 4.10, was again able to position the hMSC and HOS cells either side of it. This time, while the attachment site was clear of excess cells, the positioning of the fragment, having an "overhang" above the cells, resulted in a somewhat obscured image of the cells in position. This was due to a small movement of the fragment prior to seeding, but at this stage having already prepared the hMSC for the model, it would have been wasteful not to use these precious cells.

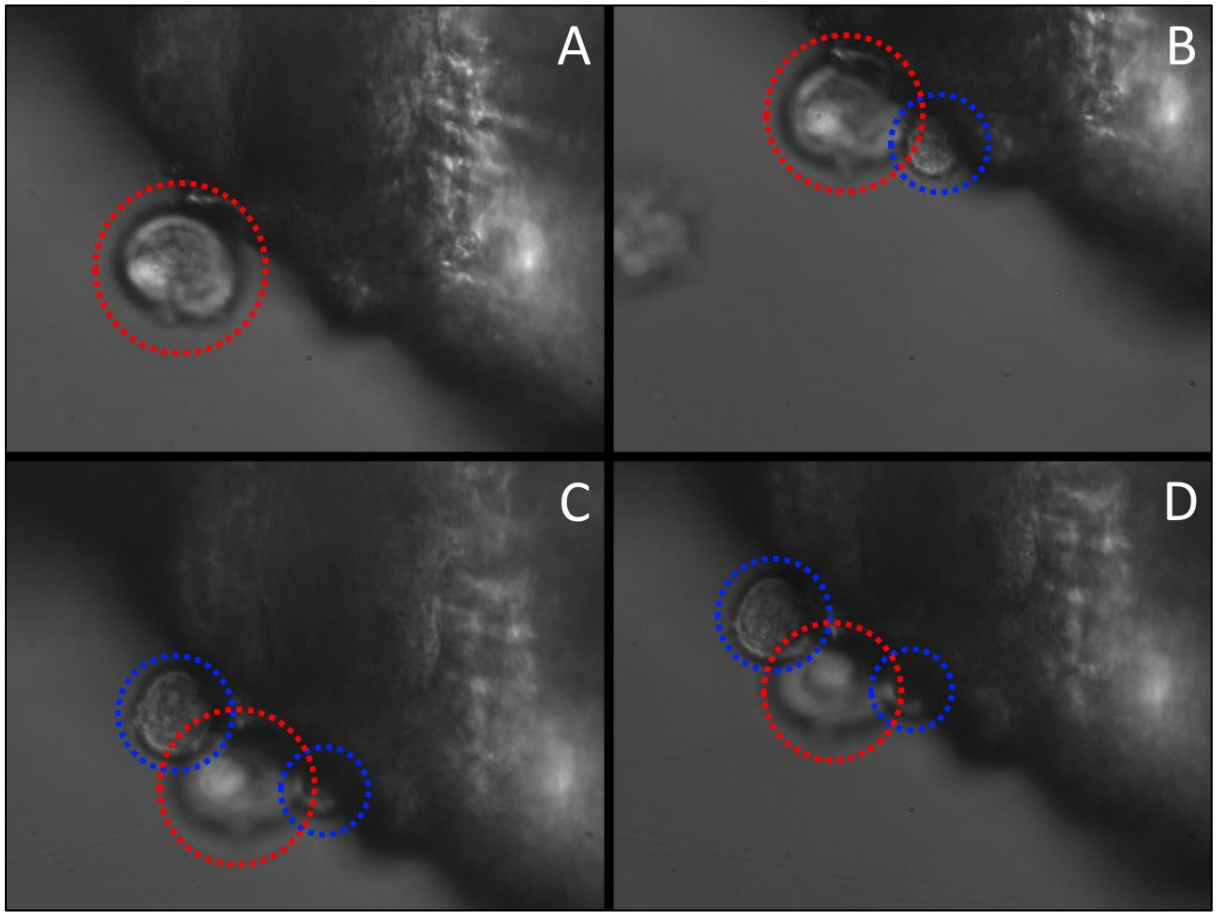

Figure 4.11: Manipulation of hMSC and HOS onto decellularised rat bone – repeat 3

Images captured through the Holographic Optical Tweezers of patterning of both hMSC and HOS cells manipulated and positioned onto a large decellularised rat bone fragment in a glass bottomed imaging dish. Images (A) through (D) were taken sequentially with the hMSC cell encircled in red and the two HOS cells in blue. (A) sees the hMSC positioned onto the bone surface while (B) and (C) see HOS cells being positioned either side of it. (D) shows the model 10 minutes after the positioning of the third cell. These set of images were the third of three repeats.

Repeat 3, Figure 4.11, was the best of the previous 2 models. The bone surface had defined edges and did not move prior to patterning. The attachment site was not obscured with cells from the source cylinders and the attached cells had a morphological change indicating proper adherence. Adherence was further confirmed by attempting to pull the cells away from the bone surface after 10 minutes with no success.

4.3 Discussion

The fundamental basis for the bone marrow stem cell niche's biological function is derived from the structural organization of its biological elements and the mechanisms that govern them. The niche is a complex and not fully understood microenvironment of different cells, chemicals and structures and its modelling has been a challenging endeavour. This is largely due to the absence of technologies capable of positioning individual cells and components at a microscopic length scale. HOTs have been used in multiple fields including optical sensing, manipulation and actuation for lab on chip systems (Padgett & Di Leonardo, 2011) developing adaptive microfluidics at the nanometre scale (Grier, 2003) but also for cell work. HOTs have the capability to manipulate individual and multiple cells in 3D (Leach et al., 2009). The potential of HOTs goes beyond just cell positioning, but can include the control of polymeric materials, controlled release chemicals and ECM into 3D structures (Kirkham et al., 2015).

The aim of the development of a microscopic model of the stem cell niche builds on the work done in the development of the macroscopic model. In the latter large numbers of cells were used; here, single cells were taken and positioned precisely where wanted. The use of HOTs to develop a system where HOS and hMSC could be repeatably patterned together at the cellular level was the goal. While the patterning of cells with HOTs had been achieved in previous studies (Kirkham et al., 2015; Leach et al., 2009), the patterning of two cell types onto bone using this system, as was done in the final model can be deemed novel.

The work done on the development of the microscopic model was a follow on from the macroscopic model. The former is, in effect, meant to be the same model, but at a much

greater magnification. With the macroscopic model, it is not possible to position cells in specific locations, to research the possible effects of their relative locations. The power of the HOTs system was demonstrated by its ability to enable positioning of cells in specific locations in 3D space and the potential of developing a microscopic model. As an example, in the bone marrow stem cell niche, the relative positions of cells is not fully comprehended. The HOTs could be used to pattern different cell types in varying patterns and the cells tracked over time and their responses compared.

The development of the method to add two different cell types independently to a single dish, and to control each group independently without cross contamination was the biggest hurdle when developing the microscopic stem cell niche. This is because it required the design of a system to keep the cell types separate, starting from the most fundamental element, an imaging dish. The final design of the mould, using an optimised 3D printed resin core piece to cast silicone, was used repeatably to pattern hMSC and HOS together on decellularised rat bone. Bringing the cells to a central location *via* different channels, engineered to be as thin as possible, ensured that hMSC and HOS during the patterning process were identifiable, based on where the cells were collected. Unlike in Chapter 3, discussing the designed macroscopic model, work done with the HOTs system was twofold: the design and testing of a model that allowed the patterning of two cell types in a single dish, and an assessment of the capabilities of HOTs to be implemented in future iterations of the model. It is believed that the steps taken in this project can lead to the creation of an advanced model to analyse cell-cell interactions and behaviour, and potentially help elucidate the positions of different cell types within the niche.

Much can be learnt from the patterning of cells in complex structures (Figure 4.3) or the patterning of cells with polymer microparticles (Figure 4.4), however in isolation they are insufficient for the creation of the unique microenvironment of the bone marrow stem cell niche. By combining all the techniques covered in the previous section, the patterning of multiple cell types, seeding them on bone matrix, the ability to introduce time release

microparticles and PLGA microparticles and fibres, it will be possible to create a tailored model of the niche. This will facilitate the characterisation of the niche at a scale far beyond the macroscopic model or any other model, facilitating novel insights that are unattainable through other technologies. Specifically, it allows investigation of the fundamental interactions between hMSC and HOS, bone and each cell type, and how the positional control influences these complex interconnections.

5. Final Remarks

5.1 Thesis Conclusion

In this research, models of the bone marrow stem cell niche were developed at the macroscopic and microscopic level to advance the understanding of its biological structure and systems. At the macroscopic level, hMSCs and HOS were co-cultured on decellularised rat bone in the presence of OCM with mechanical stimulation creating a novel model. At the microscopic level, a mould was designed to allow the patterning of both hMSCs and HOS onto decellularised rat bone fragments using HOTs, and the system tested to determine the potential of HOTs for the further expansion of the model. The HOTs facilitated the development of a novel method that can enable a level of control, and offer insights, that were previously unachievable.

5.1.1 Macroscopic Model

A successful macroscopic model is one that contains cells, ECM, chemical and physical influence, and that ultimately shows evidence of osteogenesis, detected via OPN and OCN protein levels and genetic upregulation alongside *RUNX2*, indicating cellular differentiation and normal function.

In this study the model was developed to include the following elements:

Cells and ECM: hMSCs and HOS were patterned successfully onto decellularised rat bone as a scaffold utilizing a novel technique.

Chemical influence: the influence of OCM versus BM was investigated.

Physical influence: mechanical stimulation with the Nanokick device was introduced.

The model successfully met all the established criteria for a model of the bone marrow stem cell niche and uncovered some interesting interconnections.

1. Culturing hMSCs on decellularised bone significantly increases osteogenesis compared with monolayer on tissue culture plastic.
2. Mechanical stimulation (1000Hz) further increases this upregulation.
3. Osteogenic media has a regulatory reductive effect on hMSC osteogenesis when mechanical stimulation (1000Hz) is applied to the sample, but only if hMSCs are the only cells on the bone.
4. The previous effect is negated with the introduction of HOS in co-culture (1:1 ratio) with OCM samples having significantly higher osteogenesis than BM.
5. RT-qPCR of Model 3 indicates a variance between the gene expression timeline and protein production. Despite the significant upregulation in OPN and OCN in the BM group compared to controls detected via IHC, no significant upregulation was detected in gene expression. The RT-qPCR data did, however, match the IHC data for the OCM group. This suggests the presence of the additives in OCM may influence gene expression for OPN, OPC and *RUNX2*.

5.1.2 Microscopic Model

The microscopic model built on the foundation of the macroscopic model and required the design and fabrication of a system to allow the patterning of both hMSC and HOS in co-culture. Ultimately this resulted in the creation of a 3D printed mould core piece which was cast with silicone (in an imaging dish) in the shape of three cylinders in a triangular formation with two external cylinders connected to the central one *via* 0.5mm thick channels. These allowed hMSCs to be added to a distal cylinder, trapped with the HOTs and pulled through the channel to the central cylinder. The same was done with HOS in the other distal cylinder, allowing patterning in the central one without unwanted cells flowing into the patterning area. The cells were patterned onto a decellularised rat bone fragment and tracked over a ten

minute period to assess short term stability. It is important to acknowledge that this form of model involving the precise patterning of individual cells is not possible using any other method. It is through this form of experimentation that we may better understand the importance of cellular positioning in the niche. Beyond this model, further applications of the HOTs system investigated includes the following:

1. The advanced patterning of cells into multiple configurations.
2. The patterning of polymeric material alongside cells.
3. The tracking of cell proliferation over multiple days.
4. The ability to attach cells to small decellularised bone fragments.

5.1.3 Impact of Research

Advancements in Tissue engineering: The work contributes significantly to understanding how specific scaffolds and materials, decellularized rat bone, can influence cellular behaviours such as differentiation, proliferation and osteogenesis. This has potential applications in regenerative medicine, particularly in designing effective biomaterials for repairing or replacing damaged tissues. These could be possible as the HOTs can achieve positioning at high magnification spatial resolutions. Comparable techniques don't have the same high-throughput potential, low length scale positional control, co-culture, and material/cellular co-positioning capabilities.

Improved Therapeutic Strategies: By exploring the interplay between bone cells and their microenvironment, our findings may lead to more effective treatments for skeletal disorders and injuries. The insights into mechanical stimulation and osteogenesis could inform the development of targeted therapies for osteoporosis and other bone-related conditions. Furthermore, Medical research strategies, including tissue engineering and regenerative medicine, aim to create functional tissue analogues for therapeutic applications. These approaches typically involve the integration of an appropriate cell source with a supportive scaffold. To better replicate native biological structures, the complexity of such constructs has

significantly advanced in recent years. Within this context, a novel technique has been developed using decellularized rat bone as a scaffold for hMSCs and HOS while enabling mechanical stimulation and chemical alterations. Furthermore, the novel nature of using laser capture technology to precisely pattern individual cells and structural components in three dimensions was experimented with and optimised for this purpose. This method facilitates the study of biological structures at an unmatched length scale, offering new insights into cellular and tissue organization. The work undertaken during this project has expanded the understanding of this technology's potential, paving the way for further innovative research directions.

Bone Marrow Stem Cell Niche Insights: Having a better understanding of the microenvironments within any tissue will enable better functionality of future implants and therapies. The exploration of cellular, physical and chemical interactions within the bone marrow niche deepens our understanding of MSC dynamics, particularly regarding *in-vitro* models. Of particular interest, the discovery that osteogenic media had a reductive effect on osteogenesis when cells were cultured on bone and mechanically stimulated. This research could impact the field of stem cell biology and the design of niche-mimicking environments for *ex-vivo* studies as it suggests the use of extra chemicals generally used for differentiating MSCs may not be necessary under specific conditions.

Technological Integrations: Two pieces of relatively new technologies were used throughout this project, the Nanokick platform and the HOTs system. The use of decellularized rat bone as a 3D scaffold material is also novel. The use of advanced techniques such as these, places this research at the forefront of tissue engineering, potentially influencing future methodologies in *in-vitro* cell culture modelling or used for drug discovery applications.

5.2 Future Work

This research could be extended down several avenues in the immediate and more distant future.

5.2.1 Macroscopic model

- Patient cell demographics: Incorporating primary hMSCs sourced from donors with diverse demographic backgrounds, including variations in age, gender, and health status, introduces a significant biological relevance to in vitro studies. Cellular behaviour, particularly proliferation, differentiation, and response to external stimuli can vary markedly across these demographic factors. For example, age related changes significantly influence the regenerative capacity of hMSCs, with cells from younger donors generally demonstrating higher proliferative and osteogenic potential. Furthermore, bone health exhibits well-documented differences between sexes, particularly in the context of postmenopausal women who experience a rapid decline in bone mineral density due to reduced oestrogen levels. This hormonal shift leads to an increased prevalence of osteoporosis and fracture risk, underlining the necessity of including female-derived cells in bone research. Including gender as a biological variable also aligns with emerging frameworks in research equity, diversity, and inclusion (EDI). While this consideration enhances the translational relevance of findings, current limitations persist due to restricted donor diversity in commercially available cell lines, which often lack full demographic profiling. Addressing these limitations by prioritizing diverse and transparent sourcing practices is critical to developing more inclusive and representative biomedical models.
- Bone sorting and categorisation: In the current study, no consistent pattern of osteogenic production was established with respect to the source location (leg, arm or rib) of the fragments (Chapter 3, Figure 3.23, Figure 3.27 and Figure 3.31). Fragments varied to a small degree between samples, in size and potentially

composition. To assess if this effected the models, a tiered sorting system of filters could be used to match fragments by size. Microscopy could also be used to assess any variation in fragment structure. This would potentially lead to the standardization of bone fragments which in turn would enable to measurement of OPN and OCN levels "on" the bone, instead of "around" them. All bones used in the generation of data as shown were also all sourced from a single rat. This should be expanded to see if comparable data is generated when the source varies, but could also be expanded to include human bone in the future.

- More work could be done on decellularization and validation of the protocol. This was not required for the aims of this project but would be necessary as the model is refined further for more detailed cellular response studies or development of tissue engineered implants.
- hMSCs and their interaction with their environment was the key focus in this research, however, Model 3 saw the introduction of a second cell type, HOS to the niche model. The addition of this extra cell type introduced a further complex component to an already intricate system of interactions. It is proposed that Models 1 and 2 are recreated with HOS instead of hMSCs, and the effect of different cell ratios is assessed. The combination of HOS and hMSC without mechanical stimulation, which has not been studied so far, could also be assessed in the future as it would be helpful to have this information to gain more insights and accuracy.
- In Model 2, it was deduced that the interaction of OCM diminished the osteogenic response within the model (Chapter 3, Figure 3.25). It has been proposed that the most likely active component of the OCM in this respect is dexamethasone: It is therefore proposed that the effect of removal of dexamethasone from the OCM is studied. This is of particular interest because in a therapeutic setting, minimisation of chemicals used is preferable. The model could also be used in a drug screening setting.

The research suggested dexamethasone was having an influence on cellular activity and interaction within the niche, this approach could be expanded to test other drugs.

- The number of samples tested should be upscaled to allow the testing of all models at the standard seven and 14 days, alongside the 28 already investigated. This would be dependent on developing a higher throughput system, allowing the analysis of more variables.
- OPN and OCN levels were quantified in the three models as a measure of matrix deposition. This matrix could be further characterised regarding its composition, for example determining collagen I levels and mineralisation.
- The eventual expansion of this model could ultimately include the addition of other cellular elements, such as HSCs, and the introduction of other chemical factors, such as TGF-β to try and further match the niche's constituents. Other considerations into expanding the model could be include the integration of a laminar flow system to replicate vessel activity.

5.2.2 Microscopic Model

- The first experiment conducted would be the long-term tracking of the three cell complex over three and seven days. The cell tracking potential shown in the ihMSC fluorescence data (Chapter 4, Figure 4.5) can also be implemented for the cell proliferation tracking alongside more specific proliferation assays and techniques to allow more precise monitoring of proliferation.
- Alongside the long-term tracking experiment above, assessment of cell death due to optical trapping would be conducted with both hMSCs and HOS in the same manner as past cell death experiments were conducted for the CGR8 line.
- The model could be refined further, if possible, making the channel thinner, to reduce the drift of cells out of their original position further.

- In order to determine whether the model reacts differently when cellular positions are altered cells could be patterned into different positions, for example, HOS attached to the bone surface and hMSC attached to the HOS.
- Alongside the PLGA particles patternable with HOTs as shown, time/control release particles can be controlled (Kirkham et al., 2015). This could be used in the investigation into gene expression by positioning the particles at specific sites in a patterned structure creating gradients of signalling elements. This would allow a more precise control of the niche structure.

6. Appendix

Further to Chapter 3, Figure 3.11, cell tracking of HOS on fragments was investigated over a 28 day period during optimisation, shown in Figure 6.1. This was done during optimisation of growing cells on bone as a scaffold as a way to identify if the cell had successfully adhered and proliferated over the bone surface. The same experiment was also conducted with hMSC, shown in Figure 6.2.

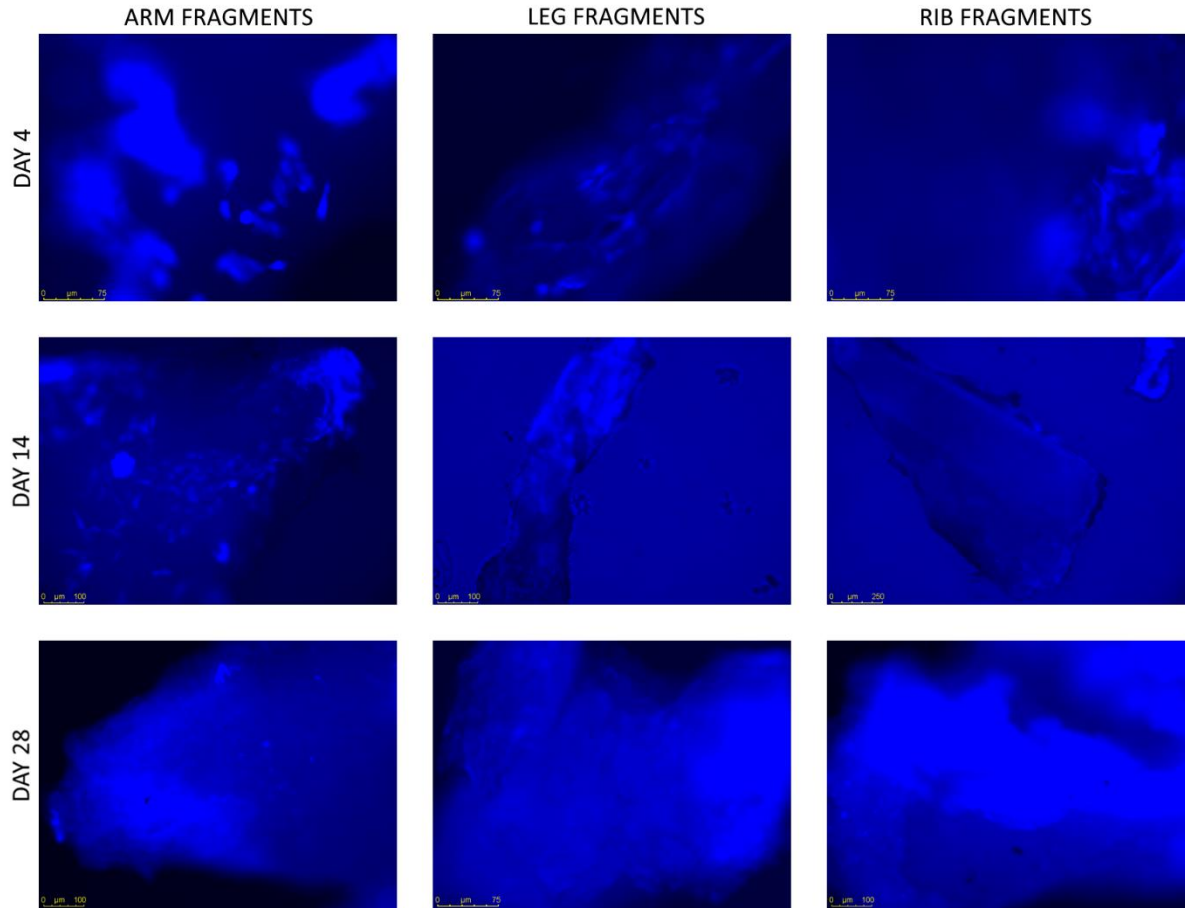

Figure 6.1: Cell tracking of HOS on bone over 28 days

Leg arm and rib decellularised rib fragments which had been seeded with HOS cells at 5000 cells/cm^2 and incubated for 4, 14 and 28 days. The fragments were relocated to a fresh well dish and incubated in CMAC cell tracker and imaged afterwards to determine the extent of cellular adhesion.

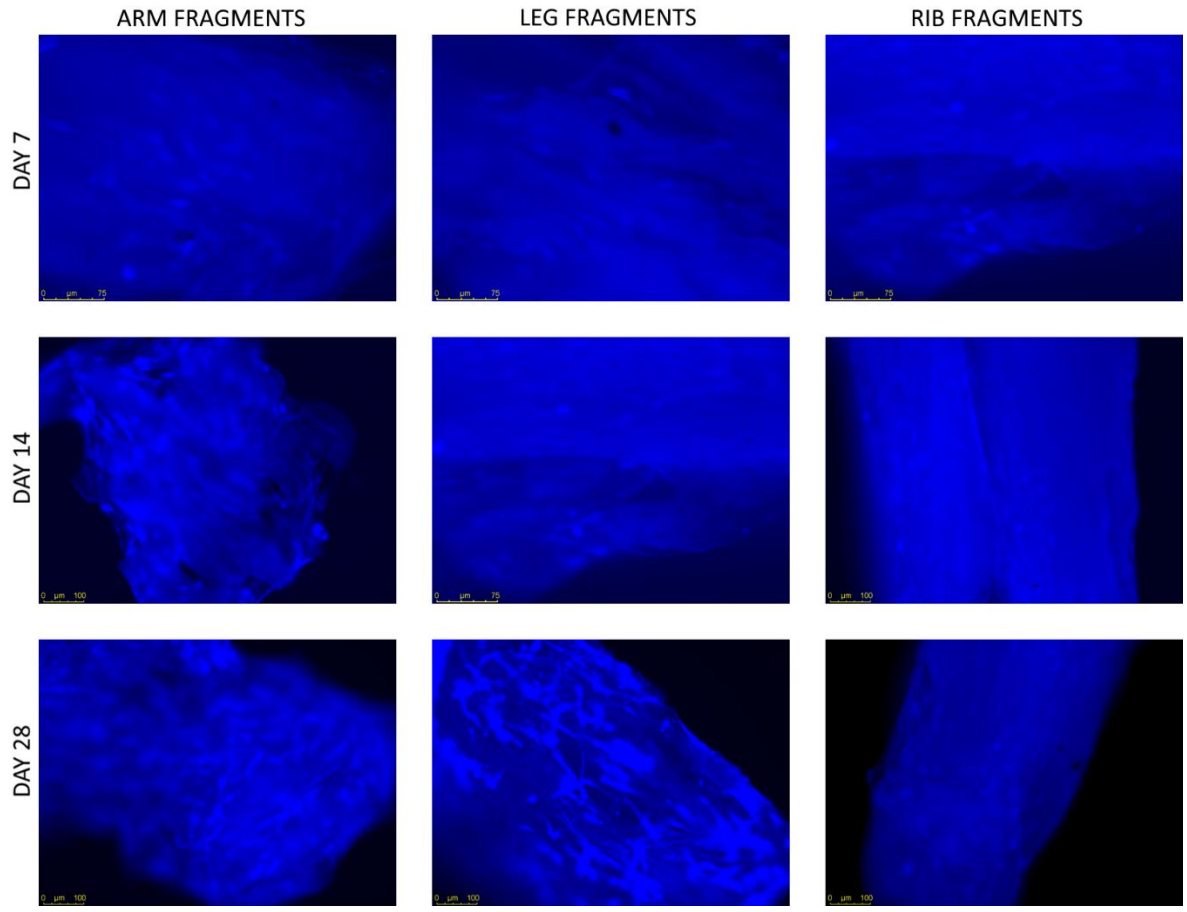

Figure 6.2: Cell tracking of hMSC on bone over 28 days

Leg arm and rib decellularised rib fragments which had been seeded with hMSC cells at 5000 cells/cm^2 and incubated for 7, 14 and 28 days. The fragments were relocated to a fresh well dish and incubated in CMAC cell tracker and imaged afterwards to determine the extent of cellular adhesion.

When testing to ensure HOS and hMSC would grow in co-culture, the two cell types were seeded at 5000 cells/cm^2 and tracked over a 48hr period using different cell trackers. Time points of 3hrs, 6hrs, 24hrs and 48hrs are shown in Figure 6.3, Figure 6.4, Figure 6.5 and Figure 6.6 respectively.

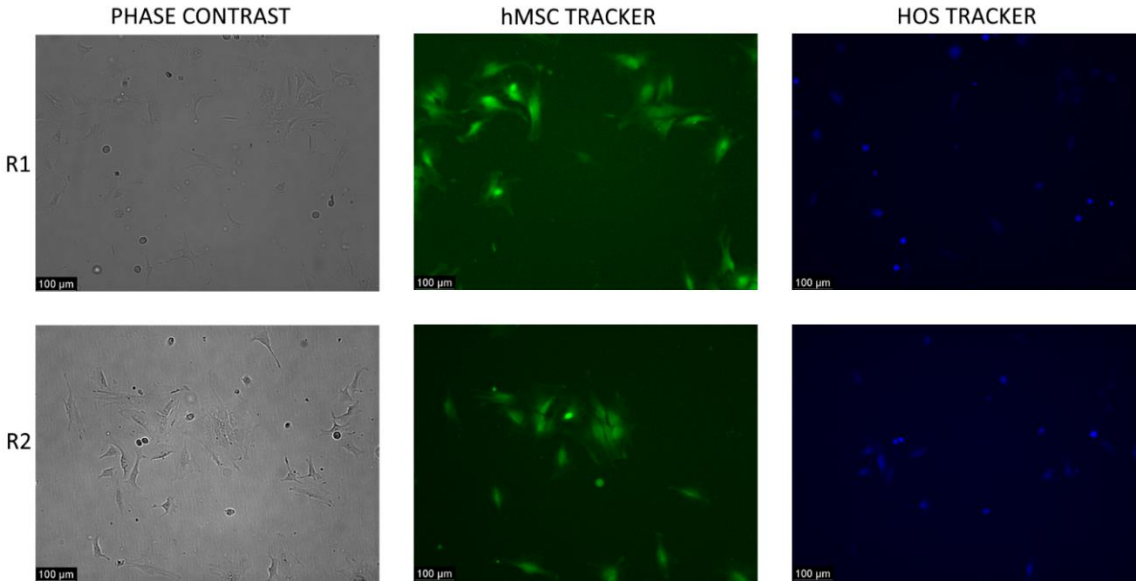

Figure 6.3: Tracking of hMSC and HOS at 3hrs

Representative images of hMSC and HOS cells grown in co-culture on tissue culture plastic at 3hrs. Both hMSC and HOS were introduced to the same well dish seeded at 5000 cells/cm^2 having each been subject to cell trackers. In the green excitation spectra, CMFDA was used to track hMSC and in the blue CMAC to track HOS. Phase contrast images were taken to view all cells. R1 and R2 show repeats one and two across the rows.

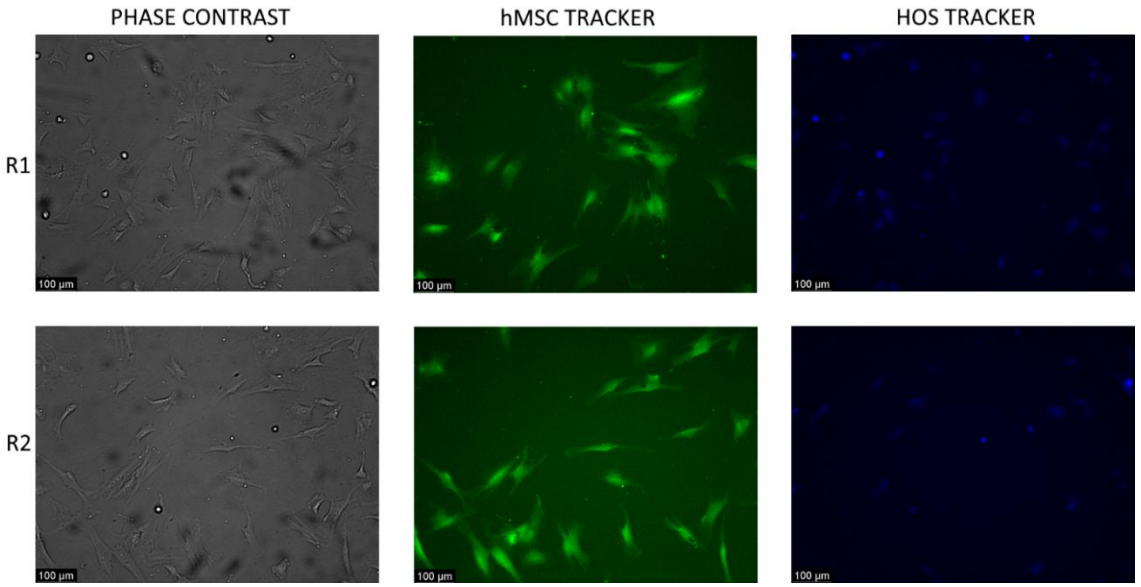

Figure 6.4: Tracking of hMSC and HOS at 6hrs

Representative images of hMSC and HOS cells grown in co-culture on tissue culture plastic at 6hrs. Both hMSC and HOS were introduced to the same well dish seeded at 5000 cells/cm^2 having each been subject to cell trackers. In the green excitation spectra, CMFDA was used to track hMSC and in the blue CMAC to track HOS. Phase contrast images were taken to view all cells. R1 and R2 show repeats one and two across the rows.

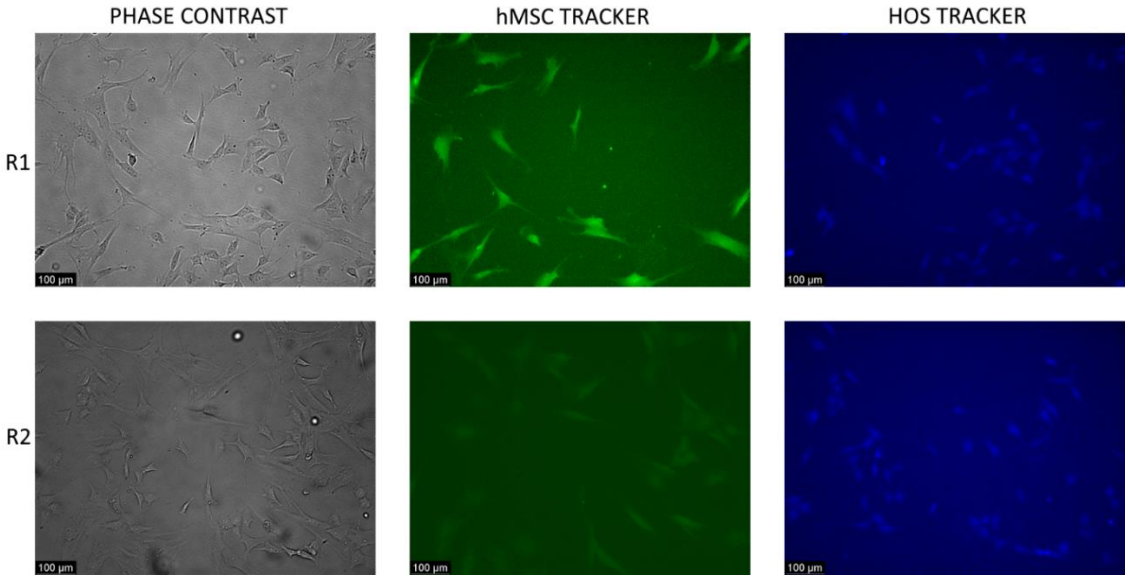

Figure 6.5: Tracking of hMSC and HOS at 24hrs

Representative images of hMSC and HOS cells grown in co-culture on tissue culture plastic at 24hrs. Both hMSC and HOS were introduced to the same well dish seeded at 5000 cells/cm^2 having each been subject to cell trackers. In the green excitation spectra, CMFDA was used to track hMSC and in the blue CMAC to track HOS. Phase contrast images were taken to view all cells. R1 and R2 show repeats one and two across the rows.

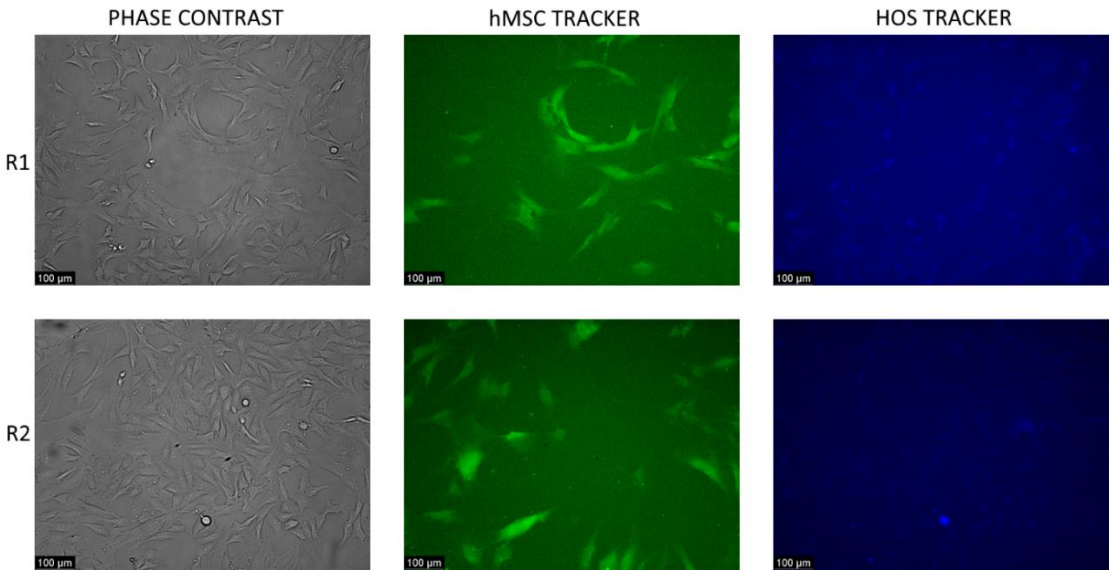

Figure 6.6: Tracking of hMSC and HOS at 48hrs

Representative images of hMSC and HOS cells grown in co-culture on tissue culture plastic at 48hrs. Both hMSC and HOS were introduced to the same well dish seeded at 5000 cells/cm^2 having each been subject to cell trackers. In the green excitation spectra, CMFDA was used to track hMSC and in the blue CMAC to track HOS. Phase contrast images were taken to view all cells. R1 and R2 show repeats one and two across the rows.

SEM analysis of bone fragments was undertaken to better understand the surface topography and variance between cortical, cancellous and rib fragments. In Chapter 3, Figure 3.13, examples of each fragment type were shown at varying magnifications. Here, in Figure 6.7, Figure 6.8 and Figure 6.9, repeat fragments of cortical, cancellous and rib fragments respectively are shown at x50, x500 and x1500.

In the same manner, SEM analysis of fragments with cells were taken, shown in Chapter 3 Figure 3.14 to Figure 3.19. Here, for cortical, cancellous and rib fragments, six micrographs at x1500 are shown respectively in Figure 6.10, Figure 6.11 and Figure 6.12.

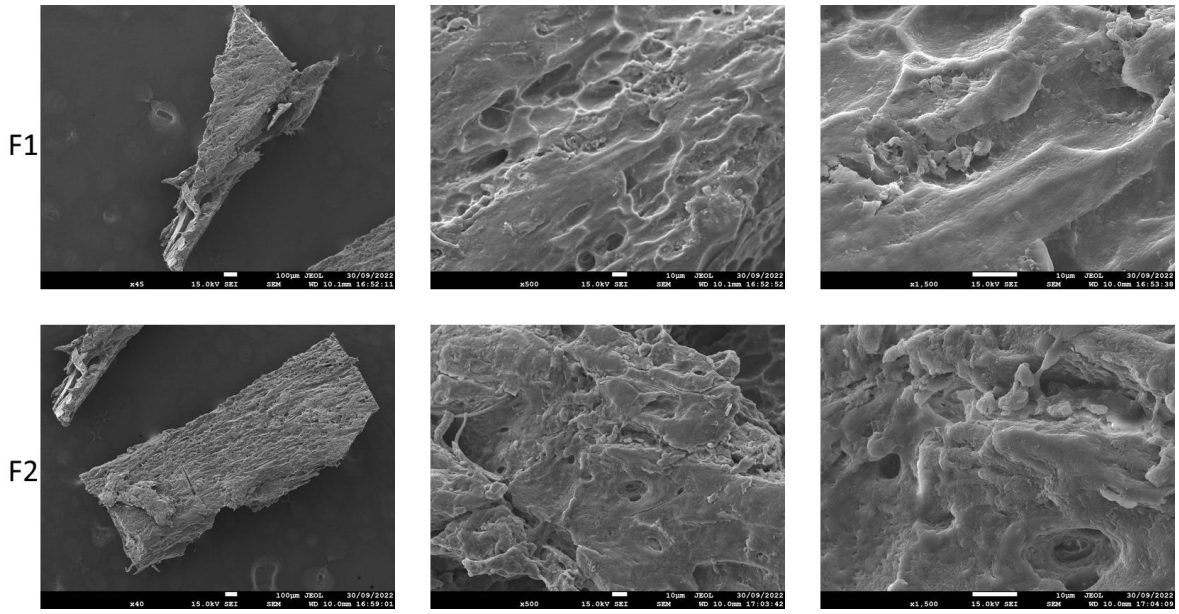

Figure 6.7: SEM micrographs of cortical fragments

SEM micrographs of decellularised rat bone cortical fragments 1 and 2. Each row of micrographs are sequential higher magnifications of the same fragment (x50, x500 & x1500).

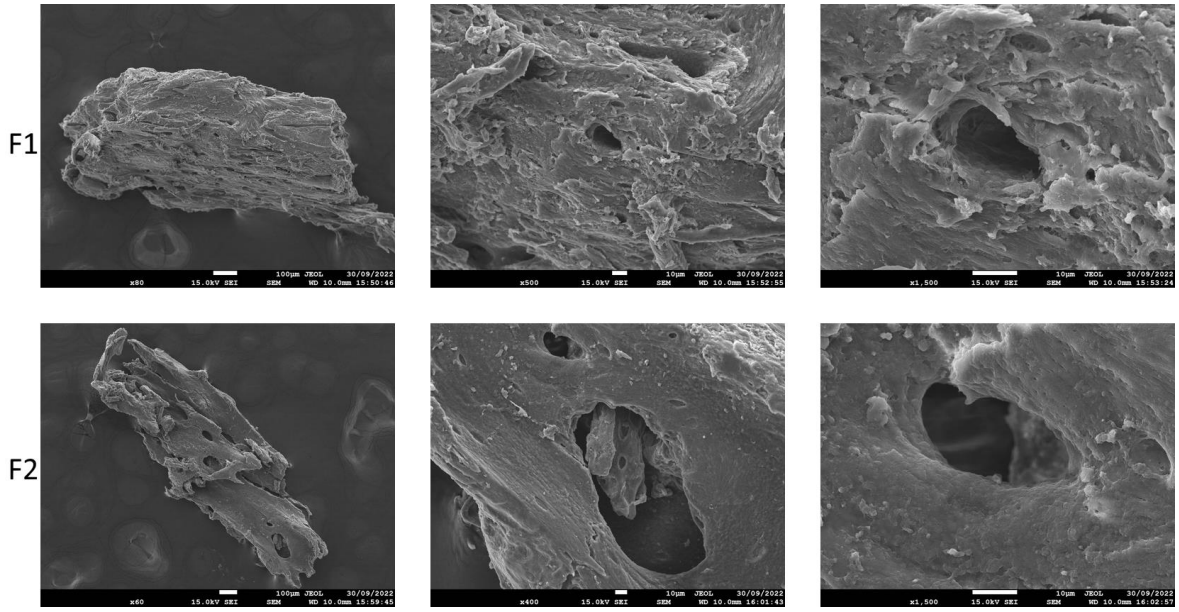

Figure 6.8: SEM micrographs of cancellous fragments

SEM micrographs of decellularised rat bone cancellous fragments 1 and 2. Each row of micrographs are sequential higher magnifications of the same fragment (x50, x500 & x1500).

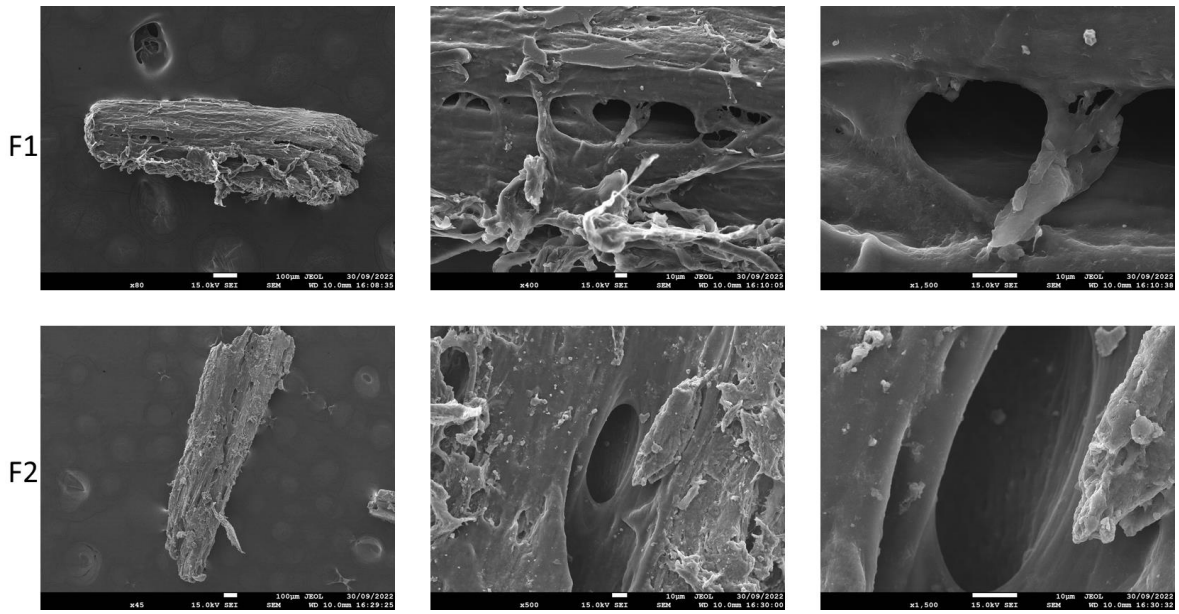

Figure 6.9: SEM micrographs of rib fragments

SEM micrographs of decellularised rat bone rib fragments 1 and 2. Each row of micrographs are sequential higher magnifications of the same fragment (x50, x500 & x1500).

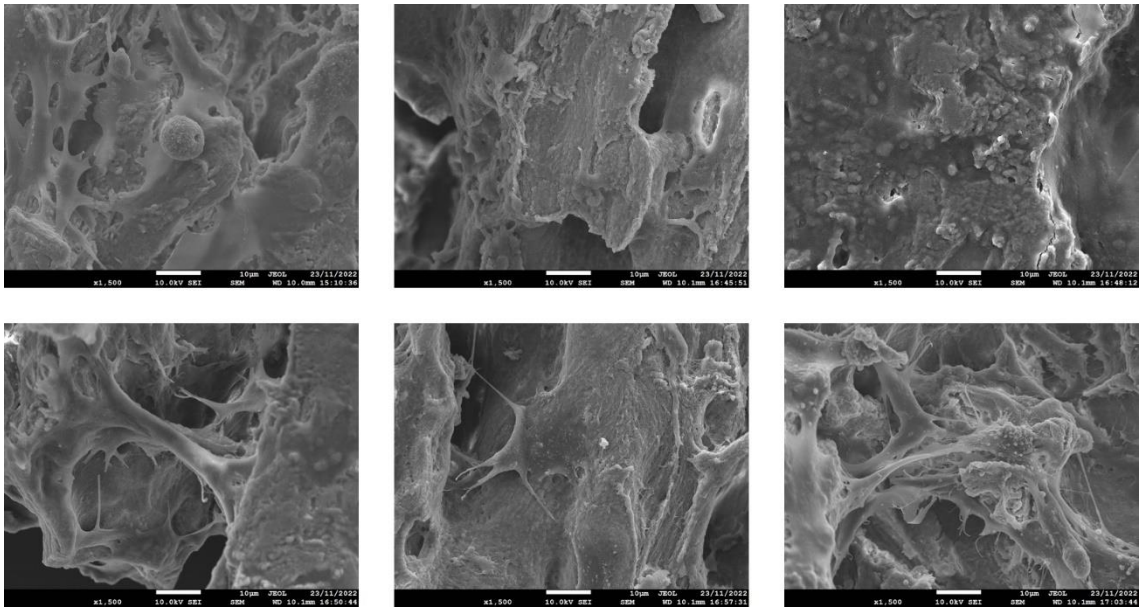

Figure 6.10: SEM micrographs of cortical fragments seeded with HOS

SEM micrographs of cortical decellularised rat bone seeded with HOS at 5000 cells/cm^2. Micrographs are all taken at x1500 taken from varying regions.

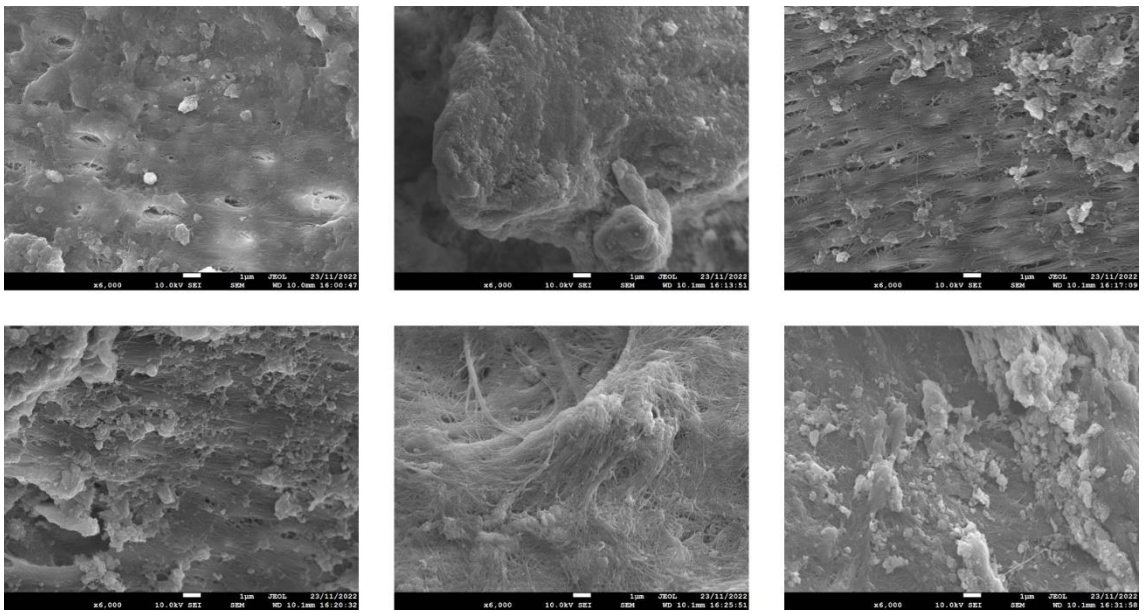

Figure 6.11: SEM micrographs of cancellous fragments seeded with HOS

SEM micrographs of cancellous decellularised rat bone seeded with HOS at 5000 cells/cm^2. Micrographs are all taken at x1500 taken from varying regions.

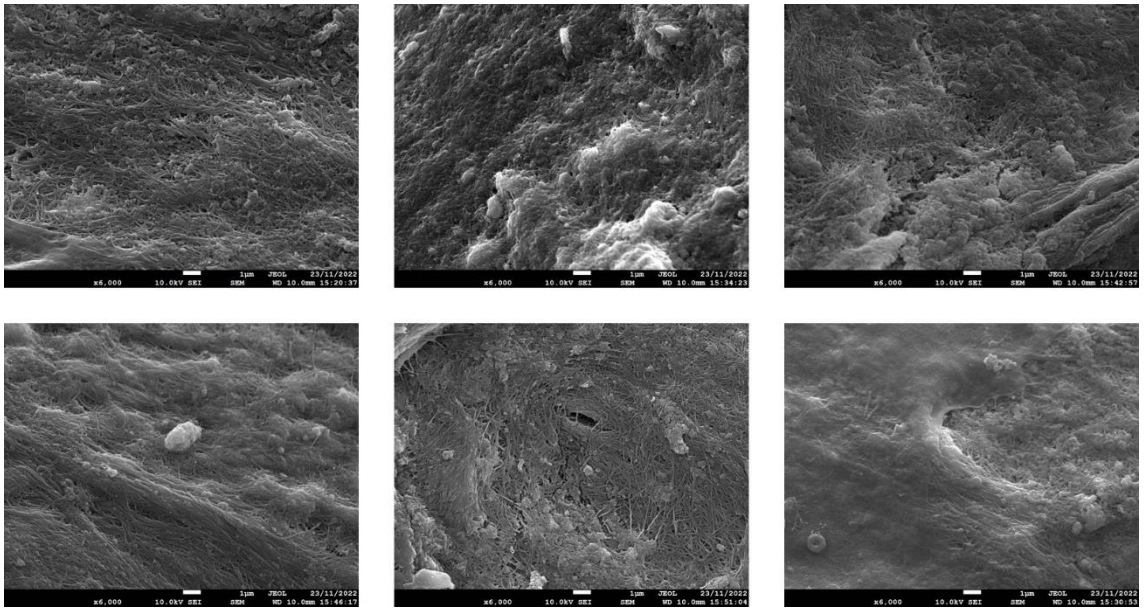

Figure 6.12: SEM micrographs of rib fragments seeded with HOS

SEM micrographs of cortical decellularised rat bone seeded with HOS at 5000 cells/cm^2. Micrographs are all taken at x1500 taken from varying regions.

Ultimately three models were developed during this project, each building on the last. Model 1 included the culturing of hMSCs on decellularized rat bone with OCM (and BM as a control). Model 2 added mechanical stimulation from the Nanokick platform. Model 3 added the HOS cell type as an analogue for osteoblasts. In order to determine the relative amount of osteogenesis across the three models developed, IHC was utilised to determine the levels of OCN and OPN in various samples of each model. The combined channels for OCN (green), OPN (red) and a nuclear stain (blue) are found below in Figure 6.13, Figure 6.14 and Figure 6.15 for models 1, 2 and 3 respectively.

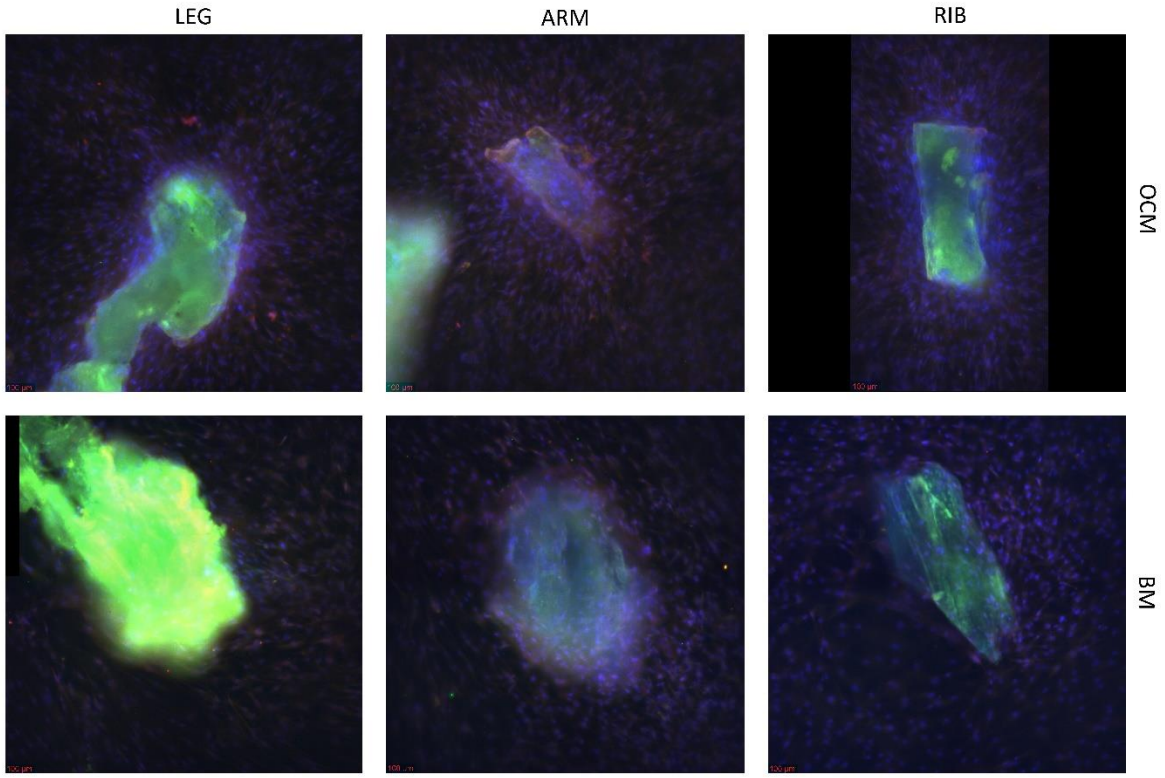

Figure 6.13: Macroscopic model, Model 1, hMSC on bone with osteogenic media IHC - Merged

Representative micrographs from Immunohistochemical staining of Model 1, hMSC seeded onto bone fragments after 28 days incubation. The three columns from left to right are of leg fragments, arm fragments and rib fragments. The top row are samples which were incubated in osteogenic media (OCM) and the bottom incubated in basal media (BM). Each image is a merging of the three channels for OCN (green), OPN (red) and nuclear stain (blue).

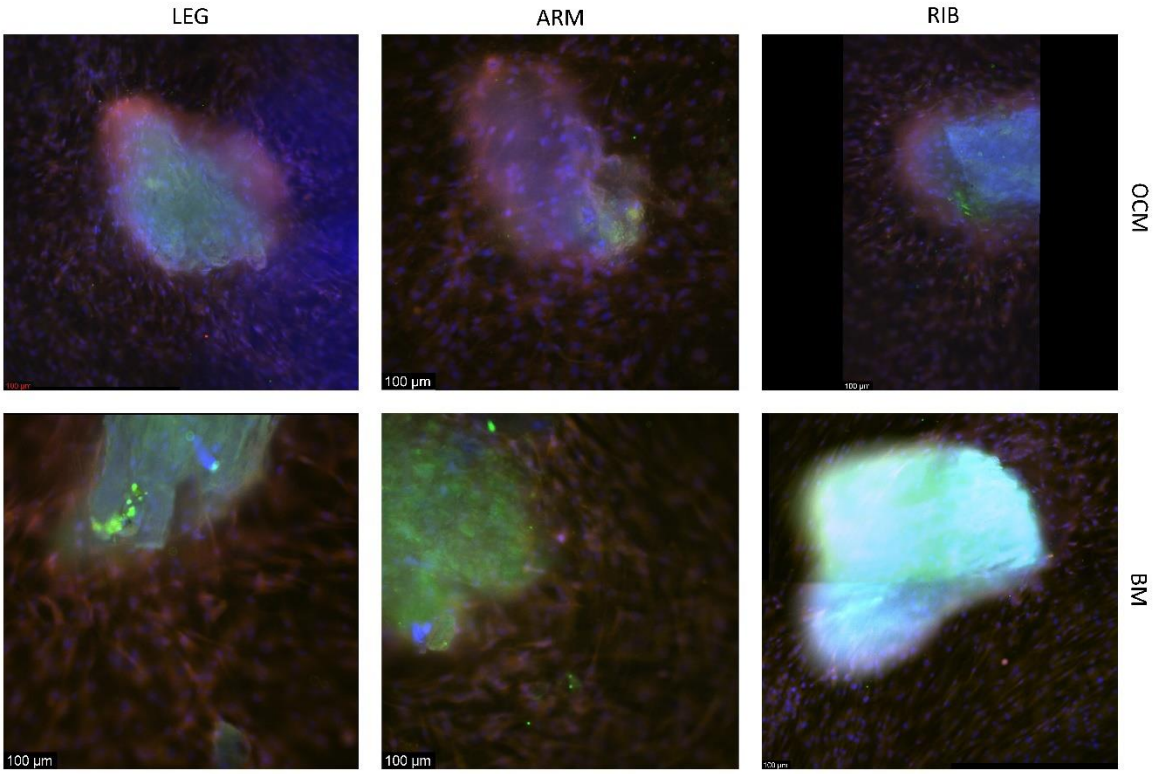

Figure 6.14: Macroscopic model, Model 2, hMSC & Hz on bone with osteogenic media - Merged

Representative micrographs from Immunohistochemical staining of Model 2, hMSC seeded onto bone fragments after 28 days incubation on the Nanokick device. The three columns from left to right are of leg fragments, arm fragments and rib fragments. The top row are samples which were incubated in osteogenic media (OCM) and the bottom incubated in basal media (BM). Each image is a merging of the three channels for OCN (green), OPN (red) and nuclear stain (blue).

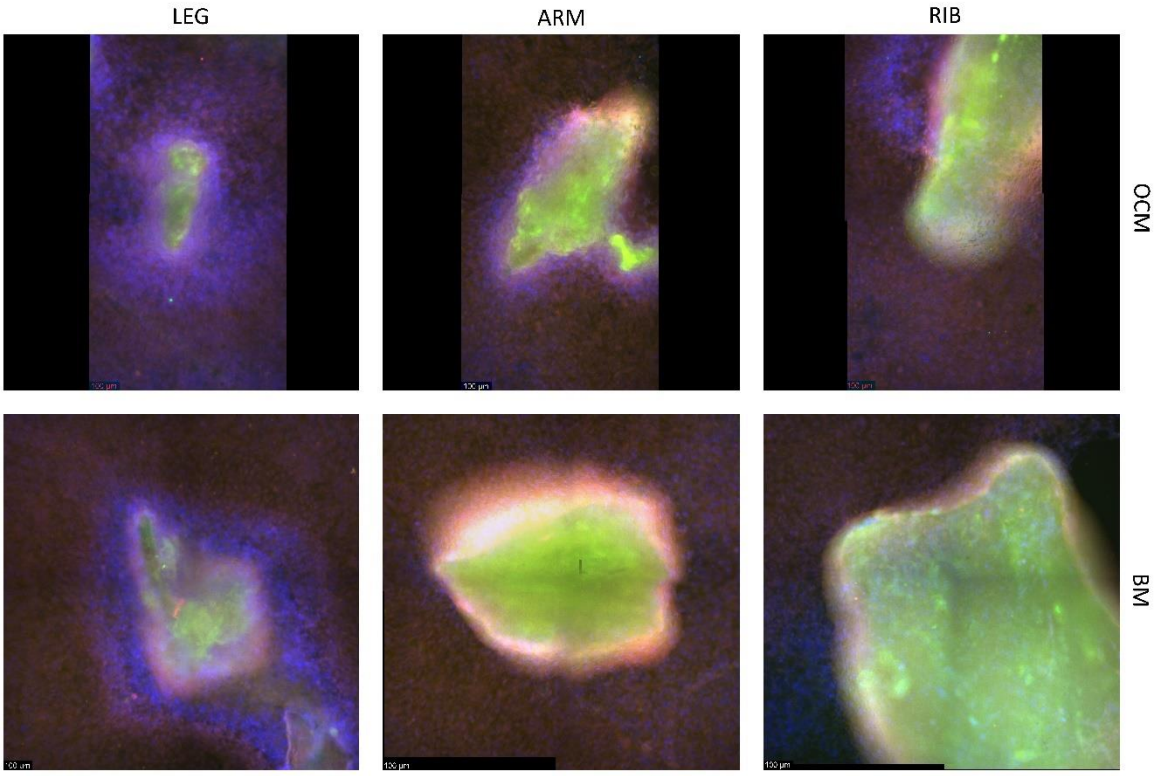

Figure 6.15: Macroscopic model, Model 3, hMSC, HOS & Hz on bone with osteogenic media - Merged

Representative micrographs from Immunohistochemical staining of Model 3, hMSC and HOS seeded onto bone fragments after 28 days incubation on the Nanokick device. The three columns from left to right are of leg fragments, arm fragments and rib fragments. The top row are samples which were incubated in osteogenic media (OCM) and the bottom incubated in basal media (BM). Each image is a merging of the three channels for OCN (green), OPN (red) and nuclear stain (blue).

Patterning of HOS and small fragments using HOTs was shown in Chapter 4, Figure 4.7. Screen shots of the operating software including the location of the traps is shown in Figure 6.16.

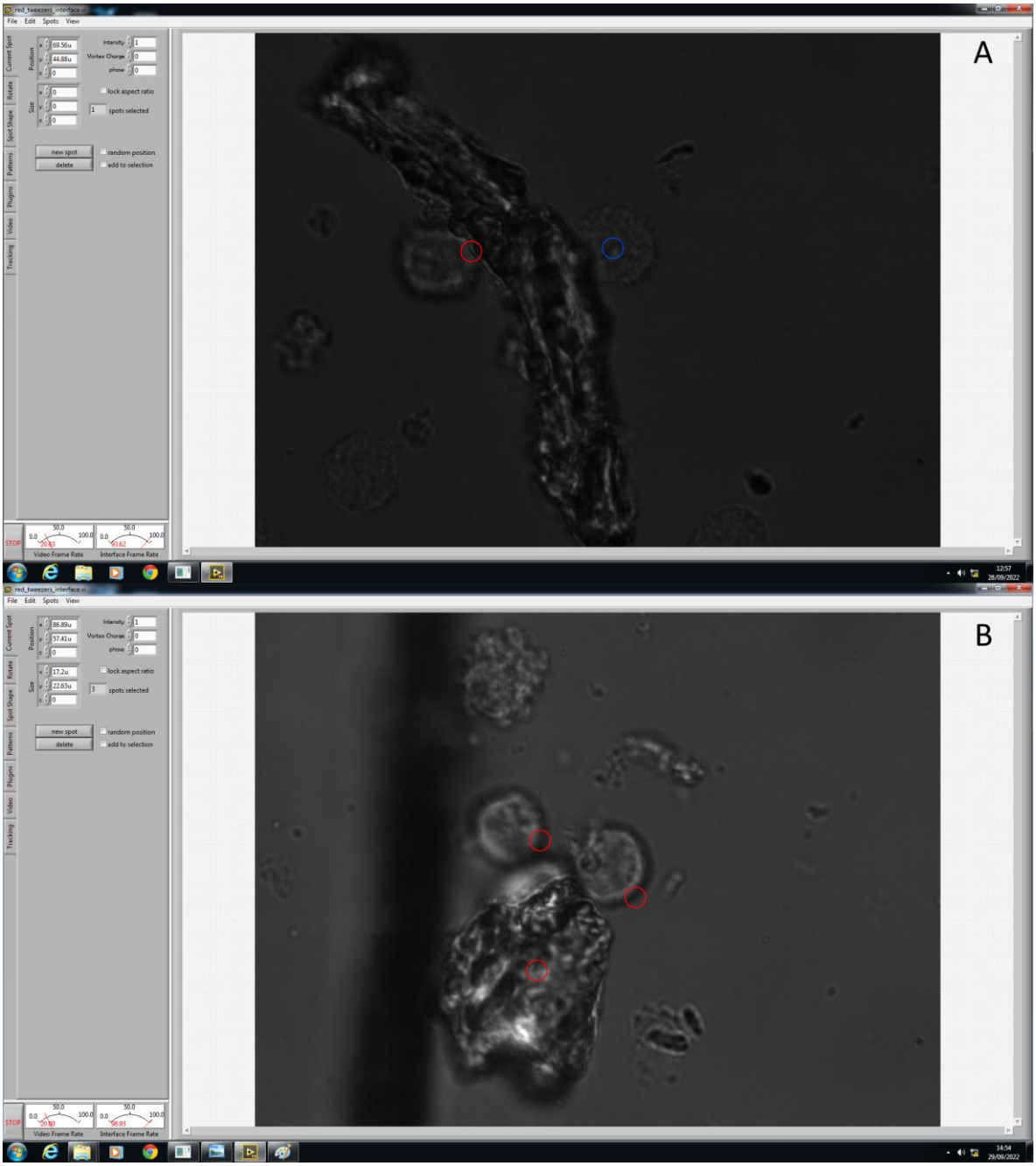

Figure 6.16: Manipulation of HOS cells patterned with small rat bone fragments using HOTs-software screenshot

Images captured through the Holographic Optical Tweezers of HOS cells being manipulated and placed onto small decellularised rat bone fragments in a glass bottomed imaging dish. Coloured circles show locations of traps.

7. References

Alom, N., Peto, H., Kirkham, G. R., Shakesheff, K. M., & White, L. J. (2018). Bone extracellular matrix hydrogel enhances osteogenic differentiation of C2C12 myoblasts and mouse primary calvarial cells. *Journal of Biomedical Materials Research - Part B Applied Biomaterials*, *106*(2), 900–908. https://doi.org/10.1002/JBM.B.33894

Aly, R. M. (2020). Current state of stem cell-based therapies: an overview. *Stem Cell Investigation*, *7*(May), 8. https://doi.org/10.21037/SCI-2020-001

Amirazad, H., Dadashpour, M., & Zarghami, N. (2022). Application of decellularized bone matrix as a bioscaffold in bone tissue engineering. *Journal of Biological Engineering 2021 16:1*, *16*(1), 1–18. https://doi.org/10.1186/S13036-021-00282-5

Anton, D., Burckel, H., Josset, E., & Noel, G. (2015). Three-Dimensional Cell Culture: A Breakthrough in Vivo. *International Journal of Molecular Sciences 2015, Vol. 16, Pages 5517-5527*, *16*(3), 5517–5527. https://doi.org/10.3390/IJMS16035517

Asada, N., Takeishi, S., & Frenette, P. S. (2017). Complexity of bone marrow hematopoietic stem cell niche. *International Journal of Hematology*, *106*(1), 45–54. https://doi.org/10.1007/S12185-017-2262-9/FIGURES/3

Ashkin, A. (1992). Forces of a single-beam gradient laser trap on a dielectric sphere in the ray optics regime. *Biophysical Journal*, *61*(2), 569–582. https://doi.org/10.1016/S0006-3495(92)81860-X

Ashkin, A. (2000). History of optical trapping and manipulation of small-neutral particle, atoms, and molecules. *IEEE Journal on Selected Topics in Quantum Electronics*, *6*(6), 841–856. https://doi.org/10.1109/2944.902132

Ashkin, A., & Dziedzic, J. M. (1971). Optical Levitation by Radiation Pressure. *Applied Physics Letters*, *19*(8), 283. https://doi.org/10.1063/1.1653919

Ashkin, A., & Dziedzic, J. M. (1975). Optical levitation of liquid drops by radiation pressure. *Science (New York, N.Y.)*, *187*(4181), 1073–1075. https://doi.org/10.1126/SCIENCE.187.4181.1073

Ashkin, A., Dziedzic, J. M., & Yamanet, T. (1987). Optical trapping and manipulation of single cells using infrared laser beams. *Nature 1987 330:6150*, *330*(6150), 769–771. https://doi.org/10.1038/330769a0

Ashok, P. C., & Dholakia, K. (2012). Optical trapping for analytical biotechnology. *Current Opinion in Biotechnology*, *23*(1), 16–21. https://doi.org/10.1016/J.COPBIO.2011.11.011

Baccin, C., Al-Sabah, J., Velten, L., Helbling, P. M., Grünschläger, F., Hernández-Malmierca, P., Nombela-Arrieta, C., Steinmetz, L. M., Trumpp, A., & Haas, S. (2019). Combined single-cell and spatial transcriptomics reveal the molecular, cellular and spatial bone marrow

niche organization. *Nature Cell Biology 2019 22:1*, *22*(1), 38–48. https://doi.org/10.1038/s41556-019-0439-6

Baker, B. M., & Chen, C. S. (2012). Deconstructing the third dimension-how 3D culture microenvironments alter cellular cues. *Journal of Cell Science*, *125*(13), 3015–3024. https://doi.org/10.1242/JCS.079509/258092/AM/DECONSTRUCTING-THE-THIRD-DIMENSION-HOW-3D-CULTURE

Balducci, L., Blasi, A., Saldarelli, M., Soleti, A., Pessina, A., Bonomi, A., Coccè, V., Dossena, M., Tosetti, V., Ceserani, V., Navone, S. E., Falchetti, M. L., Parati, E. A., & Alessandri, G. (2014). Immortalization of human adipose-derived stromal cells: Production of cell lines with high growth rate, mesenchymal marker expression and capability to secrete high levels of angiogenic factors. *Stem Cell Research and Therapy*, *5*(3), 1–15. https://doi.org/10.1186/SCRT452/FIGURES/9

Bara, J. J., Richards, R. G., Alini, M., & Stoddart, M. J. (2014). Concise Review: Bone Marrow-Derived Mesenchymal Stem Cells Change Phenotype Following In Vitro Culture: Implications for Basic Research and the Clinic. *Stem Cells*, *32*(7), 1713–1723. https://doi.org/10.1002/STEM.1649

Barabaschi, G. D. G., Manoharan, V., Li, Q., & Bertassoni, L. E. (2015). Engineering Pre-vascularized Scaffolds for Bone Regeneration. *Advances in Experimental Medicine and Biology*, *881*, 79–94. https://doi.org/10.1007/978-3-319-22345-2_5

Baron, R., & Kneissel, M. (2013). WNT signaling in bone homeostasis and disease: from human mutations to treatments. *Nature Medicine 2013 19:2*, *19*(2), 179–192. https://doi.org/10.1038/nm.3074

Barry, F., & Murphy, M. (2013). Mesenchymal stem cells in joint disease and repair. *Nature Reviews Rheumatology 2013 9:10*, *9*(10), 584–594. https://doi.org/10.1038/nrrheum.2013.109

Baryawno, N., Przybylski, D., Kowalczyk, M. S., Kfoury, Y., Severe, N., Gustafsson, K., Kokkaliaris, K. D., Mercier, F., Tabaka, M., Hofree, M., Dionne, D., Papazian, A., Lee, D., Ashenberg, O., Subramanian, A., Vaishnav, E. D., Rozenblatt-Rosen, O., Regev, A., & Scadden, D. T. (2019). A Cellular Taxonomy of the Bone Marrow Stroma in Homeostasis and Leukemia. *Cell*, *177*(7), 1915-1932.e16. https://doi.org/10.1016/J.CELL.2019.04.040/ASSET/4AEFB4A0-F4B3-4390-85B6-CD46E11AE785/MAIN.ASSETS/FIGS7.JPG

Birkedal-Hansen, H., Moore, W. G. I., Bodden, M. K., Windsor, L. J., Birkedal-Hansen, B., DeCarlo, A., & Engler, J. A. (1993). Matrix metalloproteinases: A review. *Critical Reviews in Oral Biology and Medicine*, *4*(2), 197–250. https://doi.org/10.1177/10454411930040020401

Bishop, A. E., Buttery, L. D. K., & Polak, J. M. (2002). Haematopoietic stem cells1. *The Journal of Pathology*, *197*(4), 430–440. https://doi.org/10.1002/PATH.1153

Blank, U., & Karlsson, S. (2015). TGF-β signaling in the control of hematopoietic stem cells. *Blood*, *125*(23), 3542–3550. https://doi.org/10.1182/BLOOD-2014-12-618090

Blanpain, C., & Fuchs, E. (2006). Epidermal stem cells of the skin. *Annual Review of Cell and Developmental Biology*, *22*(Volume 22, 2006), 339–373. https://doi.org/10.1146/ANNUREV.CELLBIO.22.010305.104357/CITE/REFWORKS

Bolamperti, S., Villa, I., & Rubinacci, A. (2022). Bone remodeling: an operational process ensuring survival and bone mechanical competence. *Bone Research 2022 10:1*, *10*(1), 1–19. https://doi.org/10.1038/s41413-022-00219-8

Bonewald, L. F. (2007). Osteocytes as dynamic multifunctional cells. *Annals of the New York Academy of Sciences*, *1116*, 281–290. https://doi.org/10.1196/ANNALS.1402.018

Bonewald, L. F. (2011). The amazing osteocyte. *Journal of Bone and Mineral Research : The Official Journal of the American Society for Bone and Mineral Research*, *26*(2), 229–238. https://doi.org/10.1002/JBMR.320

Bonnet, D. (2003). Biology of human bone marrow stem cells. *Clinical and Experimental Medicine 2003 3:3*, *3*(3), 140–149. https://doi.org/10.1007/S10238-003-0017-9

Boskey, A. L., & Posner, A. S. (1984). Bone structure, composition, and mineralization. *The Orthopedic Clinics of North America*, *15*(4), 597–612. https://doi.org/10.1016/s0742-0668(23)00071-7

Bowman, R. W., Gibson, G. M., Linnenberger, A., Phillips, D. B., Grieve, J. A., Carberry, D. M., Serati, S., Miles, M. J., & Padgett, M. J. (2014). "Red Tweezers": Fast, customisable hologram generation for optical tweezers. *Computer Physics Communications*, *185*(1), 268–273. https://doi.org/10.1016/J.CPC.2013.08.008

Burr, D. B., & Akkus, O. (2013). Bone Morphology and Organization. *Basic and Applied Bone Biology*, 3–25. https://doi.org/10.1016/B978-0-12-416015-6.00001-0

Buttery, L. D. K., Bourne, S., Xynos, J. D., Wood, H., Hughes, F. J., Hughes, S. P. F., Episkopou, V., & Polak, J. M. (2001). Differentiation of osteoblasts and in vitro bone formation from murine embryonic stem cells. *Tissue Engineering*, *7*(1), 89–99. https://doi.org/10.1089/107632700300003323

Calori, G. M., Mazza, E., Colombo, M., & Ripamonti, C. (2011). The use of bone-graft substitutes in large bone defects: Any specific needs? *Injury*, *42*(SUPPL. 2), S56–S63. https://doi.org/10.1016/J.INJURY.2011.06.011

Calvi, L. M., Adams, G. B., Weibrecht, K. W., Weber, J. M., Olson, D. P., Knight, M. C., Martin, R. P., Schipani, E., Divieti, P., Bringhurst, F. R., Milner, L. A., Kronenberg, H. M., & Scadden,

D. T. (2003). Osteoblastic cells regulate the haematopoietic stem cell niche. *Nature 2003 425:6960*, *425*(6960), 841–846. https://doi.org/10.1038/nature02040

Caplan, A. I. (2005). Review: mesenchymal stem cells: cell-based reconstructive therapy in orthopedics. *Tissue Engineering*, *11*(7–8), 1198–1211. https://doi.org/10.1089/TEN.2005.11.1198

Caplan, A. I. (2007). Adult mesenchymal stem cells for tissue engineering versus regenerative medicine. *Journal of Cellular Physiology*, *213*(2), 341–347. https://doi.org/10.1002/JCP.21200

Capulli, M., Paone, R., & Rucci, N. (2014). Osteoblast and osteocyte: Games without frontiers. *Archives of Biochemistry and Biophysics*, *561*, 3–12. https://doi.org/10.1016/J.ABB.2014.05.003

Carbonare, L. D., Innamorati, G., & Valenti, M. T. (2012). Transcription Factor Runx2 and its Application to Bone Tissue Engineering. *Stem Cell Reviews and Reports*, *8*(3), 891–897. https://doi.org/10.1007/S12015-011-9337-4/FIGURES/1

Charras, G., & Sahai, E. (2014). Physical influences of the extracellular environment on cell migration. *Nature Reviews Molecular Cell Biology 2014 15:12*, *15*(12), 813–824. https://doi.org/10.1038/nrm3897

Chen, N. X., Ryder, K. D., Pavalko, F. M., Turner, C. H., Burr, D. B., Qiu, J., & Duncan, R. L. (2000). Ca2+ regulates fluid shear-induced cytoskeletal reorganization and gene expression in osteoblasts. *American Journal of Physiology - Cell Physiology*, *278*(5 47-5). https://doi.org/10.1152/AJPCELL.2000.278.5.C989/ASSET/IMAGES/LARGE/ACEL00516006BW.JPEG

Chen, X. D., Dusevich, V., Feng, J. Q., Manolagas, S. C., & Jilka, R. L. (2007). Extracellular Matrix Made by Bone Marrow Cells Facilitates Expansion of Marrow-Derived Mesenchymal Progenitor Cells and Prevents Their Differentiation Into Osteoblasts. *Journal of Bone and Mineral Research*, *22*(12), 1943–1956. https://doi.org/10.1359/JBMR.070725

Childs, P. G., Boyle, C. A., Pemberton, G. D., Nikukar, H., Curtis, A. S. G., Henriquez, F. L., Dalby, M. J., & Reid, S. (2016). Use of nanoscale mechanical stimulation for control and manipulation of cell behaviour. *Acta Biomaterialia*, *34*, 159–168. https://doi.org/10.1016/J.ACTBIO.2015.11.045

Chiou, P. Y., Ohta, A. T., & Wu, M. C. (2005). Massively parallel manipulation of single cells and microparticles using optical images. *Nature*, *436*(7049), 370–372. https://doi.org/10.1038/NATURE03831

Chistiakov, D. A., Orekhov, A. N., & Bobryshev, Y. V. (2017). Effects of shear stress on endothelial cells: go with the flow. *Acta Physiologica*, *219*(2), 382–408. https://doi.org/10.1111/APHA.12725

Choi, Y., Kim, H.-J., & Min, K.-S. (2016). Effects of proanthocyanidin, a crosslinking agent, on physical and biological properties of collagen hydrogel scaffold. *Restorative Dentistry & Endodontics*, *41*(4), 296–303. https://doi.org/10.5395/RDE.2016.41.4.296

Chung, C. H., Golub, E. E., Forbes, E., Tokuoka, T., & Shapiro, I. M. (1992). Mechanism of action of β-glycerophosphate on bone cell mineralization. *Calcified Tissue International*, *51*(4), 305–311. https://doi.org/10.1007/BF00334492/METRICS

Clarke, B. (2008a). Normal bone anatomy and physiology. *Clinical Journal of the American Society of Nephrology : CJASN*, *3 Suppl 3*. https://doi.org/10.2215/CJN.04151206

Clarke, B. (2008b). Normal Bone Anatomy and Physiology The Skeleton. *Clin J Am Soc Nephrol*, *3*, 131–139. https://doi.org/10.2215/CJN.04151206

Colter, D. C., Sekiya, I., & Prockop, D. J. (2001). Identification of a subpopulation of rapidly self-renewing and multipotential adult stem cells in colonies of human marrow stromal cells. *Proceedings of the National Academy of Sciences*, *98*(14), 7841–7845. https://doi.org/10.1073/PNAS.141221698

Cowan, P. T., Launico, M. V., & Kahai, P. (2024). Anatomy, Bones. *StatPearls*. https://www.ncbi.nlm.nih.gov/books/NBK537199/

Crapo, P. M., Gilbert, T. W., & Badylak, S. F. (2011). An overview of tissue and whole organ decellularization processes. *Biomaterials*, *32*(12), 3233–3243. https://doi.org/10.1016/J.BIOMATERIALS.2011.01.057

Czekanska, E., Stoddart, M., Mater, R. R.-E. C., & 2012, undefined. (2012). In search of an osteoblast cell model for in vitro research. *Ecmjournal.OrgEM Czekanska, MJ Stoddart, RG Richards, JS HayesEur Cell Mater, 2012•ecmjournal.Org*, *24*(2012), 1–17. https://doi.org/10.22203/eCM.v024a01

Dahl, A. C. E., & Thompson, M. S. (2011). Mechanobiology of Bone. *Comprehensive Biotechnology, Second Edition*, *5*, 217–236. https://doi.org/10.1016/B978-0-08-088504-9.00419-0

Dalby, M. J., Gadegaard, N., Tare, R., Andar, A., Riehle, M. O., Herzyk, P., Wilkinson, C. D. W., & Oreffo, R. O. C. (2007). The control of human mesenchymal cell differentiation using nanoscale symmetry and disorder. *Nature Materials 2007 6:12*, *6*(12), 997–1003. https://doi.org/10.1038/nmat2013

Danen, E. H. J. (2013). *Integrins: An Overview of Structural and Functional Aspects*. https://www.ncbi.nlm.nih.gov/books/NBK6259/

Daoud, J. T., Petropavlovskaia, M. S., Patapas, J. M., Degrandpré, C. E., DiRaddo, R. W., Rosenberg, L., & Tabrizian, M. (2011). Long-term in vitro human pancreatic islet culture using three-dimensional microfabricated scaffolds. *Biomaterials*, *32*(6), 1536–1542. https://doi.org/10.1016/J.BIOMATERIALS.2010.10.036

de Bardet, J. C., Cardentey, C. R., González, B. L., Patrone, D., Mulet, I. L., Siniscalco, D., & Robinson-Agramonte, M. de los A. (2023). Cell Immortalization: In Vivo Molecular Bases and In Vitro Techniques for Obtention. *BioTech 2023, Vol. 12, Page 14*, *12*(1), 14. https://doi.org/10.3390/BIOTECH12010014

De Vlaminck, I., & Dekker, C. (2012). Recent advances in magnetic tweezers. *Annual Review of Biophysics*, *41*(1), 453–472. https://doi.org/10.1146/ANNUREV-BIOPHYS-122311-100544/CITE/REFWORKS

Denhardt, D. T., & Guo, X. (1993). Osteopontin: a protein with diverse functions. *The FASEB Journal*, *7*(15), 1475–1482. https://doi.org/10.1096/FASEBJ.7.15.8262332

Ding, L., Saunders, T. L., Enikolopov, G., & Morrison, S. J. (2012). Endothelial and perivascular cells maintain haematopoietic stem cells. *Nature 2012 481:7382*, *481*(7382), 457–462. https://doi.org/10.1038/nature10783

Ding, X., Li, P., Lin, S. C. S., Stratton, Z. S., Nama, N., Guo, F., Slotcavage, D., Mao, X., Shi, J., Costanzo, F., & Huang, T. J. (2013). Surface acoustic wave microfluidics. *Lab on a Chip*, *13*(18), 3626. https://doi.org/10.1039/C3LC50361E

Dominici, M., Le Blanc, K., Mueller, I., Slaper-Cortenbach, I., Marini, F. C., Krause, D. S., Deans, R. J., Keating, A., Prockop, D. J., & Horwitz, E. M. (2006). Minimal criteria for defining multipotent mesenchymal stromal cells. The International Society for Cellular Therapy position statement. *Cytotherapy*, *8*(4), 315–317. https://doi.org/10.1080/14653240600855905

Drinkwater, B. W. (2020). A Perspective on acoustical tweezers - Devices, forces, and biomedical applications. *Applied Physics Letters*, *117*(18). https://doi.org/10.1063/5.0028443/1061351

Drosos, G. I., Kazakos, K. I., Kouzoumpasis, P., & Verettas, D. A. (2007). Safety and efficacy of commercially available demineralised bone matrix preparations: A critical review of clinical studies. *Injury*, *38*(4 SUPPL.), S13–S21. https://doi.org/10.1016/S0020-1383(08)70005-6

Ducy, P., Zhang, R., Geoffroy, V., Ridall, A. L., & Karsenty, G. (1997). Osf2/Cbfa1: A transcriptional activator of osteoblast differentiation. *Cell*, *89*(5), 747–754. https://doi.org/10.1016/S0092-8674(00)80257-3

Dutta, R. C., & Dutta, A. K. (2009). Cell-interactive 3D-scaffold; advances and applications. *Biotechnology Advances*, *27*(4), 334–339. https://doi.org/10.1016/J.BIOTECHADV.2009.02.002

Duval, K., Grover, H., Han, L. H., Mou, Y., Pegoraro, A. F., Fredberg, J., & Chen, Z. (2017). Modeling physiological events in 2D vs. 3D cell culture. *Physiology*, *32*(4), 266–277.

https://doi.org/10.1152/PHYSIOL.00036.2016/ASSET/IMAGES/LARGE/PHY0041703840003.JPEG

Edmondson, R., Broglie, J. J., Adcock, A. F., & Yang, L. (2014). Three-Dimensional Cell Culture Systems and Their Applications in Drug Discovery and Cell-Based Biosensors. *Https://Home.Liebertpub.Com/Adt*, *12*(4), 207–218. https://doi.org/10.1089/ADT.2014.573

Eerden, B. Van der, Karperien, M., reviews, J. W.-E., & 2003, undefined. (2003). Systemic and local regulation of the growth plate. *Academic.Oup.ComBCJ Van Der Eerden, M Karperien, JM WitEndocrine Reviews, 2003•academic.Oup.Com*. https://doi.org/10.1210/er.2002-0033

Ehninger, A., & Trumpp, A. (2011). The bone marrow stem cell niche grows up: mesenchymal stem cells and macrophages move in. *The Journal of Experimental Medicine*, *208*(3), 421–428. https://doi.org/10.1084/jem.20110132

Evans, M. J., & Kaufman, M. H. (1981). Establishment in culture of pluripotential cells from mouse embryos. *Nature 1981 292:5819*, *292*(5819), 154–156. https://doi.org/10.1038/292154a0

Everts, V., Delaissié, J. M., Korper, W., Jansen, D. C., Tigchelaar-Gutter, W., Saftig, P., & Beertsen, W. (2002). The Bone Lining Cell: Its Role in Cleaning Howship's Lacunae and Initiating Bone Formation. *Journal of Bone and Mineral Research*, *17*(1), 77–90. https://doi.org/10.1359/JBMR.2002.17.1.77

Fang, Y., & Eglen, R. M. (2017). Three-Dimensional Cell Cultures in Drug Discovery and Development. *SLAS Discovery*, *22*(5), 456–472. https://doi.org/10.1177/1087057117696795/ASSET/IMAGES/LARGE/10.1177_1087057117696795-FIG3.JPEG

Fedorovich, N. E., Alblas, J., Hennink, W. E., Öner, F. C., & Dhert, W. J. A. (2011). Organ printing: The future of bone regeneration? *Trends in Biotechnology*, *29*(12), 601–606. https://doi.org/10.1016/j.tibtech.2011.07.001

Feher, J. (2017). Calcium and Phosphorus Homeostasis II. *Quantitative Human Physiology*, 933–945. https://doi.org/10.1016/B978-0-12-800883-6.00091-4

Finlay, G. A., O'Donnell, M. D., O'Connor, C. M., Hayes, J. P., & Fitzgerald, M. X. (1996). Elastin and collagen remodeling in emphysema. A scanning electron microscopy study. *The American Journal of Pathology*, *149*(4), 1405. /pmc/articles/PMC1865175/?report=abstract

Fiorentini, E., Granchi, D., Leonardi, E., Baldini, N., & Ciapetti, G. (2011). Effects of osteogenic differentiation inducers on in vitro expanded adult mesenchymal stromal cells.

International Journal of Artificial Organs, *34*(10), 998–1011. https://doi.org/10.5301/IJAO.5000001

Florencio-Silva, R., Sasso, G. R. D. S., Sasso-Cerri, E., Simões, M. J., & Cerri, P. S. (2015). Biology of Bone Tissue: Structure, Function, and Factors That Influence Bone Cells. *BioMed Research International*, *2015*(1), 421746. https://doi.org/10.1155/2015/421746

Fogh, J., Fogh, J. M., & Orfeo, T. (1977). One Hundred and Twenty-Seven Cultured Human Tumor Cell Lines Producing Tumors in Nude Mice. *JNCI: Journal of the National Cancer Institute*, *59*(1), 221–226. https://doi.org/10.1093/JNCI/59.1.221

Franceschi, R. T. (1992). The Role of Ascorbic Acid in Mesenchymal Differentiation. *Nutrition Reviews*, *50*(3), 65–70. https://doi.org/10.1111/J.1753-4887.1992.TB01271.X

Franceschi, R. T., & Iyer, B. S. (1992). Relationship between collagen synthesis and expression of the osteoblast phenotype in MC3T3-E1 cells. *Journal of Bone and Mineral Research*, *7*(2), 235–246. https://doi.org/10.1002/JBMR.5650070216

Franz-Odendaal, T. A., Hall, B. K., & Witten, P. E. (2006a). Buried alive: How osteoblasts become osteocytes. *Developmental Dynamics*, *235*(1), 176–190. https://doi.org/10.1002/DVDY.20603

Franz-Odendaal, T. A., Hall, B. K., & Witten, P. E. (2006b). Buried alive: How osteoblasts become osteocytes. *Developmental Dynamics*, *235*(1), 176–190. https://doi.org/10.1002/DVDY.20603

Fröbel, J., Landspersky, T., Percin, G., Schreck, C., Rahmig, S., Ori, A., Nowak, D., Essers, M., Waskow, C., & Oostendorp, R. A. J. (2021). The Hematopoietic Bone Marrow Niche Ecosystem. *Frontiers in Cell and Developmental Biology*, *9*, 705410. https://doi.org/10.3389/FCELL.2021.705410/BIBTEX

Fuchs, R. K., Thompson, W. R., & Warden, S. J. (2019). Bone biology. *Bone Repair Biomaterials*, 15–52. https://doi.org/10.1016/B978-0-08-102451-5.00002-0

Ganss, B., Kim, R. H., & Sodek, J. (1999). Bone sialoprotein. *Critical Reviews in Oral Biology and Medicine*, *10*(1), 79–98. https://doi.org/10.1177/10454411990100010401

Gao, F., Chiu, S. M., Motan, D. A. L., Zhang, Z., Chen, L., Ji, H. L., Tse, H. F., Fu, Q. L., & Lian, Q. (2016). Mesenchymal stem cells and immunomodulation: current status and future prospects. *Cell Death & Disease 2016 7:1*, *7*(1), e2062–e2062. https://doi.org/10.1038/cddis.2015.327

Gauthier, N. C., & Roca-Cusachs, P. (2018). Mechanosensing at integrin-mediated cell–matrix adhesions: from molecular to integrated mechanisms. *Current Opinion in Cell Biology*, *50*, 20–26. https://doi.org/10.1016/J.CEB.2017.12.014

Gęgotek, A., & Skrzydlewska, E. (2023). Ascorbic acid as antioxidant. *Vitamins and Hormones*, *121*, 247–270. https://doi.org/10.1016/BS.VH.2022.10.008

Ghassemi, T., Shahroodi, A., Ebrahimzadeh, M. H., Mousavian, A., Movaffagh, J., & Moradi, A. (2018). Current Concepts in Scaffolding for Bone Tissue Engineering. *Archives of Bone and Joint Surgery*, *6*(2), 90. https://doi.org/10.22038/abjs.2018.26340.1713

Gibson, G. M., Bowman, R. W., Linnenberger, A., Dienerowitz, M., Phillips, D. B., Carberry, D. M., Miles, M. J., & Padgett, M. J. (2012). A compact holographic optical tweezers instrument. *Review of Scientific Instruments*, *83*(11), 113107. https://doi.org/10.1063/1.4768303

Gilbert, T. W., Sellaro, T. L., & Badylak, S. F. (2006). Decellularization of tissues and organs. *Biomaterials*, *27*(19), 3675–3683. https://doi.org/10.1016/J.BIOMATERIALS.2006.02.014

Glowacki, J., & Mizuno, S. (2008). Collagen scaffolds for tissue engineering. *Biopolymers*, *89*(5), 338–344. https://doi.org/10.1002/BIP.20871

Glynn, J., Hollingworth, W., Bhimjiyani, A., Ben-Shlomo, Y., & Gregson, C. L. (2020). How does deprivation influence secondary care costs after hip fracture? *Osteoporosis International : A Journal Established as Result of Cooperation between the European Foundation for Osteoporosis and the National Osteoporosis Foundation of the USA*, *31*(8), 1573–1585. https://doi.org/10.1007/S00198-020-05404-1

Golub, E. E. (2009). Role of matrix vesicles in biomineralization. *Biochimica et Biophysica Acta (BBA) - General Subjects*, *1790*(12), 1592–1598. https://doi.org/10.1016/J.BBAGEN.2009.09.006

Golub, E. E., & Boesze-Battaglia, K. (2007). The role of alkaline phosphatase in mineralization. *Current Opinion in Orthopaedics*, *18*(5), 444–448. https://doi.org/10.1097/BCO.0B013E3282630851

Gómez-Barrena, E., Rosset, P., Lozano, D., Stanovici, J., Ermthaller, C., & Gerbhard, F. (2015). Bone fracture healing: Cell therapy in delayed unions and nonunions. *Bone*, *70*, 93–101. https://doi.org/10.1016/J.BONE.2014.07.033

Gratwohl, A., Baldomero, H., Aljurf, M., Pasquini, M. C., Bouzas, L. F., Yoshimi, A., Szer, J., Lipton, J., Schwendener, A., Gratwohl, M., Frauendorfer, K., Niederwieser, D., Horowitz, M., & Kodera, Y. (2010). Hematopoietic Stem Cell Transplantation: A Global Perspective. *JAMA*, *303*(16), 1617–1624. https://doi.org/10.1001/JAMA.2010.491

Gregory, C. A., Gunn, W. G., Peister, A., & Prockop, D. J. (2004). An Alizarin red-based assay of mineralization by adherent cells in culture: comparison with cetylpyridinium chloride extraction. *Analytical Biochemistry*, *329*(1), 77–84. https://doi.org/10.1016/J.AB.2004.02.002

Grier, D. G. (2003). A revolution in optical manipulation. *Nature 2003 424:6950*, *424*(6950), 810–816. https://doi.org/10.1038/nature01935

Gunn, K. H., Marko, J. F., & Mondragón, A. (2018). Single-Molecule Magnetic Tweezer Analysis of Topoisomerases. *Methods in Molecular Biology (Clifton, N.J.)*, *1703*, 139. https://doi.org/10.1007/978-1-4939-7459-7_10

Gunsilius, E., Gastl, G., & Petzer, A. L. (2001). Hematopoietic stem cells. *Biomedicine & Pharmacotherapy*, *55*(4), 186–194. https://doi.org/10.1016/S0753-3322(01)00051-8

Hadjidakis, D. J., & Androulakis, I. I. (2006). Bone remodeling. *Annals of the New York Academy of Sciences*, *1092*, 385–396. https://doi.org/10.1196/ANNALS.1365.035

Hare, J. M., Traverse, J. H., Henry, T. D., Dib, N., Strumpf, R. K., Schulman, S. P., Gerstenblith, G., DeMaria, A. N., Denktas, A. E., Gammon, R. S., Hermiller, J. B., Reisman, M. A., Schaer, G. L., & Sherman, W. (2009). A Randomized, Double-Blind, Placebo-Controlled, Dose-Escalation Study of Intravenous Adult Human Mesenchymal Stem Cells (Prochymal) After Acute Myocardial Infarction. *Journal of the American College of Cardiology*, *54*(24), 2277–2286. https://doi.org/10.1016/J.JACC.2009.06.055

Hatzimichael, E., & Tuthill, M. (2010). Hematopoietic stem cell transplantation. *Stem Cells and Cloning: Advances and Applications*, *3*(1), 105–117. https://doi.org/10.2147/SCCAA.S6815

Heino, T. J., Hentunen, T. A., & Kalervo Vnnen, H. (2002). Osteocytes inhibit osteoclastic bone resorption through transforming growth factor-β: Enhancement by estrogen*. *Journal of Cellular Biochemistry*, *85*(1), 185–197. https://doi.org/10.1002/JCB.10109

Ho-Shui-Ling, A., Bolander, J., Rustom, L. E., Johnson, A. W., Luyten, F. P., & Picart, C. (2018). Bone regeneration strategies: Engineered scaffolds, bioactive molecules and stem cells current stage and future perspectives. *Biomaterials*, *180*, 143–162. https://doi.org/10.1016/J.BIOMATERIALS.2018.07.017

Hsu, P. Y., Tsai, M. T., Wang, S. P., Chen, Y. J., Wu, J., & Hsu, J. T. (2016). Cortical Bone Morphological and Trabecular Bone Microarchitectural Changes in the Mandible and Femoral Neck of Ovariectomized Rats. *PLOS ONE*, *11*(4), e0154367. https://doi.org/10.1371/JOURNAL.PONE.0154367

Hughes, C. S., Postovit, L. M., & Lajoie, G. A. (2010). Matrigel: A complex protein mixture required for optimal growth of cell culture. *PROTEOMICS*, *10*(9), 1886–1890. https://doi.org/10.1002/PMIC.200900758

Humphrey, J. D., Dufresne, E. R., & Schwartz, M. A. (2014). Mechanotransduction and extracellular matrix homeostasis. *Nature Reviews Molecular Cell Biology 2014 15:12*, *15*(12), 802–812. https://doi.org/10.1038/nrm3896

Ikeda, T., Futaesaku, Y., & Tsuchida, N. (1992). In vitro differentiation of the human osteosarcoma cell lines, HOS and KHOS. *Virchows Archiv B Cell Pathology Including Molecular Pathology*, *62*(1), 199–206. https://doi.org/10.1007/BF02899683/METRICS

Jaiswal, N., Haynesworth, S., … A. C.-J. of cellular, & 1997, undefined. (1997). Osteogenic differentiation of purified, culture-expanded human mesenchymal stem cells in vitro. *Wiley Online LibraryN Jaiswal, SE Haynesworth, AI Caplan, SP BruderJournal of Cellular Biochemistry, 1997•Wiley Online Library*. https://onlinelibrary.wiley.com/doi/abs/10.1002/(SICI)1097-4644(199702)64:2%3C295::AID-JCB12%3E3.0.CO;2-I

Jana, S., Tefft, B. J., Spoon, D. B., & Simari, R. D. (2014). Scaffolds for tissue engineering of cardiac valves. *Acta Biomaterialia*, *10*(7), 2877–2893. https://doi.org/10.1016/J.ACTBIO.2014.03.014

Jauković, A., Abadjieva, D., Trivanović, D., Stoyanova, E., Kostadinova, M., Pashova, S., Kestendjieva, S., Kukolj, T., Jeseta, M., Kistanova, E., & Mourdjeva, M. (2020). Specificity of 3D MSC Spheroids Microenvironment: Impact on MSC Behavior and Properties. *Stem Cell Reviews and Reports 2020 16:5*, *16*(5), 853–875. https://doi.org/10.1007/S12015-020-10006-9

Jennison, T., & Brinsden, M. (2019). Fracture admission trends in England over a ten-year period. *Annals of the Royal College of Surgeons of England*, *101*(3), 208–214. https://doi.org/10.1308/RCSANN.2019.0002/ASSET/IMAGES/RCSANN.2019.0002-8.JPG

Joyce, N., Annett, G., Wirthlin, L., Olson, S., Bauer, G., & Nolta, J. A. (2010). Mesenchymal stem cells for the treatment of neurodegenerative disease. *Regenerative Medicine*, *5*(6), 933–946. https://doi.org/10.2217/RME.10.72

Kadler, K. E., Holmes, D. F., Trotter, J. A., & Chapman, J. A. (1996). Collagen fibril formation. *Biochem. J*, *316*, 1–11. http://portlandpress.com/biochemj/article-pdf/316/1/1/620113/bj3160001.pdf

Kang, H. W., Tabata, Y., & Ikada, Y. (1999). Fabrication of porous gelatin scaffolds for tissue engineering. *Biomaterials*, *20*(14), 1339–1344. https://doi.org/10.1016/S0142-9612(99)00036-8

Kapuscinski, J. (1995). DAPI: a DNA-Specific Fluorescent Probe. *Biotechnic & Histochemistry*, *70*(5), 220–233. https://doi.org/10.3109/10520299509108199

Katz, E. P., & Li, S. T. (1973). Structure and function of bone collagen fibrils. *Journal of Molecular Biology*, *80*(1), 1–15. https://doi.org/10.1016/0022-2836(73)90230-1

Keane, T. J., & Badylak, S. F. (2014). Biomaterials for tissue engineering applications. *Seminars in Pediatric Surgery*, *23*(3), 112–118. https://doi.org/10.1053/J.SEMPEDSURG.2014.06.010

Kennedy, J. W., Tsimbouri, P. M., Campsie, P., Sood, S., Childs, P. G., Reid, S., Young, P. S., Meek, D. R. M., Goodyear, C. S., & Dalby, M. J. (2021). Nanovibrational stimulation inhibits osteoclastogenesis and enhances osteogenesis in co-cultures. *Scientific Reports 2021 11:1*, *11*(1), 1–11. https://doi.org/10.1038/s41598-021-02139-9

Khosla, S., & Monroe, D. G. (2018). Regulation of Bone Metabolism by Sex Steroids. *Cold Spring Harbor Perspectives in Medicine*, *8*(1). https://doi.org/10.1101/CSHPERSPECT.A031211

Kim, B. S., Baez, C. E., & Atala, A. (2000). Biomaterials for tissue engineering. *World Journal of Urology*, *18*(1), 2–9. https://doi.org/10.1007/S003450050002/METRICS

Kim, J. M., Lin, C., Stavre, Z., Greenblatt, M. B., & Shim, J. H. (2020). Osteoblast-Osteoclast Communication and Bone Homeostasis. *Cells 2020, Vol. 9, Page 2073*, *9*(9), 2073. https://doi.org/10.3390/CELLS9092073

Kirkham, G. R., Britchford, E., Upton, T., Ware, J., Gibson, G. M., Devaud, Y., Ehrbar, M., Padgett, M., Allen, S., Buttery, L. D., & Shakesheff, K. (2015). Precision assembly of complex cellular microenvironments using holographic optical tweezers. *Scientific Reports*, *5*, 1–7. https://doi.org/10.1038/srep08577

Koh, N. Y. Y., Miszkiewicz, J. J., Fac, M. L., Wee, N. K. Y., & Sims, N. A. (2024). Preclinical Rodent Models for Human Bone Disease, Including a Focus on Cortical Bone. *Endocrine Reviews*, *45*(4), 493–520. https://doi.org/10.1210/ENDREV/BNAE004

Komori, T. (2010). Regulation of osteoblast differentiation by runx2. *Advances in Experimental Medicine and Biology*, *658*, 43–49. https://doi.org/10.1007/978-1-4419-1050-9_5

Komori, T. (2011). Signaling networks in RUNX2-dependent bone development. *Journal of Cellular Biochemistry*, *112*(3), 750–755. https://doi.org/10.1002/JCB.22994

Kubista, M., Akerman, B., & Norden, B. (1987). Characterization of Interaction between DNA and 4',6-Diamidino-2-phenylindole by Optical Spectroscopy. *Biochemistry*, *26*(14), 4545–4553. https://doi.org/10.1021/BI00388A057/ASSET/BI00388A057.FP.PNG_V03

Kumbar, S. G., James, R., Nukavarapu, S. P., & Laurencin, C. T. (2008). Electrospun nanofiber scaffolds: engineering soft tissues. *Biomedical Materials*, *3*(3), 034002. https://doi.org/10.1088/1748-6041/3/3/034002

Kurosawa, H. (2007). Methods for inducing embryoid body formation: in vitro differentiation system of embryonic stem cells. *Journal of Bioscience and Bioengineering*, *103*(5), 389–398. https://doi.org/10.1263/JBB.103.389

Kwon, M., Kim, B. S., Yoon, S., Oh, S. O., & Lee, D. (2024). Hematopoietic Stem Cells and Their Niche in Bone Marrow. *International Journal of Molecular Sciences 2024, Vol. 25, Page 6837*, *25*(13), 6837. https://doi.org/10.3390/IJMS25136837

Lacroix, D. (2019). Biomechanical aspects of bone repair. *Bone Repair Biomaterials*, 53–64. https://doi.org/10.1016/B978-0-08-102451-5.00003-2

Langenbach, F., & Handschel, J. (2013a). Effects of dexamethasone, ascorbic acid and β-glycerophosphate on the osteogenic differentiation of stem cells in vitro. *Stem Cell Research and Therapy*, *4*(5), 1–7. https://doi.org/10.1186/SCRT328/FIGURES/1

Langenbach, F., & Handschel, J. (2013b). Effects of dexamethasone, ascorbic acid and β-glycerophosphate on the osteogenic differentiation of stem cells in vitro. *Stem Cell Research and Therapy*, *4*(5), 1–7. https://doi.org/10.1186/SCRT328/FIGURES/1

Langhans, S. A. (2018). Three-dimensional in vitro cell culture models in drug discovery and drug repositioning. *Frontiers in Pharmacology*, *9*(JAN), 334617. https://doi.org/10.3389/FPHAR.2018.00006/BIBTEX

Le Blanc, K., Rasmusson, I., Sundberg, B., Götherström, C., Hassan, M., Uzunel, M., & Ringdén, O. (2004). Treatment of severe acute graft-versus-host disease with third party haploidentical mesenchymal stem cells. *Lancet*, *363*(9419), 1439–1441. https://doi.org/10.1016/S0140-6736(04)16104-7

Leach, J., Howard, D., Roberts, S., Gibson, G., Gothard, D., Cooper, J., Shakesheff, K., Padgett, M., & Buttery, L. (2009). Manipulation of live mouse embryonic stem cells using holographic optical tweezers. *Http://Dx.Doi.Org/10.1080/09500340802488565*, *56*(4), 448–452. https://doi.org/10.1080/09500340802488565

Leal, J., Gray, A. M., Prieto-Alhambra, D., Arden, N. K., Cooper, C., Javaid, M. K., & Judge, A. (2016). Impact of hip fracture on hospital care costs: a population-based study. *Osteoporosis International : A Journal Established as Result of Cooperation between the European Foundation for Osteoporosis and the National Osteoporosis Foundation of the USA*, *27*(2), 549–558. https://doi.org/10.1007/S00198-015-3277-9

Lee, K., Seo, I., Choi, M. H., & Jeong, D. (2018). Roles of Mitogen-Activated Protein Kinases in Osteoclast Biology. *International Journal of Molecular Sciences 2018, Vol. 19, Page 3004*, *19*(10), 3004. https://doi.org/10.3390/IJMS19103004

Lee, K. Y., & Mooney, D. J. (2001). Hydrogels for tissue engineering. *Chemical Reviews*, *101*(7), 1869–1879. https://doi.org/10.1021/CR000108X/ASSET/CR000108X.FP.PNG_V03

Lee, N. K., Sowa, H., Hinoi, E., Ferron, M., Ahn, J. D., Confavreux, C., Dacquin, R., Mee, P. J., McKee, M. D., Jung, D. Y., Zhang, Z., Kim, J. K., Mauvais-Jarvis, F., Ducy, P., & Karsenty, G. (2007). Endocrine Regulation of Energy Metabolism by the Skeleton. *Cell*, *130*(3), 456–469. https://doi.org/10.1016/j.cell.2007.05.047

Lin, X., Patil, S., Gao, Y. G., & Qian, A. (2020). The Bone Extracellular Matrix in Bone Formation and Regeneration. *Frontiers in Pharmacology*, *11*, 757. https://doi.org/10.3389/FPHAR.2020.00757/BIBTEX

Lomas, R. J., Gillan, H. L., Matthews, J. B., Ingham, E., & Kearney, J. N. (2001). An evaluation of the capacity of di!erently prepared demineralised bone matrices (DBM) and toxic residuals of ethylene oxide (EtOx) to provoke an in#ammatory response in vitro. *Biomaterials*, *22*, 913–921.

Malaval, L., Modrowski, D., Gupta, A. K., & Aubin, J. E. (1994). Cellular expression of bone-related proteins during in vitro osteogenesis in rat bone marrow stromal cell cultures. *Journal of Cellular Physiology*, *158*(3), 555–572. https://doi.org/10.1002/JCP.1041580322

Malige, A., Gates, C., & Cook, J. L. (2024). Mesenchymal stem cells in orthopaedics: A systematic review of applications to practice. *Journal of Orthopaedics*, *58*, 1–9. https://doi.org/10.1016/J.JOR.2024.06.026

Manolagas, S. C. (2000). Birth and Death of Bone Cells: Basic Regulatory Mechanisms and Implications for the Pathogenesis and Treatment of Osteoporosis. *Endocrine Reviews*, *21*(2), 115–137. https://doi.org/10.1210/EDRV.21.2.0395

Matheson, L. A., Fairbank, N. J., Maksym, G. N., Santerre, J. P., & Labow, R. S. (2006). Characterization of the Flexcell^{TM} Uniflex^{TM} cyclic strain culture system with U937 macrophage-like cells. *Biomaterials*, *27*(2), 226–233. https://doi.org/10.1016/J.BIOMATERIALS.2005.05.070

Matthieu, R., Farkasdi, S., Pons, C., Panayotov, I., Collart-Dutilleul, P.-Y., Taillades, H., Desoutter, A., Bousquet, P., Varga, G., Cuisinier, F., & Yachouh, J. (2015). A New Rat Model for Translational Research in Bone Regeneration. *Https://Home.Liebertpub.Com/Tec*, *22*(2), 125–131. https://doi.org/10.1089/TEN.TEC.2015.0187

Mauney, J. R., Sjostorm, S., Blumberg, J., Horan, R., O'Leary, J. P., Vunjak-Novakovic, G., Volloch, V., & Kaplan, D. L. (2004). Mechanical Stimulation Promotes Osteogenic Differentiation of Human Bone Marrow Stromal Cells on 3-D Partially Demineralized Bone Scaffolds in Vitro. *Calcified Tissue International*, *74*(5), 458–468. https://doi.org/10.1007/S00223-003-0104-7/FIGURES/5

McAllister, R. M., Gardner, M. B., Greene, A. E., Bradt, C., Nichols, W. W., & Landing, B. H. (1971). Cultivation in vitro of cells derived from a human osteosarcoma. *Cancer*, *27*(2), 397–402. https://doi.org/10.1002/1097-0142(197102)27:2<397::AID-CNCR2820270224>3.0.CO;2-X

McCoy, R. J., & O'Brien, F. J. (2010). Influence of Shear Stress in Perfusion Bioreactor Cultures for the Development of Three-Dimensional Bone Tissue Constructs: A Review. *Https://Home.Liebertpub.Com/Teb*, *16*(6), 587–601. https://doi.org/10.1089/TEN.TEB.2010.0370

McGee-Lawrence, M. E., Secreto, F. J., & Syed, F. A. (2013). Animal Models of Bone Disease-B. *Animal Models for the Study of Human Disease*, 391–417. https://doi.org/10.1016/B978-0-12-415894-8.00017-8

Meng, L., Cai, F., Li, F., Zhou, W., Niu, L., & Zheng, H. (2019). Acoustic tweezers. *Journal of Physics D: Applied Physics*, *52*(27), 273001. https://doi.org/10.1088/1361-6463/AB16B5

Middleton, J. C., & Tipton, A. J. (2000). Synthetic biodegradable polymers as orthopedic devices. *Biomaterials*, *21*(23), 2335–2346. https://doi.org/10.1016/S0142-9612(00)00101-0

Mohamed, A. M. F. S. (2008). An Overview of Bone Cells and their Regulating Factors of Differentiation. *The Malaysian Journal of Medical Sciences : MJMS*, *15*(1), 4. /pmc/articles/PMC3341892/

Mohseny, A. B., MacHado, I., Cai, Y., Schaefer, K. L., Serra, M., Hogendoorn, P. C. W., Llombart-Bosch, A., & Cleton-Jansen, A. M. (2011). Functional characterization of osteosarcoma cell lines provides representative models to study the human disease. *Laboratory Investigation 2011 91:8*, *91*(8), 1195–1205. https://doi.org/10.1038/labinvest.2011.72

Mori, T., Kiyono, T., Imabayashi, H., Takeda, Y., Tsuchiya, K., Miyoshi, S., Makino, H., Matsumoto, K., Saito, H., Ogawa, S., Sakamoto, M., Hata, J.-I., & Umezawa, A. (2005). Combination of hTERT and bmi-1 , E6, or E7 Induces Prolongation of the Life Span of Bone Marrow Stromal Cells from an Elderly Donor without Affecting Their Neurogenic Potential . *Molecular and Cellular Biology*, *25*(12), 5183–5195. https://doi.org/10.1128/MCB.25.12.5183-5195.2005/SUPPL_FILE/SUPPLEMENTARYFIG_1S.PDF

Morrison, S. J., & Scadden, D. T. (2014). The bone marrow niche for haematopoietic stem cells. *Nature 2014 505:7483*, *505*(7483), 327–334. https://doi.org/10.1038/nature12984

Mow, V. C., Holmes, M. H., & Michael Lai, W. (1984). Fluid transport and mechanical properties of articular cartilage: A review. *Journal of Biomechanics*, *17*(5), 377–394. https://doi.org/10.1016/0021-9290(84)90031-9

Naing, M. W., & Williams, D. J. (2011). Three-dimensional culture and bioreactors for cellular therapies. *Cytotherapy*, *13*(4), 391–399. https://doi.org/10.3109/14653249.2011.556352

Naito, H., Yoshimura, M., Mizuno, T., Takasawa, S., Tojo, T., & Taniguchi, S. (2013). The advantages of three-dimensional culture in a collagen hydrogel for stem cell differentiation. *Journal of Biomedical Materials Research Part A*, *101*(10), 2838–2845. https://doi.org/10.1002/JBM.A.34578

Neto, A. H. C., Queiroz, K. C., Milani, R., Paredes-Gamero, E. J., Justo, G. Z., Peppelenbosch, M. P., & Ferreira, C. V. (2011). Profiling the changes in signaling pathways in ascorbic

acid/β-glycerophosphate-induced osteoblastic differentiation. *Journal of Cellular Biochemistry*, *112*(1), 71–77. https://doi.org/10.1002/JCB.22763

NICE. (2023, December). *Osteoarthritis: Prevalence [Online]*. National Institute for Health and Care Excellence. https://cks.nice.org.uk/topics/osteoarthritis/background-information/prevalence

Nikukar, H., Reid, S., Tsimbouri, P. M., Riehle, M. O., Curtis, A. S. G., & Dalby, M. J. (2013). *Osteogenesis of Mesenchymal Stem Cells by Nanoscale Mechanotransduction*. https://doi.org/10.1021/nn400202j

O'Brien, F. J. (2011). Biomaterials & scaffolds for tissue engineering. *Materials Today*, *14*(3), 88–95. https://doi.org/10.1016/S1369-7021(11)70058-X

Oftadeh, R., Entezari, V., Spörri, G., Villa-Camacho, J. C., Krigbaum, H., Strawich, E., Graham, L., Rey, C., Chiu, H., Müller, R., Hashemi, H. N., Vaziri, A., & Nazarian, A. (2015). Hierarchical analysis and multi-scale modelling of rat cortical and trabecular bone. *Journal of the Royal Society Interface*, *12*(106), 20150070. https://doi.org/10.1098/RSIF.2015.0070

Oldberg, A., Franzen, A., & Heinegard, D. (1988). The primary structure of a cell-binding bone sialoprotein. *Journal of Biological Chemistry*, *263*(36), 19430–19432. https://doi.org/10.1016/s0021-9258(19)77651-0

Omatsu, Y. (2023). Cellular niches for hematopoietic stem cells in bone marrow under normal and malignant conditions. *Inflammation and Regeneration*, *43*(1), 1–7. https://doi.org/10.1186/S41232-023-00267-5/FIGURES/2

Padgett, M., & Di Leonardo, R. (2011). Holographic optical tweezers and their relevance to lab on chip devices. *Lab on a Chip*, *11*(7), 1196–1205. https://doi.org/10.1039/C0LC00526F

Paluch, E. K., Nelson, C. M., Biais, N., Fabry, B., Moeller, J., Pruitt, B. L., Wollnik, C., Kudryasheva, G., Rehfeldt, F., & Federle, W. (2015). Mechanotransduction: Use the force(s). *BMC Biology*, *13*(1), 1–14. https://doi.org/10.1186/S12915-015-0150-4/TABLES/1

Pampaloni, F., Reynaud, E. G., & Stelzer, E. H. K. (2007). The third dimension bridges the gap between cell culture and live tissue. *Nature Reviews Molecular Cell Biology 2007 8:10*, *8*(10), 839–845. https://doi.org/10.1038/nrm2236

Papachroni, K. K., Karatzas, D. N., Papavassiliou, K. A., Basdra, E. K., & Papavassiliou, A. G. (2009). Mechanotransduction in osteoblast regulation and bone disease. *Trends in Molecular Medicine*, *15*(5), 208–216. https://doi.org/10.1016/J.MOLMED.2009.03.001

Pemberton, G. D., Childs, P., Reid, S., Nikukar, H., Monica Tsimbouri, P., Gadegaard, N., Curtis, A. S. G., & Dalby, M. J. (2015). Nanoscale Stimulation of Osteoblastogenesis from

Mesenchymal Stem Cells: Nanotopography and Nanokicking. *Nanomedicine*, *10*(4), 547–560. https://doi.org/10.2217/NNM.14.134

Pereira, A. L., Galli, S., & Nombela-Arrieta, C. (2024). Bone marrow niches for hematopoietic stem cells. *HemaSphere*, *8*(8), e133. https://doi.org/10.1002/HEM3.133

Perkins, T. T., Smith, D. E., & Chu, S. (1994). Direct Observation of Tube-Like Motion of a Single Polymer Chain. *Science*, *264*(5160), 819–822. https://doi.org/10.1126/SCIENCE.8171335

Peterman, E. J. G., Gittes, F., & Schmidt, C. F. (2003). Laser-induced heating in optical traps. *Biophysical Journal*, *84*(2 I), 1308–1316. https://doi.org/10.1016/S0006-3495(03)74946-7

Pethig, R. (2010). Review Article—Dielectrophoresis: Status of the theory, technology, and applications. *Biomicrofluidics*, *4*(2). https://doi.org/10.1063/1.3456626

Pirosa, A., Gottardi, R., Alexander, P. G., & Tuan, R. S. (2018). Engineering in-vitro stem cell-based vascularized bone models for drug screening and predictive toxicology. *Stem Cell Research & Therapy 2018 9:1*, *9*(1), 1–23. https://doi.org/10.1186/S13287-018-0847-8

Pittenger, M. F., Mackay, A. M., Beck, S. C., Jaiswal, R. K., Douglas, R., Mosca, J. D., Moorman, M. A., Simonetti, D. W., Craig, S., & Marshak, D. R. (1999a). Multilineage potential of adult human mesenchymal stem cells. *Science*, *284*(5411), 143–147. https://doi.org/10.1126/SCIENCE.284.5411.143/SUPPL_FILE/983855S5_THUMB.GIF

Pittenger, M. F., Mackay, A. M., Beck, S. C., Jaiswal, R. K., Douglas, R., Mosca, J. D., Moorman, M. A., Simonetti, D. W., Craig, S., & Marshak, D. R. (1999b). Multilineage potential of adult human mesenchymal stem cells. *Science*, *284*(5411), 143–147. https://doi.org/10.1126/SCIENCE.284.5411.143/SUPPL_FILE/983855S5_THUMB.GIF

Place, E. S., Evans, N. D., & Stevens, M. M. (2009). Complexity in biomaterials for tissue engineering. *Nature Materials 2009 8:6*, *8*(6), 457–470. https://doi.org/10.1038/nmat2441

Raggatt, L. J., & Partridge, N. C. (2010). Cellular and molecular mechanisms of bone remodeling. *Journal of Biological Chemistry*, *285*(33), 25103–25108. https://doi.org/10.1074/jbc.R109.041087

Ramaswamy, G., Bidez, M. W., & Misch, C. E. (2015). Bone Response to Mechanical Loads. *Dental Implant Prosthetics*, 107–125. https://doi.org/10.1016/B978-0-323-07845-0.00006-3

Ramos, T. L., Sánchez-Abarca, L. I., Muntión, S., Preciado, S., Puig, N., López-Ruano, G., Hernández-Hernández, Á., Redondo, A., Ortega, R., Rodríguez, C., Sánchez-Guijo, F., & Del Cañizo, C. (2016). MSC surface markers (CD44, CD73, and CD90) can identify human MSC-derived extracellular vesicles by conventional flow cytometry. *Cell Communication and Signaling*, *14*(1), 1–14. https://doi.org/10.1186/S12964-015-0124-8/FIGURES/6

Rana, D., Zreiqat, H., Benkirane-Jessel, N., Ramakrishna, S., & Ramalingam, M. (2017). Development of decellularized scaffolds for stem cell-driven tissue engineering. *Journal of Tissue Engineering and Regenerative Medicine*, *11*(4), 942–965. https://doi.org/10.1002/TERM.2061

Ravichandran, A., Lim, J., Chong, M. S. K., Wen, F., Liu, Y., Pillay, Y. T., Chan, J. K. Y., & Teoh, S. H. (2017). In vitro cyclic compressive loads potentiate early osteogenic events in engineered bone tissue. *Journal of Biomedical Materials Research Part B: Applied Biomaterials*, *105*(8), 2366–2375. https://doi.org/10.1002/JBM.B.33772

Reznikov, N., Shahar, R., & Weiner, S. (2014). Three-dimensional structure of human lamellar bone: The presence of two different materials and new insights into the hierarchical organization. *Bone*, *59*, 93–104. https://doi.org/10.1016/J.BONE.2013.10.023

Rezwan, K., Chen, Q. Z., Blaker, J. J., & Boccaccini, A. R. (2006). Biodegradable and bioactive porous polymer/inorganic composite scaffolds for bone tissue engineering. *Biomaterials*, *27*(18), 3413–3431. https://doi.org/10.1016/J.BIOMATERIALS.2006.01.039

Riehl, B. D., Donahue, H. J., & Lim, J. Y. (2017). Fluid Flow Control of Stem Cells With Investigation of Mechanotransduction Pathways. *Biology and Engineering of Stem Cell Niches*, 257–272. https://doi.org/10.1016/B978-0-12-802734-9.00017-2

Robertson, S. N., Campsie, P., Childs, P. G., Madsen, F., Donnelly, H., Henriquez, F. L., Mackay, W. G., Salmerón-Sánchez, M., Tsimbouri, M. P., Williams, C., Dalby, M. J., & Reid, S. (2018a). Control of cell behaviour through nanovibrational stimulation: nanokicking. *Philosophical Transactions of the Royal Society A*, *376*(2120). https://doi.org/10.1098/RSTA.2017.0290

Robertson, S. N., Campsie, P., Childs, P. G., Madsen, F., Donnelly, H., Henriquez, F. L., Mackay, W. G., Salmerón-Sánchez, M., Tsimbouri, M. P., Williams, C., Dalby, M. J., & Reid, S. (2018b). Control of cell behaviour through nanovibrational stimulation: nanokicking. *Philosophical Transactions. Series A, Mathematical, Physical, and Engineering Sciences*, *376*(2120). https://doi.org/10.1098/RSTA.2017.0290

Robinson, J. A., Chatterjee-Kishore, M., Yaworsky, P. J., Cullen, D. M., Zhao, W., Li, C., Kharode, Y., Sauter, L., Babij, P., Brown, E. L., Hill, A. A., Akhter, M. P., Johnson, M. L., Recker, R. R., Komm, B. S., & Bex, F. J. (2006). Wnt/β-Catenin Signaling Is a Normal Physiological Response to Mechanical Loading in Bone. *Journal of Biological Chemistry*, *281*(42), 31720–31728. https://doi.org/10.1016/S0021-9258(19)84086-3/ASSET/B2CF3DB1-FF97-4530-B8EF-F627943E3C03/MAIN.ASSETS/GR7.JPG

Robinson, N. B., Krieger, K., Khan, F., Huffman, W., Chang, M., Naik, A., Yongle, R., Hameed, I., Krieger, K., Girardi, L. N., & Gaudino, M. (2019). The current state of animal models in

research: A review. *International Journal of Surgery*, *72*, 9–13. https://doi.org/10.1016/J.IJSU.2019.10.015

Rodrigues, C. V. M., Serricella, P., Linhares, A. B. R., Guerdes, R. M., Borojevic, R., Rossi, M. A., Duarte, M. E. L., & Farina, M. (2003). Characterization of a bovine collagen–hydroxyapatite composite scaffold for bone tissue engineering. *Biomaterials*, *24*(27), 4987–4997. https://doi.org/10.1016/S0142-9612(03)00410-1

Rogers, C. M., Morris, G. E., Gould, T. W. A., Bail, R., Toumpaniari, S., Harrington, H., Dixon, J. E., Shakesheff, K. M., Segal, J., & Rose, F. R. A. J. (2014). A novel technique for the production of electrospun scaffolds with tailored three-dimensional micro-patterns employing additive manufacturing. *Biofabrication*, *6*(3), 035003. https://doi.org/10.1088/1758-5082/6/3/035003

Romaniuk, A., Lyndina, Y., Sikora, V., Lyndin, M., Karpenko, L., Gladchenko, O., & Masalitin, I. (2016). Structural features of bone marrow. *Akjournals.Com*. https://doi.org/10.1556/1646.8.2016.3.3

Rosiak, J. M., & Yoshii, F. (1999). Hydrogels and their medical applications. *Nuclear Instruments and Methods in Physics Research Section B: Beam Interactions with Materials and Atoms*, *151*(1–4), 56–64. https://doi.org/10.1016/S0168-583X(99)00118-4

Rossant, J. (2008). Stem Cells and Early Lineage Development. *Cell*, *132*(4), 527–531. https://doi.org/10.1016/j.cell.2008.01.039

Rowe, P., Koller, A., & Sharma, S. (2023). Physiology, Bone Remodeling. *StatPearls*. https://www.ncbi.nlm.nih.gov/books/NBK499863/

Sánchez-Lanzas, R., Kalampalika, F., & Ganuza, M. (2022). Diversity in the bone marrow niche: Classic and novel strategies to uncover niche composition. *British Journal of Haematology*, *199*(5), 647–664. https://doi.org/10.1111/BJH.18355

Santi, P. A., Aldaya, R., Brown, A., Johnson, S., Stromback, T., Cureoglu, S., & Rask-Andersen, H. (2016). Scanning Electron Microscopic Examination of the Extracellular Matrix in the Decellularized Mouse and Human Cochlea. *JARO - Journal of the Association for Research in Otolaryngology*, *17*(3), 159–171. https://doi.org/10.1007/S10162-016-0562-Z/FIGURES/16

Santos, A., Bakker, A. D., & Klein-Nulend, J. (2009). The role of osteocytes in bone mechanotransduction. *Osteoporosis International*, *20*(6), 1027–1031. https://doi.org/10.1007/S00198-009-0858-5/FIGURES/2

Sarkar, R., & Rybenkov, V. V. (2016). A guide to magnetic tweezers and their applications. *Frontiers in Physics*, *4*(DEC), 231444. https://doi.org/10.3389/FPHY.2016.00048/BIBTEX

Sawkins, M. J., Bowen, W., Dhadda, P., Markides, H., Sidney, L. E., Taylor, A. J., Rose, F. R. A. J., Badylak, S. F., Shakesheff, K. M., & White, L. J. (2013). Hydrogels derived from demineralized and decellularized bone extracellular matrix. *Acta Biomaterialia*, *9*(8), 7865–7873. https://doi.org/10.1016/J.ACTBIO.2013.04.029

Siminovitch, L., McCulloch, E. A., & Till, J. E. (1963). The distribution of colony-forming cells among spleen colonies. *Journal of Cellular and Comparative Physiology*, *62*(3), 327–336. https://doi.org/10.1002/JCP.1030620313

Simmons, P. J., & Torok-Storb, B. (1991). Identification of stromal cell precursors in human bone marrow by a novel monoclonal antibody, STRO-1. *Blood*, *78*(1), 55–62. https://doi.org/10.1182/BLOOD.V78.1.55.55

Singh, A., Gill, G., Kaur, H., Amhmed, M., & Jakhu, H. (2018). Role of osteopontin in bone remodeling and orthodontic tooth movement: a review. *Progress in Orthodontics*, *19*(1), 1–8. https://doi.org/10.1186/S40510-018-0216-2/FIGURES/3

Singh, M. R., Patel, S., & Singh, D. (2016). Natural polymer-based hydrogels as scaffolds for tissue engineering. *Nanobiomaterials in Soft Tissue Engineering: Applications of Nanobiomaterials*, 231–260. https://doi.org/10.1016/B978-0-323-42865-1.00009-X

Sinha, K. M., & Zhou, X. (2013). Genetic and molecular control of osterix in skeletal formation. *Journal of Cellular Biochemistry*, *114*(5), 975–984. https://doi.org/10.1002/JCB.24439

Smith, S. B., Cui, Y., & Bustamante, C. (1996). Overstretching B-DNA: The Elastic Response of Individual Double-Stranded and Single-Stranded DNA Molecules. *Science*, *271*(5250), 795–799. https://doi.org/10.1126/SCIENCE.271.5250.795

Sodek, J., CHEN, J., NAGATA, T., KASUGAI, S., TODESCAN, R., LI, I. W. S., & KIM, R. H. (1995). Regulation of osteopontin expression in osteoblasts. *Annals of the New York Academy of Sciences*, *760*(1), 223–241. https://doi.org/10.1111/J.1749-6632.1995.TB44633.X

Steward, A. J., & Kelly, D. J. (2015). Mechanical regulation of mesenchymal stem cell differentiation. *Journal of Anatomy*, *227*(6), 717–731. https://doi.org/10.1111/JOA.12243

Stolzing, A., Jones, E., McGonagle, D., & Scutt, A. (2008). Age-related changes in human bone marrow-derived mesenchymal stem cells: Consequences for cell therapies. *Mechanisms of Ageing and Development*, *129*(3), 163–173. https://doi.org/10.1016/J.MAD.2007.12.002

Stone, R. N., Frahs, S. M., Hardy, M. J., Fujimoto, A., Pu, X., Keller-peck, C., & Oxford, J. T. (2021). Decellularized Porcine Cartilage Scaffold; Validation of Decellularization and Evaluation of Biomarkers of Chondrogenesis. *International Journal of Molecular Sciences*, *22*(12), 6241. https://doi.org/10.3390/IJMS22126241

Sun, Y., Wan, B., Wang, R., Zhang, B., Luo, P., Wang, D., Nie, J. J., Chen, D., & Wu, X. (2022). Mechanical Stimulation on Mesenchymal Stem Cells and Surrounding Microenvironments in Bone Regeneration: Regulations and Applications. *Frontiers in Cell and Developmental Biology*, *10*, 2. https://doi.org/10.3389/FCELL.2022.808303/BIBTEX

Tare, R. S., Babister, J. C., Kanczler, J., & Oreffo, R. O. C. (2008). Skeletal stem cells: Phenotype, biology and environmental niches informing tissue regeneration. *Molecular and Cellular Endocrinology*, *288*(1–2), 11–21. https://doi.org/10.1016/J.MCE.2008.02.017

Tattersall, L., Davison, Z., & Gartland, A. (2020). Osteosarcoma. *Encyclopedia of Bone Biology*, 362–378. https://doi.org/10.1016/B978-0-12-801238-3.62259-6

Teitelbaum, S. L. (2000). Bone Resorption by Osteoclasts. *Science*, *289*(5484), 1504–1508. https://doi.org/10.1126/SCIENCE.289.5484.1504

Terpos, E., & Christoulas, D. (2015). Involvement of osteocytes in cancer bone niche. *Bone Cancer: Primary Bone Cancers and Bone Metastases: Second Edition*, 65–72. https://doi.org/10.1016/B978-0-12-416721-6.00006-6

Teti, A. (2011). Bone development: Overview of bone cells and signaling. *Current Osteoporosis Reports*, *9*(4), 264–273. https://doi.org/10.1007/S11914-011-0078-8/METRICS

Thompson, W. R., Rubin, C. T., & Rubin, J. (2012). Mechanical regulation of signaling pathways in bone. *Gene*, *503*(2), 179–193. https://doi.org/10.1016/J.GENE.2012.04.076

Timmins, P. A., & Wall, J. C. (1977). Bone water. *Calcified Tissue Research 1977 23:1*, *23*(1), 1–5. https://doi.org/10.1007/BF02012759

Travlos, G. S. (2006a). Histopathology of Bone Marrow. *Toxicologic Pathology*, *34*, 566–598. https://doi.org/10.1080/01926230600964706

Travlos, G. S. (2006b). Normal Structure, Function, and Histology of the Bone Marrow. *Toxicologic Pathology*, *34*, 548–565. https://doi.org/10.1080/01926230600939856

Valenti, M. T., Carbonare, L. D., & Mottes, M. (2016). Osteogenic Differentiation in Healthy and Pathological Conditions. *International Journal of Molecular Sciences 2017, Vol. 18, Page 41*, *18*(1), 41. https://doi.org/10.3390/IJMS18010041

Versus Arthritis. (2024). *The State of Musculoskeletal Health 2024 [Online]*. Versus Arthritis. https://www.versusarthritis.org/media/tffdkiax/va_state-of-msk-report-nov2024-1.pdf

Vimalraj, S. (2020). Alkaline phosphatase: Structure, expression and its function in bone mineralization. *Gene*, *754*, 144855. https://doi.org/10.1016/J.GENE.2020.144855

Voldman, J. (2006). Electrical forces for microscale cell manipulation. *Annual Review of Biomedical Engineering*, *8*, 425–454. https://doi.org/10.1146/ANNUREV.BIOENG.8.061505.095739

Wang, J. H. C. (2006). Mechanobiology of tendon. *Journal of Biomechanics*, *39*(9), 1563–1582. https://doi.org/10.1016/J.JBIOMECH.2005.05.011

Wang, X., Wang, Y., Gou, W., Lu, Q., Peng, J., & Lu, S. (2013). Role of mesenchymal stem cells in bone regeneration and fracture repair: A review. *International Orthopaedics*, *37*(12), 2491–2498. https://doi.org/10.1007/S00264-013-2059-2/METRICS

Weiner, S., & Wagner, H. D. (1998). The material bone: Structure-mechanical function relations. *Annual Review of Materials Science*, *28*(1), 271–298. https://doi.org/10.1146/annurev.matsci.28.1.271

Weissman, I. L. (2000). Stem cells: Units of development, units of regeneration, and units in evolution. *Cell*, *100*(1), 157–168. https://doi.org/10.1016/S0092-8674(00)81692-X/ASSET/529FCFC0-793A-46E6-B5A8-9B3F4DCDA929/MAIN.ASSETS/GR5.JPG

White, L. J., Kirby, G. T. S., Cox, H. C., Qodratnama, R., Qutachi, O., Rose, F. R. A. J., & Shakesheff, K. M. (2013). Accelerating protein release from microparticles for regenerative medicine applications. *Materials Science and Engineering: C*, *33*(5), 2578–2583. https://doi.org/10.1016/J.MSEC.2013.02.020

Willers, C., Norton, N., Harvey, N. C., Jacobson, T., Johansson, H., Lorentzon, M., McCloskey, E. V., Borgström, F., & Kanis, J. A. (2022). Osteoporosis in Europe: a compendium of country-specific reports. *Archives of Osteoporosis*, *17*(1). https://doi.org/10.1007/S11657-021-00969-8

Wilson, A., & Trumpp, A. (2006). Bone-marrow haematopoietic-stem-cell niches. *Nature Reviews Immunology*, *6*(2), 93–106. https://doi.org/10.1038/nri1779

Wu, A. M., Bisignano, C., James, S. L., Abady, G. G., Abedi, A., Abu-Gharbieh, E., Alhassan, R. K., Alipour, V., Arabloo, J., Asaad, M., Asmare, W. N., Awedew, A. F., Banach, M., Banerjee, S. K., Bijani, A., Birhanu, T. T. M., Bolla, S. R., Cámera, L. A., Chang, J. C., … Vos, T. (2021). Global, regional, and national burden of bone fractures in 204 countries and territories, 1990–2019: a systematic analysis from the Global Burden of Disease Study 2019. *The Lancet Healthy Longevity*, *2*(9), e580–e592. https://doi.org/10.1016/S2666-7568(21)00172-0

Xiao, Y., McGuinness, C. A. S., Doherty-Boyd, W. S., Salmeron-Sanchez, M., Donnelly, H., & Dalby, M. J. (2022). Current insights into the bone marrow niche: From biology in vivo to bioengineering ex vivo. *Biomaterials*, *286*, 121568. https://doi.org/10.1016/J.BIOMATERIALS.2022.121568

Yang, J., Cao, C., Wang, W., Tong, X., Shi, D., Wu, F., Zheng, Q., Guo, C., Pan, Z., Gao, C., & Wang, J. (2010). Proliferation and osteogenesis of immortalized bone marrow-derived mesenchymal stem cells in porous polylactic glycolic acid scaffolds under perfusion culture. *Journal of Biomedical Materials Research - Part A*, *92*(3), 817–829. https://doi.org/10.1002/JBM.A.32378

Yao, Q., Cosme, J. G. L., Xu, T., Miszuk, J. M., Picciani, P. H. S., Fong, H., & Sun, H. (2017). Three dimensional electrospun PCL/PLA blend nanofibrous scaffolds with significantly improved stem cells osteogenic differentiation and cranial bone formation. *Biomaterials*, *115*, 115–127. https://doi.org/10.1016/J.BIOMATERIALS.2016.11.018

Yourek, G., McCormick, S. M., Mao, J. J., & Reilly, G. C. (2010). Shear Stress Induces Osteogenic Differentiation of Human Mesenchymal Stem Cells. *Regenerative Medicine*, *5*(5), 713–724. https://doi.org/10.2217/RME.10.60

Zhang, J., Niu, C., Ye, L., Huang, H., He, X., Tong, W. G., Ross, J., Haug, J., Johnson, T., Feng, J. Q., Harris, S., Wiedemann, L. M., Mishina, Y., & Li, L. (2003). Identification of the haematopoietic stem cell niche and control of the niche size. *Nature 2003 425:6960*, *425*(6960), 836–841. https://doi.org/10.1038/nature02041

Zhang, S., Xu, B., Elsayed, M., Nan, F., Liang, W., Valley, J. K., Liu, L., Huang, Q., Wu, M. C., & Wheeler, A. R. (2022). Optoelectronic tweezers: a versatile toolbox for nano-/micro-manipulation. *Chemical Society Reviews*, *51*(22), 9203–9242. https://doi.org/10.1039/D2CS00359G

Zhang, T., Lin, S., Shao, X., Shi, S., Zhang, Q., Xue, C., Lin, Y., Zhu, B., & Cai, X. (2018). Regulating osteogenesis and adipogenesis in adipose-derived stem cells by controlling underlying substrate stiffness. *Journal of Cellular Physiology*, *233*(4), 3418–3428. https://doi.org/10.1002/JCP.26193

Zhao, P., Gu, H., Mi, H., Rao, C., Fu, J., & Turng, L. sheng. (2018). Fabrication of scaffolds in tissue engineering: A review. *Frontiers of Mechanical Engineering*, *13*(1), 107–119. https://doi.org/10.1007/S11465-018-0496-8/METRICS

Zhou, B. O., Yu, H., Yue, R., Zhao, Z., Rios, J. J., Naveiras, O., & Morrison, S. J. (2017). Bone marrow adipocytes promote the regeneration of stem cells and haematopoiesis by secreting SCF. *Nature Cell Biology*, *19*(8), 891–903. https://doi.org/10.1038/NCB3570

Zhu, J. (2010). Bioactive Modification of Poly(ethylene glycol) Hydrogels for Tissue Engineering. *Biomaterials*, *31*(17), 4639. https://doi.org/10.1016/J.BIOMATERIALS.2010.02.044

Zoch, M. L., Clemens, T. L., & Riddle, R. C. (2016a). New insights into the biology of osteocalcin. *Bone*, *82*, 42–49. https://doi.org/10.1016/J.BONE.2015.05.046

Zoch, M. L., Clemens, T. L., & Riddle, R. C. (2016b). New Insights into the Biology of Osteocalcin. *Bone*, *82*, 42. https://doi.org/10.1016/J.BONE.2015.05.046

Zura, R., Xiong, Z., Einhorn, T., Watson, J. T., Ostrum, R. F., Prayson, M. J., Della Rocca, G. J., Mehta, S., McKinley, T., Wang, Z., & Steen, R. G. (2016). Epidemiology of Fracture Nonunion in 18 Human Bones. *JAMA Surgery*, *151*(11). https://doi.org/10.1001/JAMASURG.2016.2775